CONVECTIVE CELLS AND THEIR RELATIONSHIP
TO VORTEX DIFFUSION IN THE WISCONSIN LEVITATED OCTUPOLE

BY

ALICIA BUTCHER EHRHARDT

A thesis submitted in partial fulfillment of the
requirements for the degree of

DOCTOR OF PHILOSOPHY
(Nuclear Engineering)

at the

UNIVERSITY OF WISCONSIN - MADISON

1978

CONVECTIVE CELLS AND THEIR RELATIONSHIP TO
VORTEX DIFFUSION IN THE WISCONSIN LEVITATED OCTUPOLE

Alicia Butcher Ehrhardt
Under the supervision of Associate Professor R. S. Post

Non-azimuthally symmetric floating potential structure
(also called vortices or convective cells) were examined to
determine whether the structure is responsible for enhanced
diffusion in the Octupole. Two gun plasma were used: a
collisionless H plasma ($n_o \sim 5\times10^9 cm^{-3}$, $T_{io} \sim 30eV$); and a col-
lisional He plasma ($n_o \sim 2\times10^{11} cm^{-3}$, $T_{i,e} \sim .2eV$).

The floating potential was measured as a function of
the coordinates perpendicular to the magnetic field by a
Langmuir probe mounted on a cart which could be moved azi-
muthally along the bottom of the Octupole; the results are
presented as two-dimensional contour plots. For a purely
poloidal field, the floating potential was found to be
constant along a magnetic field line, and the two-dimen-
sional contours can be rotated about one of the internal
rings to show the three-dimensional potential structure.

The results can all be understood within the frame-
work of vortex diffusion with a non-thermal energy spec-
trum. For the collisionless plasma in a purely poloidal
field, machine-sized, long-lived convective cells were
observed. The diffusion coefficient calculated using
the toroidal electric field spectrum agrees with measure-
ments by other authors of the diffusion in this plasma.
With an added toroidal field, vortex structure is measured
on the low-field side of the ring; this is consistent with
the theory if the vortices are supported by trapped elec-
trons in the poloidal field mirrors.

For the collisional plasma, at high fields (.5-2kG) vortices are observed. The electric field spectrum is peaked at the longest wavelengths. The diffusion calculated from the spectrum agrees with the previously measured diffusion in the Octupole for this case. At lower fields ($\sim$300G), the vortices are observed to damp when the diffusion in the plasma makes a transition from vortex to classical diffusion scaling. At very low field ($\sim$100G) the cell structure is much smaller than at high fields by the earliest times observed.

With an added weak toroidal field the cells are observed to decay and the longest-wavelength modes are damped preferentially. This agrees with previous diffusion studies that have shown that classical diffusion is dominant for this case.

The physical model that emerges from the theory and the data is as follows. The initial injection process creates a plasma with a large amount of energy (from charge separation) in turbulent vortex modes. During the first few milliseconds, this initial, non-reproducible distribution evolves into a reproducible structure with the energy concentrated at the longest wavelengths. The spectrum then retains this shape, and decays on a much longer time scale than the one required to produce the long-wavelength distribution. Diffusion is caused by the vortex modes when the electric fields become uncorrelated. The magnitude of D_V depends on both the magnitude of the electric fields, and the correlation times. This interpretation also accounts for the enhanced magnitude of D_V obtained in the diffusion studies over the Okuda-Dawson diffusion coefficient, while preserving the scaling.

Richard S. Post

ACKNOWLEDGMENTS

My thanks to Dr. Richard S. Post for his patience and support, and especially for his advice and critiques of the thesis manuscript.

Many helpful conversations with Dr. Jerry Navratil are acknowledged, as well as several interesting discussions with Dr. David Montgomery.

I would like to extend thanks to Mike Zarnstorff for patient answers to endless questions about computers, to Jon Twichell for TADC (the 8-channel, 12-bit digitizer), and to John Laufenberg for technical support on the Octupole. Special thanks also are due to Paul Nonn for tips on constructing the delicate cart probes.

I am grateful also for the encouragement from my boss, Herbert L. Pass, Jr., and that of the Johns Hopkins University - Applied Physics Lab, during the final year of this dissertation.

This thesis is dedicated to my husband, Bill Ehrhardt, who also proofread and helped edit the manuscript, and my family, the Butchers, for their love and support during this undertaking.

TABLE OF CONTENTS

CHAPTER I - INTRODUCTION

The purpose of this thesis is two-fold: first, to present floating potential structure for different plasmas and operating parameters in the Wisconsin Levitated Octupole. Second, to show how the observed potential structure can be used, within the framework of vortex diffusion, to account for enhanced diffusion in the appropriate parameter regimes.

Throughout this paper the words "convective cells", "floating potential cells", and "vortices", will be used interchangeably to mean 'non-azimuthally-symmetric floating potential structure'. [Reference 14 contains a discussion of the various types of cells presented in the literature, as well as a compendium of experimental papers on cells.]

I.1 HISTORICAL BACKGROUND

The presence of non-azimuthally symmetric floating potential structure in the large Wisconsin Levitated Octupole was first reported by Drake[1]. The structure was measured by a Langmuir probe, mounted on a cart which could be moved azimuthally along the bottom of the machine. Drake also noted the effect of the potential contours (open or closed) on the orbits of single particles, including the effect of azimuthal ∇B drifts.

Earlier work on the small Wisconsin Toroidal Octupole had shown asymmetries in the floating potential both during the injection process and subsequent motion of

plasma around the machine[2,3], and during the later phases of the experiments when the plasma was more uniformly distributed[4,5]. Although the plasma was stable to flutes[2], the plasma losses were still much larger than what would be expected from classical diffusion[6], even with the addition of a toroidal field[7].

When the Wisconsin Levitated Octupole was built, experiments were begun to understand the cross-field diffusion. Particle losses to the hoops were measured with striped particle collectors[8,9] by Cavallo[10,11] and Drake[1,12]. For a low density ($n \propto 10^9 cm^{-3}$) collisionless gun plasma in a 1kG average field, a diffusion coefficient was estimated from the measured particle flux to the ring and the density gradient near the ring, and was found to be roughly independent of B, and proportional to an inverse power of the density[13]. In addition to scaling differently than classical diffusion ($D_c \propto n/B^2$), the diffusion coeffi-cient was several orders of magnitude larger (750cm^2/sec [10] vs .2cm^2/sec [14]). Drake[12] also showed that the particle flux was 100 times smaller than expected if the diffusion were Bohm-like ($D_B \propto 1/B$).

Work by Greenwood[13], Drake and Berryman[16], Navratil[15], and others concentrated on first solving the diffusion equation in Octupole coordinates, and then parametrizing the scaling of the diffusion coefficient. These results are summarized in the next section.

I.2   DIFFUSION COEFFICIENT SCALING IN THE WISCONSIN LEVITATED OCTUPOLE

Greenwood[13], and Drake and Berryman[16], set up and solved the diffusion equation in Octupole geometry, and confirmed the independence of the diffusion on B, and determined a density dependence of $n^{-1/2}$ for the collisionless plasma in a 1kG poloidal field.

The next step was to extend the range of plasma parameters available in the Octupole. Navratil[15] built a second plasma gun designed to produce a colder, denser, collisional plasma. Modifications to the capacitor banks allowed operation at very low fields (<40G near the lower outer hoop surface)[25]. Using the diffusion equation, density profile shapes and time decays were then fit to predict the scaling of D over a wide range of parameters[15,25,26].

The results of the profile evolution with a purely poloidal field can all be explained within the framework of vortex diffusion:

$$D_V \propto \frac{1}{B} \frac{T}{\varepsilon} \tag{1.1}$$

where $\varepsilon = 1 + .018n(cm^{-3})/B^2(G)$. Because classical collisional diffusion is always present, it will be dominant over vortex diffusion at sufficiently low fields for a dense enough plasma.

The collisional plasma exhibits classical diffusion ($D_c = D_o n/B^2$) at low fields (B∿100G). As B is increased, there is a transition to vortex diffusion scaling, D proportional to $(T^*/n)^{1/2}$ and independent of B. The

magnitude of D indicates an "effective temperature" T^* of 10^6eV [26].

For the lower-density collisionless plasma, vortex diffusion scaling persisted until the density was reduced to the point where the dielectric constant approached unity, where the scaling became independent of density, and proportional to B^{-1} as predicted by equation (1.1). After an initial cooling period of 20ms[15] (during which the electron temperature decays) the collisionless plasma with $\varepsilon > 1$ had a constant T^* of 10^4eV [25]. T_e was also constant after 20 ms.

With an added toroidal magnetic field the collisionless plasma still diffuses independently of B, but the density dependence changes from $n^{-1/2}$ to n^{-1}, as seen in computer simulations by Kamimura and Dawson[27]. In the case of the collisional plasma, a very small toroidal field ($\sim$20G) added to the poloidal field ($B_t/B_p \sim .03$) doesn't affect the vortex diffusion scaling. A larger toroidal field ($B_t/B_p \sim .1$) causes the diffusion to become classical[28].

I.3 OUTLINE OF THESIS

The work to be described was done concurrently with the diffusion studies. As cell structure was plotted for different regimes, it became apparent that cells could be very large (machine-sized), and very long-lived. Questions then arose as to what effect the cells can have on plasma transport across B, what are the causes (or sources) of cells, and how can they be destroyed or damped. The object of this thesis is to answer those questions.

At the same time as the diffusion and cell studies, theoretical work was being done on two-dimensional plasmas from several points of view. The results are summarized in the following paragraphs, and discussed in more detail later. The importance of the theory lies in that, with a few modifications and extensions, 2-D fluid theory can be used to predict both vortex diffusion and macroscopic vortex structure, remarkably like that observed in the Octupole.

For the purpose of this thesis we will be mainly interested in the plasma regimes where the diffusion scales like "vortex diffusion", $D_v \propto (T^*/n)^{1/2}$, where $T^* \propto T_e$, and independent of B. The vortex diffusion coefficient can be derived in several ways. Taylor and McNamara[17] studied the 2-D electrostatic guiding-center plasma (with $\varepsilon = 1$), and found D for an arbitrary electric field spectrum,

$$D = \frac{1}{B} \ \Sigma \ \frac{E^2(k)}{k^2} \tag{1.2}$$

Okuda and Dawson[18] calculated the diffusion coefficient for a 2-D thermal plasma from the linearized two-fluid equations, without making the guiding-center approximation, to obtain

$$D \propto \frac{T}{n} \ , \quad \text{independent of B} \tag{1.3}$$

Okuda and Dawson pointed out that if the guiding-center approximation is not used, the energy distribution in thermal equilibrium is $\varepsilon E^2/8\pi$ rather than $E^2/8\pi$, with $\varepsilon > 1$, and showed that with this substitution into equation (1.2), Taylor and McNamara's result would be the same as equation (1.3).

The statistical mechanics of the 2-D guiding center plasma with $\epsilon=1$ was examined by Joyce and Montgomery[19,20], and by Taylor[22], for a non-thermal spectrum. For the parallel charged rod model with a certain minimum energy, the equilibrium state was spatially non-homogeneous, corresponding, in the large energy limit, to two counter-rotating vortices filling the system. With a different guiding-center model (a truncated Fourier series representation) Montgomery[23] and Seyler et al.[24] obtained similar results using the theory for a Navier-Stokes fluid: under the proper initial conditions on the energy, both theory and numerical simulation showed macroscopic vortices as the equilibrium solution. The macroscopic cell stuctures measured by Drake, and those presented in this paper are similar in many ways to the macroscopic vortices predicted by the guiding center models, and have an electric field energy much larger than the thermal spectrum.

The Okuda-Dawson diffusion coefficient predicted the correct scaling for the collisionless plasma but was too small by several orders of magnitude if the thermodynamic temperature was used. However, there is no a priori reason to expect the electric field spectrum in the plasma to be given by a thermal spectrum.

In summary, using the various interrelated aspects of the theories, we will attempt to show that the vortex structures observed in the plasma are the source of enhanced vortex diffusion in the appropriate regimes in the Octupole.

Experiments were made with the collisionless gun plasma and with a colder, denser collisional plasma. The plasma parameters are summarized in Table I.1. More
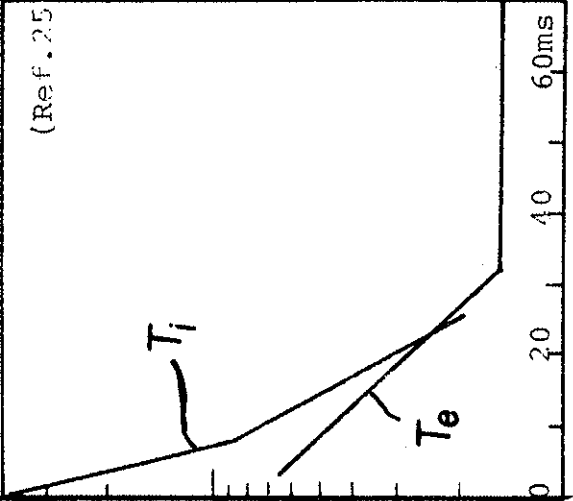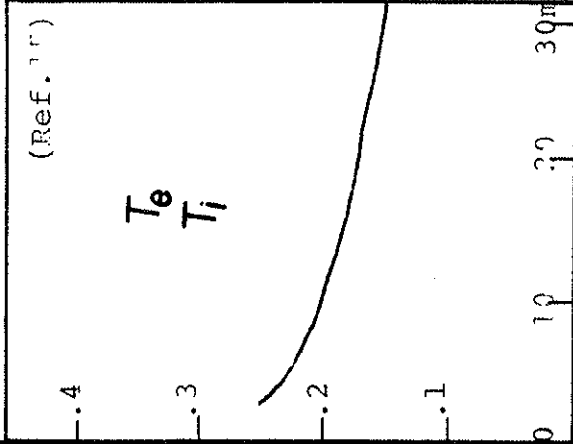
PLASMA PARAMETERS

	I. Hydrogen	II. Helium
Gas		
Density: n_o	5×10^9 cm^{-3}	2×10^{11} cm^{-3}
Background pressure:	3×10^{-7} Torr	6×10^{-6} Torr
	Collisionless	Collisional
Temperature: (eV)		

Table I.1

detailed information about these plasmas is given in
Navratil[15], Chapter II. The poloidal bank voltage was
varied to operate the machine with the same parameters as
in the diffusion studies. Data was also taken with an
added toroidal field (B_t=0-300G on axis). Except where
specifically noted, densities (n) are given in cm^{-3},
temperatures (T_e, T^*) are in eV, and all other quantities
are MKS.

Chapter II presents the diagnostics employed. The
first part of Chapter III shows how the results from 2-D
fluid theory can be considered appropriate to plasmas in
the Octupole with a purely poloidal field, and the second
part covers the development of the theory of vortex diffu-
sion. Chapter IV concerns the application of the theory
to Octupole coordinates, and a discussion on the creation
of convective cells in the Octupole. Chapter V presents
data taken with a poloidal field for both plasmas; and
Chapter VI contains the data for both plasmas with a
poloidal and toroidal field. The conclusions are presented
in Chapter VII, along with recommendations for further
work.

It is strongly suggested that the data portions of
Chapter V be skimmed before reading the theory; this will
make it easier to understand why certain theoretical
developments are investigated. In particular note the
presence (or absence) of non-azimuthally-symmetric float-
ing potential structure and the shape and magnitude of the
azimuthal potential and electric field spectra.

CHAPTER II - DIAGNOSTICS

II.1 GENERAL MACHINE DESCRIPTION

The Wisconsin Levitated Octupole (Fig. 2.1) has been extensively described elsewhere [1,10,13,29]. The basic operating parameters are shown in Table II.1 for maximum voltage on the poloidal field bank (5kV). The Octupole is a pulsed machine; the four internal hoops are the secondary of a 90-to-1 transformer. The magnetic field and lines of constant field strength (mod. B lines) are shown in Fig. 2.2; Octupole coordinates are sketched in Fig. 2.3 (differential operators in this coordinate system are given in Appendix A). The average magnetic field in the private flux is defined[25] as one-half of the average field strength on the surface of the large-major-radius ring; B_{ave} is roughly twice as large in the private flux of the inner hoops.

Data to be presented was all taken with the field crowbarred at 25ms, slightly after peak field. The L/R decay time for the magnetic field varies from ∿95ms near the rings to ∿165ms near the center of the machine[30]. This allows experiments to be done in a slowly-varying magnetic field. A high current SCR and solid state diode[15] allow operation with a crowbarred field even at very low bank voltages. The four internal rings can be levitated for a period of approximately 20ms. A typical time sequence for a levitated experiment is shown in Fig. 2.4.
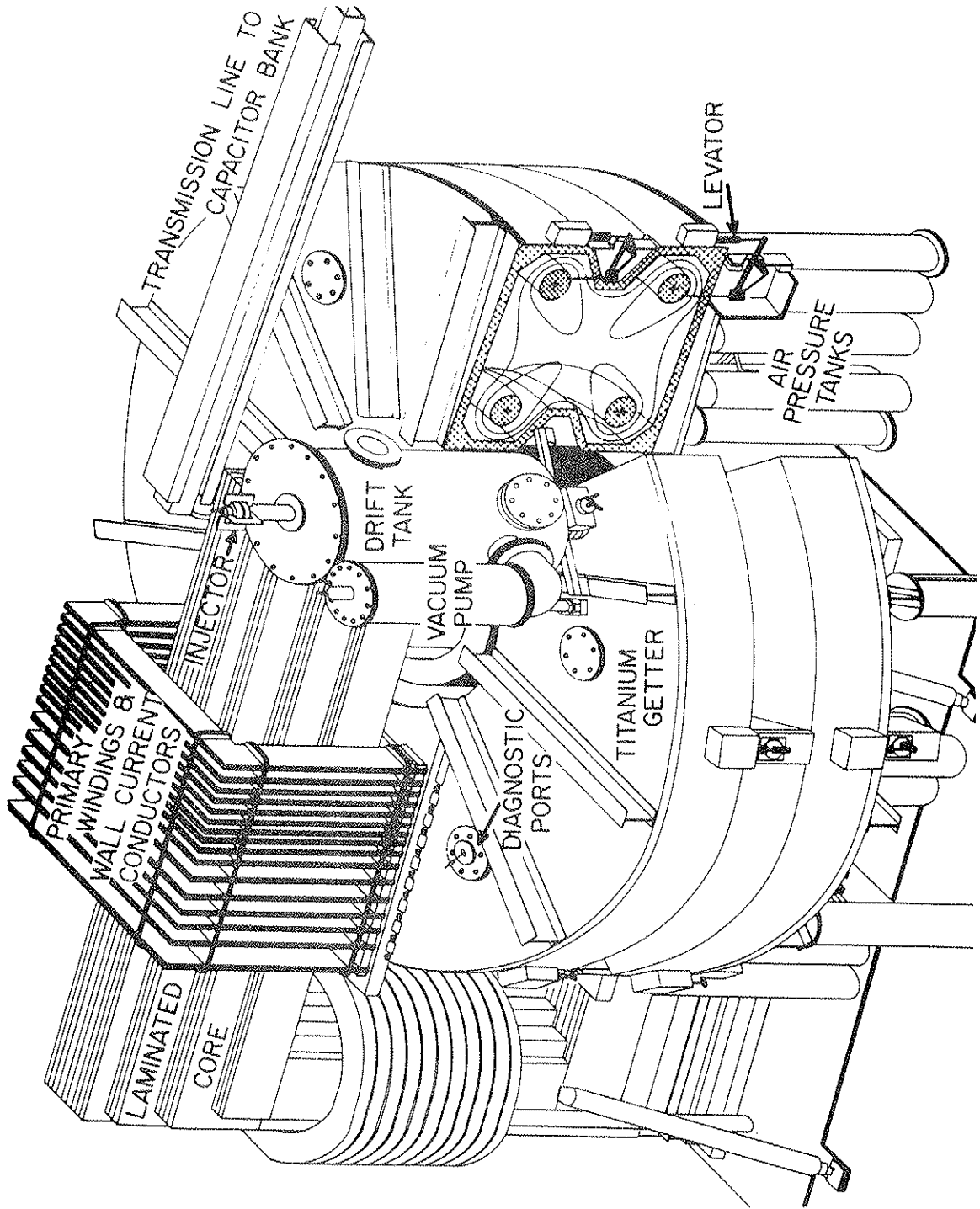
FIG. 2.1   WISCONSIN LEVITATED OCTUPOLE

Table II.1

Operating Parameters of the Levitated Octupole[*]

Current[**]	Wall	Inner Hoop	Outer Hoop
	1.4×10^6 A	0.5×10^6 A	0.25×10^6 A
B max (at surface)[**]	6 kG	12.0 kG	5.5 kG
B min (at surface)[**]	1 kG	5.3 kG	3.4 kG
B_t (on axis)[*]	768 G		

Poloidal bank voltage	5 kV
Energy of pulse	0.6×10^6 J
Total peak core flux	0.72 Wb
Inductance L: $L = N^2 L_o$, N=90, $L_o = 0.6$ µH (calculated)	
Capacitance	0.048 F
Volume of vacuum region	8.6 m^3
Volume inside ψ-critical @ 20ms	7.7 m^3
Hoop minor radius	8.9 cm
Inner hoop major radius	0.99 m
Outer hoop major radius	1.79 m
Half-sine period (B_p)	43 ms
Half-sine period ($B_p + B_t$)	47 ms
Crowbar time	23 ms
Cowbarred field decay time	65-90 ms

*All parameters are for full amplitude at 20 ms.
**Approximate values.
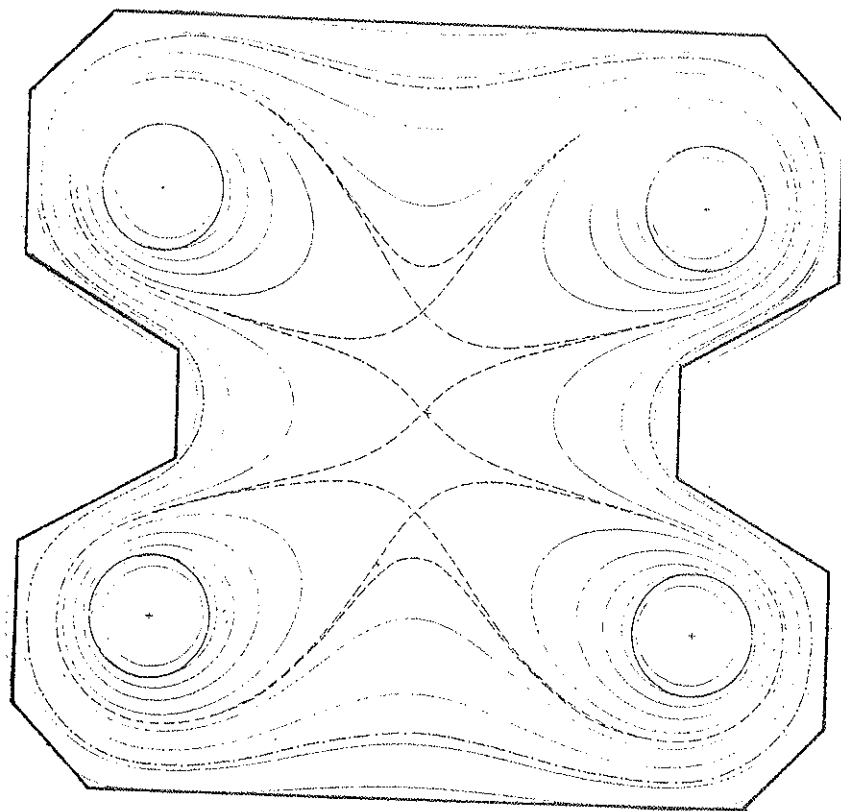
A. MAGNETIC
FIELD
LINES AT
25ms.
FROM
START OF
FIELD
PULSE.
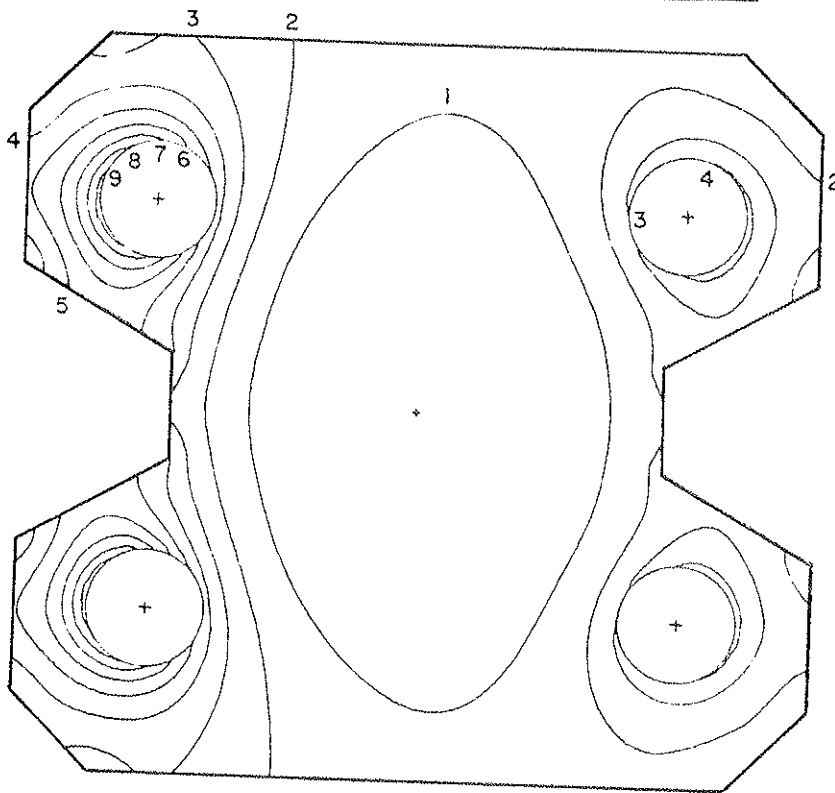
B. LINES OF
CONSTANT
MAGNETIC
FIELD
(MOD B
LINES).

FIG. 2.2 FIELD LINES AND MOD B LINES AT 25ms.

FLUX COORDINATES
$$\hat{\psi} \times \hat{\chi} = \hat{\theta}$$

Upper outer
hoop

z

R

ψ

χ

θ

Lower outer
hoop

FIG. 2.3 OCTUPOLE COORDINATE SYSTEM.

FIG. 2.4   TIME SEQUENCE FOR LEVITATED SHOT (NORMAL
LEVITATION).
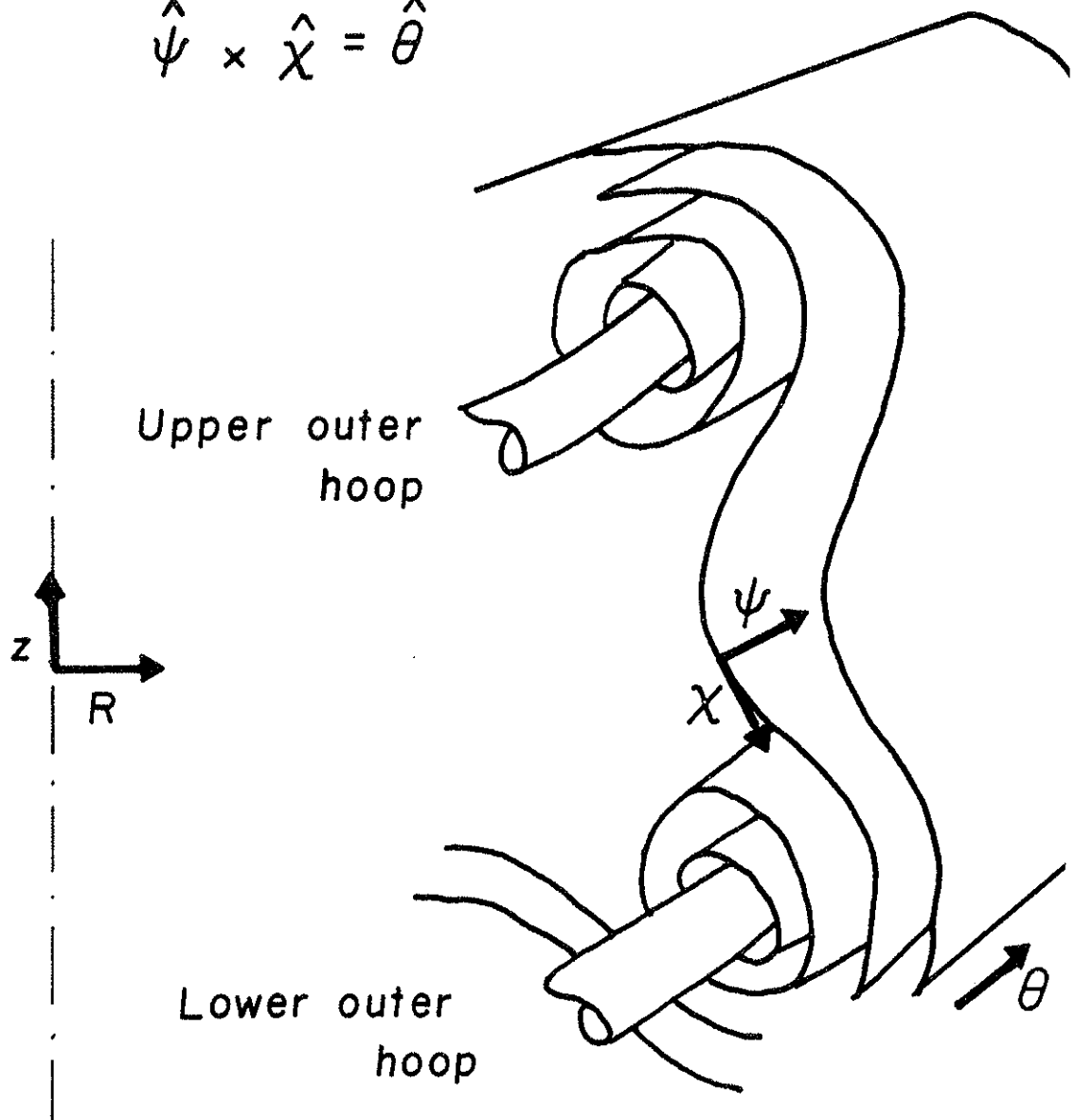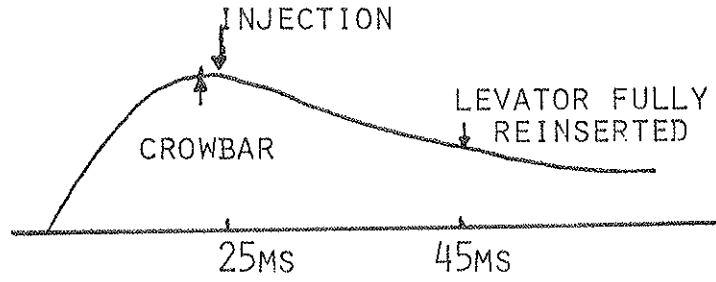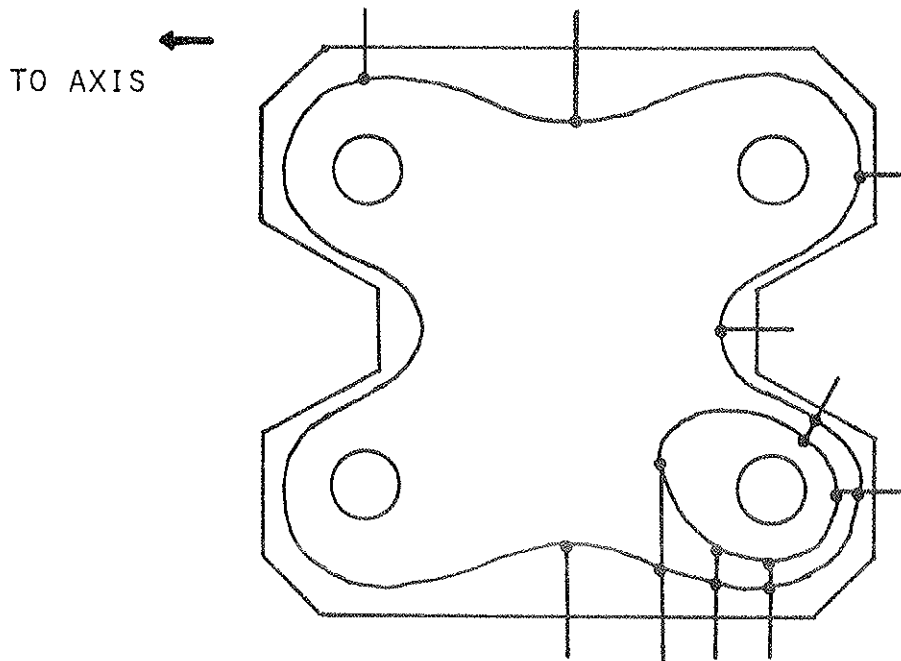

FIG. 2.5   ACCESS PROBE PORTS AT 45°.

II.2 FLOATING POTENTIAL CONTOUR PLOTS

To meet the two thesis objectives stated in Chapter
I, it was necessary to map the three-dimensional potential
structure in the Octupole for a variety of parameters. It
has always been assumed that there would be no potential
gradients along an Octupole field line in a purely poloidal
field because parallel flow would quickly short out local
imbalances. To verify this, the floating potential was
measured with Langmuir probes for several field lines in
the private flux of the lower outer hoop, and several in
the common flux, at various positions along the field
line. At 45° in θ from the gap it is possible to access
the same field line from several different probe ports, as
shown in Fig. 2.5. The field lines cannot be located to
within better than 1/8"-1/4" for several reasons: 1) the
probe tips are $\sim$1/8" long; 2) the dimensions of the
Octupole and those of the flux plots do not exactly
coincide (for example, the lower lid is 1/2" higher than
the flux plot shows); 3) the approximation used for the
current does not duplicate the real current in the walls
and rings. The floating potential profiles measured had
the same shape in ψ, and, to within experimental error in
locating the field lines, the potential was constant along
a field line.

The potential depends only on θ (azimuthal angle) and
ψ (flux surface). Therefore, to obtain a 3-D picture of
the floating potential structure, it is enough to measure
the value of ϕ at one position on each field line as a
function of θ. Drake designed a cart with a movable probe
to do this. The cart is permanently mounted on rails on
the bottom lid, at a radius slightly greater than the

lower inner hoop (at R~1.1m). The cart can be moved through an azimuthal angle of 350°, from -90°, past the gap (at 0°), through 240°. The cart is insulated from the rails and the machine by Teflon wheels, and carries four miniature coaxial signal cables.

The probe located on the cart can carry up to 4 probe tips. As shown in Fig. 2.6, the probe can be rotated through an angle α of approximately 100°, so as to sweep through portions of the lower lid mid-cylinder and inner nose common flux, and the mid-cylinder side of the private flux of both lower hoops. The position of the probe tips along the probe body determines what ψ-surface the probe tips are on at a given value of the angle α.

Several different probes have been used on the cart. They have all had had the general shape indicated in Fig. 2.6, with a shallow bend in the middle. This enables access quite close to the inner nose and inner ring (position A), and allows the probe to avoid hitting the microwave mirrors, etc., on the lower lid (position B). The probe tips were 2mm and 3mm gold balls mounted on 1/32" ceramic stalks; the probe body is of 1/8" ceramic. The probes had either 1 or 2 tips at the bend and 2 tips at the end. The probe frequency response is limited to ~1kHz by the cable capacitance.

The probe angle α can only be changed at an azimuth $\theta=-90^O$ by a special screwdriver tool pushed through from the lower lid; therefore, floating potential scans were taken by setting the angle α at one value, and then moving the cart around the machine to obtain $\phi(\theta)$ on one psi-surface (per probe tip) at a time. The early data was
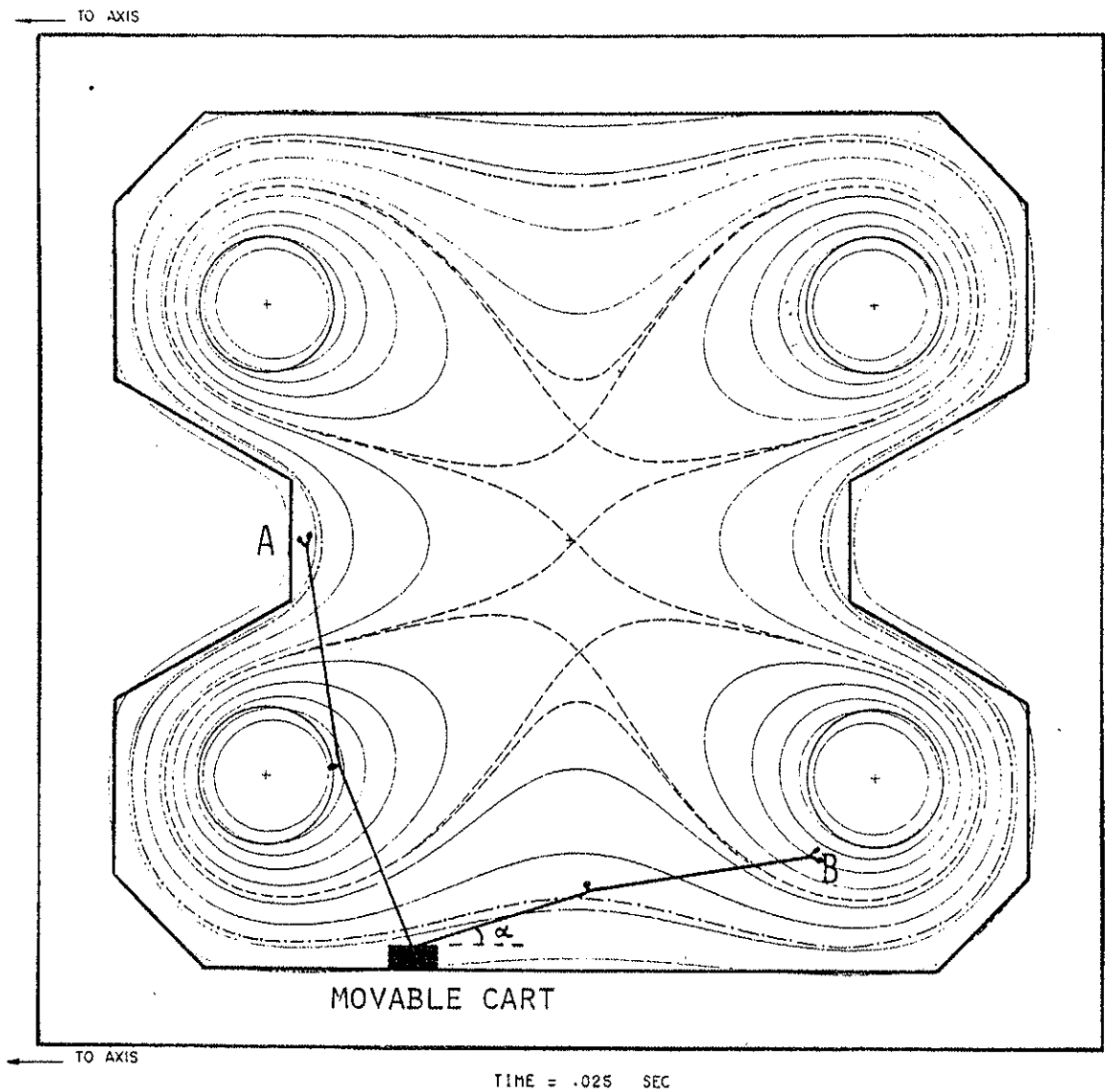
FIG. 2.6 PROBE POSITIONS; CART PROBE.

digitized using the Biomations (with a maximum resolution
of 1/64 full scale). Later data was digitized with Jon
Twichell's TADC (nominally 12 bits) with a minimum resolu-
tion of 1/256, and usually better (1/1024). The data was
taken using Greenwood and Zarnstorff's program CARTSCAN.
The Octupole was operated on a 1-1/2 minute cycle; during
this time the experimenter could examine the digitized
signals from the cart and monitor probes, and a "movie"
showing $\phi(\theta)$ for the current ψ-surface scan. A sample
shot of data, and a scan in θ for one psi-surface, are
shown in Fig. 2.7.

Floating potential contours were plotted by repeating
this procedure for several values of ψ to construct a 2-D
grid. To obtain a 3-D picture, the plots can be rotated
around a ring (stretched to follow the field line shape).
Typically 4 to 6 psi-surfaces per tip were scanned; the
grid step size in θ varied from about $.4^\circ$ to 6° depending
on the experiment. Care was taken to approach grid
points from the same direction to minimize the effect of
backlash from the cart's driving mechanism. A typical
experiment would involve $5 \times 111 = 555$ shots on the machine.
Unfortunately the Octupole could rarely be counted on to
provide that many shots in a row without some of the
operating parameters changing (or a levator leaking,
etc.). The monitor varied enough from day to day to make
it necessary to take all shots for one scan on the same
day. A compromise was reached by not taking every point
on the grid, except where there were obstacles (Fabry-
Perot Interferometer, supports, the gap, gun ports) which
could be expected to affect V_f; or where gaps in the data
were observed in the movie. The missing points were later
interpolated from the rest of the points on the same ψ-
surface.

V_F – 15 CONSECUTIVE SHOTS (He)
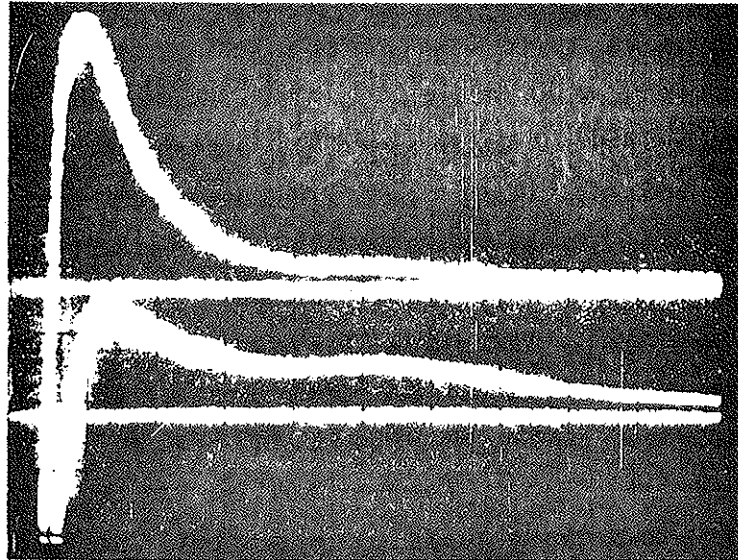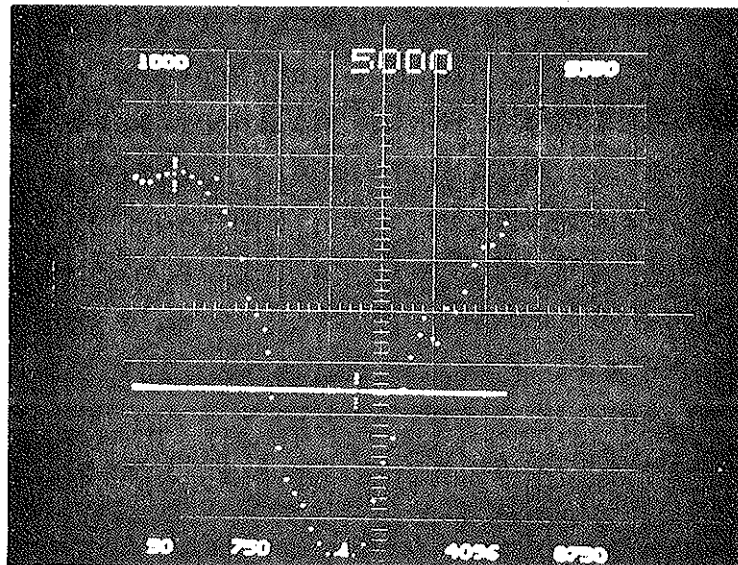

AZIMUTHAL POTENTIAL SCAN (MOVIE)

FIG. 2.7   SAMPLE DATA SHOT AND AZIMUTHAL POTENTIAL SCAN,
COLLISIONAL He PLASMA; LOH

Fig. 2.8 shows an idealized sketch of a contour plot. Plotted data is presented separately for the private and common flux regions. The ψ coordinate is labelled with the value of ψ at 25ms. (Drake's contours are plotted in flux-space, with $\psi=\psi(t)$.) As mentioned by Greenwood[13], the cells are stationary in real space rather than in flux space, and plotting them with respect to ψ_{25ms} emphasizes this. The magnetic field will be normal to the plots, and for a given plot will be either into, or out of, the page, but not both. The physical dimensions for the full range of values in ψ (0-10 Dories) are on the order of 10-50cm, and for 360° in θ, $2\pi R \sim 2\pi(1.4m) \sim 9m$. If the plots were done in real space they would be sectors of a thin annulus, and if shown more nearly to scale, the contour plots would be long and skinny.

A fixed monitor probe was inserted in a probe port on the lower outer hoop to keep track of whether the plasma was reproducible. The changes in V_f for a fixed position of the cart probe did not correlate with changes in V_f at the monitor probe, making it impossible to normalize the data using the monitor probe. Instead a norm was defined as the area under the curve for the monitor signal, and an acceptance criterion was defined about the norm - shots in which the monitor was outside of this percentage were rejected. The acceptance range was 10% about the norm for the high density plasma (this plasma tends to be very reproducible - most shots fell within 5%), and 15% for the low density plasma.

Early work concentrated on producing floating potential contours, and efforts were made to measure all of the structure by using a relatively fine grid of points in θ;

FLOATING POTENTIAL CELLS IN THE OCTUPOLE
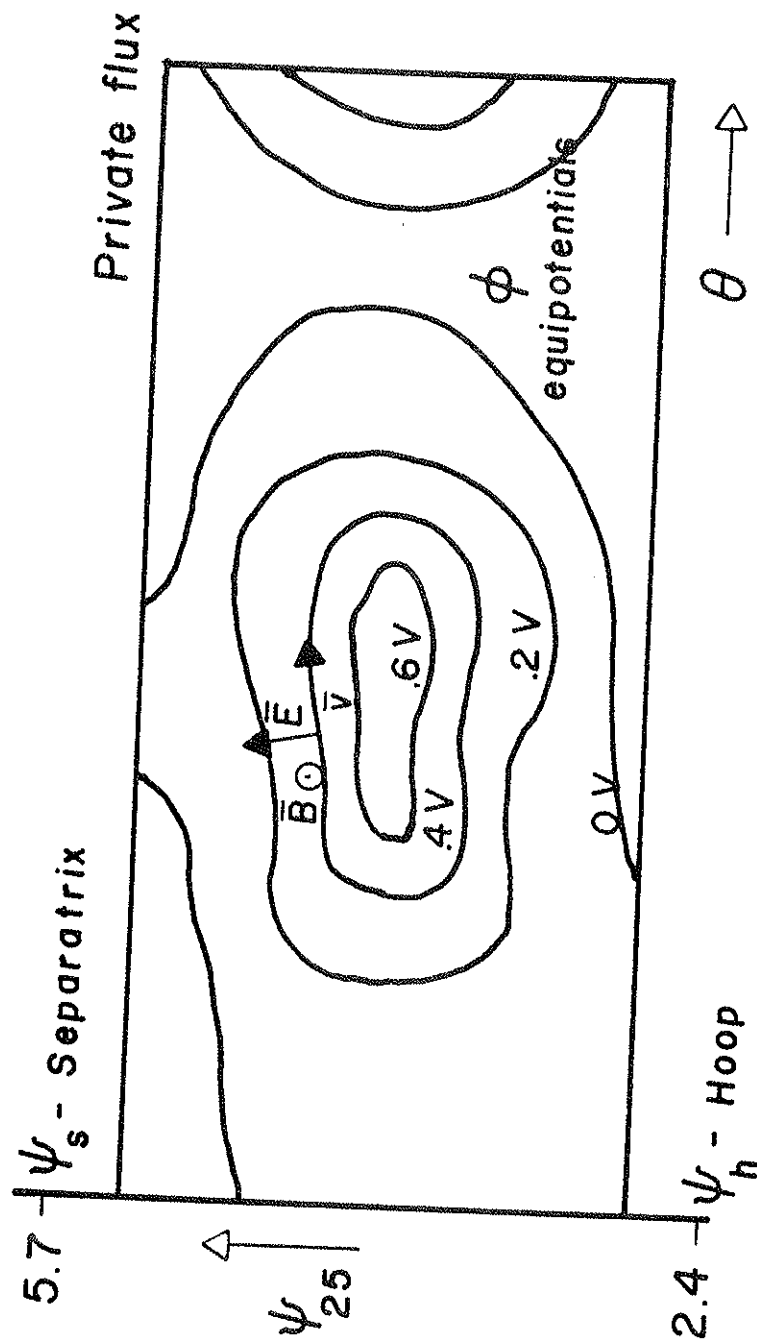
FIG. 2.8. IDEALIZED SKETCH OF FLOATING POTENTIAL CONTOUR PLOT (PRIVATE FLUX).

this limited the azimuthal extent of the plots. When it
later became evident that the spectrum was a useful quanti-
ty, the plots were extended to cover 360°, and the distance
between grid points became larger. Ultimately we will be
analyzing the cross-field diffusion from the turbulent
velocity spectra. In the guiding-center approximation,
drifts in ψ are due to the θ-components of the electric
fields, and vice versa. Because the Octupole is a torus
we are not interested in the diffusion in θ; therefore we
want to obtain the electric field spectrum for the θ-
component, which leads to a drift velocity parallel to $\hat{\psi}$.
This will be discussed further in Chapter IV.

The relationship between the plasma potential and the
floating potential is given by

$$V_p = V_f + \frac{kT_e}{2e} \ln \frac{m_e}{M_i} \tag{2.1}$$

We will be interested in Chapter III in the gradient of
the potential rather than its absolute value. Because the
gun plasmas in the Octupole have uniform temperatures[13,15],
$\nabla T_e = 0$, and therefore we can use the floating potential
contours to infer the electric fields in the plasma.
Schmidt and Schmidt[31] measured electron cooling at the
supports in the small Wisconsin octupole; the effect on
the calculated E-field spectrum of this local cooling will
be discussed in connection with the power spectrum in
Chapter V. The symbols ϕ and V_f will be used interchange-
ably in this paper to represent the floating potential.

II.3 POTENTIAL MEASUREMENTS IN TIME-VARYING FIELDS

Evans[33-35] has pointed out the need to be careful when measuring potential differences in time-dependent fields. The problem when measuring potentials with the cart can be illustrated quite simply: in Fig. 2.9a the potential difference between points A and B includes the emf induced in the measuring circuit by the changing core flux through the loop. The contribution of this azimuthally-dependent vector potential must be removed to find the true potential difference between two points separated in θ. Following Evans, we will first examine the general problem of measuring potentials in a time-varying field, and then discuss two methods which have been used to correct the floating potential data taken with the cart.

Fig. 2.9b shows a circuit which might be used to measure a potential difference. The voltage measured by the voltmeter is given by

$$V = (\phi_A - \phi_B) + emf \tag{2.2}$$

Here the emf is the voltage induced by the changing magnetic flux through the loop including the dotted line, which completes the circuit. There is no question how to calculate the emf _if_ it is known exactly where the dotted portion of the circuit lies (for example, if it is a length of wire). This is because we know how much flux is enclosed by the loop in this case.

When the circuit is closed by a plasma it is impossible to say exactly where the dotted line should lie. However, Evans[35] has shown that one can still calculate the potential
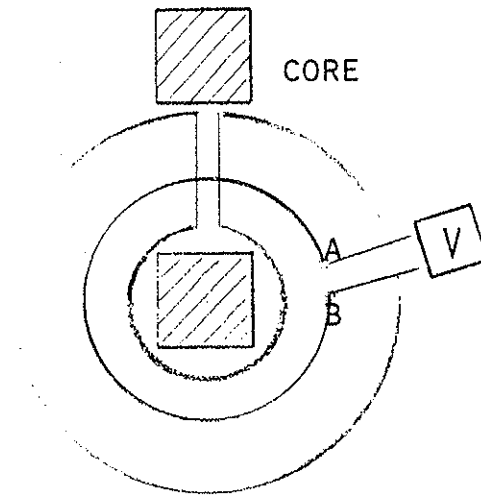
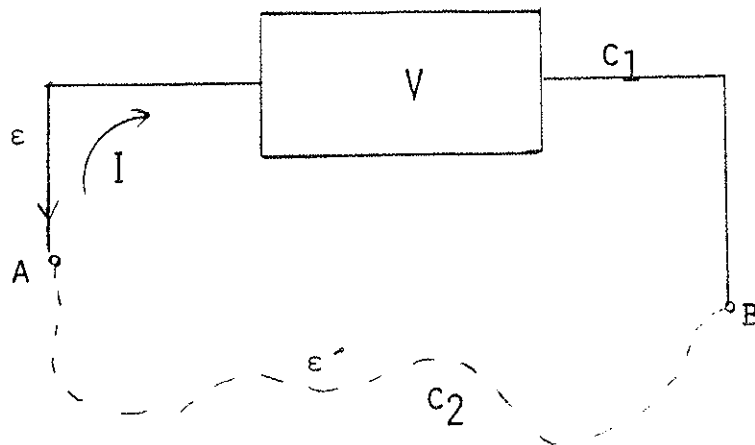FIG. 2.9A POTENTIAL DIFFERENCE OF A CIRCUIT ENCLOSING
THE CHANGING CORE FLUX.

FIG. 2.9B PATH OF INTEGRATION, SHOWING CONTOURS c_1 AND c_2.

difference between A and B without any knowledge of where the closing contour c_2 lies if the vector potential $\vec{A}$ is given along the known part of the measuring circuit (c_1). The potential difference is given by

$$\phi_A - \phi_B = V - \frac{1}{c} \int_{c_1} \frac{\partial A}{\partial t} \cdot d\ell \qquad (2.3)$$

where the voltmeter reading V is independent of gauge, and the potential drop $\phi_A - \phi_B$ will depend on the particular gauge used for $\vec{A}(\Psi, \theta, t)$. To apply equation (2.3) we need to know where the measuring circuit c_1 lies, and the value of $\dot{\vec{A}}$ along the contour c_1.

With this equation in mind we will now discuss two methods of correcting the potential measured by the cart for the effect of $\dot{\vec{A}}$. The first method is the one used by Drake[1] to correct his data; this method was also used to correct the early data taken for this thesis. The effect on the results and a comparison with the second method will be presented at the end of this section.

In the first method the cart was grounded at the oscilloscope where the cables come out of the machine, at -90°. The measuring circuit is shown in Fig. 2.10. It runs from the probe tip (a) through the probe body in a constant-azimuth plane to (b); from (b) to (c) along the center conductor of the μ-dot cable; from (c) to the oscilloscope (d) and back to the grounding point (e), also in a constant-azimuth plane. $\dot{\vec{A}}$ is a purely toroidal vector $(\dot{\vec{A}} = \dot{\vec{A}})$, and $\dot{\vec{A}} \cdot d\ell$ is zero along (ab) and along (cde). To calculate the potential difference between (a) and (e), $\phi_a - \phi_e$, we need to know only the value of $\dot{\vec{A}}$ along the cable (bc).
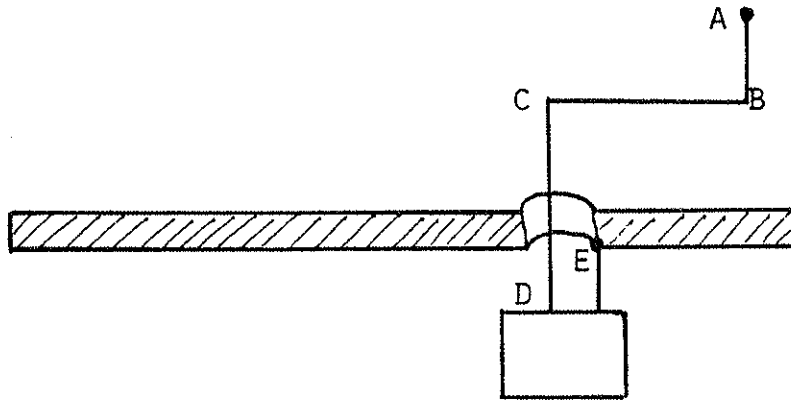
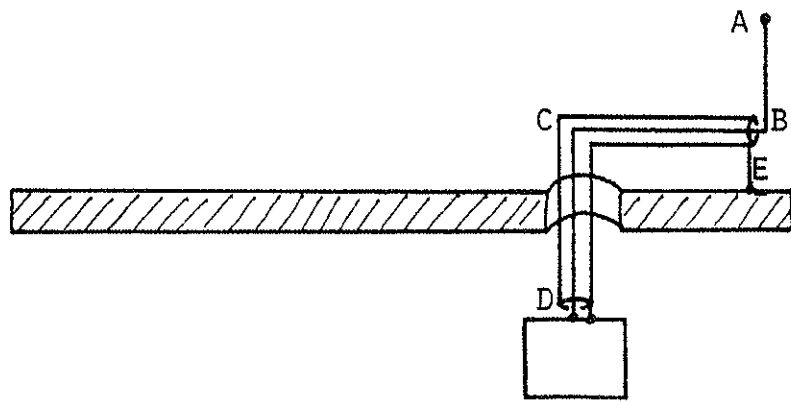FIG. 2.10 MEASURING CIRCUIT (c_1), DRAKE'S METHOD.

FIG. 2.12 MEASURING CIRCUIT (c_1), CART GROUNDED AT
AZIMUTH OF PROBE.

Drake, Greenwood, and Zarnstorff calculated $\vec{A}$ by
assuming that since, when the cart goes once around the
Octupole the measuring circuit (μdot cable) encloses all
the changing core flux, then $\Delta\theta$ degrees around would
enclose $\Delta\theta/360$ of the core flux. Zarnstorff set up an
algorithm[32] to calculate $\vec{A}$ and the correction was made in
the programs θSCAN and CARTSCAN before punching out the
data. The correction is in the form of a constant (which
depends on the poloidal bank voltage) times a function of
t. It hasn't been satisfactorily explained why they chose
to calculate $\vec{A}$ rather than measure it on the machine. The
algorithm for $\vec{A}$ does not take into account that the vector
potential is a function of ψ as well as of θ, and can
therefore be correct for only one psi-surface. In addition,
this algorithm does not account correctly for $\vec{A}$ when the
power crowbar is used, even if the method is correct.

The partial-θ correction is based on Evans' picture
of how the flux penetrates a dielectric plasma[33-35]; if ε
in the plasma is high enough, the flux enters at the gap,
spreads around the machine azimuthally until the flux
becomes azimuthally symmetric in the vacuum between the
plasma and the wall, and then penetrates the plasma
radially towards the rings. If the flux is not azimu-
thally symmetric, the algorithm will not account correctly
for the azimuthal variation of $\vec{A}$ even if it will give the
correct answer for one complete turn.

The separatrix has $\varepsilon\to\infty$ at the field null, and a very
high average ε. For this reason it has always been
assumed that ψ_s would be symmetric in V_f, and that perturba-
tions in the electric field outside ψ_s would not penetrate
into the private flux. Data taken by Drake which showed

large potential variations at the azimuth of the gap inside the separatrix were interpreted by him to mean that something other than the electric field at the gap was responsible for creating structure inside ψ_s. However, as Fig. 2.11 illustrates, even though the flux inside the separatrix may be uniformly distributed, the flux through the measuring circuit (between the wire carried by the cart and the bottom lid) is not azimuthally symmetric because the plasma edge does not have a high average dielectric constant. The cart wires come through the lid at about -90° from the gap. Therefore, the measuring circuit, for measurements near the gap, would enclose more flux than the partial-θ correction algorithm calculates, and the gap structure reported by Drake would be in error. In summary, the main problem with this method is the difficulty in calculating $\vec{A}$ along the measuring circuit, which occurs because the plasma edge is not a perfect con- ductor.

Before discussing the second method of correcting for $\vec{A}$, we want to estimate the magnitude of the possible error in the first method. The gap potential step for a crow- barred field (but without a power crowbar) at 2.5kV on the poloidal bank is on the order of 1.2V at 1ms after injec- tion, and decreases to $\sim$.5V 35ms after injection. If the flux is symmetrically distributed around the machine, this corresponds to a maximum of .0033V/^{O} at the largest bank voltage used in these experiments. If there is as much as a factor of 2 difference in the flux density around the machine, the appropriate $\vec{A}$ correction would be .0067V/^{O} at the gap, for a difference of .0033V/^{O}. These numbers are estimates, and will be used in Chapter V to show that the voltages in the plasma at the gap for the crowbarred case
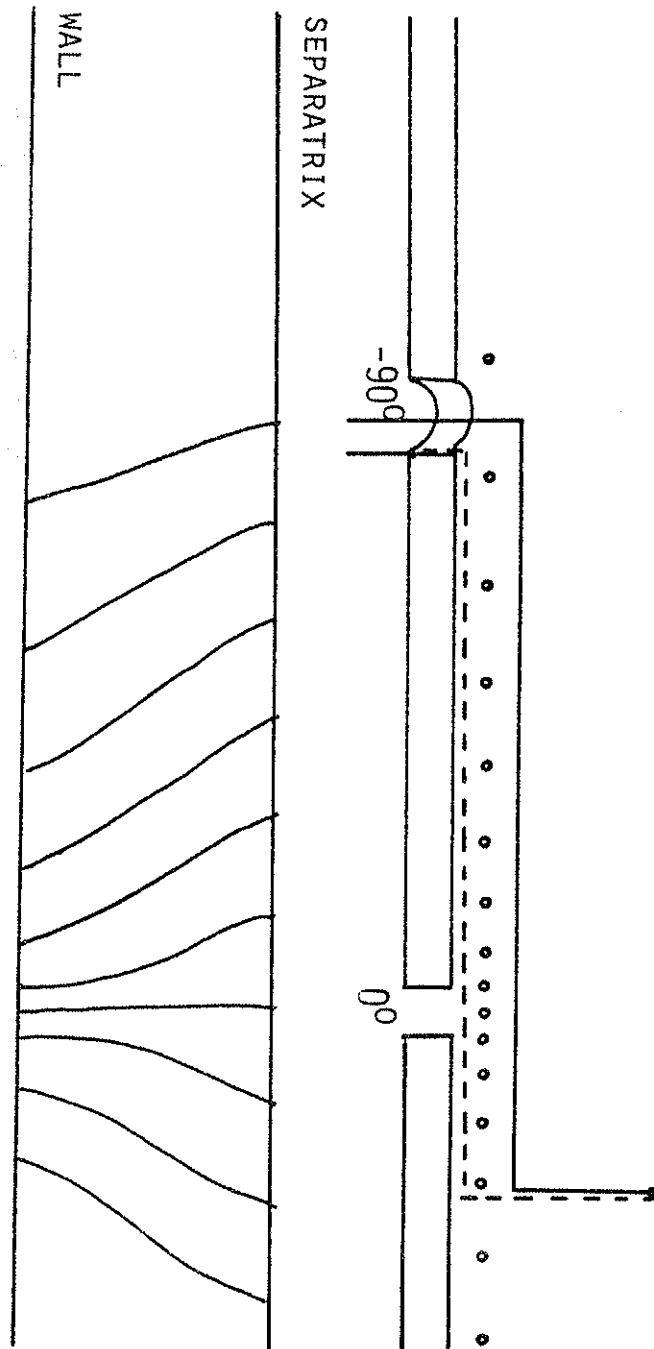
FIG. 2.11 FLUX THROUGH MEASURING CIRCUIT NEAR THE GAP
(DRAKE'S METHOD).

cannot be accounted for by citing an incorrect $\vec{A}$ adjustment.

A second method of correcting for the changing
vector potential, which we prefer, is to ground the cart
at the azimuth of the probe by means of a metal 'finger'
resting on the rail. As shown in Fig. 2.12, there is no
emf generated in the measuring circuit (a coaxial cable)
this way, because $\int \vec{A} \cdot d\ell$ is the same for the center conductor
and outer conductor in magnitude, but opposite in sign.
The only correction necessary to compare voltages at two
azimuths is to subtract the difference between the poten-
tials at the two grounding points, which is simply the IR
drop in the bottom lid. This avoids making any assumptions
about the dielectric coefficient of the plasma, and has
the advantage of being equally as good in the common flux,
where it is not possible to make the argument about the
infinite dielectric on the separatrix.

To recapitulate: Both methods can give the correct
value of the potential at a point, if used correctly.
However, the first method requires knowledge of $\vec{A}$ along
the measuring circuit; also, the algorithm used is incor-
rect if the flux is not azimuthally symmetric. The errors
will be largest for the Octupole operated in a half-sine-
wave mode, and least when the power crowbar is used. In
the second method it is not necessary to know the vector
potential at all. The only assumption made is that the IR
drop in the bottom lid is linear in θ.

II.4 SUMMARY

The object of this chapter has been to show how the
floating potential measurements were made. The information
obtained will be used later to infer the electric field
power spectrum for the plasmas studied, and it will show
how these fields are related to the diffusion.

Any errors in the data corrected by Drake's method
due to assuming incorrectly that the flux was symmetric
are expected to be small because the machine was crowbarred
for all the experiments. This is discussed further in
Chapter V when the data is presented.

CHAPTER III - THEORY OF VORTEX DIFFUSION

The purpose of this chapter is to set up the equations of motion for fluid turbulence, and to derive an equation for the diffusion coefficient from the turbulent velocity spectrum. The suitability of using two-dimensional fluid theory in the Octupole is discussed in Section III.1. In the next section (III.2) we will start from the three-dimensional Navier-Stokes equations with viscosity. Then, as a result of setting $k_z=0$, we will obtain a set of two-dimensional equations, and will examine the predictions of statistical mechanics for this system. In Section III.3 the 2-D equations will be solved for the case of an electrostatic guiding-center (e.s. g.c.) plasma, where the fluid velocity is given by the $\vec{E} \times \vec{B}$ drift velocity. In Section III.4 an expression for the energy spectrum is obtained, and the concept of an 'enhanced temperature' is examined. In Section III.5 we derive an equation for the time-dependent diffusion coefficient given an arbitrary velocity spectrum, and calculate D using the electric field spectrum to infer the velocity spectrum for the guiding-center plasma. In Section III.6 the vortex solutions are discussed, and Section III.7 contains a brief description of the general time behavior of the diffusion coefficient. The final section (III.8) contains a summary of the main points developed.

III.1   USE OF 2-D FLUID THEORY IN THE OCTUPOLE

Previous diffusion studies (summarized in Chapter I) have shown that the theory of vortex diffusion predicts

the correct diffusion scaling in the Octupole, with a purely poloidal field. The scaling holds for both the collisionless plasma, and for the collisional plasma with a magnetic field large enough so that viscous damping does not destroy cells on the experiment time scale. Vortex diffusion has been derived theoretically from fluid theory by Okuda and Dawson[18] for a two-dimensional thermal plasma. It has also been derived for a plasma with an arbitrary (i.e., non-thermal) spectrum using the model of an electrostatic guiding center plasma[17]; this approach has been modified to include the effect of a dielectric plasma $(\omega_p/\omega_c \; 0^{18,21})$. The second method was shown to give results identical to the first for a thermal plasma.

Plasmas in the Octupole are not in thermal equilibrium, and the modified formulation using the guiding center model predicts several interesting features similar to ones that appear in the data, such as large vortices in the potential, and an electric field power spectrum that decreases with wavenumber, k. These features are the result of solving the full non-linear fluid equations. (The Okuda-Dawson derivation is linearized, and does not predict macroscopic vortices; however, it does predict the correct scaling of D with density and magnetic field.) Because macroscopic vortices are seen in the data, we will use the second formulation, and examine the theoretical development leading to vortex solutions in more detail in the following sections.

The guiding-center model requires that the motion of the plasma be due only to the $\vec{E} \times \vec{B}$ drift of the guiding centers, an approximation that is exact only in the limit of very large magnetic fields, where the dielectric cons-

tant is unity, and there is no dielectric screening of the electric fields. However, the dielectric constant for both the collisional plasma, and the collisionless plasma (except for very small n[25]) is much larger than 1, and we will use the $\varepsilon > 1$ modification where appropriate. The effect of the ∇B drift is discussed further in Chapter IV.

A convenient way to view the e.s. g.c. plasma is as a collection of charged rods, infinitely long, aligned parallel to a uniform magnetic field, which interact with each other purely by electrostatic forces, and where the equation of motion is simply $\vec{v} = \vec{E} \times \vec{B}$. As will be shown, in this representation (and another due to Montgomery[36] to be presented in III.3), the equations of motion are formally identical to those of a two-dimensional, inviscid Navier-Stokes fluid.

Before we go on to discuss the fluid theory, we need to examine whether a real plasma in the Octupole can be represented by the model of an e.s. g.c. plasma. The basic assumptions made to obtain macroscopic fluid vortex solutions are that the plasma be inviscid, two-dimensional, and that it have a certain minimum amount of energy of interaction.

The first requirement, that the fluid be inviscid, can be modified; the presence of macroscopic vortex solutions will then depend on the time scale of any dissipative mechanisms present. These damping time scales are discussed in Chapter IV when the theory is applied to the Octupole, and also when the experimental results are presented (V and VI).

The second requirement is actually not as stringent as it appears: J. B. Taylor[21] has shown that 3-D systems have contributions to diffusion from both vortex modes and from collisions. The vortex contribution will dominate if there is sufficient energy in the $k_{//}=0$ modes.

With a poloidal field and no toroidal field, Octupole field lines close upon themselves after one circuit around the minor axis (common flux field lines, $\sim$4m) or around a ring (private flux, $\sim$80cm) in a constant-azimuth plane. If these field lines acquire an excess charge, it cannot be easily dissipated by flow along a field line, but must be damped by collisions. Because the potential and density are constant along a field line (even if B is not), all of the vortex energy is in the $k_{//}=0$ modes, and we will expect to see vortex diffusion except for very dense, cold plasmas in small magnetic fields, or for plasmas where the vortex spectrum has damped away.

The third requirement, that the fluid have a certain minimum energy, ε_m[20], is a difficult one to treat for a real plasma. For the charged rod model in a box, it has been shown that any quantity of positive interaction energy among the charged rods (in addition to the 'self energy') leads to vortex-like solutions. Positive inter-action energies are obtained in the numerical simulations[19] by randomly loading pairs of charged rods initially (random loading of individual rods does not result in a positive interaction energy): the maximum interaction energy comes about when all the positive rods are clumped together on one side of the box, and all the negatively-charged rods are close together on the other. The velocity streamlines

(equipotentials) then correspond to a pattern of macroscopic vortices filling the box.

For the charged-rod model, clumps of charged rods correspond to $\varepsilon > \varepsilon_m$, and spatially homogeneous charge distributions correspond to $\varepsilon < \varepsilon_m$. For a real plasma we will assume the reverse, that a nonhomogeneous charge distribution indicates $\varepsilon > \varepsilon_m$, will lead to macroscopic vortices, and that it is reasonable to try to apply 2-D fluid theory to plasmas in the Octupole with a purely poloidal field.

III.2 NAVIER-STOKES TURBULENCE

The development in this section follows Montgomery[36]. We start from the 3-D equation of motion for a Navier-Stokes fluid, and a condition of incompressibility,

$$\left(\frac{\partial}{\partial t} + \vec{v} \cdot \vec{\nabla}\right)\vec{v} = -\vec{\nabla}p + \nu \nabla^2 v \tag{3.1}$$

$$\vec{\nabla} \cdot \vec{v} = 0 \tag{3.2}$$

where p is the pressure, $\vec{v}$ the fluid velocity, and ν the viscosity. We expand $\vec{v}$ in Fourier components in a large but finite box,

$$\vec{v} = \sum_k \vec{v}(\vec{k}) \, e^{i\vec{k}\cdot\vec{x}} \tag{3.3}$$

Taking the divergence of (3.1) and using (3.2) leads to an equation for $p(\vec{v})$,

$$\nabla^2 p = -\vec{\nabla} \cdot (\vec{v} \cdot \vec{\nabla}\vec{v}) \tag{3.4}$$

The solution depends on the boundary conditions, and can be substituted back into (3.1) to obtain an equation in terms of $\vec{v}(\vec{k})$ alone:

$$\frac{dv_\alpha(\vec{k})}{dt} = \sum_{\vec{p}+\vec{r}=\vec{k}} M_{\alpha\beta\gamma}(\vec{k}) v_\beta(\vec{p}) v_\gamma(\vec{r}) - \nu k^2 v_\alpha(\vec{k}) \qquad (3.5)$$

The first term on the RHS is the non-linear term, with $M_{\alpha\beta\gamma}(\vec{k})$ a coupling coefficient defined by

$$M_{\alpha\beta\gamma} = -\frac{i}{2}\left[k_\beta\left(\delta_{\alpha\gamma} - \frac{k_\alpha k_\gamma}{k^2}\right) + k_\gamma\left(\delta_{\alpha\beta} - \frac{k_\alpha k_\beta}{k^2}\right)\right] \qquad (3.6)$$

Repeated indices are summed over all wavenumbers $\vec{p}$ and $\vec{r}$ which can be added vectorially to give $\vec{k}$.

The second term on the RHS of (3.5) is a viscous damping term, is linear, and represents the dissipation in the fluid. Terms may be added to the RHS of the equation of motion (3.1) to represent other forces such as stirring, water falls, etc. Equivalently, the Fourier transform (FT) of the force can be included on the RHS of equation (3.5).

The rate of change of the energy in the fluid is given by[36]

$$\frac{d}{dt} \sum_k |v_\alpha(k)|^2 = -2\nu \sum_k k^2 |v_\alpha(k)|^2 \qquad (3.7)$$

so that for a case with no viscosity there will be conservation of energy. Again we can add a term to the RHS to represent other dissipative forces, and if the viscosity is small, the other dissipative terms may be responsible for the decay of $\Sigma v^2(k)$. The effect of plasma cooling as

a dissipation mechanism is discussed in section III.3 in
the context of the guiding-center plasma, and in Chapter V
with regard to the experimental data.

We now examine the equations of motion when the flow
is independent of one coordinate. In accordance with a
physical picture of the Octupole, we will pick this to be
the coordinate parallel to $\vec{B}$. The velocity vector will be
in the plane normal to $\vec{B}$. The vorticity vector is defined
as the curl of $\vec{v}$,

$$\vec{\Gamma} = \vec{\nabla} \times \vec{v} = \Gamma \hat{b} \tag{3.8}$$

Turbulence in two dimensions is intrinsically diffe-
rent from that in three dimensions. Taking the curl of
eq. (3.1) gives us an equation for the rate of change of
vorticity in a fluid element,

$$\left(\frac{\partial}{\partial t} + \vec{v}\cdot\vec{\nabla}\right)\vec{\Gamma} = \nu\nabla^2\vec{\Gamma} \tag{3.9}$$

Therefore, in an inviscid two-dimensional fluid, the
vorticity is constant in direction and in magnitude, and
the enstrophy (mean-square vorticity) is also a constant.

In two dimensions equation (3.5) becomes

$$\frac{d\Gamma(\vec{k})}{dt} = \sum_{\vec{p}+\vec{r}=\vec{k}} M(\vec{r},\vec{p})\,\Gamma(\vec{p})\,\Gamma(\vec{r}) - \nu k^2 \Gamma(\vec{k}) \tag{3.10}$$

where

$$M(\vec{r},\vec{p}) = \frac{\hat{b}\cdot(\vec{p}\times\vec{r})}{2}\left(\frac{1}{r^2} - \frac{1}{p^2}\right) \tag{3.11}$$

Equations (3.10) and (3.11) (or (3.5) and (3.6) in
the three-dimensional case) are perfectly general and
exact, merely being limited by a suitable expansion in

Fourier components, and an appropriate set of boundary conditions.

We are interested in comparing the results of the fluid theory to experimental data, and for this we will examine the predictions of theory for 1) diffusion, and 2) relaxation of the velocity spectrum to thermal equilibrium. The development leading to a diffusion coefficient will be postponed until after the g. c. plasma has been introduced, as the actual form of D will depend on the particular velocity spectrum used.

Although equations (3.10) and (3.11), together with an initial distribution, completely determine the behavior of the system, there are an infinite number of them, and we will turn to the methods of statistical mechanics for solutions, treating the v_k as random variables with a probabilistic distribution over an ensemble. Each member of the ensemble will evolve deterministically from the initial conditions; averages over the ensemble will then be used to predict a most probable state for the system. The magnitude of fluctuations about the ensemble averages will be an indication of how good the predictions are.

We will return to the question of dissipation later, but for now we want to examine the equilibrium state for a fluid described by the Navier-Stokes equations with zero viscosity. The first approximation that we will make is to limit the sum over k to a large, but finite, wavenumber k_{max}. This means that we will no longer be able to see any effects which happen on a spatial scale smaller than $1/k_{max}$. This will be done by setting $v_k=0$ for $k>k_{max}$. Physically this is justified in our case by the fact that

the spectra of the velocities will be seen to be rapidly decreasing functions of k. The following discussion will be for the 2-D system in particular because there are certain important features of the equilibrium solutions which do not show up in 3-D.

A phase space, with the real and imaginary parts of the v_k as coordinates[37], can be defined for the system. With $\nu=0$, the divergence of (3.5) proves incompressible flow,

$$\frac{\partial}{\partial v_\alpha(\vec{k})}\left[\frac{dv_\alpha(\vec{k})}{dt}\right] = 0 \qquad (3.12)$$

leading to a Liouville theorem in this phase space. This opens the possibility of ensembles[24], and of a description in terms of an equilibrium 'most probable state' to which the system will relax from given initial conditions. The constants of the motion will be used to construct the equilibrium state.

The constants of the motion which survive the truncation in k-space (Montgomery calls them "rugged" constants of the motion) are the energy, ε, and the enstrophy, Ω (mean-square vorticity),

$$\varepsilon = \sum_k |v_\alpha(k)|^2 \qquad (3.13)$$

$$\Omega = \sum_k k^2 |v_\alpha(k)|^2 \qquad (3.14)$$

Because energy and enstrophy are constant if $\nu=0$, any flow of energy to higher wave-numbers is accompanied by a simultaneous transfer towards the smallest k's, resulting

in large amplitudes at the lowest modes until some kind of equilibrium is reached (whereas in 3-D, $\nu=0$ leads to equipartition of energy). This can be seen from equations (3.13) and (3.14) if we let the spectrum consist of three modes $0<k_1<k_2<k_3$. Then, if we transfer energy from mode k_2 to k_3 (which does not violate $\varepsilon=$constant), we see that the enstrophy is increased. To maintain $\Omega=$constant it is necessary to effect a simultaneous transfer of energy to k_1.

A canonical distribution can be constructed from the energy and the enstrophy:

$$P = C\, e^{(-\alpha\varepsilon-\beta\Omega)} \tag{3.15}$$

where the multipliers α^{-1} and β^{-1} are the "temperatures" for the energy and enstrophy, respectively, and C is a normalizing constant.

The expectation value for v_k^2 is given by

$$<|v_\alpha(k)|^2> = (\alpha + \beta k^2)^{-1} \tag{3.16}$$

where α and β can be found by solving

$$\varepsilon = \sum_k (\alpha + \beta k^2)^{-1} \tag{3.17}$$

$$\Omega = \sum_k k^2(\alpha + \beta k^2)^{-1} \tag{3.18}$$

Because of (3.16), either α or β, but not both, can be negative, subject to energy and enstrophy being positive, which defines three sets of equilibria depending on the ratio Ω/ε.

Regime I $\alpha<0,\ \beta>0$ $\beta k_{min}^2 + \alpha > 0$

Regime II $\alpha > 0$, $\beta > 0$

Regime III $\alpha > 0$, $\beta < 0$ $\alpha + \beta k_{max}^2 > 0$

Regime III ultimately reduces to I if ϵ and Ω are held constant while k_{max} is increased; it corresponds to a spectrum which is an increasing function of k^2 up to k_{max}.

The most interesting is Regime I, where $\alpha < 0$, $\beta > 0$, and $\alpha + \beta k_{min}^2 > 0$; for this regime the thermodynamic temperature is negative[20]. In the limit of very large ϵ the equilibrium consists of a pair of large counter-rotating vortices filling the box, and the spectrum is strongly peaked at the lowest frequency mode. For fluids with less energy, but still in Regime I, the negative temperature states will also consist of vortices. As the energy decreases, the vortices get smaller, and may move about within the box. The equilibria would not then be stationary in configuration space.

Montgomery points out that the usual prediction of a "most probable state" for systems in Regime I may not look like the actual states at all: for example, the ensemble-averaged vorticity density for the case $\alpha < 0$, β slightly greater than $-\alpha/k_{min}^2$ is zero, but the individual realizations of the ensemble have a highly nonuniform distribution of vortices.

The above results are valid for a 2-D system with $\nu = 0$. In three dimensions the only constant of the motion is ϵ, and the corresponding canonical distribution is the familiar one, $P = C \exp(-\epsilon/T)$.

The addition of viscosity to a system in Regime I affects the process of equilibration. There are two time scales, one for the approach to (inviscid) equilibrium, and the other for the thermalization (which depends on ν and any other dissipative mechanisms which can remove energy from the convective cells). If the first time constant is short, or if the system is close to the inviscid-type equilibrium initially, then it seems reasonable that this type of vortex structure would be observed. The critical parameter which determines which regime the system will be in is Ω/ε: systems with energy above some number $\varepsilon_m{}^{20}$ will tend to vortex equilibria; otherwise the final state, even without viscosity, will be a spatially homogeneous equilibrium. Montgomery indicates[23] that although the shape of the spectrum in k may be dependent on whether the viscosity is exactly zero, in two dimensions the addition of a small viscosity still gives qualitatively similar solutions.

Several papers have attempted to determine a numerical value for $\varepsilon_m{}^{19,55}$. (For the charged-rod model, $\varepsilon_m = 0^{19}$.) Unfortunately, they are suitable only for comparison with numerical simulations, where k_{max} and k_{min} are predetermined, and do not readily extend to a real plasma.

III.3   THE ELECTROSTATIC GUIDING-CENTER PLASMA

The equation of motion for the e.s. g.c. plasma is

$$\vec{v} = \frac{\vec{E} \times \vec{B}}{B^2} \qquad (3.19)$$

where B is a uniform magnetic field $\vec{B}=B\hat{b}$. The requirement that E be electrostatic ($\vec{E}=-\vec{\nabla}\phi$, $\vec{\nabla}\times\vec{E}=0$) leads, using (3.19), to a condition of incompressibility, $\vec{\nabla}\cdot\vec{v}=0$, and the equation of continuity for electric charge becomes

$$\left(\frac{\partial}{\partial t} + \vec{v}\cdot\vec{\nabla}\right)\rho = 0 \tag{3.20}$$

Contours of constant ϕ (electrostatic potential) at fixed t are streamlines. The set is closed by Poisson's equation,

$$\vec{\nabla}\cdot\vec{E} = -\nabla^2\phi = \rho/\varepsilon_o \tag{3.21}$$

Two discretizations of the e.s. g.c. plasma have been studied extensively. Montgomery[23] reviews their similarities and differences, and the predictions that can be made for both formulations. The first is the parallel charged rod model[17] in which the charge density is represented by a collection of charged field lines,

$$\rho(\vec{x},t) = \sum_i (e_i/\ell)\,\delta(\vec{x} - \vec{x}_i) \tag{3.22}$$

The other, which will be used in this section, represents the quantities ϕ, ρ, $\vec{E}$, and $\vec{v}$ as a sum of Fourier components as in equation (3.3), up to a maximum wavenumber k_{max},

$$\rho(\vec{x},t) = \sum_k \rho(\vec{k},t)\,e^{i\vec{k}\cdot\vec{x}}, \text{ etc.} \tag{3.23}$$

The transforms will be related by

$$i\vec{k}\cdot\vec{E}(\vec{k},t) = \rho(\vec{k},t)/\varepsilon_O = k^2\phi(\vec{k},t) \qquad (3.24)$$

$$\vec{v}(\vec{k},t) = \hat{b} \times \vec{E}(\vec{k},t)/B \qquad (3.25)$$

with

$$\vec{k} \times \vec{E}(\vec{k},t) = \vec{k}\cdot\vec{v}(\vec{k},t) = 0 \qquad (3.26)$$

Equation (3.20) is identical to the vorticity equation for the inviscid Navier-Stokes fluid (equation (3.9), with $\nu=0$) if we identify ρ with Γ, and we can use the fluid results to write

$$<|v(k)|^2> = <|E(k)|^2>/B^2 = (\alpha + \beta k^2)^{-1} \qquad (3.27)$$

The energy and enstrophy are still given by (3.17) and (3.18); using (3.27) they can be written as

$$\varepsilon = \sum_k |\vec{E}(\vec{k},t)|^2 \qquad (3.28)$$

$$\Omega = \sum_k |\rho(\vec{k},t)|^2 = \sum_k k^2|\vec{v}(\vec{k},t)|^2 \qquad (3.29)$$

All of the predictions from the 2-D fluid solutions carry over, and we can expect to see an energy spectrum peaked at small k values, and conservation of vorticity (charge) in the absence of viscosity.

There is no equivalent to the enstrophy in the charged-rod model. However, macroscopic vortex solutions are also obtained in this discretization as an equilibrium state corresponding, again, to a negative temperature[19,20,21].

A brief discussion of the effect of cooling is in order here. Because the plasma has a finite temperature,

potentials on the order of kT/e can exist in the plasma. Larger fields cannot be supported; if they exist, the plasma particles will quickly rearrange themselves to short out the fields. Thus, if the plasma cools, the electric fields may also drop. It is not clear how this term should be included in the equations for the energy dissipation (3.7). However, if the viscosity is small, as in the case of the collisionless plasma, the total energy decay can be used to find this term, as will be done in Chapter V.

III.4 ENERGY SPECTRUM

The energy in the vortex spectrum resides in the electric fields in the plasma, and is due to charge separation. For a plasma in thermal equilibrium, the relation between the energy in the electric field fluctuations and the thermodynamic temperature is given by

$$\frac{T(k)}{2} = \frac{<E(k)^2>}{8\pi} L_{/\!/} L_{\perp}^2 \tag{3.30}$$

with $L_{/\!/}$ and $L_{\perp}$ the dimensions of the system. The thermal equilibrium spectrum is independent of k (equipartition of energy) until $k^2\lambda_D^2$ becomes ~ 1.

For a non-thermal plasma we can define an effective temperature T^* in the same way as equation (3.30). However, there is no reason the energy should be divided equally among the modes. T^* can be much larger than the thermodynamic temperature. The "negative temperature" phenomenon that leads to macroscopic vortices is an example of a non-thermal spectrum.

Equation (3.30) is an adequate representation of the vortex spectrum for the electrostatic guiding-center plasma in thermal equilibrium. If the g.c. approximation is not made, Okuda and Dawson have pointed out[18] that the energy T/2 per mode is shared by the zero-frequency vortex modes and by modes above the gyrofrequency (upper-and lower-hybrid waves and Bernstein waves); the energy associated with a vortex mode is not $E_k^2/8\pi$, but $\varepsilon E_k^2/8\pi$. This changes the relationship between the temperature and the electric field fluctuations responsible for vortex diffusion.

Plasmas in the Octupole have $\omega_p/\omega_c >> 0$, and are not in thermal equilibrium. The measured spectrum E_k^2 corresponds to the part of the spectrum below the gyrofrequency, and is related to the effective temperature T^* by

$$\frac{T^*}{\varepsilon} = \sum \frac{T(k)^*}{\varepsilon} \propto \Sigma E(k)^2 \qquad (3.31)$$

III.5 DEVELOPMENT OF THE DIFFUSION COEFFICIENT

If the velocity for all the particles in an ensemble is known at all times, the coefficient of self-diffusion can be written as

$$\overset{\leftrightarrow}{D} = \left\langle \frac{\vec{x}(0)\,\vec{x}(t)}{2t} \right\rangle \qquad (3.32)$$

where

$$\vec{x}(t) = \int_0^t \vec{V}(t)\ dt \qquad (3.33)$$

Here $\vec{V}(t)$ is the Lagrangian velocity of the particle. To find an expression for D in terms of the more convenient

Eulerian statistics of the system (such as might be measured by probes at fixed points), we need to find an approximation for $\vec{V}(t)$ in terms of $\vec{v}(\vec{x},t)$. Using (3.3),

$$\vec{D} = \int_0^t <\vec{V}(0) \ \vec{V}(t)> \ dt \qquad (3.34)$$

$$= \int_0^t \sum_{k_1} \sum_{k_2} <\vec{v}(\vec{k}_1,0) \ \vec{v}^*(\vec{k}_2,t) \ \exp[-i\vec{k}_2 \cdot \vec{x}(t)]>dt$$

The ensemble average is approximated by Taylor and McNamara (based on a hypothesis by Corrsin[38]) as

$$<\vec{v}(\vec{k}_1,0) \ \vec{v}^*(\vec{k}_2,t)> \ <\exp[-i\vec{k}_2 \cdot \vec{x}(t)]> \qquad (3.35)$$

$\vec{x}(t)$ depends on all the Fourier coefficients at times between 0 and t, so this approximation assumes the velocity field has a broad enough spectrum so that $\vec{x}(t)$ depends only weakly on the modes $\vec{k}_1$ and $\vec{k}_2$.

To evaluate the ensemble average of the exponential, Taylor and McNamara make the assumption that the fluctuating electric field can be represented by a normal distribution (Appendix A of Ref. 17) so the probability of $\vec{E}(t)$ can be expressed in terms of the desired autocorrelation,

$$<\exp[-i\vec{k}\cdot\vec{x}]> \ = \ \exp[-k^2R] \qquad (3.36)$$

where
$$R(t) = \frac{1}{2}\int_0^t dt_1 \int_0^t dt_2 \ <\vec{V}(t_1) \ \vec{V}(t_2)> \qquad (3.37)$$

Essentially this corresponds to a Lagrangian auto-correlation that varies as

$$S_k(t) = <|E_k(t)|^2> \exp[-k^2 R(t)] \tag{3.38}$$

This approximation was tested numerically[39] and was found to give reasonable agreement, with 'experimental' autocorrelations showing slightly weaker damping than predicted by the theory.

R(t) is the mean dispersion of a group of diffusing particles, and is given by the differential equation

$$\frac{S(t)}{B^2} = \frac{d^2 R(t)}{dt^2} = \frac{1}{2B^2} \sum_k E^2(\vec{k}, t) \, e^{-2k^2 R(t)} \tag{3.39}$$

where the velocity $\vec{E}(\vec{k}, t)/B$ is the solution of equation (3.5) or (3.10) with any additional forces added to the right hand side.

The diffusion equation is given by the first integral of (3.39), and the integration can be performed explicitly if E_k is not a function of t.

$$\frac{D(t)}{2} = \frac{dR}{dt} = \frac{1}{2B^2} \sqrt{\sum_k \frac{<E^2(k)>}{k^2} [1 - e^{-2k^2 R(t)}]} \tag{3.40}$$

For very long times R(t) is unbounded, and the diffusion equation is given by

$$D_\infty = \frac{1}{B} \left[\sum_k \frac{E_k^2}{k^2} \right]^{1/2} \tag{3.41}$$

In addition to the total amount of vortex energy available, its distribution in k-space is important in determining the magnitude of the diffusion; the diffusion is dominated by the longest wavelength modes unless $E^2(k)$

increases faster than k^2. For the thermal spectrum, E^2 is independent of k (up to $k^2 \lambda_D^2 \sim 1$), and for the data from the Octupole to be presented, $E(k)^2$ decreases rapidly as k is increased; this means that the first few modes are the most damaging to confinement. This was also shown in a numerical simulation by Okuda and Dawson, in which they artificially removed the smallest k-modes and found that diffusion was greatly reduced, even though the energy in those modes was a small fraction of the total energy[18]. Taylor and McNamara[17] also pointed out that the longest wavelength fluctuations are the slowest to disperse, and the modes for which the guiding-center approximation is most accurate.

The time dependence of (3.40) will be discussed in some detail in the next section, but before we do, it is convenient to look at the forms that result for D_∞, given various electric field spectra. Taylor and McNamara used the thermal equilibrium spectrum for the two-dimensional plasma in the g.c. limit,

$$<E_k^2> = \frac{4\pi KT}{\ell} \frac{1}{1+k^2\lambda_D^2} \qquad \text{(c.g.s.)} \qquad (3.42)$$

which, replacing the sum by an integral cut off at $k=2\pi/L$, leads to

$$D = \frac{c}{B} \left(\frac{2KT}{\ell} \ln \frac{L}{2\pi\lambda} \right)^{1/2} \propto \sqrt{\frac{T}{B}} \qquad \text{(c.g.s.)} \qquad (3.43)$$

Thus, for the 2-D g.c. plasma the diffusion coefficient has a Bohm-like dependence on field strength, even in thermal equilibrium.

The model described is valid when $B \to \infty$, or to be more precise, when $(\omega_p/\omega_c)^2 \ll 1$. With finite ω_p/ω_c, we replace E^2 with ϵE^2. Since E_k^2 is not a function of k at low k's for the thermal spectrum, it can be taken out of the sum[25,26] in equation (3.41), and, converting to an integral, we obtain the Okuda-Dawson diffusion coefficient,

$$D_{OD} = \frac{2}{B}\left[\frac{T}{\epsilon L_{/\!/}} \ln \frac{k_{max}}{k_{min}}\right]^{1/2} \propto \frac{1}{B}\sqrt{\frac{T}{1+.019n/B^2}} \qquad (3.44)$$

so that at large fields D reduces to the previous case, but if $\epsilon > 1$, $D \propto (T/n)^{1/2}$. For a non-thermal spectrum, we replace $T(k)$ with $T^*(k)$, as in equation (3.31). When E_k^2 is a function of k, there is in general no simple analytical expression for D.

III.6 FLUID SOLUTIONS; BOUNDARY CONDITIONS

Time-dependent solutions $\vec{v}(\vec{x},t)$ can be obtained from simulations by plotting the equipotentials (streamlines) at any given time, but there is no general theory to predict what they will be, or how they will develop in time. However, for a conservative system in equilibrium, the equilibrium distribution can be used to write Poisson's equation[20] as

$$\nabla^2 \phi = -4\pi e n_o \left[\exp(-\beta e \phi) - \exp(\beta e \phi)\right] \qquad (3.45)$$

where $\beta < 0$ is the coefficient corresponding to the negative temperature. This equation can be made dimensionless on a square box of side L by letting $\Psi = e\beta\phi$, $\lambda^2 = -8\pi e^2 n\beta L^2$:

$$\nabla^2 \Psi + \lambda^2 \sinh\Psi = 0 \qquad (3.46)$$

Analytic solutions to the $\sinh\Psi$ equation have not been found; the numerical solutions (found by McDonald[48] by using special iterative techniques) for a given energy and λ are not unique. The most probable state for a given λ is determined by the solution with maximum entropy,

$$S = \ln W = 2\beta E = - \frac{\ell}{4\pi e^2} \frac{\lambda^2}{n_o} E \qquad (3.47)$$

The shape of the streamlines is determined by the boundary conditions. Typical solutions (with a perfectly conducting boundary) are given in Refs. 47 and 48; for the $L/2$ by L rectangular box, this method predicts the same solutions as those obtained in simulations by Joyce and Montgomery[19,20]. (It should be noted that these solutions were obtained for systems with a total net charge of zero.)

The vortex solutions and boundary conditions will be discussed further in Chapter IV in the context of boundary conditions appropriate for plasmas in the Octupole.

III.7 SOLUTION OF THE TIME-DEPENDENT PROBLEM

Because the Octupole is not a steady-state device, it is important to consider the time scale on which $D(t) \rightarrow D_\infty$. This time is of the order of that necessary for the longest-lived correlation to go to zero. The time behavior of R, $\dot{R}$ and $\ddot{R}$ is shown in Fig. 3.1, assuming a non-dissipative (constant energy) spectrum.
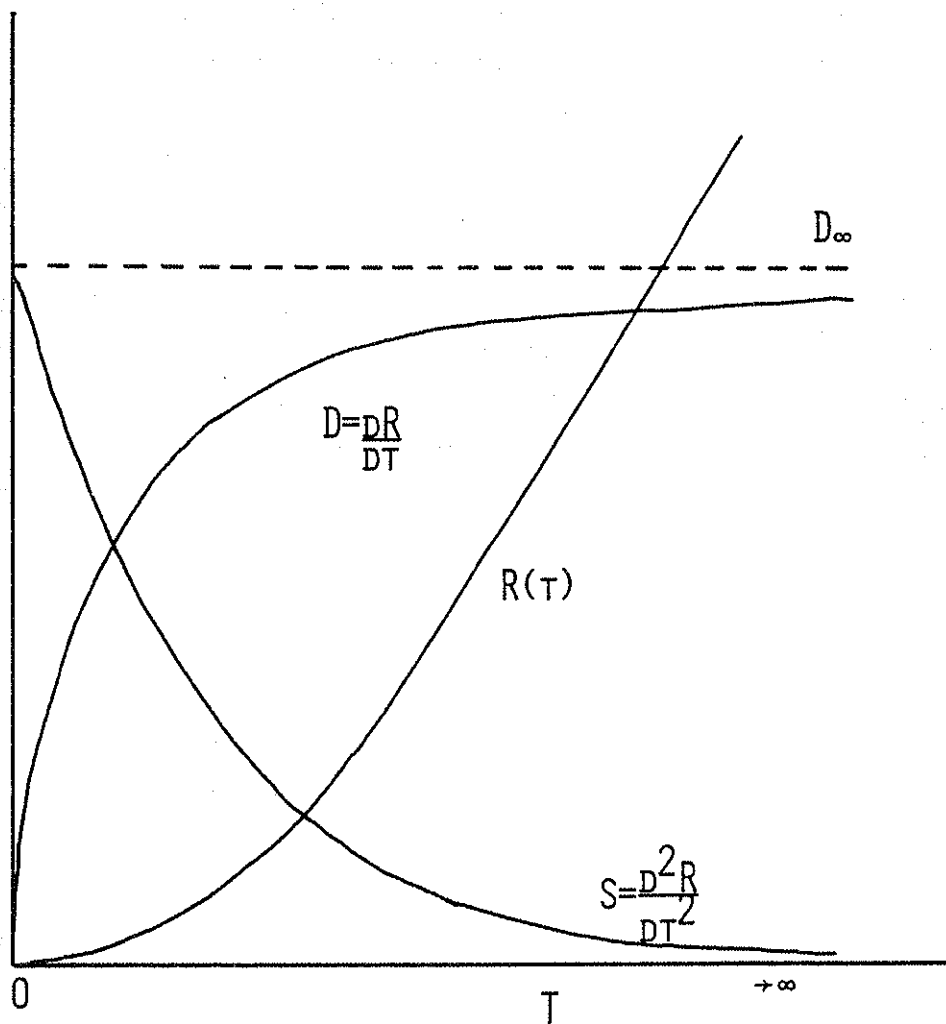
FIG. 3.1   SKETCH OF THE SOLUTION TO EQUATIONS (3.39) AND
           (3.40).
           S - ELECTRIC FIELD CORRELATION
           D - DIFFUSION COEFFICIENT
           R - MEAN-SQUARE DISPERSION

We can divide the time axis into two time regions depending on whether $t < \tau$ or $t > \tau$, where τ can be roughly defined as the time for the electric field correlation to drop to a small fraction of its initial value. For $t > \tau$ we can represent D by the long-time solution (3.41), but for $t < \tau$ the full, time-dependent, equations must be solved.

It is useful at this point to get an idea of the time scales for the plasmas we will consider in the Octupole. Using typical parameters for the two plasmas considered (Table III.1), the equations for R, $\dot{R}$ and $\ddot{R}$ were solved numerically using ACSL (Advanced Continuous Simulation Language). The electric field spectrum used was

$$E^2 = \sum_k E_k^2 = E_o^2 \, e^{-2t/\tau(t)} \sum_k \frac{1}{k^2} \qquad (3.48)$$

The time decays $\tau(t)$ were chosen to match the time decays of experimental spectra. Figs. 3.2 and 3.4 show R, $\dot{R}$ (RD) and $\ddot{R}$ (RDD) for the collisionless and collisional simulations, and Figs. 3.3 and 3.5 show the time decay of ΣE_k^2 (energy) and $\Sigma k^2 E_k^2$ (enstrophy). It can be seen for the 'collisionless' plasma that the rapid initial damping of the spectrum leads to a D at large times two orders of magnitude smaller than the D which would be calculated using E_o^2. In the 'collisional' plasma case, a long-time solution has not yet been reached even after 50ms because the electric fields are smaller initially. This shows that for plasmas in the Octupole it is necessary to consider the time dependence of the diffusion coefficient.

For insight into the process, we will examine the solution to (3.40) in the limiting cases where analytical solutions are possible. For a single k-mode the solution is

Table III.1

	collisionless	collisional
E_o^2	$(1V/m)^2$	$(.2V/m)^2$
B	1kG	600G
τ	2ms, $0 < t < 5$ms 20ms, $5 < t < 30$ms 66ms, $t > 30$ms	1ms, $t < 3$ms 60ms, $t > 3$ms
D	$1.2 \times 10^5 cm^2/sec$	$4.2 \times 10^4 cm^2/sec$

Table III.1   Parameters used in the solution of the
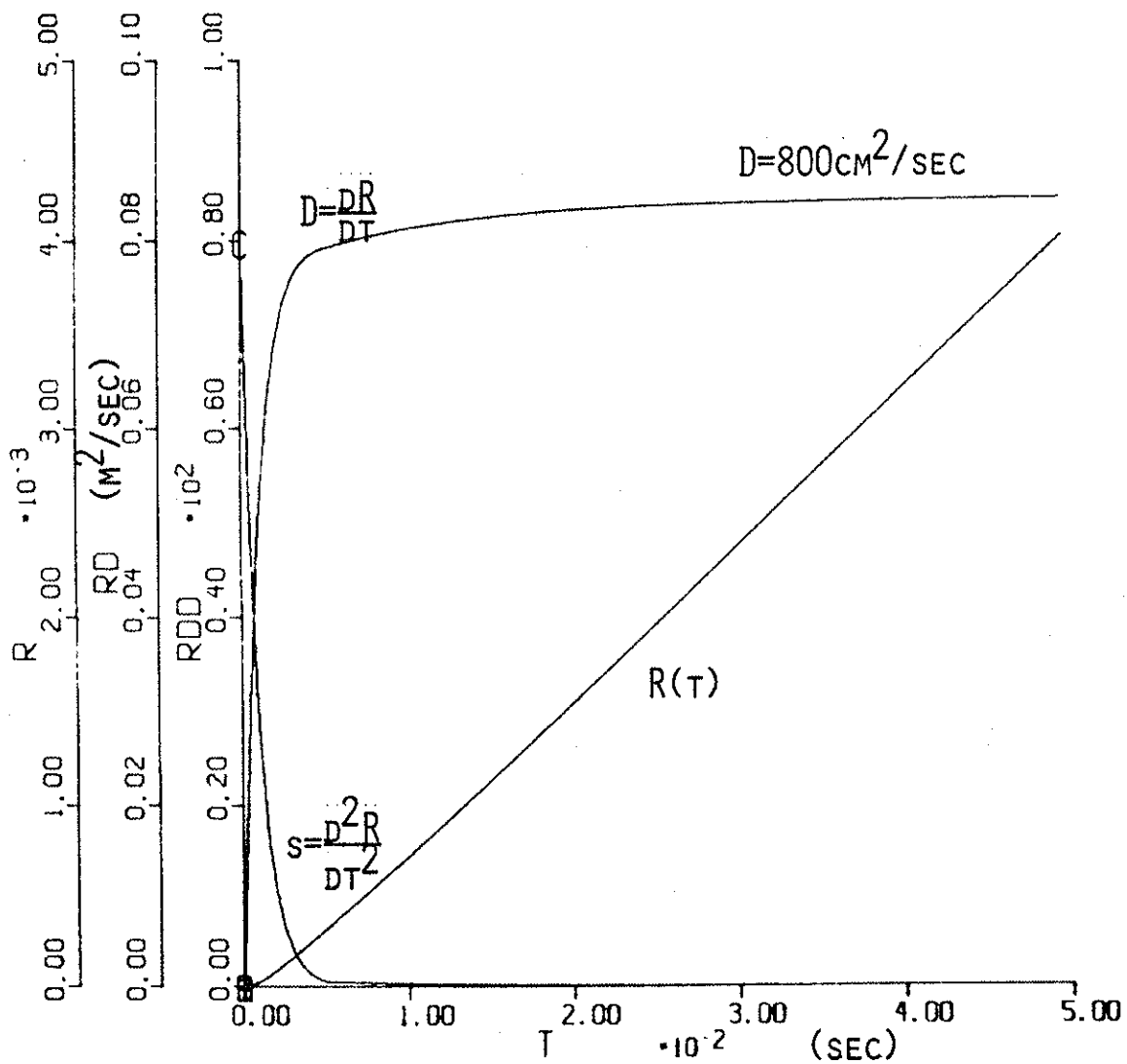differential equation for the diffusion
(ACSL).

$D = 800 \, \text{CM}^2/\text{SEC}$

$D = \dfrac{DR}{DT}$

$R(T)$

$S = \dfrac{D^2 R}{DT^2}$

R · 10^{-3}

RD · 10^{-3} (M^2/SEC)

RDD · 10^2

5.00 4.00 3.00 2.00 1.00 0.00

0.10 0.08 0.06 0.04 0.02 0.00

1.00 0.80 0.60 0.40 0.20 0.00

0.00   1.00   2.00   3.00   4.00   5.00

T   · 10^{-2} (SEC)

FIG. 3.2 SOLUTION OF EQUATIONS (3.39) AND (3.40) USING
PARAMETERS TYPICAL OF THE COLLISIONLESS PLASMA.
(TABLE III.1)
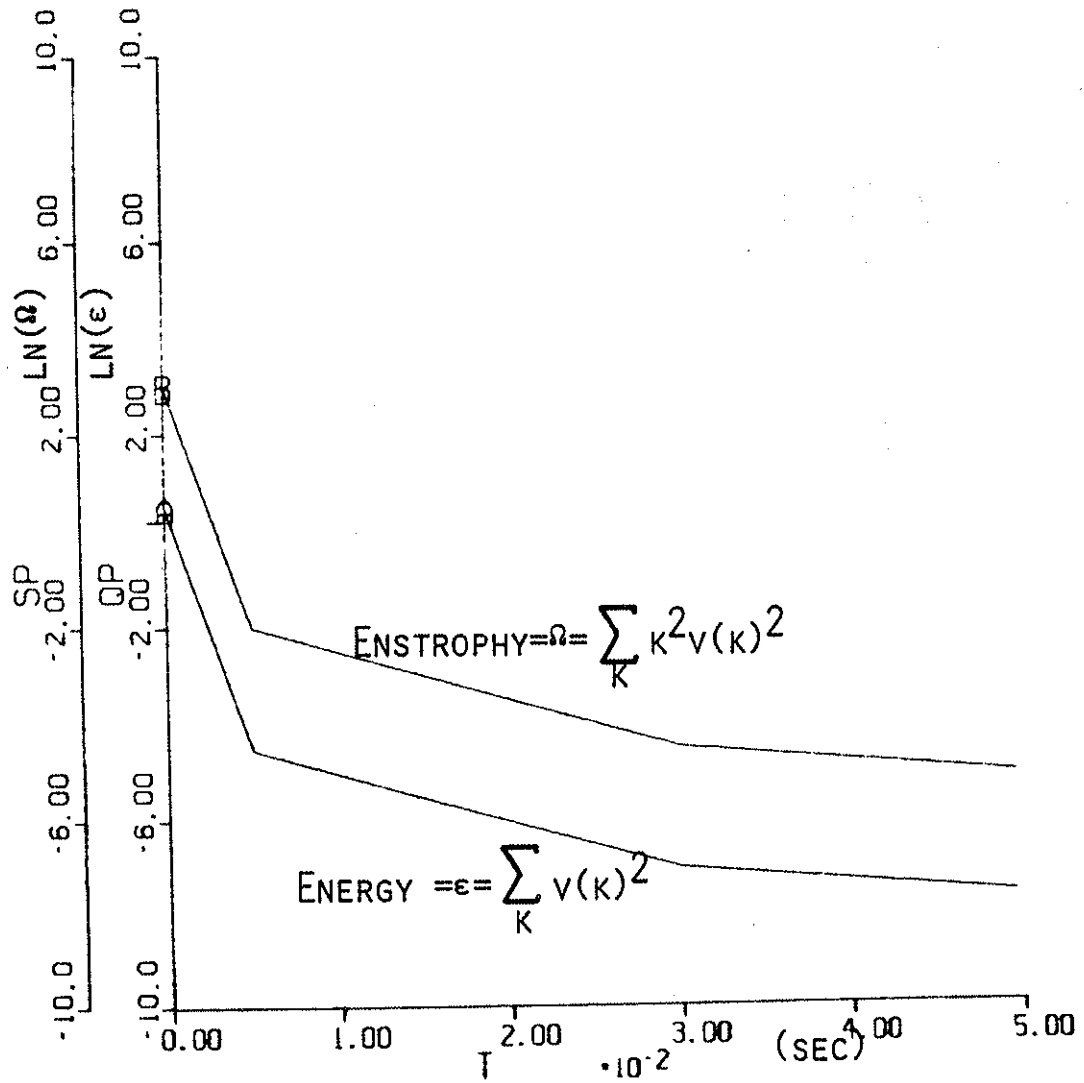
FIG. 3.3 TIME DECAY OF ENERGY AND ENSTROPHY FOR PARAMETERS TYPICAL OF THE COLLISIONLESS PLASMA (TABLE III.1).
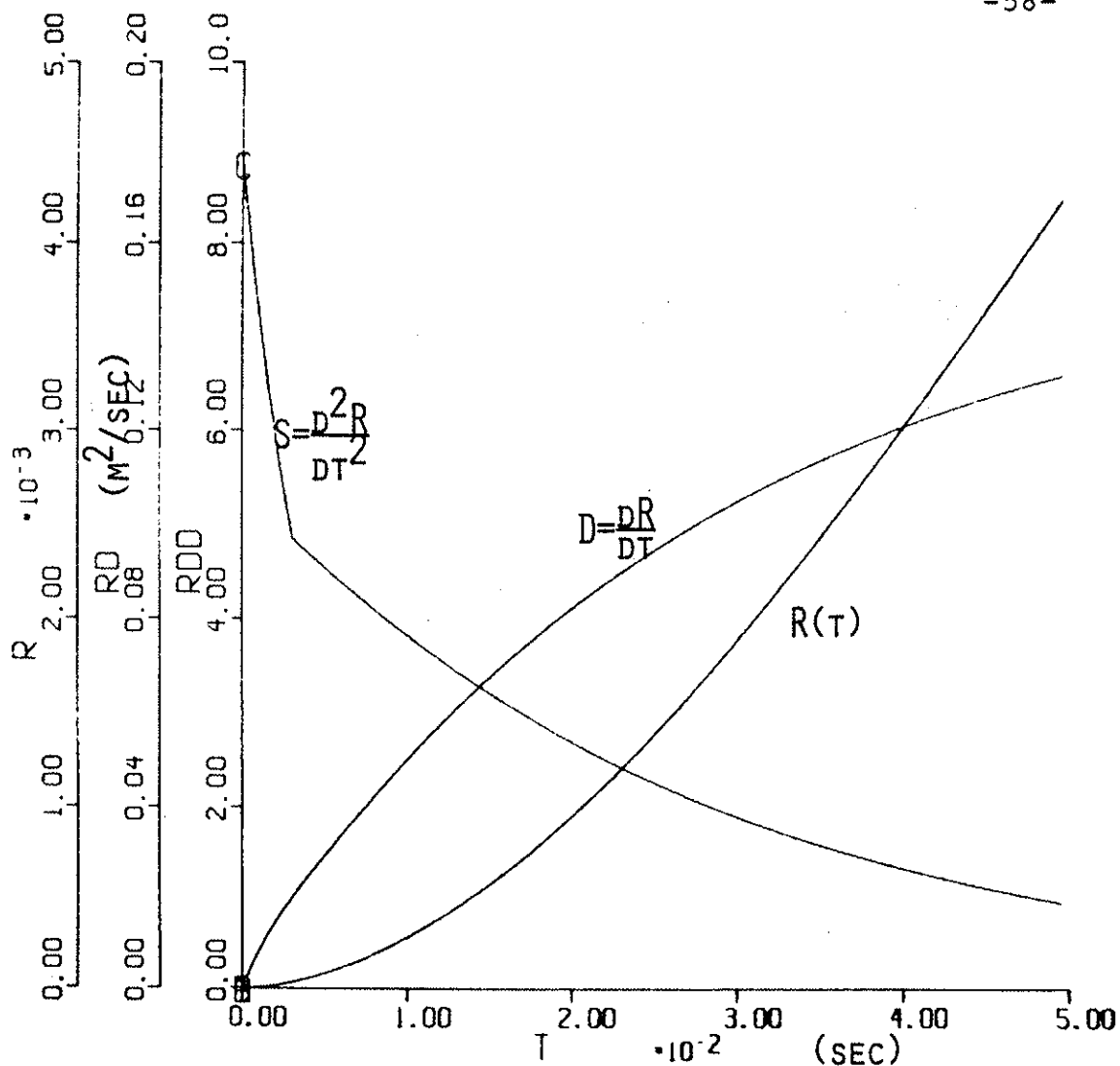
FIG. 3.4 SOLUTION OF EQUATIONS (3.39) AND (3.40) USING
PARAMETERS TYPICAL OF THE COLLISIONAL PLASMA.
(TABLE III.1)
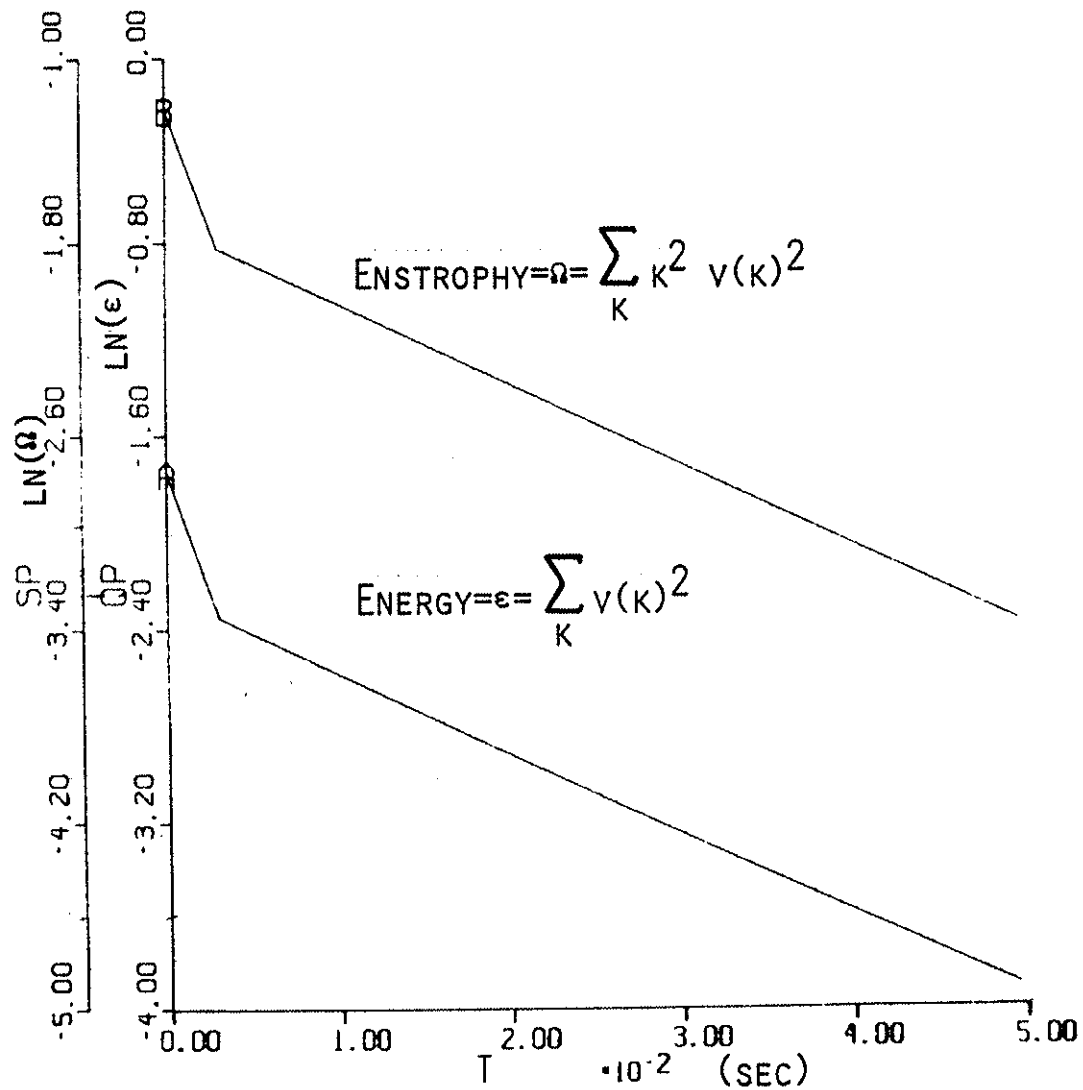
FIG. 3.5 TIME DECAY OF ENERGY AND ENSTROPHY FOR PARAMETERS
TYPICAL OF THE COLLISIONAL PLASMA (TABLE III.1).

$$R(t) = \frac{1}{2k^2} \ln (\cosh^2 \omega t) \qquad (3.49)$$

$$\frac{dR}{dt} = \frac{\omega}{k^2} \tanh \omega t \qquad (3.50)$$

$$\omega^2 = \frac{1}{2B^2} k^2 E^2(k) \qquad (3.51)$$

The time it takes $D(t)$ to reach its full value depends on the time constant, $\omega^2 \propto k^2 v^2(k)$, which is of the order of the time it takes a fluid particle to go half-way around a cell.

The limit as $t \to \infty$ is the steady state solution given in the previous section.

The other interesting limit is where $k^2 R(t)$ is very small, and the term in the square brackets in (3.40) is approximately equal to $k^2 R$. The solution is then

$$R(t) = \frac{t^2}{4} \sum_k \frac{E^2(k)}{B^2} \qquad (3.52)$$

$$\frac{dR}{dt} = \frac{t}{2} \sum_k \frac{E^2(k)}{B^2} \qquad (3.53)$$

D increases linearly in time at a rate proportional to the total energy, again dominated by the mode with the largest amplitude. For a spectrum that is a decreasing function of k, diffusion will be largely due to the longest wave-lengths. Recalling that

$$R(t) = \frac{1}{4} [\Delta r(t)]^2 \qquad (3.54)$$

is the mean dispersion of a group of particles[17], equation
(3.54) states that for very small times $\Delta r(t) = v_E t$. This
corresponds to the inertial range: the particles are
free-streaming under the influence of the applied electric
field, and there is as yet no diffusion. The 2-D fluid
theory of evolving turbulence[24,60,61] is beyond the scope
of this paper, and not much is known about $D(t)$ for a
decaying plasma. The assumption we have made is that we
can use the measured spectra in equation (3.40) to obtain
the time dependence of D.

III.8 SUMMARY

With a purely poloidal field, plasmas in the Octupole
can be treated as two-dimensional fluids. We will use the
guiding-center formulation, modified to account for a
dielectric constant greater than unity, to calculate
diffusion. The spectrum $E(k)^2$ will be obtained from the
measured potentials. The details and extensions to the
theory for use in the Octupole are presented in Chapter
IV.

Vortices cause diffusion when they become uncorrelated;
in an equilibrium plasma this is caused by statistical
fluctuations about the ensemble average. The process of
diffusion is increased if the spectrum is decaying and
there is a density gradient.

The large plasma vortices, first examined by Drake[1]
in the Wisconsin Levitated Octupole, and presented later
in the data chapters, can be predicted from the fluid
theory if we assume that the plasma has a non-thermal

spectrum. The vortex solutions are a consequence of the two-dimensional non-linear nature of the problem, and correlate with a non-thermal spectrum peaked at the lowest spatial frequencies (we don't expect large vortices in thermal equilibrium, where the spectrum is flat).

We have followed the derivation proposed by Montgomery rather than that of Okuda and Dawson, because Montgomery emphasizes the non-linear nature of the problem, which then leads naturally to the phenomena of negative temperatures and large vortices for a non-themal spectrum.

CHAPTER IV - APPLICATION OF THEORY TO THE OCTUPOLE

The fluid theory solutions for the equipotentials (streamlines) and the expression for a diffusion coefficient (3.40) presented in Chapter III were developed for a very special set of conditions:
* equilibrium spectrum
* non-dissipative forces
* isotropic spectrum
* motion of plasma due only to guiding-center drifts
* straight uniform magnetic field
* uniform plasma (no density or temperature gradients)
* two-dimensional, rectangular coordinate system

None of the above are strictly true in the Octupole, and the various changes and approximations that have to be made to obtain even a very simplified theory to use in the Octupole are considered in Section IV.6. These factors are discussed in Sections IV.1-IV.5. A brief summary of the sources of cell structure in the Octupole is given in Section IV.7.

IV.1 NON-EQUILIBRIUM STATES; ENSEMBLE AVERAGES

There are two time scales to be considered for the time-dependent diffusion coefficient. We examine a system in equilibrium to understand the first time scale: the diffusion of a group of particles released from $\vec{x}=0$ at t=0 is described by equation (3.40) until R(t) is large enough so that the exponential term vanishes, and $D(t) \rightarrow D_\infty$ (3.41). This time scale was considered by Taylor and

McNamara[17], who have evaluated the diffusion for a stationary spectrum in which the total energy is constant and the decay of the autocorrelation in time is due to fluctuations of $\vec{E}(\vec{k},t)$ about an average $<\vec{E}(\vec{k})>$. This time scale is not emphasized in much of the theoretical work, which usually presents the long-time D_∞ solution (Okuda and Dawson[18], Taylor[21]).

The second time scale is associated with a non-equilibrium situation which arises either because a system is not in its most probable state (typical of simulations by Joyce and Montgomery[19] and others[24]), and/or because there are dissipative forces acting on the system. Simulations for given intitial conditions include both this time scale and the previous one.

The time-dependent turbulence theory[24,60,61] is very complicated even in a simple coordinate system; no attempt has been made to apply the theory to the Octupole. The results to be presented later will make the assumption that the effect of the various time scales is correctly represented by using the measured time-decaying spectrum.

To use equation (3.40) we need the correlation of the velocity field over an ensemble; this is especially important if the number of 'most probable states' is large - and they are substantially different. This is the case if the energy is concentrated in small vortices, for example, which fit into the 'box' in many ways. When the most probable states are few or essentially indistinguishable, as in the case where the structure tends towards a large vortex, or pair of vortices, which can fit in only one or two ways, the most probable state should be the same as the actual state of the system.

The observed vortex structure in the Octupole seems to correspond to the latter case - the smaller cells are much less important, and the structure of the large vortices is reproducible. Therefore, the assumption is made that the reproducible structure measured in the Octupole represents the most probable state, and that the ensemble average can be replaced by the measured spectra.

IV.2   DISSIPATIVE FORCES

Diffusion for the fluid model depends on the energy in the vortex spectrum, and any mechanism which removes energy from the vortex spectrum will reduce the diffusion. Because of this, the diffusion at long times is smaller than that which would result if the total energy in the spectrum were constant. This effect was illustrated in the numerical examples in Chapter III where we used a time-dependent energy spectrum.

As will be discussed when the data is presented, at least two mechanisms reduce the energy of the spectrum in the Octupole. One is ion viscosity, and the other is cooling. Again the assumption is made that any dissipative effects are correctly accounted for by using the measured spectra.

IV.3   NON-ISOTROPIC FLUID VORTEX THEORY

Although the 'square box' is useful for numerical simulations and theory, the question naturally arises when applying the theory to the Octupole of what the effect is

of a (possibly) non-isotropic velocity spectrum. The
first thing to note is that for an e.s. g.c. plasma, the
velocity is perpendicular to the electric field. The
diffusion equation is actually a tensor equation, which
Taylor and McNamara simplified by assuming isotropy to
obtain an analytical solution. In this section we will
choose simplifying assumptions more suitable for the
Octupole, based on experimental results, and will not
require the spectrum to be isotropic.

The analytical solution is more complicated when the
spectrum is not isotropic. For simplicity we will show
the equation for the electric field correlation (3.39)
rather than the diffusion equation, which is its first
integral (3.40). The results will apply equally to the
equations for dR/dt and R(t). (This method was used in
the examples in Chapter III because numerical integration
is more accurate and more stable than numerical differenti-
ation.) Equation (3.39), in tensor form, is

$$\frac{d^2 \overset{\leftrightarrow}{R}(t)}{dt^2} = \frac{1}{2B^4} \sum_k < (\vec{E}(\vec{k}) \times \vec{B})(\vec{E}(\vec{k}) \times \vec{B}) >$$

$$\times \exp \left[-\frac{2}{B^2} (\vec{k} \times \vec{B}) \cdot \overset{\leftrightarrow}{R}(t) \cdot (\vec{k} \times \vec{B}) \right] \quad (4.1)$$

If the spectrum is isotropic then

$$\overset{\leftrightarrow}{R} = \begin{bmatrix} R_{xx} & R_{xy} \\ R_{yx} & R_{yy} \end{bmatrix} \quad (4.2)$$

reduces to $R\overset{\leftrightarrow}{I}$. As equation (4.1) indicates, diffusion is
two-dimensional for the vortex modes. To see this, note
that the exponential term in (4.1) is dependent on both x
and y. If we assume that the cross terms are negligible,
equation (4.1) reduces to a pair of coupled differential
equations,

$$\frac{d^2R_{xx}}{dt^2} = \frac{1}{2B^2} \sum_k <E_y^2> \exp\left[-\frac{2}{B^2}(k_y^2R_{xx}+k_x^2R_{yy})\right] \quad (4.3)$$

and equivalently for d^2R_{yy}/dt^2. Note that the diffusion in x depends on the spectrum in y and vice versa, even if the cross terms are ignored.

IV.4 MAGNETIC FIELD AND DENSITY INHOMOGENEITIES; NON-UNIFORM ε

The straight, uniform magnetic field required by the 2-D g.c. theory is non-physical. (Under some experimental circumstances the plasma could be located in the straight uniform part of the field, but then the question of potential and density gradients along the field line would probably arise.) Confinement systems, the Octupole in particular, have inhomogeneous fields with curvature. There are two consequences of this that have to be considered when applying the g.c. theory to the Octupole. First, the non-uniform field contributes to a position-dependent dielectric coefficient; this effect is discussed later in this section. The second effect is that the guiding-center drift is no longer the only drift. With a density gradient there is also a diamagnetic drift (Ref. 46, Chapter III), which in the Octupole is azimuthal (if there are no azimuthal density gradients), and in opposite directions for ions and electrons. Fluid theory is still applicable; however, the formal correspondence between the 2-D Navier-Stokes equation (3.9) and the fluid equation (3.20) holds only when $\vec{v}=\vec{E}\times\vec{B}$. The single-particle picture includes a ∇B drift and a curvature drift (Ref. 46, Chapter II and III) not present in the fluid description; both are also azimuthal in the Levitated Octupole.

It has not been determined how to include the azimuthal diamagnetic drifts formally in the theory. However, the azimuthal drifts may play a role in symmetrizing azimuthal density gradients, as discussed by Navratil in his "picket fence" model (Ref. 15, p.76-79).

Little theoretical work has been done on the problem of vortex diffusion with a density gradient. Okuda and Dawson included a 20% density gradient in one of the two dimensions of their simulations, and found that the vortex diffusion smoothed out the inhomogeneity[18]. True and Okuda (Ref. 40) reported that convective modes were un-changed by the presence of a density gradient, but that ion flute modes became unstable (however, in the Octupole flute modes are stabilized by the good curvature of the field in the private flux and the average good curvature in the common flux[41]).

We are interested in whether density gradients can affect the fluid solutions, and especially in how they change the magnitude or shape of the spectrum. As will be shown in Chapter V, the potential contour plots for plasmas in a purely poloidal field tend to show relatively little structure in the region near the separatrix (near the density peak), and more in the region closer to the rings. The vortex diffusion coefficient density dependence obtained from the study of the profile evolution is $D \propto [n(\psi)]^{-1/2}$. However, the diffusion coefficient obtained from the fluid theory in Chapter III (without a density gradient) is independent of position.

One important effect of inhomogeneous density and magnetic field is the variation of the dielectric constant,

from $\epsilon \to \infty$ at the field null, to $\epsilon \to 1$ near the plasma edge.
(Note that there would be a variation in ϵ even for a
system with uniform B if there were a density gradient.)
It is believed that the inclusion of the effects of a
density gradient in ψ on the distribution of the electric
field energy will account for the ψ-dependence of D_v. For
the purpose of numerical computations, the electric field
spectrum used will be $E_\theta^2(\psi,k,t)$.

If $T^* \propto \epsilon E^2$ is a constant in the plasma as the diffusion
studies[25] suggest, then we expect the electric field
spectrum to vary in ψ. This variation is seen in the
data. The principal result of the gradients in the Octupole
appears to be a dielectric effect: the azimuthal potential
gradients measured in the plasma are lower near the separ-
atrix where the dielectric constant is higher (due to the
peak of the density profile and the low average value of B
along the separatrix field line). We will account for the
variation with ψ by using the local values of the variables
on each ψ-surface.

IV.5 BOUNDARY CONDITIONS AND FLUID SOLUTIONS IN THE
OCTUPOLE

The fluid solutions discussed in Chapter III were
obtained for equilibrium plasmas in a box with perfectly
conducting (equipotential) boundaries. In addition, all
but one of the solutions presented by McDonald[48] (and the
Joyce and Montgomery simulations[19,20]) correspond to a
total net charge of zero.

Boundary conditions are different for the Octupole. ϕ and $\vec{E}=-\vec{\nabla}\phi$ are both continuous functions of the azimuthal angle θ. The rings are equipotentials; the boundary conditions at the walls are discussed in Chapter V. The separatrix flux surface would also be an equipotential if the magnetic field were zero everywhere along ψ_s; this would divide the Octupole into two separate regions, a private flux region and a common flux region. The closed cells observed in the data (Chapter V) do not cross the separatrix from one region to the other; however, the potential on the separatrix is itself a function of time. In addition, for the collisionless plasma the electrons have an anomalous diffusion rate across B which exceeds the ion rate, the plasma potential is positive in the Octupole (see, for example, potential profiles taken by Greenwood Ref. 13, section III.5) and $\int \rho dV \neq 0$.

It has not been shown that the kinds of numerical solutions obtained by McDonald are the only kinds possible. The multiplicity of solutions corresponds to local maxima of the entropy and it is difficult to determine whether a given state has the absolute maximum entropy. Because there are many solutions, the iterative procedures are very dependent on initial guesses. This means that, especially for more complicated geometries such as the Octupole, even though we may be able to obtain a numerical solution for the theoretical equipotentials which solves the differential equation and boundary conditions, we may not be able to prove that it is, in fact, the equilibrium solution corresponding to maximum entropy. However, even though a solution may not have maximum entropy, the local maxima may represent the possibility of meta-stable states. Interesting results in this context were obtained by

Saison, Wimmel and Sardei[49] for two-fluid trapped-ion transport in Tokamaks.

The solutions to (3.46) in the Octupole will have to be obtained numerically, but we can make a first estimate by expanding on a topological trick suggested by Fisher[50]. He investigated the similarity between some of the solutions to (3.46) in Cartesian coordinates and solutions in cylindrical coordinates. We have taken the additional step of noting that the two-dimensional plot of $\Delta\theta=360^{O}$ by $\psi=\psi_{w}-\psi_{r}$ is topologically equivalent to an annulus if we map onto r. The transformation can be thought of as deforming the topology continuously while maintaining (3.46).

The solutions we are interested in are the ones which fulfill the boundary conditions $\Psi=a$ at ψ_{w} and $\Psi=b$ at ψ_{r}. Sketched in Fig. 4.1a, b, and c, are three such solutions. In the first column is the solution given by McDonald[48] in Cartesian coordinates (McDonald calls these three solutions s-s, d-d, and diagonal d-d). The second column has the solutions as they might look deformed into cylindrical coordinates, and in the third column an equipotential surface of circular shape has been replaced by the inner boundary of the annulus. Solving for these directly using (3.46) in Octupole coordinates has not yet been attempted. It should be noted, however, that even though the boundary conditions would be met by this method, the net charge enclosed by the 'box' could change (this is not necessarily a disadvantage since we have already seen that the net charge is not zero in the Octupole). This would have to be accounted for when obtaining a solution.
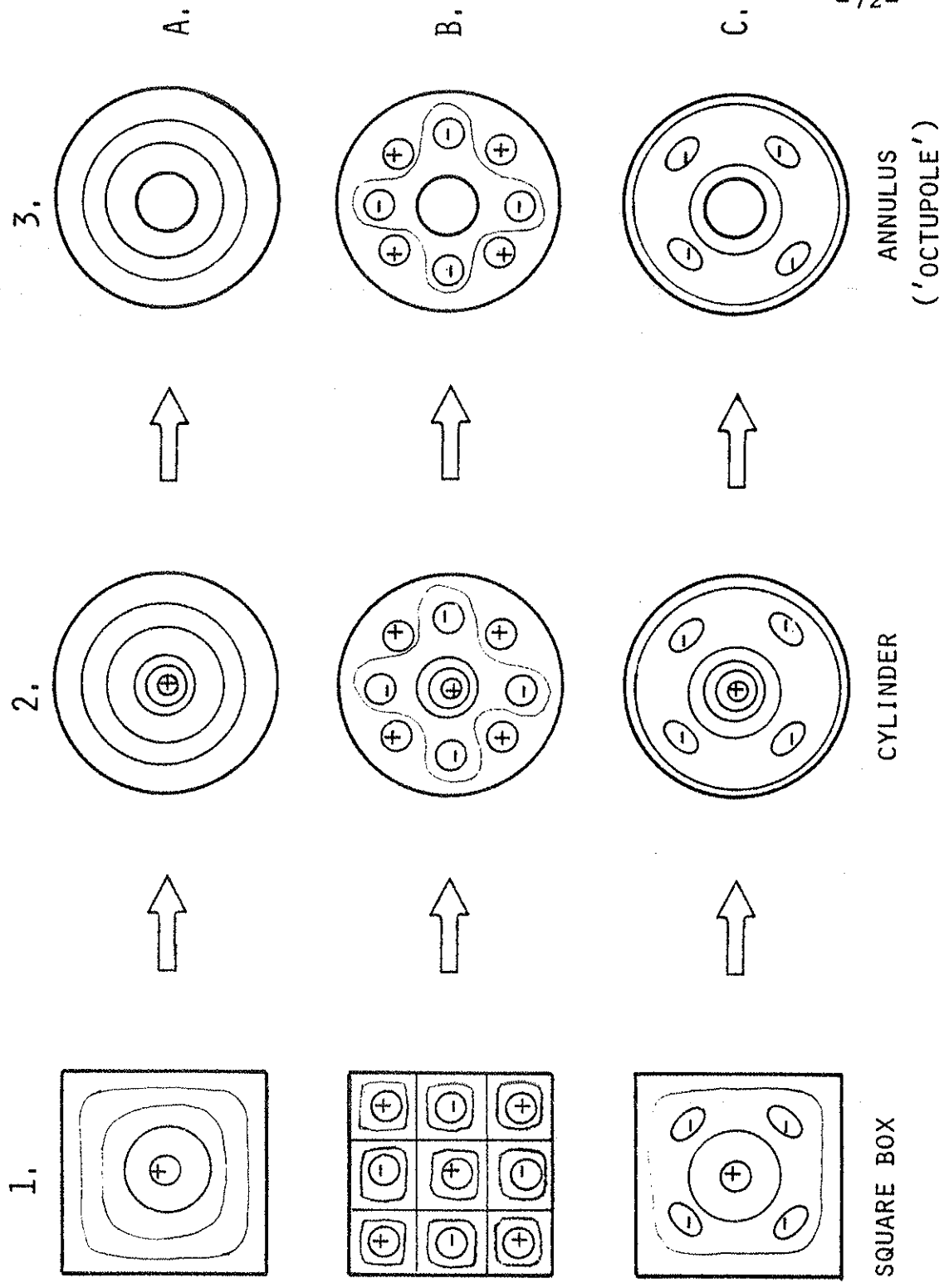
Fig. 4.1 Possible deformation of solutions to the sinhψ equation, from solutions in a square box (Ref.48) to an annulus.

The most probable state for a given value of the energy depends on λ. If the energy is too high, for example, there may be no s-s solution (Fig. 4.1a, col. 1), and in this case something like Fig. 4.1c, col. 3, might be the highest-entropy solution compatible with all the constraints.

The question of time-varying solutions is not addressed by the analysis of the $\sinh\Psi$ equation (see Section III.6), which refers only to the long-time equilibrium state of a conservative system. For the Octupole, though, it is interesting to consider what would happen to a system in equilibrium with an energy E, if the energy were decreased. It is possible to imagine that as the energy decreased, a transition could be made to a state that was previously not allowed, with a higher entropy, for a new equilibrium.

We speculate that something of this nature may occur during the transition from vortex diffusion to classical diffusion[26] as the energy spectrum is damped. A comparison of Figs. 4.2a, b, and c, shows that one shape can be obtained from the other by a continuous deformation as the amplitude of the azimuthal variation (along the dotted line) is reduced. We note also that the entropy, $S=2\beta E$, is negative; equation (3.46) was derived for $\beta < 0$. The maximum entropy possible for any solution will be zero.

By a continuous process, then, as the energy spectrum is damped, the electric field shape can go from one in which gradients in θ lead to radial diffusion, to one in which there are still radial fields but only collisional diffusion.
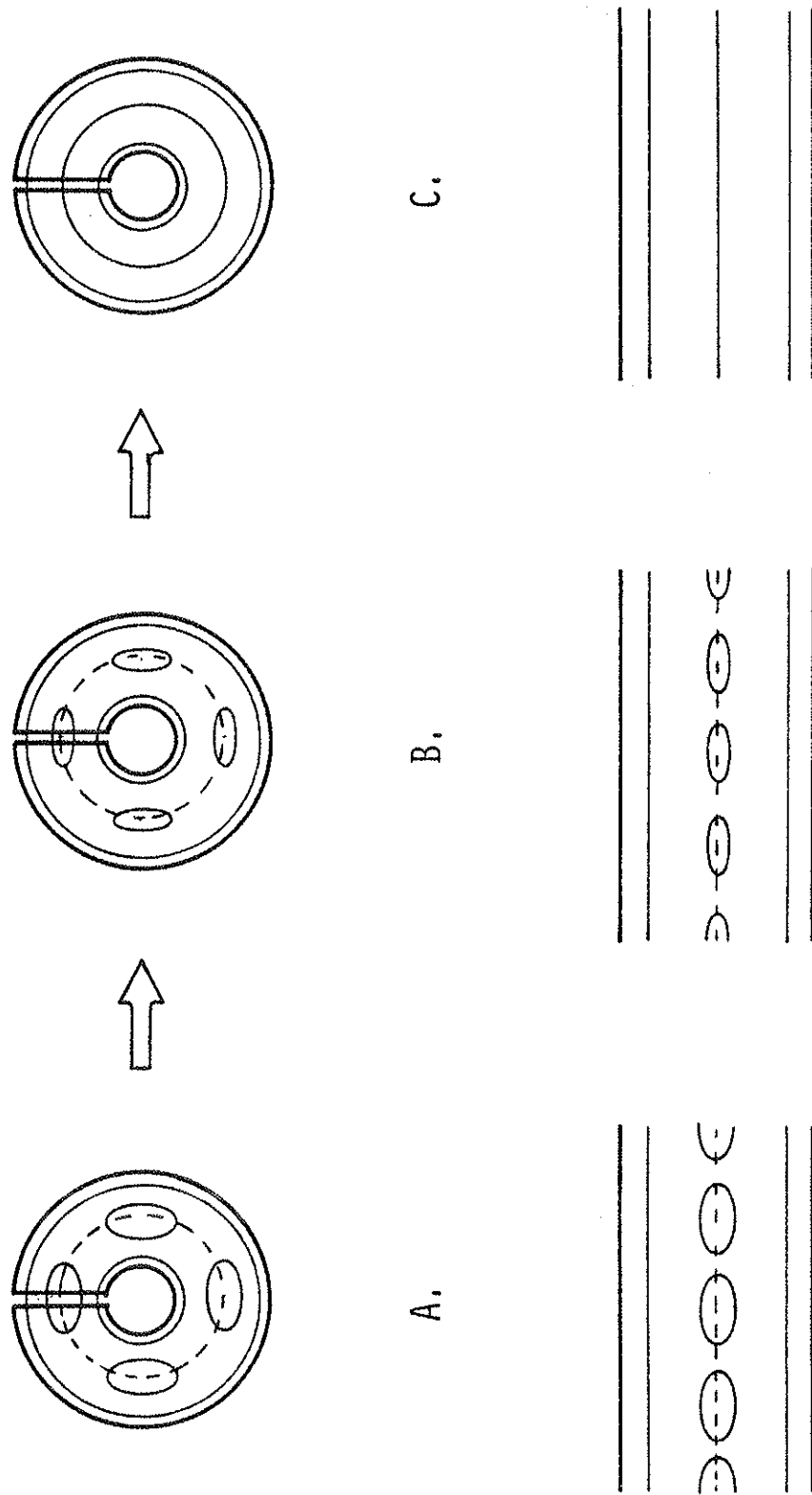
FIG. 4.2 POSSIBLE DECAY OF A TOROIDAL MODE (M=4).

If we consider only the private flux region, with the ring and the separatrix ψ-surface as the boundaries of this region, and assume that the appropriate boundary conditions are that ψ_s and ψ_r each be an equipotential, then the longest-wavelength mode is sketched in Fig. 4.3a. Typically, the width in ψ of the private flux region is ~ 10cm, and in θ, 10^3cm. The wavenumber, $\vec{k}$, is a vector. Therefore, the mode with the second smallest wavenumber is as sketched in Fig. 4.3b rather than Fig. 4.3c. The first 10-20 longest-wavelength modes thus all share the same $k_{1\psi}$.

We wish to emphasize that although the above development is plausible it has not been checked numerically. Even if the sketches are indeed solutions, we cannot know if we have a complete set for a given situation, nor can we prove that we have the maximum-entropy solution, and, in addition, we still have to consider the time dependence for real plasmas.

The discussion of the deformation of boundaries from a box to an annulus does not include the effects of introducing additional boundary conditions, such as supports, during the process. The symmetry of the box (4 corners) is not a natural one to the circle; rather we can see the possibility of any integer number of toroidal modes. This discussion is intended to show a possible class of solutions rather than justify a particular one.

IV.6 APPLICATION TO OCTUPOLE COORDINATES

In the previous sections of this chapter we have discussed the various effects which have to be considered
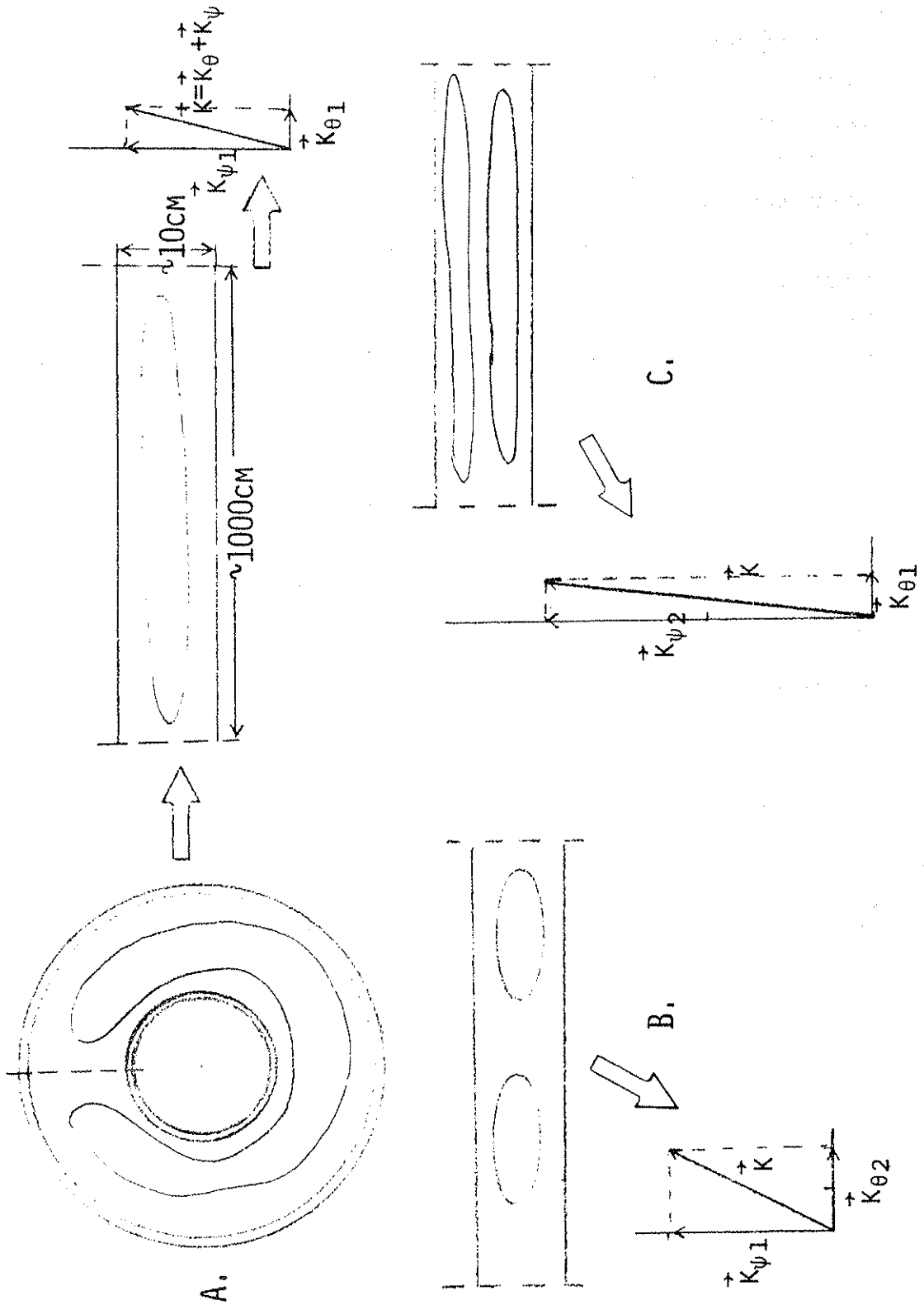
FIG. 4.3 SKETCH OF LONGEST-WAVELENGTH MODES IN OCTUPOLE.

when applying vortex diffusion theory to the Octupole. In this section we will examine what equation (4.1) looks like in Octupole coordinates, and what assumptions are necessary to estimate D from the experimental data.

The tensor equation, (4.1), consists of four separate equations, coupled by the exponential term. To solve this equation completely we need to expand the electric field in eigenfunctions suitable for the Octupole, and then solve the four coupled equations simultaneously.

The Octupole coordinates perpendicular to $\vec{B}$ are ψ and θ. Eigenfunctions in these coordinates can be found by considering Poisson's equation. Using the differential operators in Appendix A, it can be shown that Poisson's equation is separable in Octupole coordinates. The eigenfunctions in θ are the toroidal eigenfunctions, $e^{im\theta}$; the potential structure can be Fourier transformed in θ to obtain the amplitudes of the toroidal modes if 1) the data covers at least one complete period of the lowest spatial frequency present, and 2) the sampling rate is high enough to prevent aliasing. The eigenfunctions in ψ cannot be expressed in terms of analytic functions, but can be obtained numerically.

As discussed in Chapter II, contour plots were constructed using ~ 5 ψ values and 10-100 θ positions. This means that we can get a reasonable approximation to the toroidal electric field spectrum; aliasing is not a problem because the spectrum drops rapidly with increasing wavenumber. However, unless the toroidal spectrum has most of its energy in a mode $m \overset{\geq}{=} 4$, only 360° scans will provide a correct spectrum.

The spectrum in ψ cannot be obtained from the contour plot data because there are at best, using private and common flux data, about 10 points in ψ between the ring and the wall. Because of this limitation in the data, in the rest of this chapter we will obtain an approximate solution for D_V that uses only the toroidal spectrum.

We are interested in the net diffusion across a ψ-surface, so we need only the solutions to the equations for $d^2R_{\psi\psi}/dt^2$ and $d^2R_{\psi\theta}/dt^2$ (the net diffusion in θ is zero). The exponential in (4.1), in Octupole coordinates, is

$$\exp\ [-2\ (k^2_\psi R_{\theta\theta} - k_\psi k_\theta\ (R_{\psi\theta} + R_{\theta\psi}) + k^2_\theta R_{\psi\psi})] \qquad (4.4)$$

The first assumption we will make is that $D_{\psi\psi} \gg D_{\psi\theta}$. The second assumption is that the exponential is dominated by the term $k^2_\theta R_{\psi\psi}$. These assumptions imply that the diffusion is caused by the energy in the azimuthal electric fields. Not enough is known about the $\langle E_\psi E_\theta \rangle$ and $\langle E_\psi E_\psi \rangle$ correlations yet to prove definitely that this ordering is correct; however, as the discussion on fluid solutions in Sections III.6 and IV.5 has implied, there should be no diffusion across a ψ-surface due to vortex modes unless there are azimuthal potential gradients.

With these assumptions, equation (4.1) reduces to

$$\frac{d^2R_{\psi\psi}}{dt^2} = \frac{1}{2B^2} \sum_k E^2_\theta\ \exp\ (-2k^2_\theta R_{\psi\psi}) \qquad (4.5)$$

This equation is very similar to Taylor and McNamara's equation, (3.40), with the exception that it emphasizes

that the toroidal spectrum and eigenmodes should be used to determine diffusion ($D=dR_{\psi\psi}/dt$) in the ψ direction.

The expressions given for the diffusion coefficient in (3.30) and (3.40) give a result dependent only on the amplitude of the electric field spectrum and its distribution in k-space. There is no x dependence in either equation. In the Octupole it has been observed that the azimuthal electric field spectrum E_θ^2 depends on which ψ-surface the measurement is made on. Near the separatrix E_θ^2 is small relative to its magnitude nearer the rings and wall. (This is what would be expected from equation (3.30), $T^*\propto\varepsilon E^2$, where T^* is a constant[13,15] and ε varies as a function of ψ and χ.)

Because of this variation with ψ and χ, and because we are interested primarily in diffusion in ψ, we will obtain the diffusion across a ψ-surface by integrating (4.5) on the closed flux surface.

Using the toroidal eigenmodes $e^{im\theta}$, we express ϕ as

$$\phi(\theta) = \sum_m \phi(m)\ e^{im\theta} \tag{4.6}$$

(From this point on we will use k interchangeably with m to represent a toroidal eigenmode.) The differential operators in Octupole coordinates are given in Appendix A. The equations for E_θ, v_ψ, and D, are given by

$$E_\theta(m) = -\frac{im}{R}\ \phi(m) \tag{4.7}$$

$$v_\psi(m) = -\frac{im}{RB}\ \phi(m) \tag{4.8}$$

$$D = \frac{R}{B}\left[\sum_m \frac{<E^2(m)>}{m^2}\right]^{1/2} \qquad (4.9)$$

In ψ-coordinates, the gradient of n is $\nabla n = 2\pi RB \partial n / \partial \psi$. Substituting this into the equation for D (assuming the $t \to \infty$ limit), and averaging the flux over a ψ-surface, we can calculate $\mathcal{D}(\psi)$,

$$\Gamma_{av} = \frac{\int D \cdot \nabla n \ dA}{\int dA} = \frac{\int D\nabla n \ R \ d\theta d\ell}{\int R \ d\theta d\ell}$$

$$= 2\pi \left[\sum_m <\phi(m)^2>\right]^{1/2} \frac{\int R^2 d\theta d\ell}{\int R d\ell} \cdot \frac{\partial n}{\partial \psi}$$

$$= \mathcal{D}(\psi) \ \frac{\partial n}{\partial \psi} \qquad (4.10)$$

$\mathcal{D}(\psi)$ consists of a function of ψ which does not depend on θ and a geometrical factor. The geometrical factor is nearly constant in each of the three regions in the Octupole;

1.7	outer hoop	private flux
1.1	inner hoop	private flux
1.5		common flux

To put the diffusion coefficient in units appropriate to compare with Γ, we multiply $\partial n / \partial \psi$ by an average value of $2\pi RB$ over the ψ-surface.

$$\Gamma_{av} = \frac{\mathcal{D}(\psi)}{<2\pi RB>_{av}} \cdot \nabla n = \mathcal{D}_{av} \cdot \nabla n \qquad (4.11)$$

The units of ϕ are volts; in MKS $\mathcal{D}(\psi)$ is in Vm, and $\mathcal{D}_{av}$ is in m^2/sec. We have chosen to use MKS units throughout, and multiply by 10^4 at the end to obtain $\mathcal{D}_{av}$ in cm^2/sec.

The geometrical terms were obtained from PLP 703. Two factors have to be accounted for: the difference between the Dory (=1/10 peak core flux for a given bank voltage) and Webers; and the decay of B with time. The magnetic field was assumed to vary in time as $B_O \exp(-t/150ms)$, where B_O is the value of B at peak field. This approximation assumes that the flux plot retains its shape as it decays.

The time-dependent diffusion equation is obtained by using the time-dependent form of (4.9); the rest of the derivation is identical. The differential equation was solved numerically using a predictor-corrector algorithm. The approximation for small $k^2 R$ (3.52) was used to find the initial conditions to start the solution (Runge-Kutta algorithms cannot handle R(0)=0, dR/dt=0 at t=0). This approximation was kept to the same accuracy as the solution to the differential equation (10^{-5}).

The spectrum is peaked at the lowest mode numbers. It was found that the numerical solution involving 50 modes (Fig. 4.4) was essentially identical to that involving 20 modes (Fig. 4.5); including fewer than 20 modes led to variations in the results. Therefore, the numerical solutions were evaluated using the 30 longest-wavelength modes.

Note: Instead of multiplying by $<2\pi RB>$ we could also use the value of $2\pi RB$ at the point in space where the comparison with the flux is to be made, in the bridge region of the LOH. This would result in a numerical factor smaller by about 1/4.
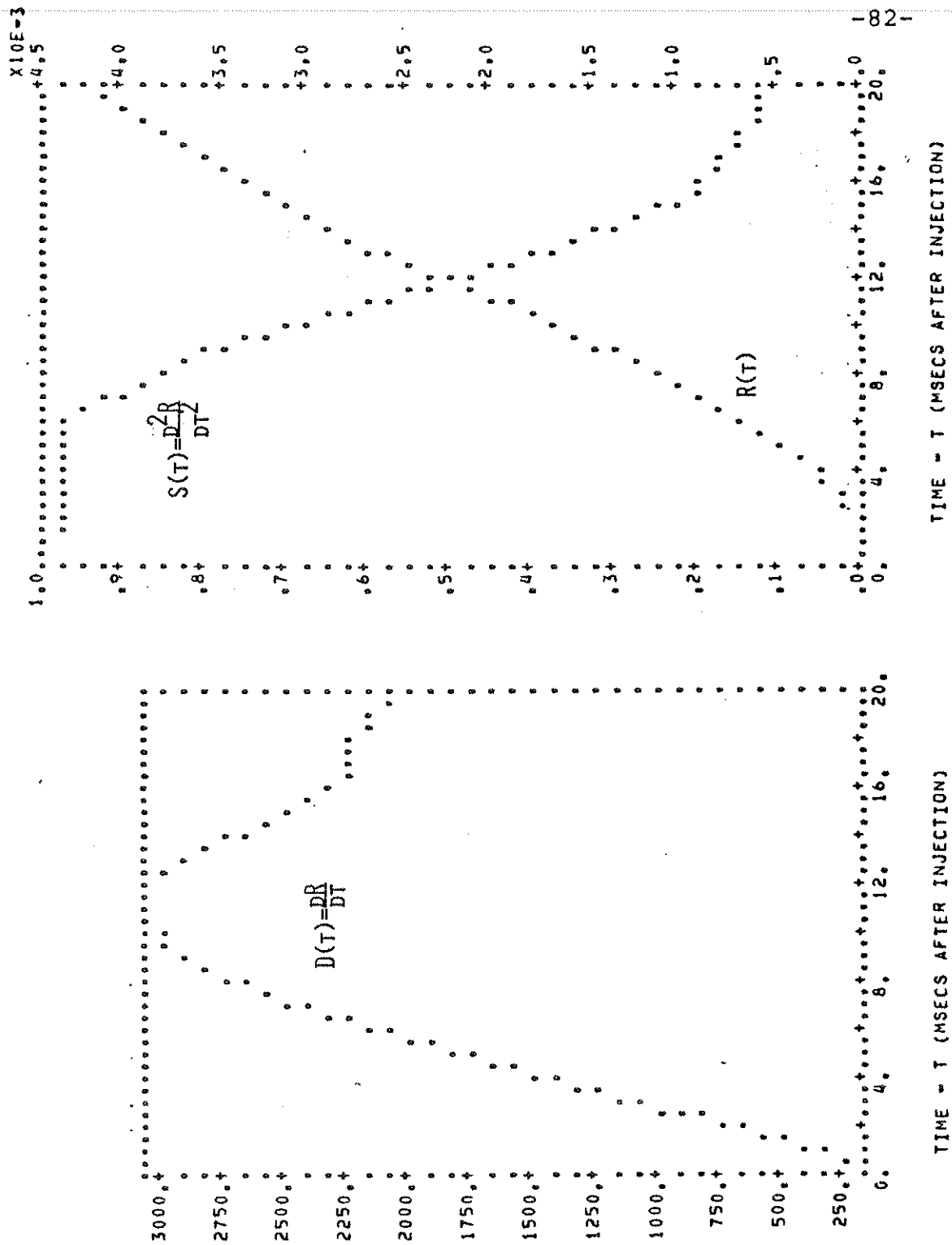
FIG. 4.4 SOLUTION TO EQUATION (4.5) USING 20 MODES.
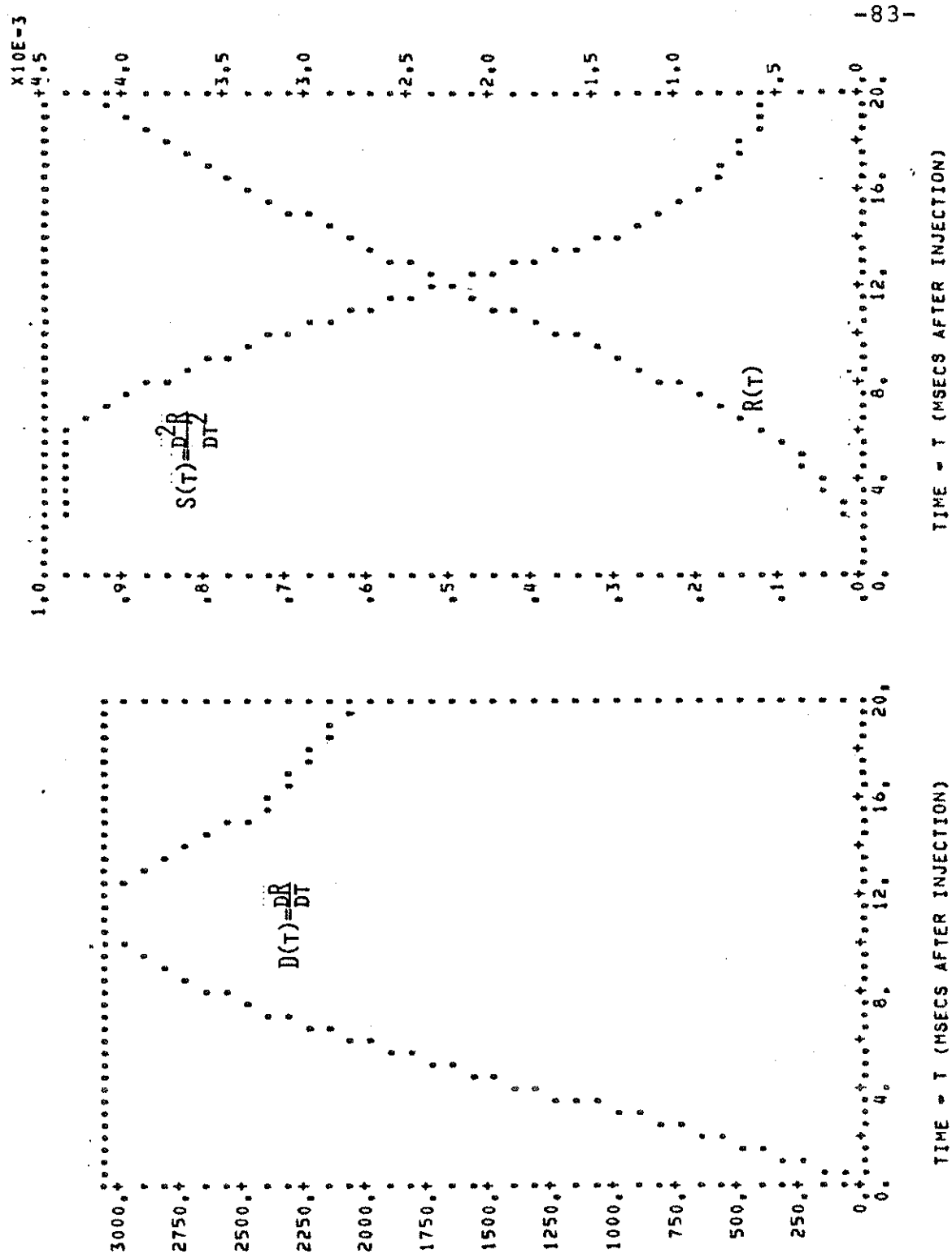
FIG. 4.5 SOLUTION TO EQUATION (4.5) USING 50 MODES.

Plots of $D(\psi)$ vs t will be shown in Chapter V and VI. The numbers plotted will be $\mathscr{D}_{av}$ from (4.11) in cm^2/sec; these estimates will be compared with the results of the studies of density profile evolution[25,26].

IV.7 SOURCES OF CONVECTIVE CELLS

Any mechanism which leads to charge separation is a potential source of convective cells. The only exception is when charge separation leads to drift surfaces (equipotentials) that are azimuthally symmetric, in which case there is no diffusion across a ψ-surface.

For gun plasmas in the Octupole, injection appears to be the principal mechanism for the creation of cells. The process was described in detail for the small Octupole by Dory, et. al.[2], as follows. The plasma beam from the gun polarizes as it crosses the magnetic field, and the directed velocity causes charges to separate until the polarization electric field cancels the average magnetic force on the plasma. Then the interior of the cloud is free to continue moving forward (into the magnetic well) due to the $\vec{E} \times \vec{B}$ drift. When the plasma first encounters a field line the polarization causes the field line to become charged; when encountering the same field line on the other side of the Octupole, the field and the polarization are in the opposite direction. The propagation of charge of opposite sign along the field line then shorts out the electric fields, and the plasma stops. After the initial penetration, the plasma is flute-unstable inwards and azimuthally.

The plasma cloud splits and proceeds around the torus and the two clouds collide at 180° from the gun port. During this phase, theory[44] and experiment[2] show the development of double vortex equipotentials. (Ref. 45 shows the same process in a linear quadrupole.)

The gun plasmas have an initial directed energy of $\sim 30eV$[15], and very large potentials ($\sim 100V$) have been measured near the gun port and around the machine during the injection process. This electric field energy is available for convective cells, although the plasma will short out potentials greater than KT/e after the initial turbulence damps out. It is interesting to note that the process puts energy into long-wavelength modes initially; if it did not, the energy spectrum might damp (by cooling or viscosity) before the cells coalesced into macroscopic (observable) vortices.

Other processes create charge separations in the Octupole. One is the effect of supports[1], which may preferentially drain electrons from the plasma. Non-azimuthally symmetric boundary conditions (due to electric fields at the gap, portholes, particle collectors, field errors, supports, etc.[1,10,13,15]) also play a role in determining what the electric field spectrum will be.

Drift waves (which require finite k_z) have been proposed as a means of effecting a charge separation at short wavelengths; convective cells can form from non-linear mode coupling. This is discussed further in Chapter VI for the collisionless plasma with an added toroidal field, but is not a mechanism for cell creation when $k_z=0$, as in the case with closed field lines.

With a poloidal and toroidal field, where flow along
a field line is expected to short out potential structure,
particles that are trapped in magnetic mirrors can be a
means of maintaining the charge separation necessary for
convective cells. An example of this is given in Chapter
VI for the collisionless plasma.

CHAPTER V - FLOATING POTENTIAL CONTOURS
IN A PURELY POLOIDAL FIELD

As noted previously by Drake[1] in the large Octupole, and by others in the small Octupole, the floating potential with a purely poloidal field in many cases is not azimuthally symmetric, even with the machine levitated, and the long-wavelength structure can be both reproducible and long-lived. Along a field line, however, V_f is constant, and the field lines are contained in constant azimuth planes. Because of this we can measure ϕ in the Octupole by constructing two-dimensional plots using the cart probe (Chapter II); 3-D structure can be found by rotating the contour plots around the rings, stretching to follow the magnetic field lines.

The 2-D character of the Octupole with a purely poloidal field suggests examining two-dimensional fluid theory; this is discussed in detail in Chapter III, and extended to Octupole coordinates in Chapter IV. In the present chapter we will compare several fluid theory results, such as macroscopic potential cells, shape of the electric field spectrum, and calculation of a diffusion coefficient, with the experimental measurements.

Potential structure was measured for a wide range of parameters; special effort was made to examine cases for which the profile evolution studies had also been done. Data is presented for the collisionless plasma, and for the collisional plasma over a range of field strengths. Levitated data is presented as well as supported data. The contours to be shown were all taken with the field crowbarred.

The data to be presented in this chapter shows that
cell structure is present when vortex diffusion is measured,
and much reduced when the diffusion scales like classical
diffusion. The vortex diffusion coefficient calculated
from the E^2 spectrum agrees in magnitude and shape with
the results of the profile decay experiments.

V.1 COLLISIONLESS PLASMA

A. Supported Data. Two sets of supported data are
presented for the collisionless plasma. Data was taken
with 2.5 kV on the poloidal bank (this corresponds to B_{av}
[Ref. 26] $\sim$1kG on the bridge side of the private flux of
the LOH). Data from two experiments is shown: an 80° scan
of the private flux of the LOH, and a 360° scan of the
private flux of the LIH.

1. Experimental Observations. Figs. 5.1a-f
show the floating potential in the private flux of the
LOH. The scan covers an 80° segment of the Octupole from
298°, through 0°, to 20°, for 5 ψ-surfaces. The scan
includes the support at 318° and a probe port at 330°.
The data shows a large cell which closes at the position
of the support (at 318°). The next support is at 30° and
the contours seem to be closing at the right side of the
plot (20°). This cell remains in the same position for
the entire experimental period. Its amplitude decays for
about the first 20-30ms, and then remains roughly constant
for the remainder of the pulse. There is some structure in
the separatrix region, but the potential variation is
largest in the region $3.5 \lesssim \psi \lesssim 4.5$.
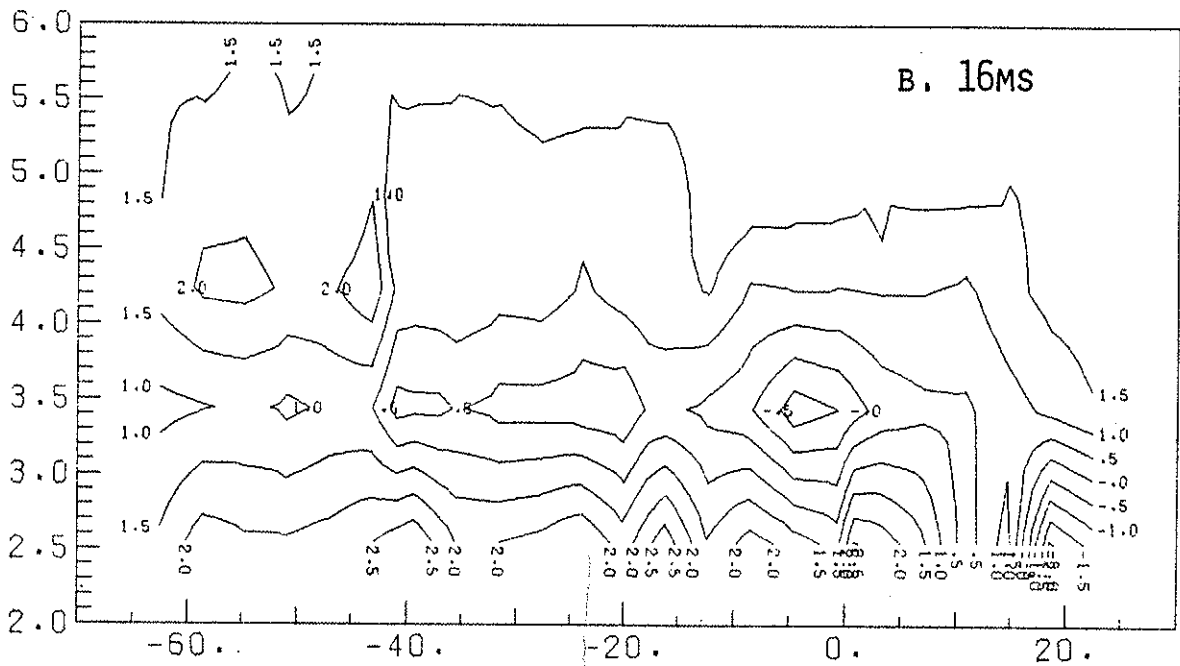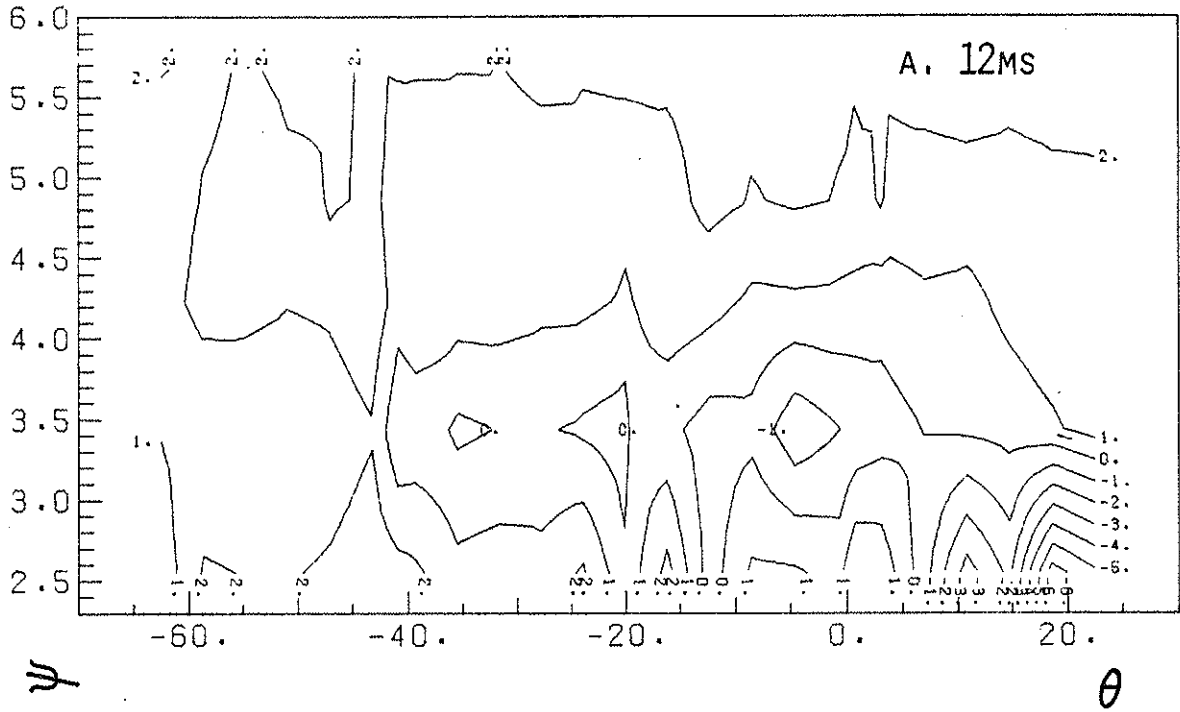
FIG. 5.1A AND B. FLOATING POTENTIAL CONTOURS; COLLISIONLESS
H PLASMA; SUPPORTED PRIVATE FLUX OF THE LOH;
$B_{P\ AVE}$=1KG (2.5KV).
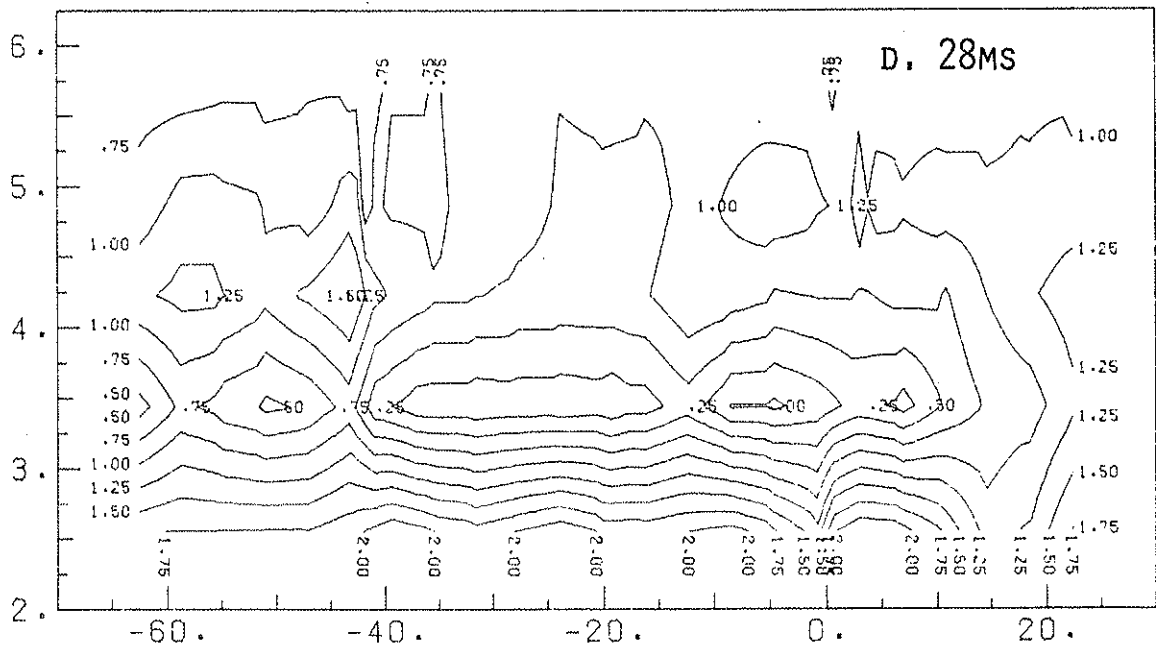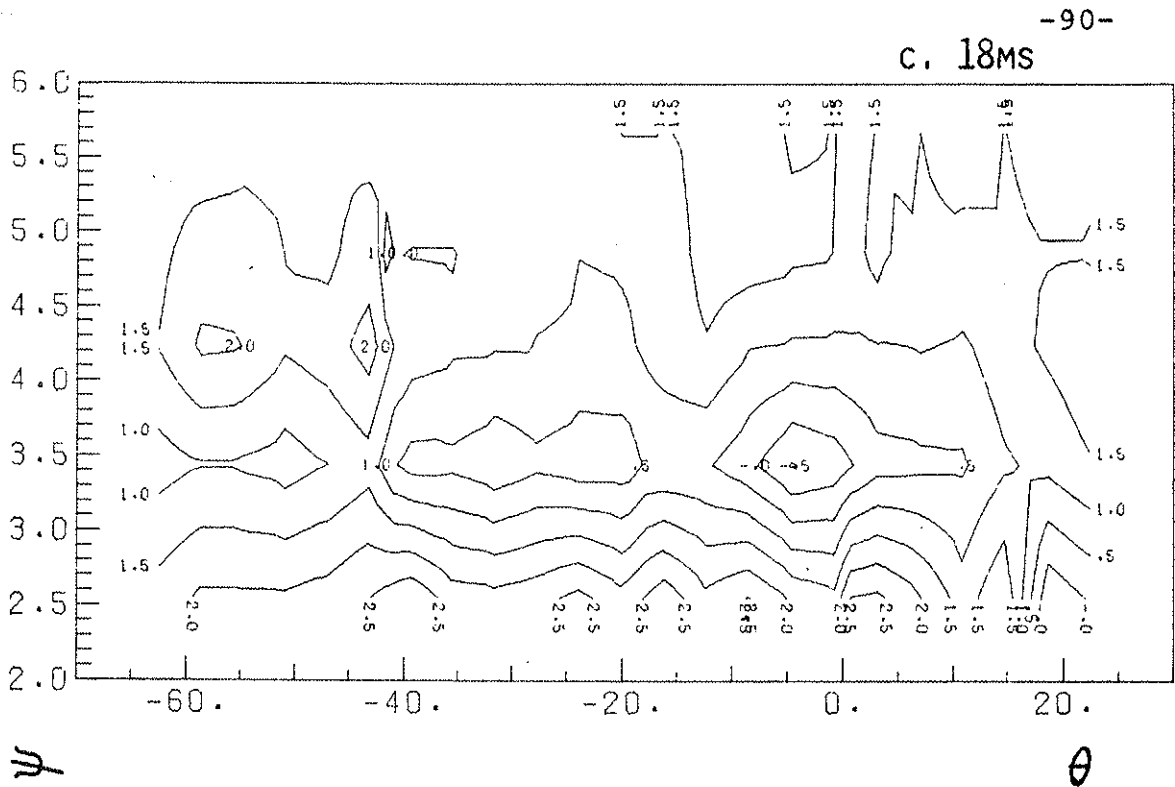
Fig. 5.1c and d. Floating potential contours; collisionless
H plasma; supported; private flux of the LOH;
$B_{P\ AVE}$=1KG (2.5(KV).
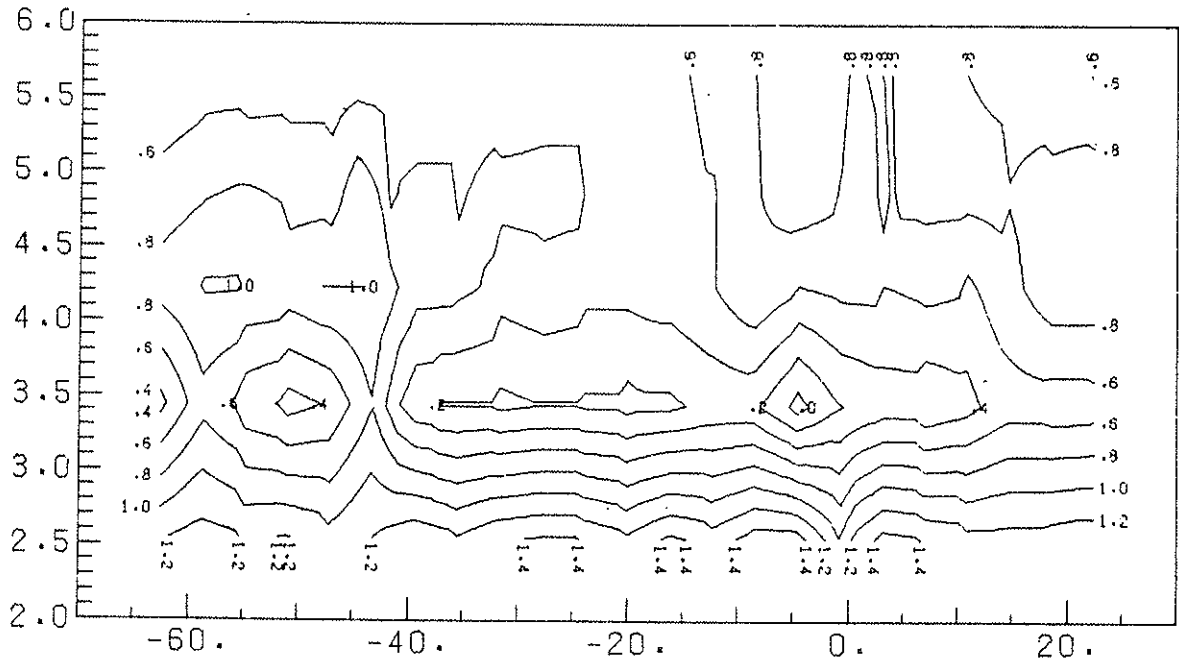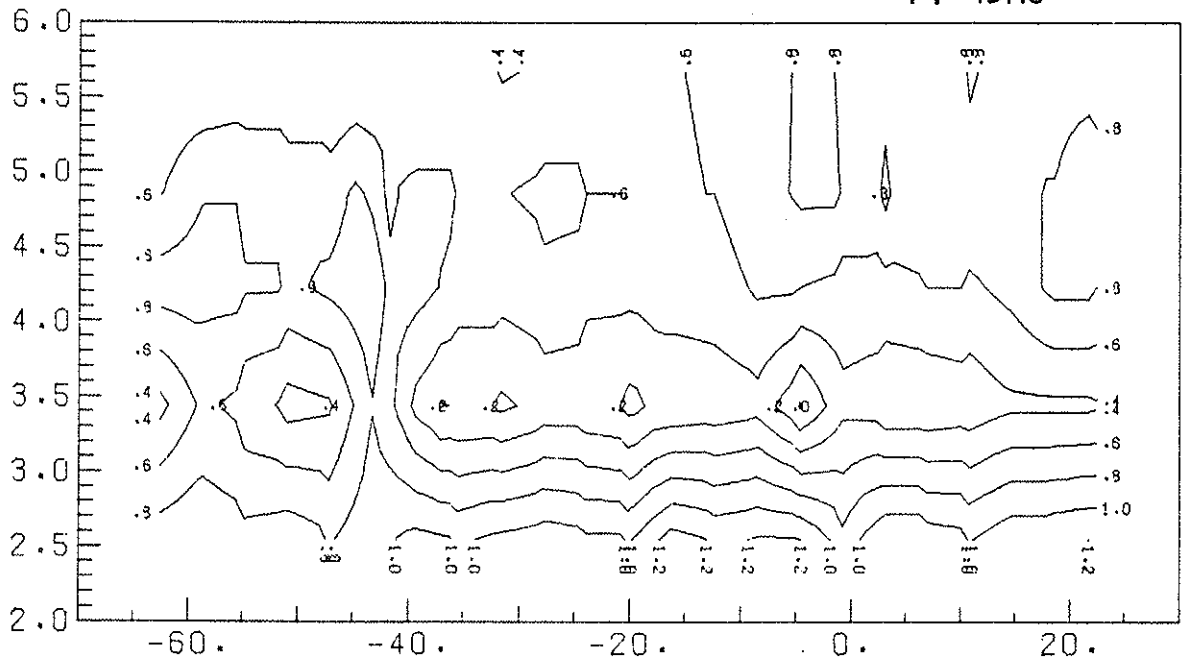
FIG. 5.1E AND F. FLOATING POTENTIAL CONTOURS; COLLISIONLESS
H PLASMA; SUPPORTED; PRIVATE FLUX OF THE LOH;
$B_{P\ AVE}$=1KG (2.5KV).

The floating potential contours for a full scan
(360°) of the LIH are given in Figs. 5.2a-d (private flux)
and 5.3a-d (common flux). This data had large variations
in the monitor, and is presented mainly to show the charac-
teristic cell pattern for a collisionless plasma with the
machine supported: the three inner supports are clearly
visible in the private flux contours.

The data for the common flux (see, for example, Fig.
5.3b at 7ms after injection) shows an oscillation in the
potential corresponding to the azimuthal position of all
the supports, both inner and outer, and also that of the
gap. Since this data was taken in the common flux region
near the inner nose, it shows that the entire field line
is affected by the support. However, the effect is not
quite as marked as for the private flux. We also note
that there is some evidence of outer supports in the
private flux of the inner hoop (Fig. 5.2b). All of the
psi-surfaces in the common flux are not at the same
potential at a support; this occurs because the support is
floating relative to the wall. There don't appear to be
closed cells in the main body of the plasma in the common
flux, but there may be some[1] closer to the wall in the
region the probe can't reach.

The cell structure is stationary; although the field
lines are soaking into the rings and walls, the cells do
not move with them. The boundary condition required at
the ring is an equipotential, but the probe cannot get
close enough to the boundaries to determine what the
structure looks like at the wall. The containment volume
extends to the critical ψ-surface, with $\psi_c \sim 7.8$ at 25ms
after the start of the pulse (see Fig. 2.2); in some parts
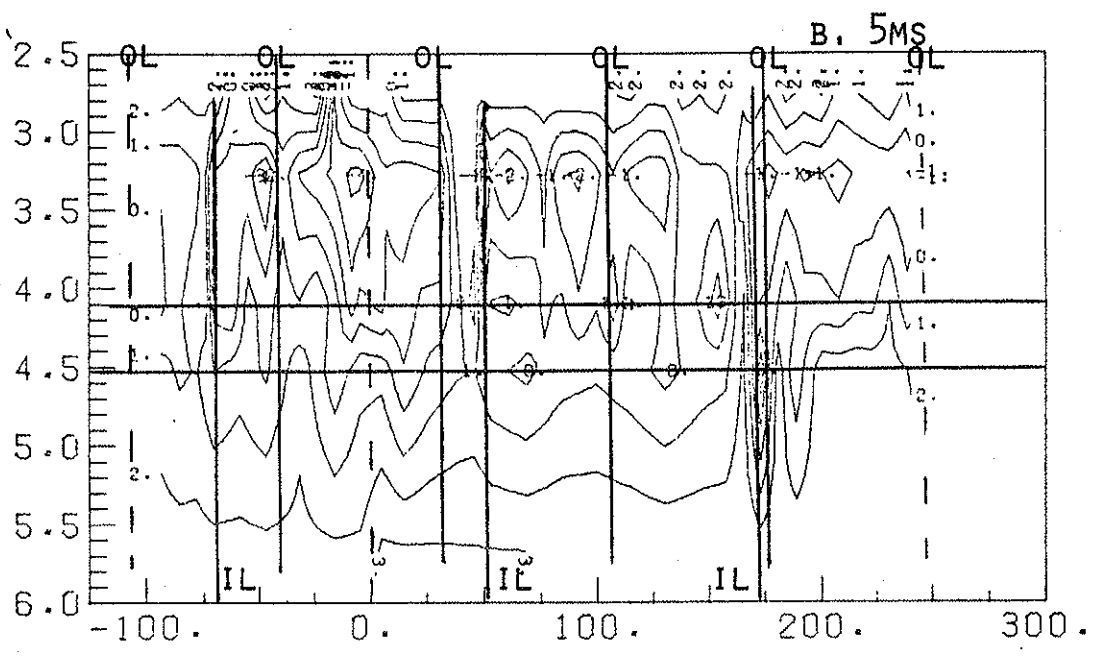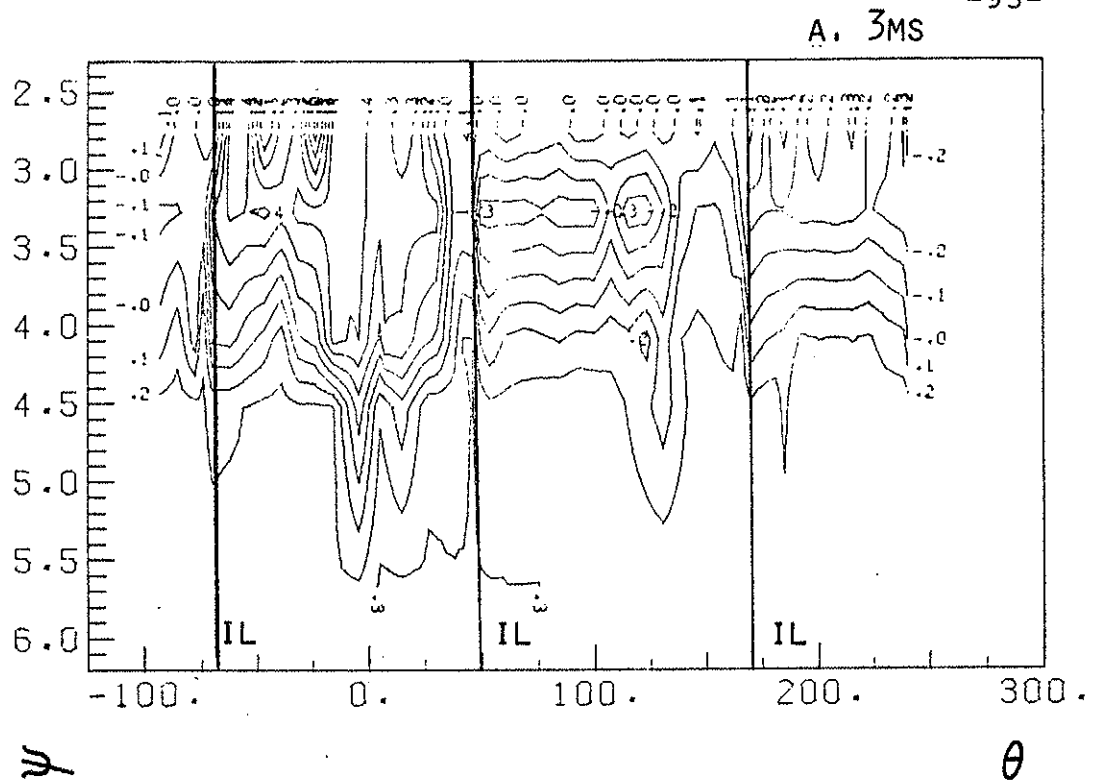
FIG. 5.2A AND B. FLOATING POTENTIAL CONTOURS; SUPPORTED;
COLLISIONLESS H PLASMA; PRIVATE FLUX OF THE LIH;
$B_{P\ AVE}$=2KG (2.5KV).
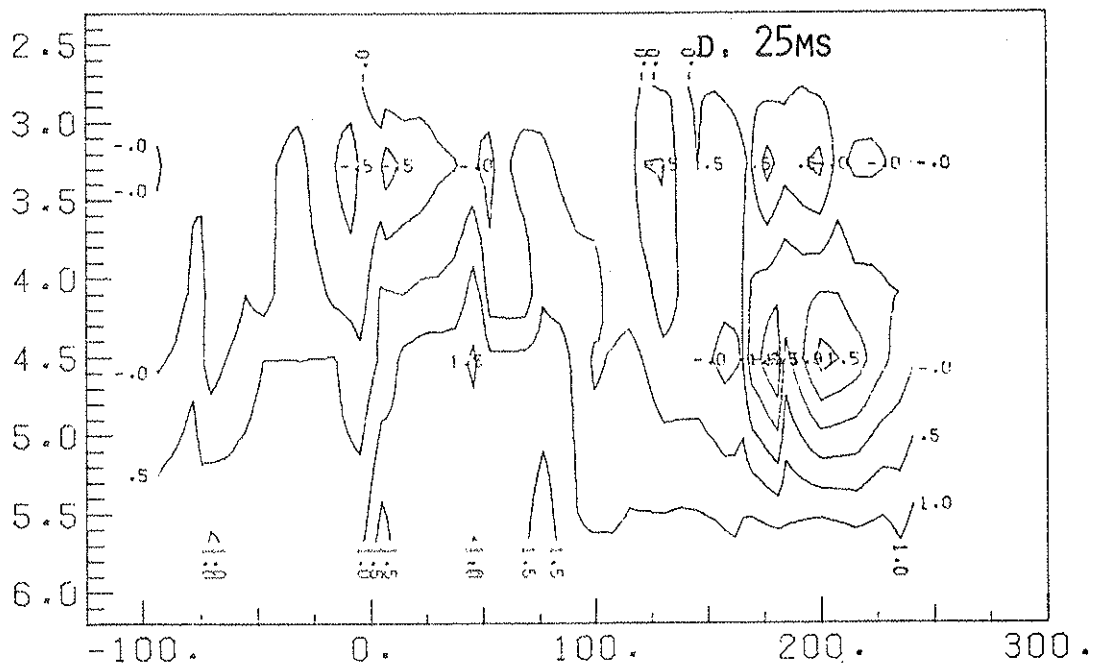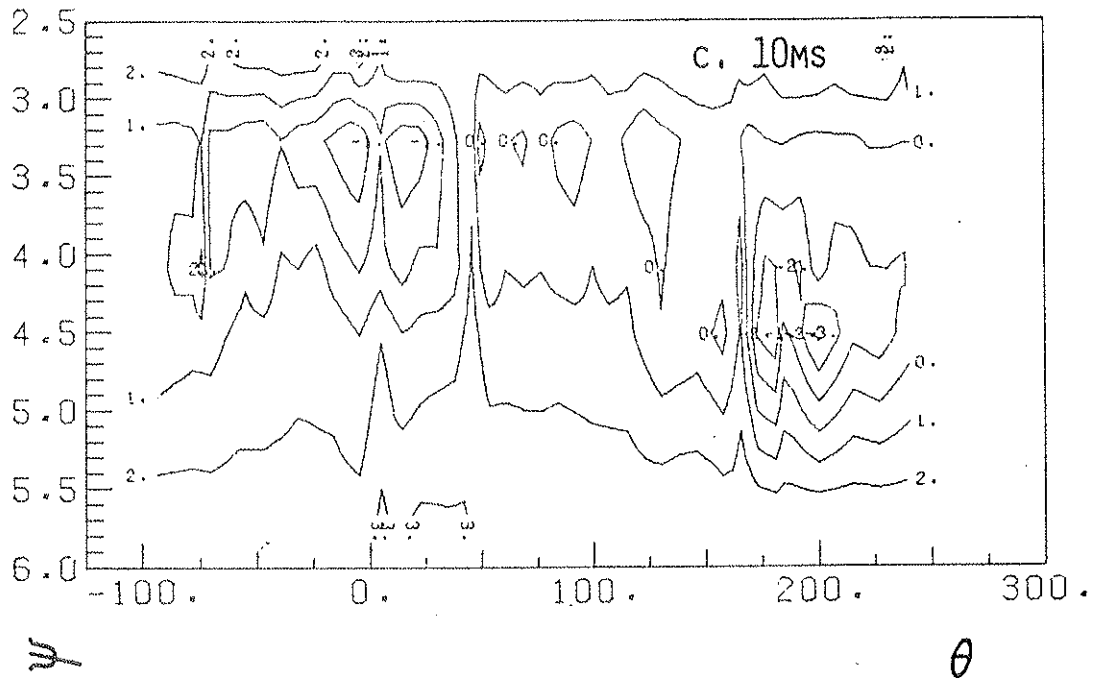
FIG. 5.2c AND D. FLOATING POTENTIAL CONTOURS; SUPPORTED; COLLISIONLESS H PLASMA; PRIVATE FLUX OF THE LIH; $B_{P\,AVE}$=2KG (2.5KV).

A. 3MS

B. 7MS
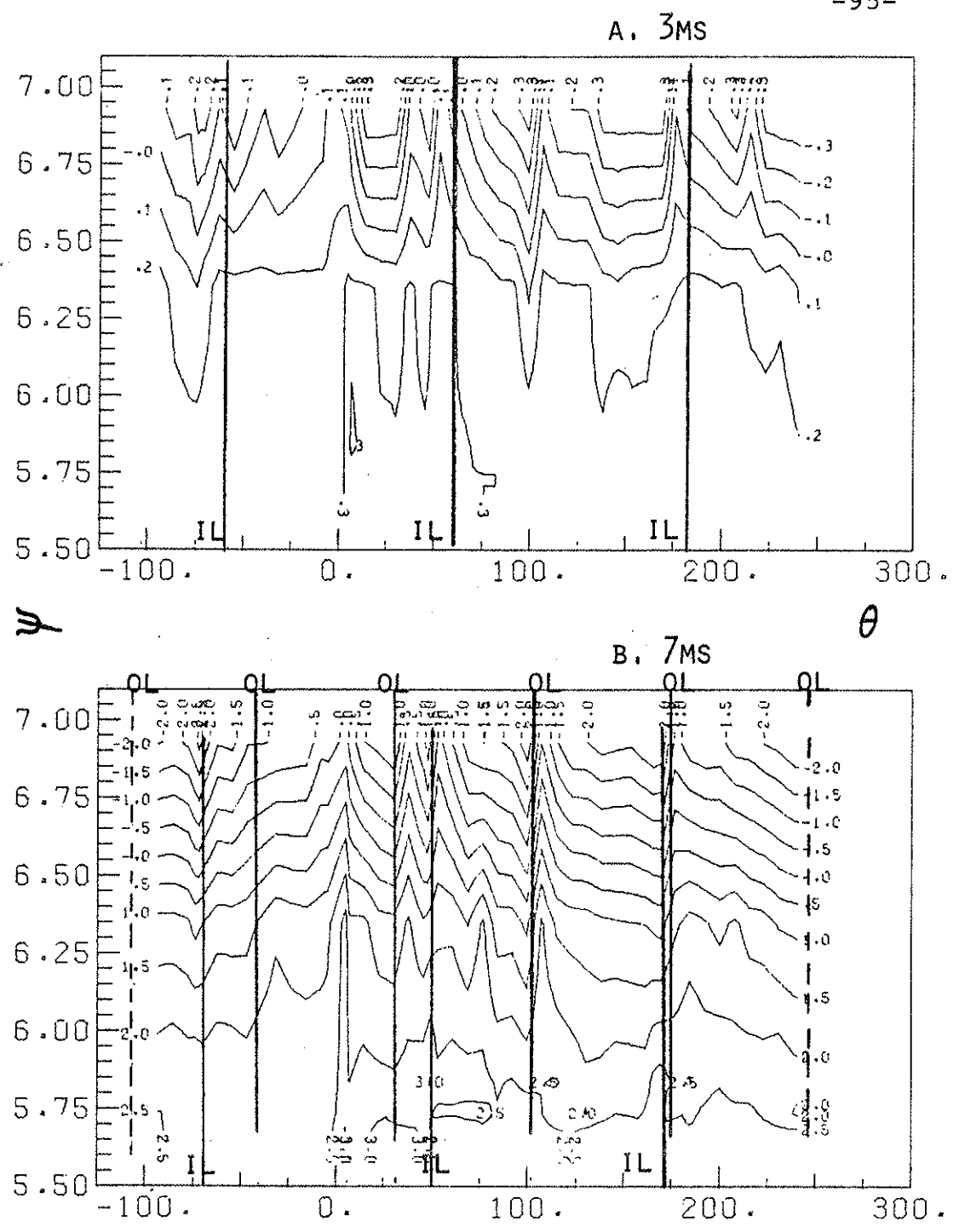
FIG. 5.3A AND B. FLOATING POTENTIAL CONTOURS; SUPPORTED;
COLLISIONLESS H PLASMA; COMMON FLUX - INNER NOSE;
$B_{P \ AVE}$=2KG (2.5KV).

c. 15ms

γ

θ
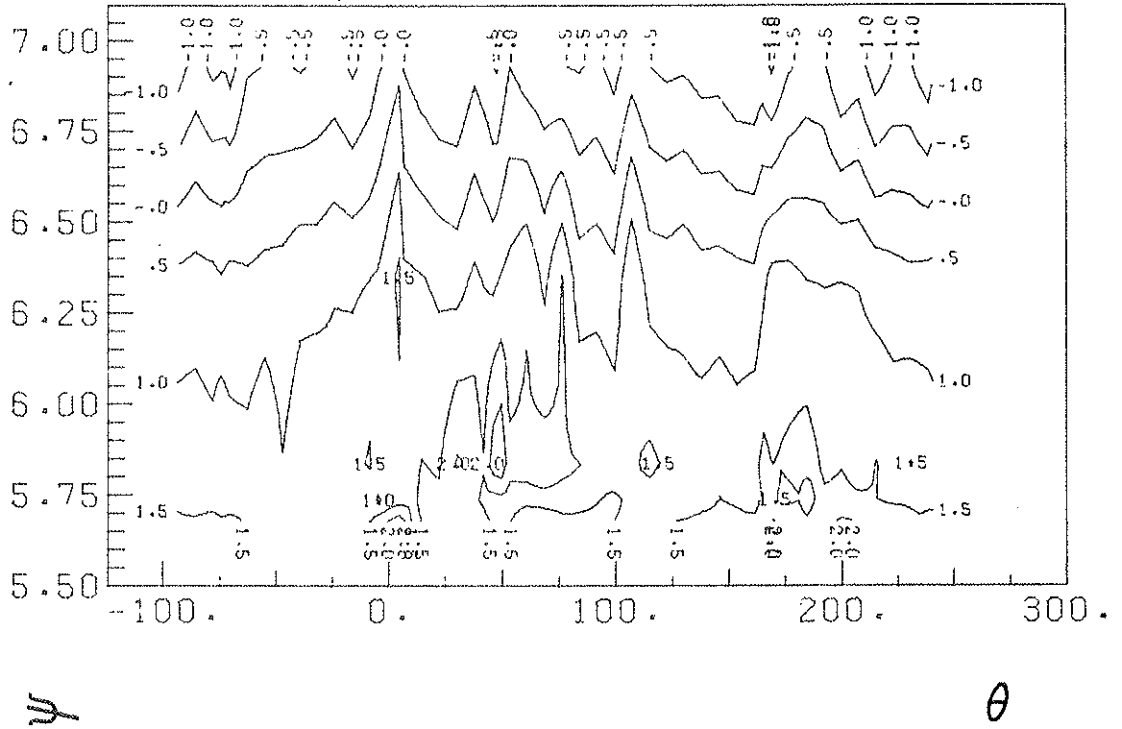
d. 20ms
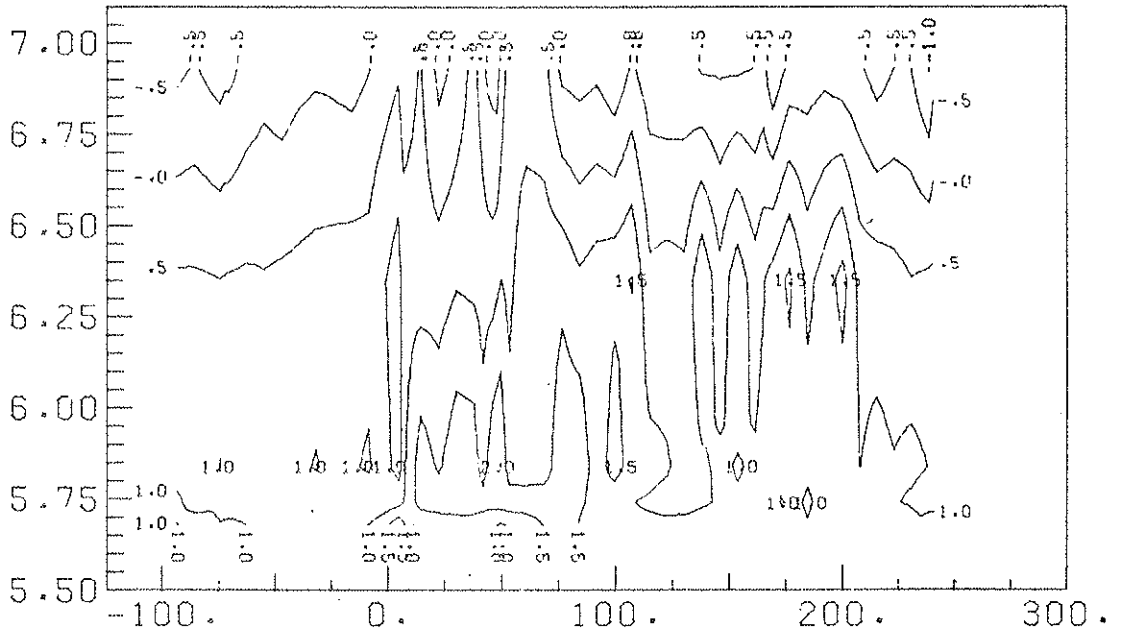
Fig. 5.3c AND D. FLOATING POTENTIAL CONTOURS; SUPPORTED;
COLLISIONLESS H PLASMA; COMMON FLUX - INNER NOSE;
$B_{P\ AVE}$=2KG (2.5KV).

of the Octupole there is a region between ψ_c and the wall, and in other places ψ_c intersects the wall (for example, at the inner nose). We do not yet know what effect this has on the cell structure near the Octupole walls. Local perturbations (such as collectors on the hoops) can also affect the shape of the equipotentials near the ring.

The toroidal spectrum of the electric field is shown in Figs. 5.4 and 5.5 for two psi-surfaces in the private flux of the LIH (ψ=4.09 and 4.52). The figures show that the energy spectrum of the toroidal vortex modes is a rapidly decreasing function of k, and decays in time. Note that, because what is plotted is $E^2(k)$ and not $E(k)$, the resolution of the plot corresponds to a factor of 30 in the potential rather than 10^3. This means that the 'bump' at the higher mode numbers is well within the resolution of the digitizer, and is not just noise.

2. Discussion. When considering the data for the collisionless plasma in a purely poloidal field, we want to examine three main areas, to see if the proposed theory provides a reasonable framework for understanding the data. These areas are: first, the shape of the measured vortices and spectra; second, the time decays and possible damping mechanisms; and third, the magnitude of the vortex diffusion coefficient and enhanced temperature T^* that can be estimated from the data.

Potential Contours. The full scan contours, Figs. 5.2 and 5.3 (LIH), show a pattern of three large cells. The plots are similar to the fluid solutions proposed in Fig. 4.2c, col. 3, if we allow three toroidal modes rather than four. Data on the shape of the potential
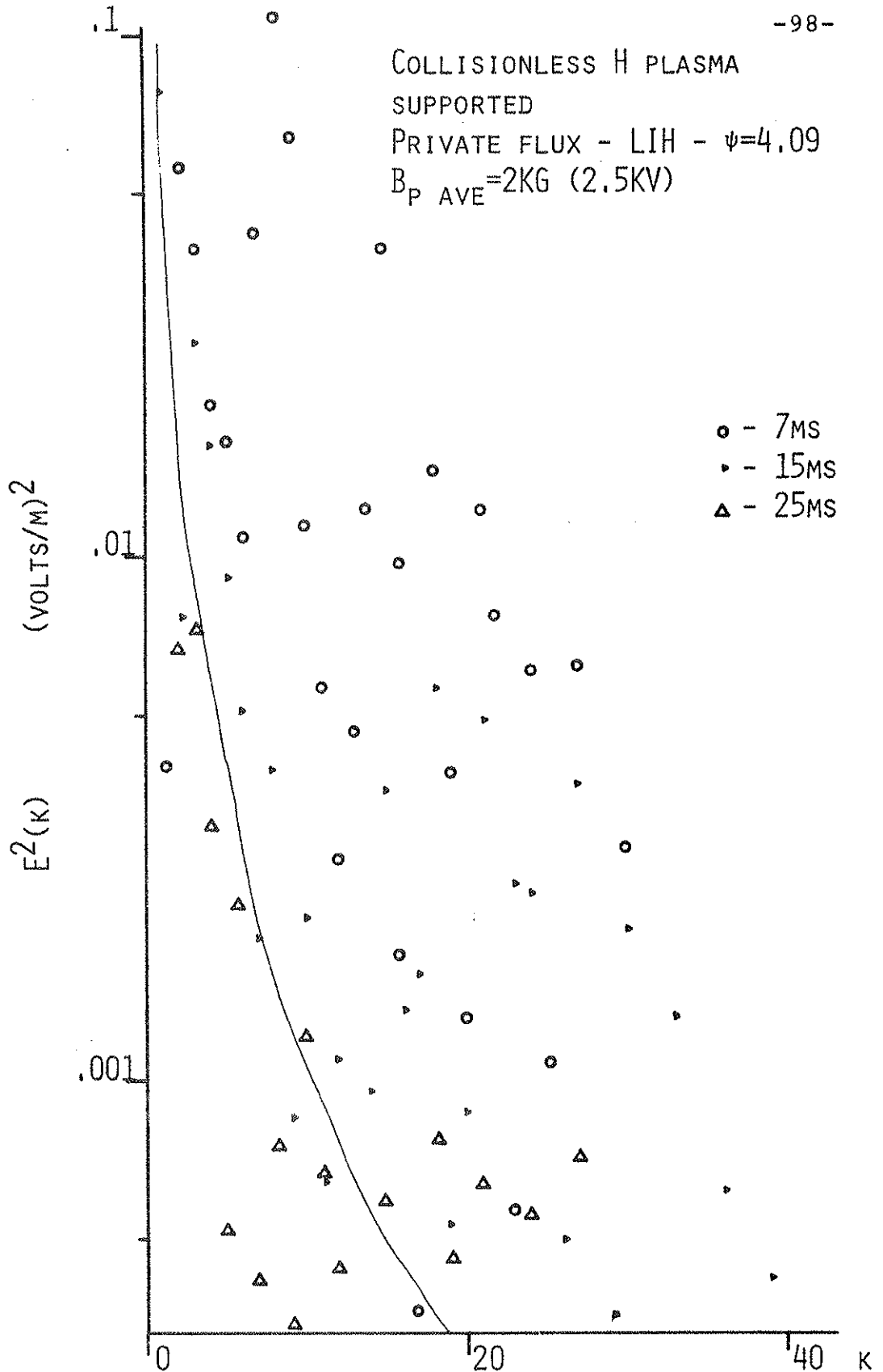
FIG. 5.4 TOROIDAL ELECTRIC FIELD POWER SPECTRUM, $\psi=4.09$
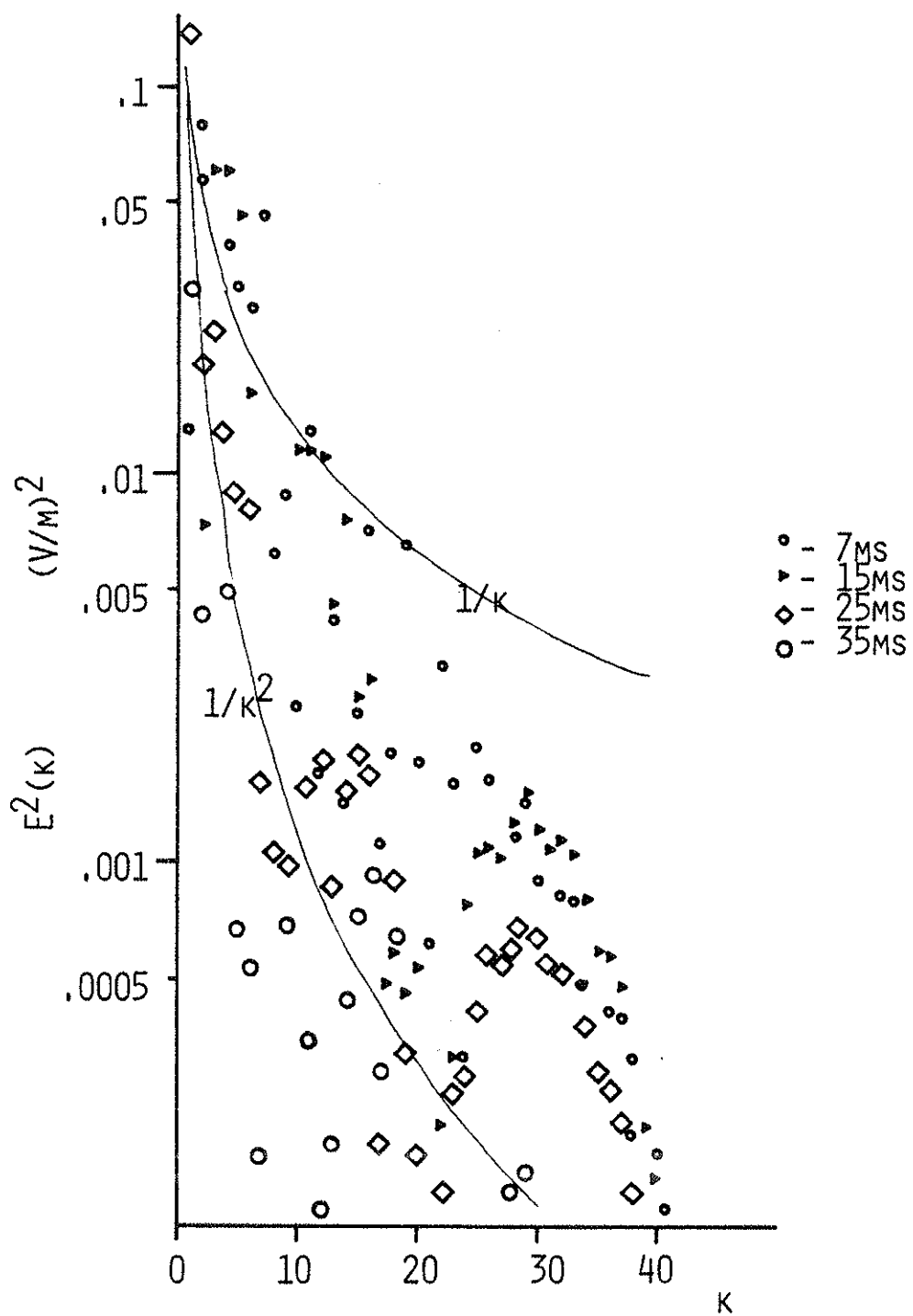
FIG. 5.5 TOROIDAL POWER SPECTRUM; COLLISIONLESS H PLASMA;
SUPPORTED; ψ=4.5 LIH; $B_{P\ AVE}$=2KG (2.5KV).

profile in ψ was taken by Greenwood[13], who measured the floating potential profile and the density profile for the collisionless plasma at the probe port at 330° on the LOH (Figs. 3.6 and 3.8 in Ref. 13). The density and floating potential profiles have approximately the same shape at that azimuth, but the floating potential cannot have the same normal mode solution as the density at all azimuths because although the density is azimuthally symmetric, V_f is not.

The mean-free-path for the collisionless plasma is ~100m, and there is very good communication along the field line. The levators are in electrical contact with the ring but can float from the walls; thus the supports can act as an additional boundary, creating an equipotential surface out of the field lines intersected at the azimuth of a support. From the data for the collisionless plasma it appears that all field lines in the private flux at the azimuth of the support are at the same potential.

One might expect that the support as an additional boundary condition might make the mode m=3 (or m=5 for the outer hoops) the longest-wavelength mode, but the spectra (Figs 5.4 and 5.5) for the private flux psi-surfaces do not support this, but show that m=1 is the longest mode. Instead we can think of the support as a local perturbation in the potential extending in θ for no more than a few degrees. From Drake's detailed data for the cell structure in the vicinity of a support (Ref. 1, Fig. 5.15, p. 153) we can estimate a perturbation width of $5-15^O$, which corresponds to a mode number 24-72, and is probably the source of the bump at $m\sim30$ on the spectrum of E^2.

The shape of the toroidal spectra (Figs. 5.4 and 5.5) indicates a non-thermal plasma, as in thermal equilibrium E is independent of k (up to $k^2\lambda_D^2 \sim 1$). Lines proportional to $1/k$ and $1/k^2$ have been drawn on Fig. 5.5; the scale factor is such that the lines pass through the data. This shows that E_θ^2 is approximately proportional to $1/k^2$, as is predicted in equation (3.27) for the equilibrium vortex spectrum, and similar to numerical simulations by Seyler, et al.[24]. [Note that the theory predicts this dependence for a non-thermal equilibrium corresponding to a negative temperature.] However, the spectrum is too noisy to obtain estimates of the parameters α and β; the values vary by large amounts, and even change sign, depending on how many modes are used.

Damping. For this plasma the ion viscosity[52] is very small (a few cm^2/sec), and the ion viscous damping time, $\tau_\mu \propto L^2/\mu$, is on the order of seconds even for cells as small as a centimeter. Therefore, we do not expect to see the large cells damped by ion viscosity, and any damping is due to some other mechanism. (However, the non-linear mode coupling may transfer energy from the long-wavelength cells to short-wavelength cells where viscous damping is important.) The fluid loses energy, and we observe experimentally that the amplitudes are tied to the electron temperature. Therefore, we will examine in particular the effect of cooling, which can damp the vortex spectrum because as the plasma cools it is not able to support the large electric fields measured during the injection and filling process.

The electron temperature for this plasma decays with $\tau_e \sim 20ms$ for the first 20ms, and then remains approximately

constant at 1.5eV for the remainder of the experimental period[25]. The partial scans of the LOH (Fig. 5.1) show qualitatively the same behavior: for about the first 20ms the amplitude of the large cell in the private flux decays, and then remains roughly constant. The potentials in the plasma are on the order of the electron temperature, but it is not possible to estimate a decay rate for the electric field from the partial scan contour.

The time decay of the power spectrum of the potential is shown in Fig. 5.6 for the two psi-surfaces in the private flux from the 360° scan of the LIH. (Because this set of data was noisy we have analyzed only the two psi-surfaces with the smallest variation in the monitor.) Although more information is needed about the two-dimensional character of the spectrum, we note that the decay of $\Sigma\phi(k)^2$ has a time behavior similar to that of the electron temperature. For a stationary spectrum this would also be true of $\Sigma E(k)^2$. The decay is exponential over the whole experimental period, with $\tau_E 2 \sim 8ms$. This corresponds to a decay for the electric field of roughly twice this value ($\sim 16ms$) which is close to the known value for T_e ($\tau \sim 20ms$) during the first 30ms; however, T_e becomes a constant at $\sim 30ms$, while ΣE_θ^2 continues to decrease on these two ψ-surfaces.

The time decays of several individual modes from the same two psi-surfaces are plotted in Figs. 5.7 and 5.8. The individual modes also decay with $\tau_E 2$ 8ms; this agrees with the discussion of Section IV.5, that the first 20-30 modes in θ share a single k_ψ. Data is not plotted earlier than 10ms after injection because it is not reproducible during the early times. Arbitrary initial distributions evolve

$\Sigma_{K} \phi(k)^2$ (VOLTS)^2

COLLISIONLESS H PLASMA
SUPPORTED
PRIVATE FLUX - LIH
$B_{P\ AVE}$=2KG (2.5KV)

2MS

7MS

.01

.001

16MS

12MS

35MS

25MS

$\triangle$ - ψ=4.09
$\circ$ - ψ=4.52
LIH

0

20

40MS AFTER
INJECTION
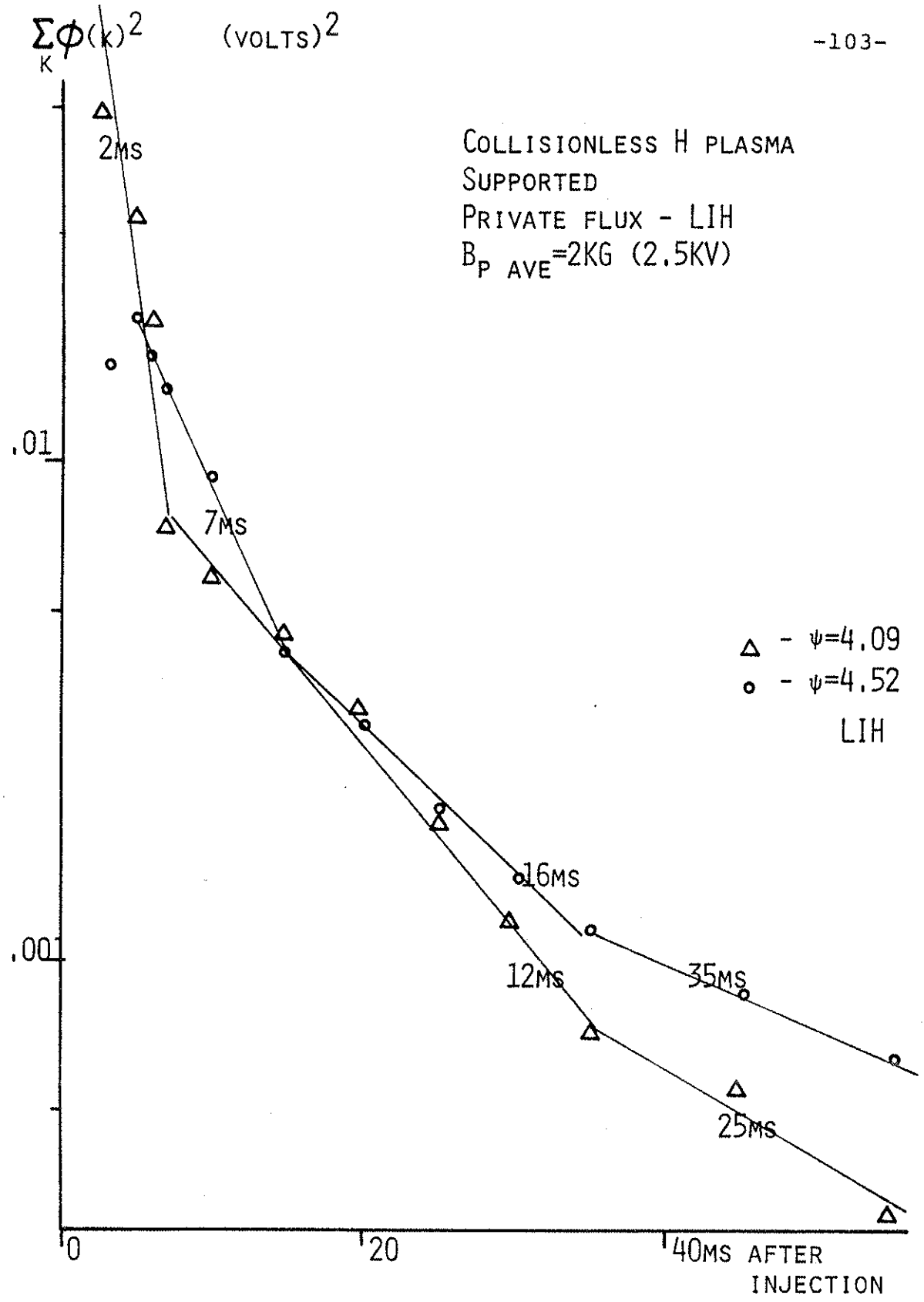
FIG. 5.6 TIME DECAY OF ENERGY SUMMED OVER K VS. TIME.
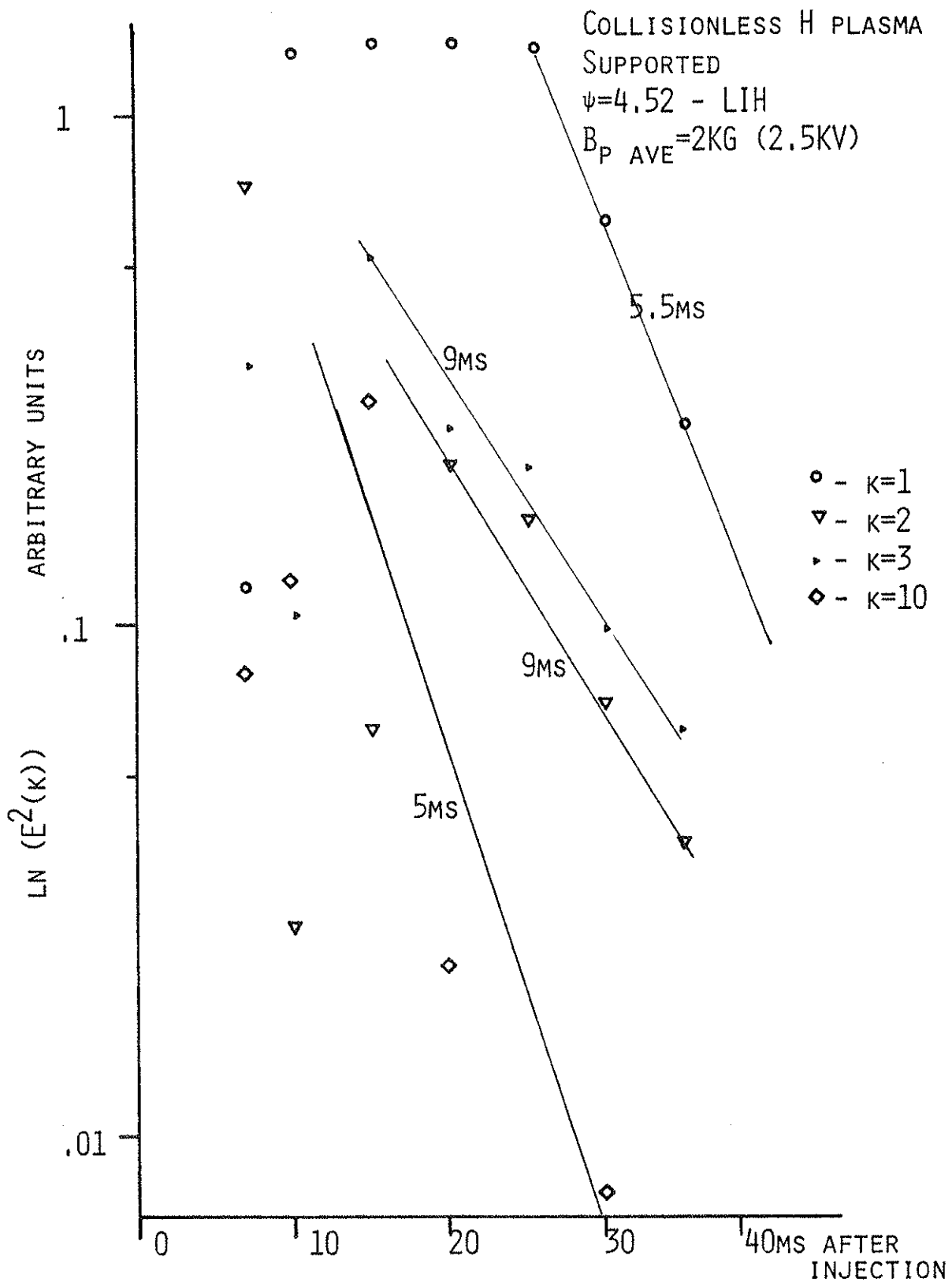
FIG. 5.7 TIME DECAY OF INDIVIDUAL MODES, $\psi=4.52$
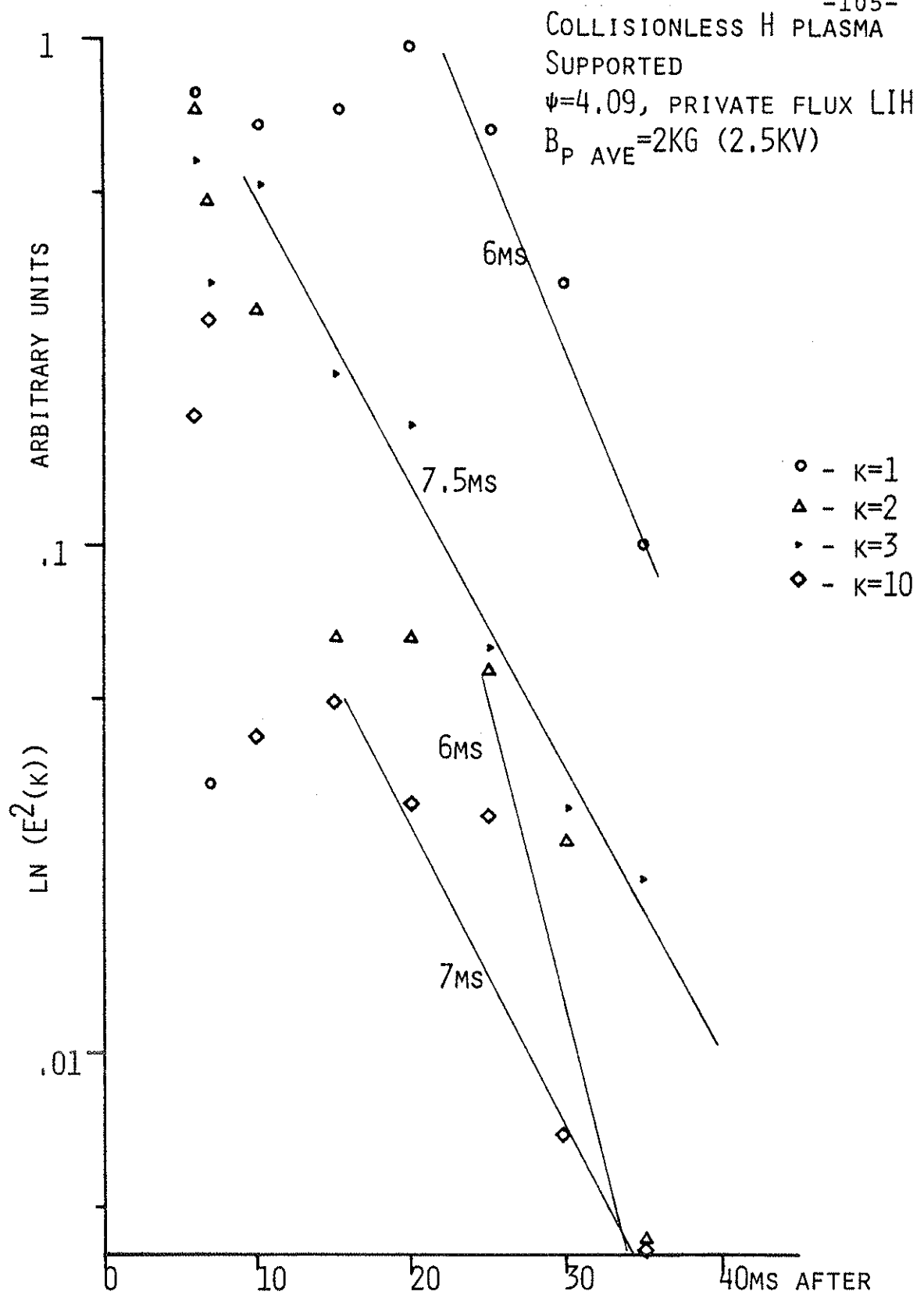
FIG. 5.8 TIME DECAY OF INDIVIDUAL MODES, $\psi=4.09$

into the same long-wavelength structures. This agrees with the argument in Section IV.1 that the observed potential cells represent the most probable state of the system.

The LOH partial scan shows that the contours, while retaining their shape, decay for about the first 25-30ms, and then remain approximately constant. Greenwood[13] took a constant-azimuth scan of V_f through the probe port at 330° for the same plasma. To get an idea of the time decays we have plotted the voltage at the peak as a function of time (Fig. 5.9). The peak voltage decreases exponentially with an 8ms time constant for the first 20ms. During the next 20ms the profile becomes severely distorted (see Ref. 13, Fig. 3.8) and the characterization of the decay by a single mode in ψ becomes less and less valid. The time decay of the peak slows by a factor of 2 (to ∿17ms); however, an average, such as the value at the flat spot, continues to decrease at about the same initial rate (9ms).

From the supported data for the collisionless plasma we conclude that plasma cooling can account for the damping of the vortex spectrum in the first 20-30ms. In the latter part of the experiment, the evidence is contradictory: the contours (Fig. 5.1 and 5.2) do not change much but the spectra from the two ψ-surfaces in the LIH private flux continue to decay. It would be necessary to look at more ψ-surfaces to resolve this question.

Vortex Diffusion Coefficient; T^*. If the study of the convective cells is going to yield useful information about plasma lifetimes in the Octupole, we need to be able to calculate parameters such as T^* and D_v from the vortex
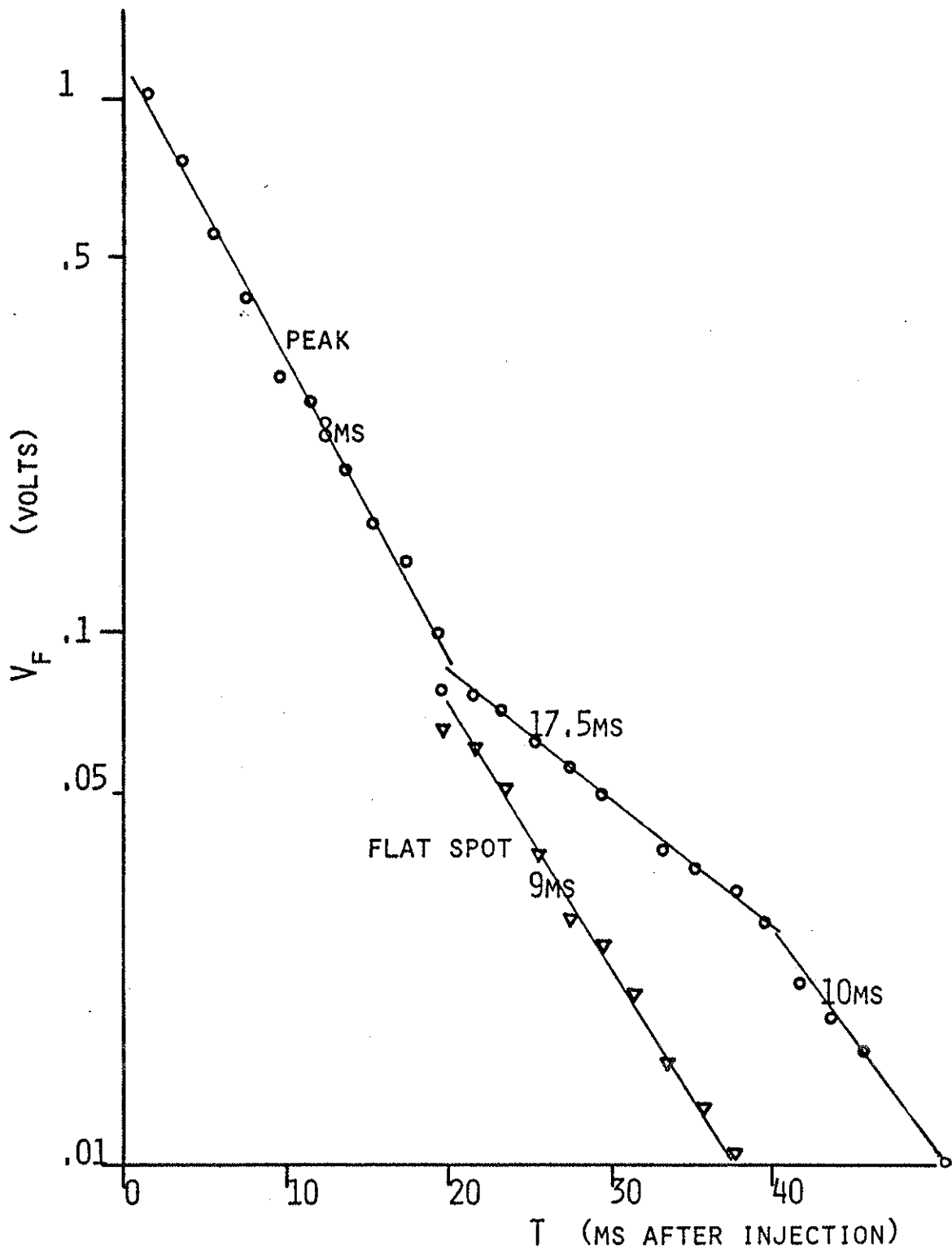
FIG. 5.9 DECAY OF THE FLOATING POTENTIAL PROFILE IN ψ.
(DATA TAKEN FROM REF. 13, FIG. 3.8)

spectra. The following calculations use the local values
on a psi-surface as discussed in Chapter IV; these numbers
should be seen as giving an order of magnitude since the
two-dimensional spectrum has not yet been fully developed
and the effects of inhomogeneities, etc., are not included
in the simple theory of Sec. IV.6.

The value of the diffusion coefficient D(t) obtained
using equation (4.10) for the two ψ-surfaces in the LIH
private flux is plotted in Fig. 5.10a. D_v is on the order
of $10^4 cm^2$/sec 5ms after injection, decreases to $\sim 2.5-$
$3.5 \times 10^3 cm^2$/sec by 20ms, and then levels off, and begins to
climb very slowly. The decay of D(t) at early times is
plotted in Fig. 5.10b on a log scale; from 5 to 20ms after
injection, D(t) decays exponentially with $\tau_D \sim 13ms$. The
behavior of D(t) agrees in general with the diffusion study
results[25]: Initially, T^* decays rapidly, and because
$D \propto (T^*/n)^{1/2}$, D will also decrease; after 30 ms, T^* is cons-
tant, but n is still decaying, so that D will increase in
time. The magnitude of D_v calculated using (4.10) after
20ms is larger by a factor of 2-5 than the $800 cm^2$/sec
quoted in Ref. 25, Fig. 2. This is remarkably good agree-
ment from the relatively crude model proposed in Chapter
III and IV.

The effect of diffusion due to long-wavelength vortex
modes on a finite-size plasma can be seen in the density
profile decay data presented in Ref. 25, Fig. 5. The
profile becomes distorted by the effect of the large cell
observed in Fig 5.1 between $\psi=3.5$ and $\psi=4.5$. We note from
the full scan of the LIH (Fig. 5.2) that cells are present
from the earliest time plotted, and the "flat spot" appears
on the profile at $\sim 10-15ms$ after injection, which is on the
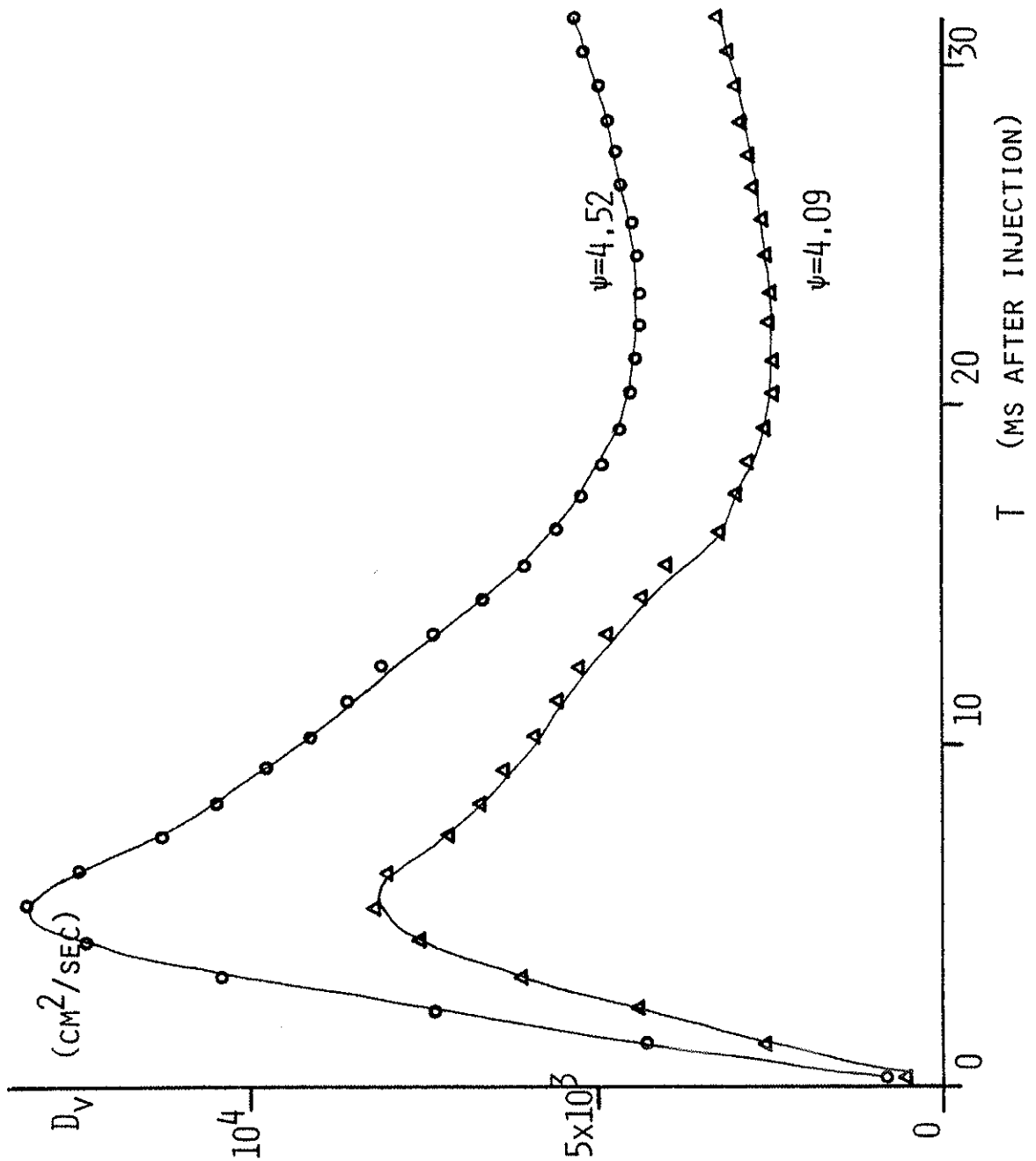
FIG. 5.10A DIFFUSION COEFFICIENT VS. TIME; COLLISIONLESS
H PLASMA; SUPPORTED; ψ=4.52 AND ψ=4.09, LIH; .
$B_{P\ AVE}$=2KG (2.5KV).
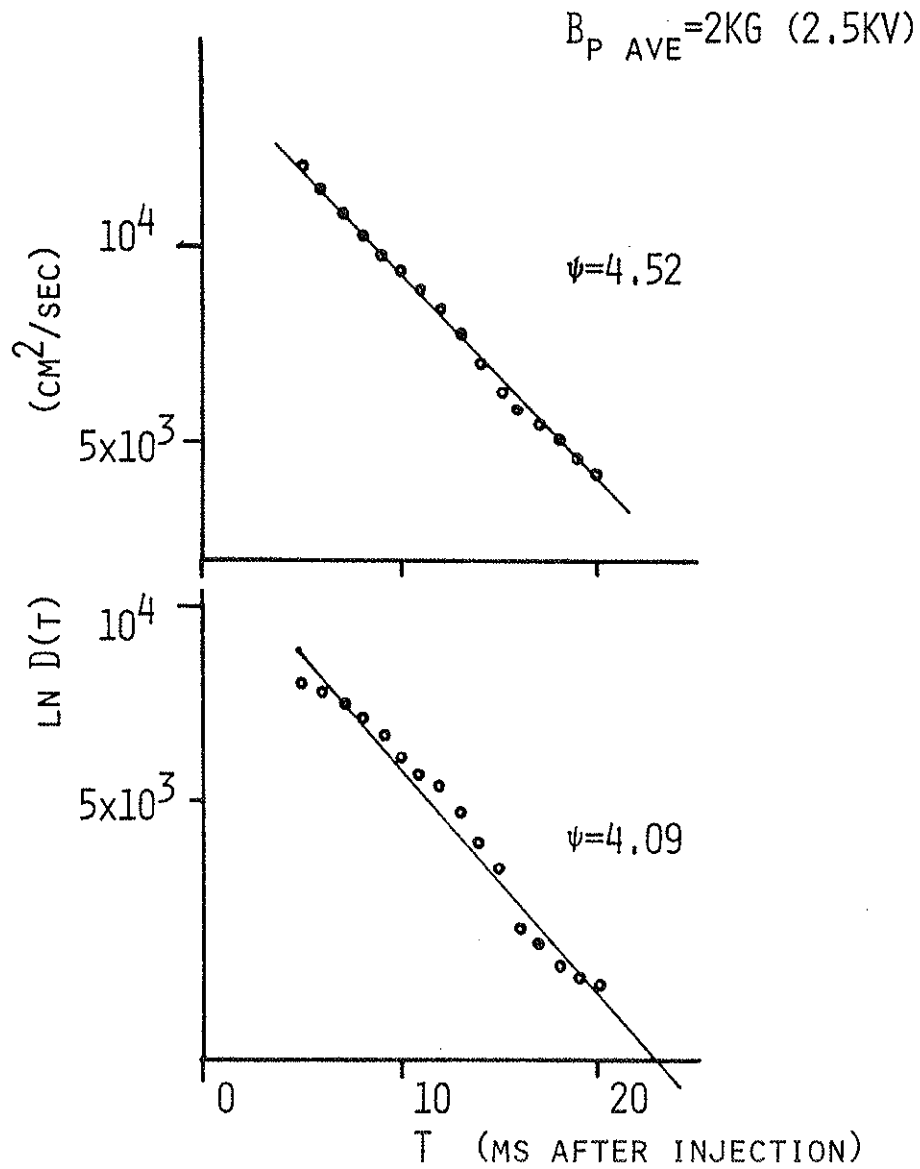
FIG. 5.10B DIFFUSION COEFFICIENT VS. TIME (LOG SCALE),
EARLY TIMES (0-20MS); COLLISIONLESS H PLASMA;
SUPPORTED; $\psi=4.52$ AND $\psi=4.09$, LIH PRIVATE FLUX.

order of the time it takes a particle to $\vec{E} \times \vec{B}$ drift half-way around the cell. Because the collision time is of the same order as the circulation time around a cell, particles can move across the magnetic field by following an equipotential.

The enhanced temperature T^* can be estimated using equation (3.30):

$$\frac{T^*(k)}{2} = \frac{\varepsilon E^2(k)}{8\pi} L_{||} L_{\perp}^2 \qquad (5.1)$$

using the value of $E^2(m=1)=.075V^2/m^2$ at 25ms from Fig. 5.4 ($\psi=4.1$), with $n \sim 2 \times 10^8/cm^3$, $B \sim 2kG$, $V=8 \times 10^4 cm^3$, we find $T^*(m=1)=2.4 \times 10^5 eV$. This estimate is very rough, but it shows that there is enough energy in the vortex spectrum to account for the observed diffusion.

B. Levitated Data. Two experiments were performed to investigate the effect of supports in the collisionless plasma. In the first the rings were levitated, and the plasma injected into a fully levitated machine. In the second experiment the levators were pulled out after the plasma had been injected.

1. Experimental Observations. Figs. 5.11a-f present potential contours in the private flux for normal levitation - the machine is fully levitated at the time the plasma is injected. Late levitation data for the private flux is shown in Fig 5.12a-f, where the machine is fully levitated $\sim 20ms$ after plasma injection. The levators are pulling out of the machine for the first 20ms of this experiment. Both scans cover the same section of the

FIG. 5.11A AND B. COLLISIONLESS H PLASMA; NORMAL LEVITA-
TION; PRIVATE FLUX OF THE LOH; $B_{P\ AVE}$=1KG (2.5KV)
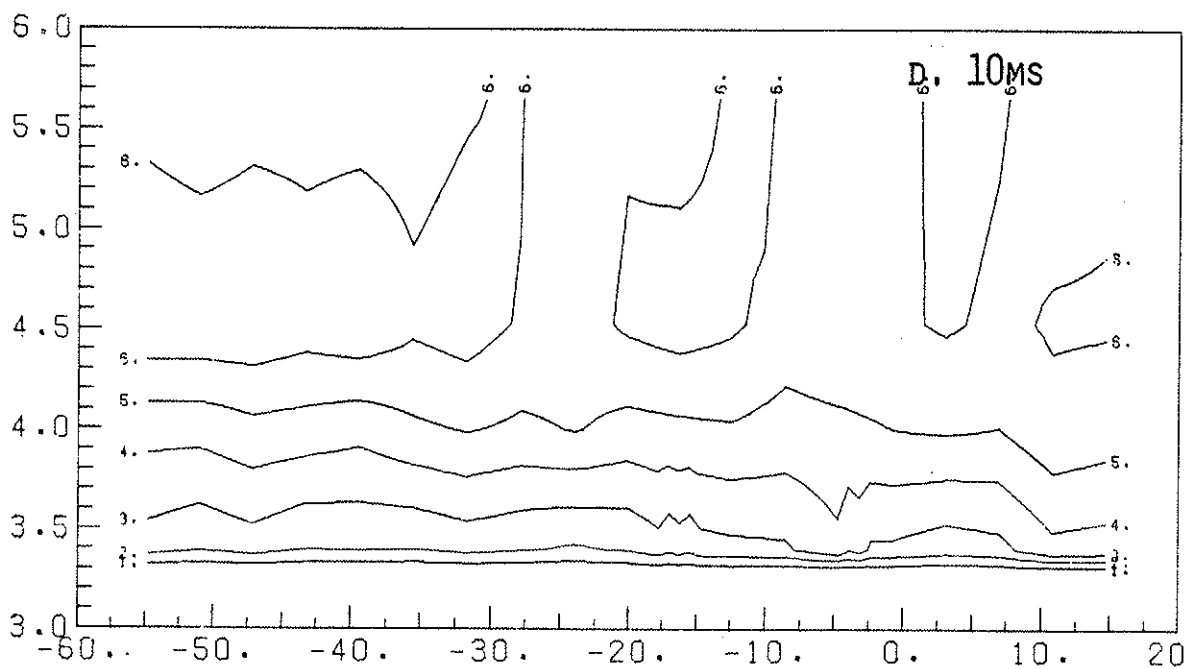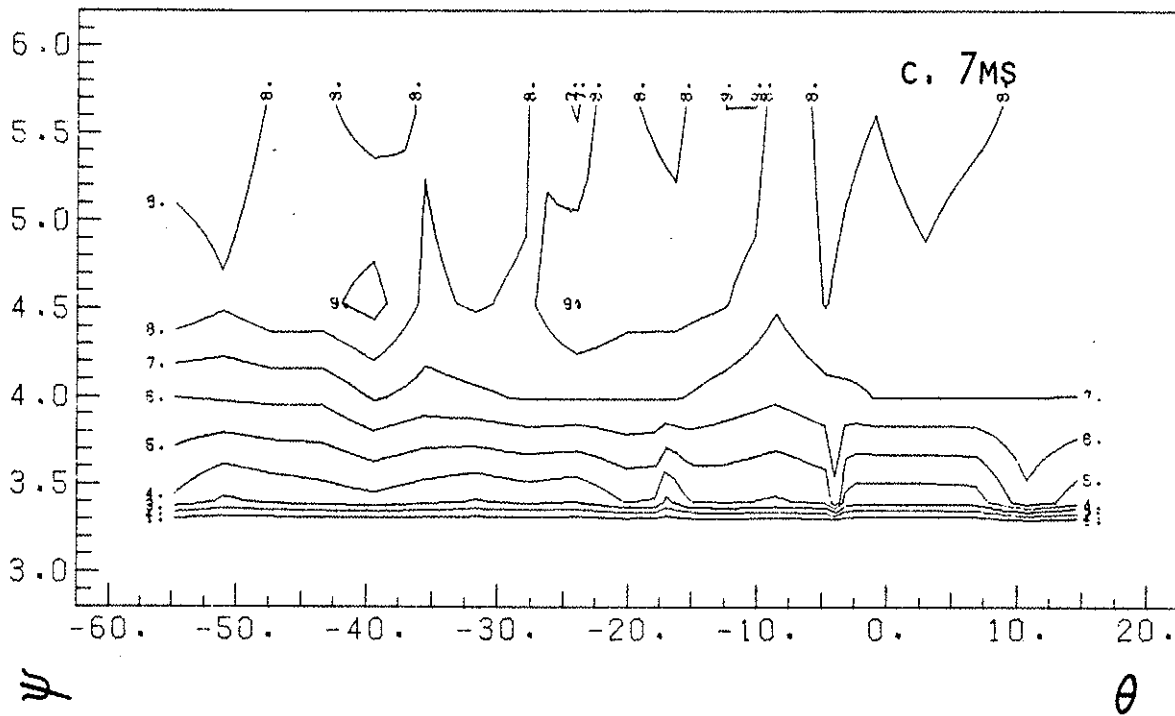
Fig. 5.11c and d. Collisionless H plasma; normal levita-
tion; private flux of the LOH; $B_{P\ AVE}$=1KG (2.5KV).
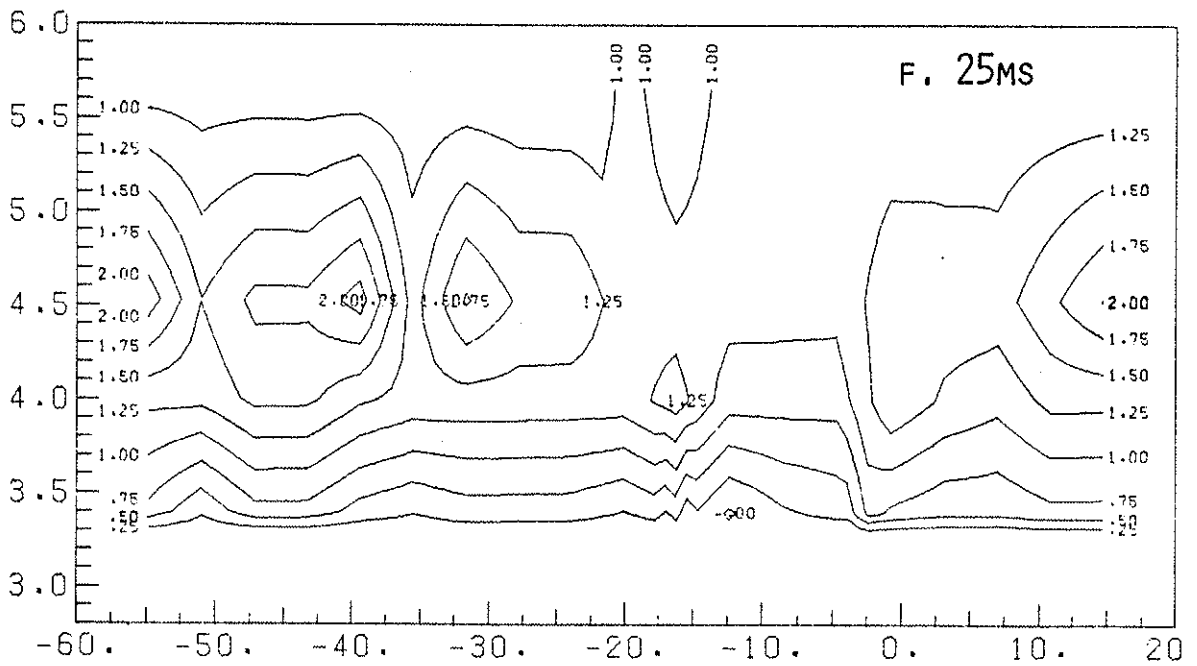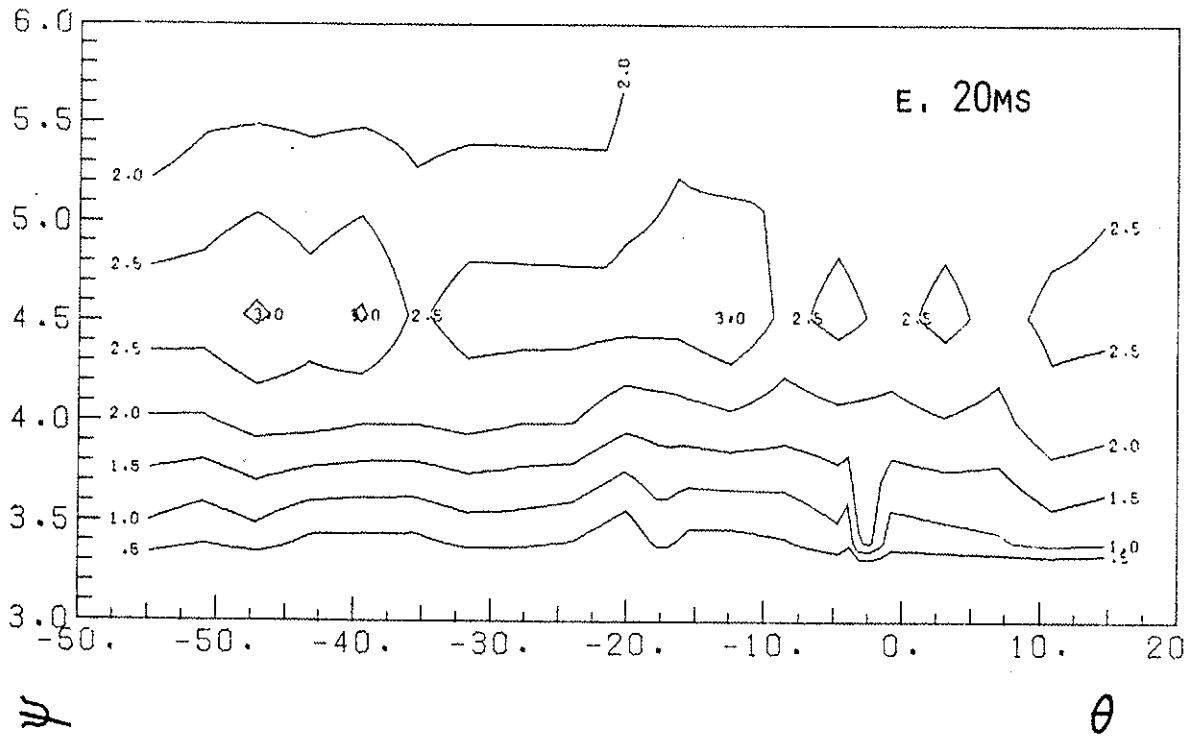
FIG. 5.11 E AND F. COLLISIONLESS H PLASMA; NORMAL LEVITA-
TION; PRIVATE FLUX OF LOH; $B_{P\ AVE}$=1KG (2.5KV).
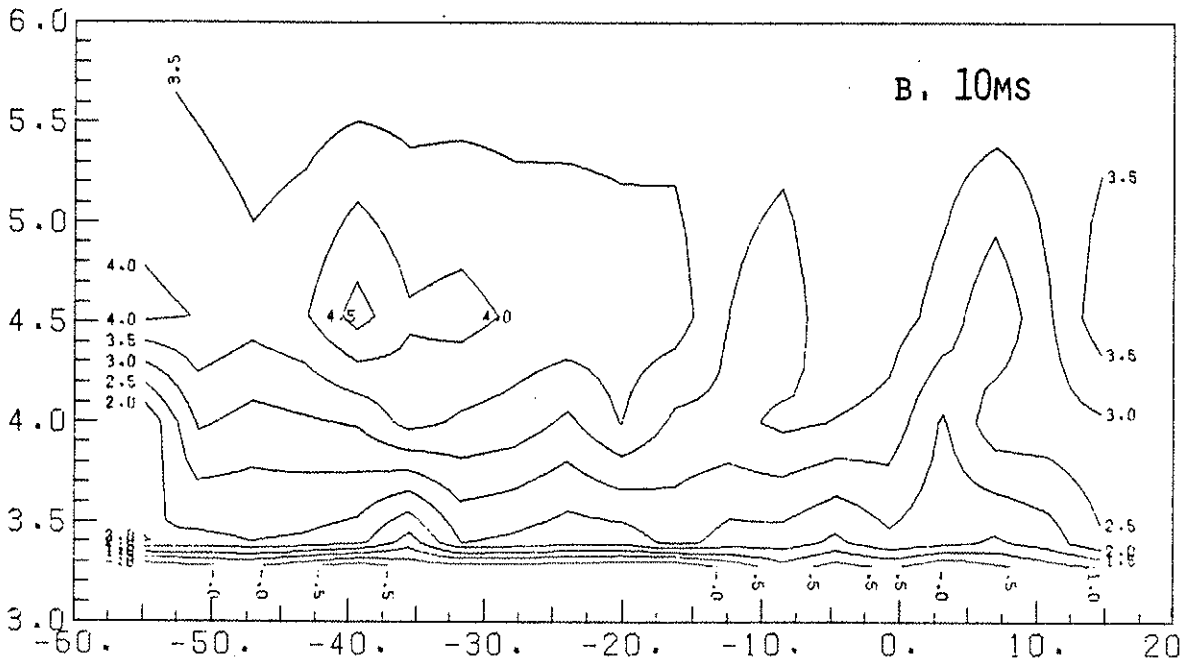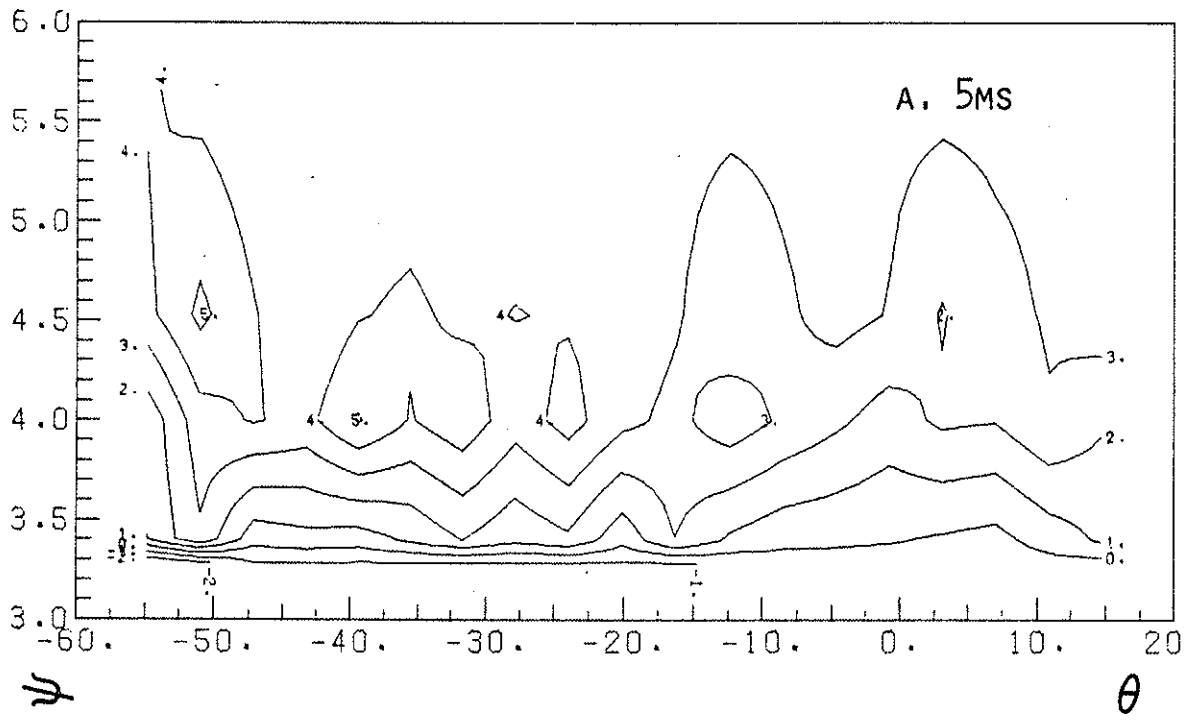
FIG. 5.12A AND B. COLLISIONLESS H PLASMA; LATE LEVITATION; PRIVATE FLUX OF THE LOH; $B_{P \ AVE}$=1KG (2.5KV).
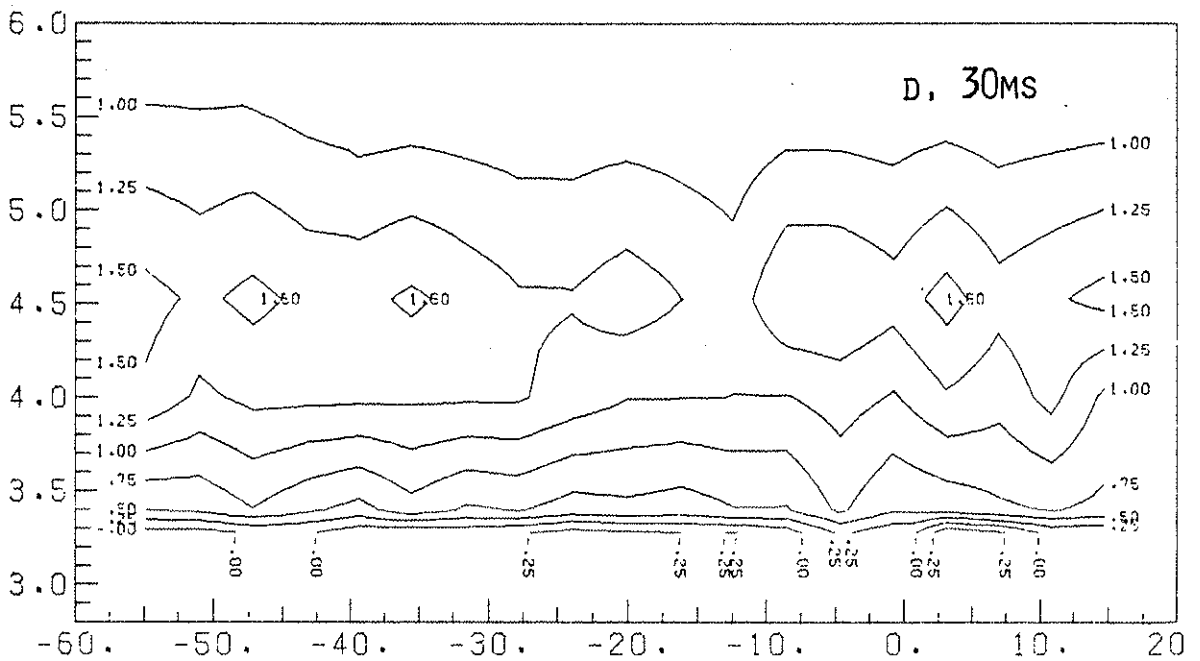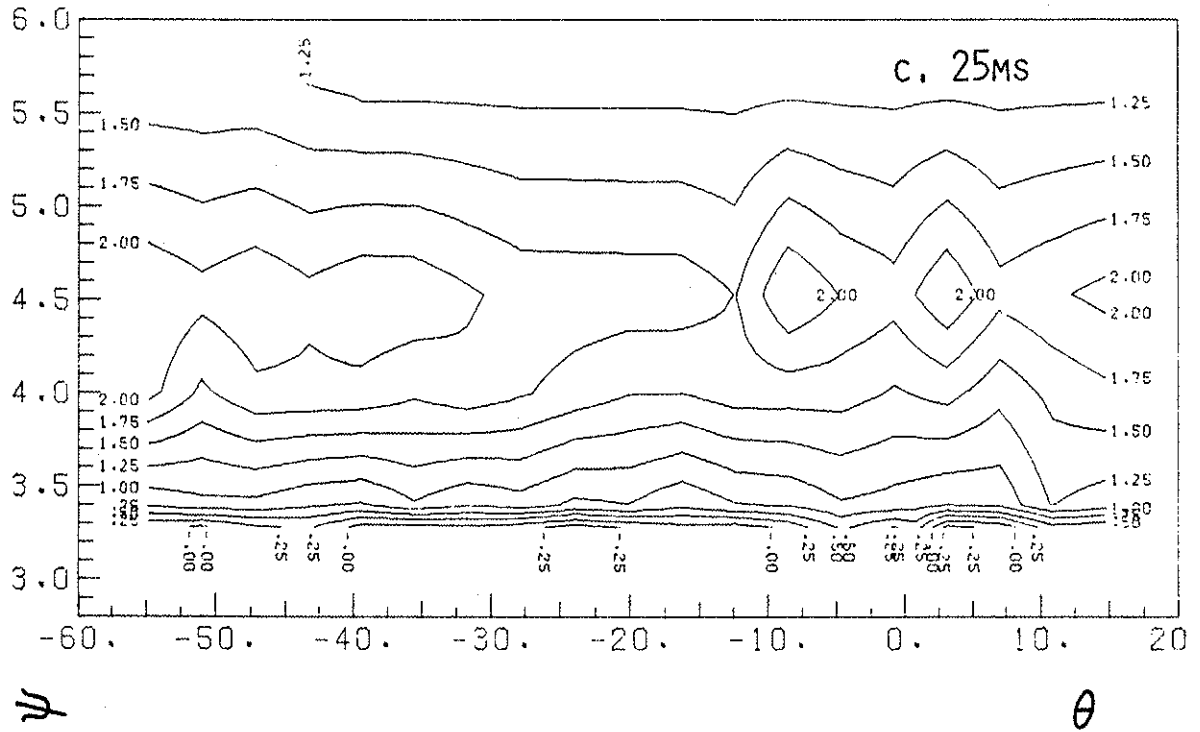
FIG. 5.12c AND D. COLLISIONLESS H PLASMA; LATE LEVITATION;
PRIVATE FLUX OF THE LOH; $B_{P \; AVE}$=1KG (2.5KV).
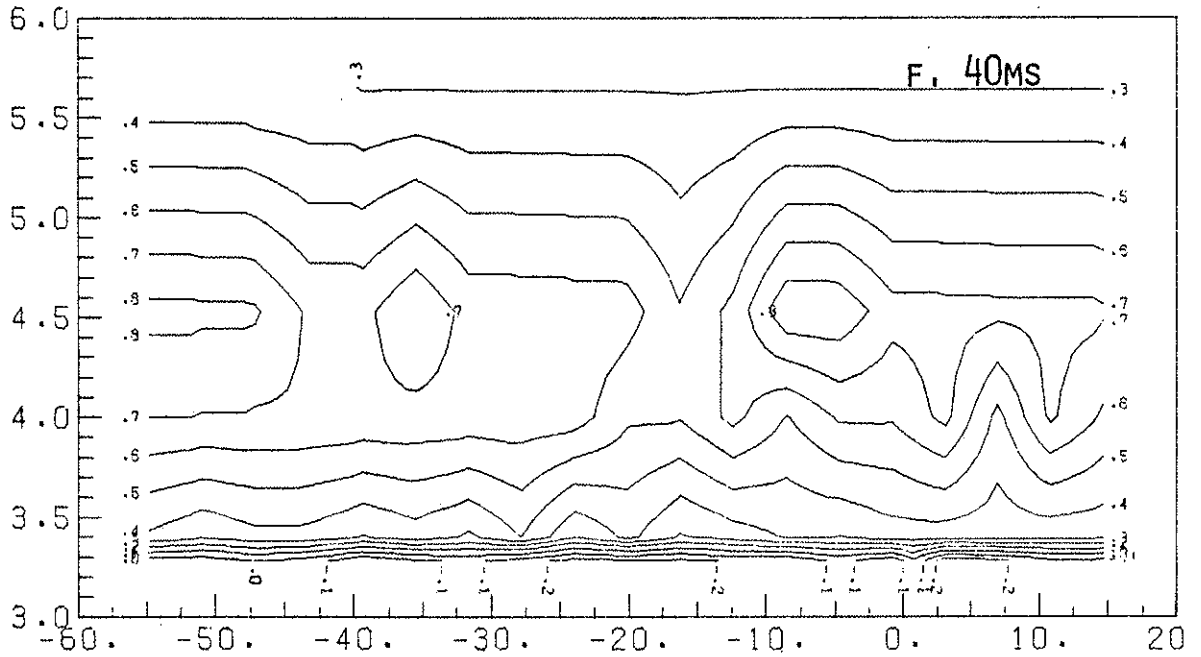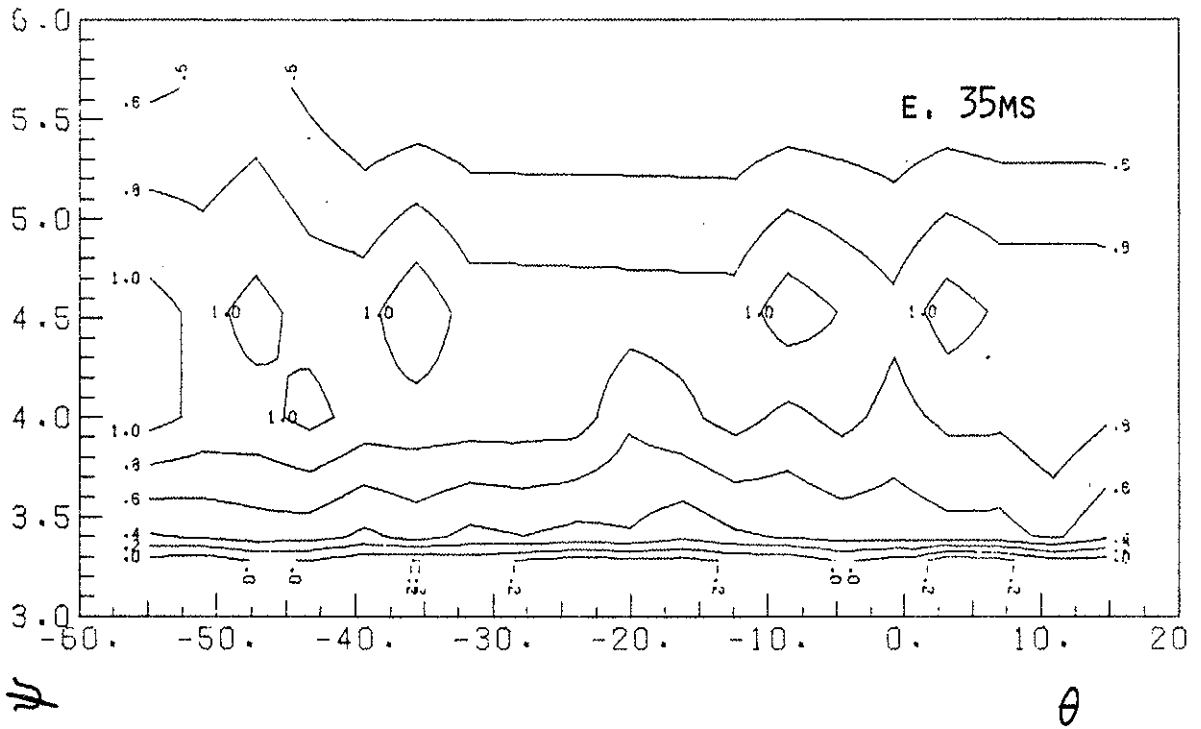
FIG. 5.12E AND F. COLLISIONLESS H PLASMA; LATE LEVITATION;
PRIVATE FLUX OF THE LOH; $B_{P \; AVE}$=1KG (2.5KV).

machine as the supported partial scan of the LOH, Fig. 5.1:
an 80° segment of the private flux of the lower outer hoop,
including an outer support at 318°, and the gap at 0°.
Common flux data was not taken.

The normal levitation data is different from the
supported data shown previously in that, in addition to not
showing the characteristic closed contour at the azimuth of
the support, the potentials are a factor of 2-3 larger.
The levitated contours appear relatively flatter than the
supported contours (i.e., no large closed cells) in the
azimuthal direction, and remain so for the levitation
period of ∿20ms, although the potentials drop by a factor
of 2 from 3ms to 10ms. Starting at around 20ms we see the
support coming back into the plasma, and by 25ms after
injection the vortex pattern at the support is very clearly
defined. The pattern remains in the vicinity of the
support, but its magnitude has decreased by a factor of 25
by 35ms, and the resolution of the Biomation becomes too
small to follow the cell. The time sequence for this
experiment is shown in Fig. 5.13a.

The contours for the late levitation experiment are
shown in Fig. 5.12a-f. The timing sequence is shown in
Fig. 5.13b. The machine is fully levitated ∿20ms into the
pulse. The early times, while the support is pulling out,
show structure in the vicinity of the support. When the
support is fully out V_f appears somewhat flatter, but the
structure does not damp away. When the supports come back
the structure is accentuated. This data is very similar in
shape to the supported data for this plasma, although the
potential at the separatrix is about twice as large. There
appears to be somewhat less variation in the azimuthal
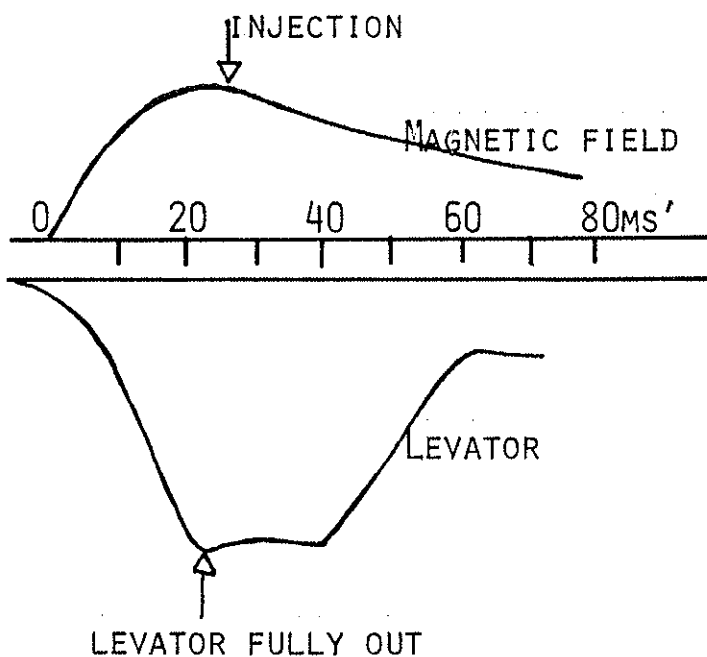
FIG. 5.13A NORMAL LEVITATION (50MS DELAY)
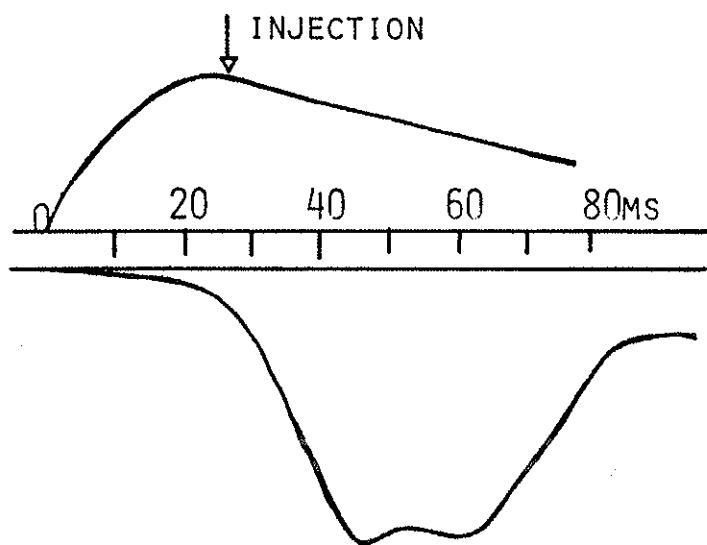
FIG. 5.13B LATE LEVITATION (30MS DELAY BETWEEN LEVATOR
AND FIELD TRIGGERS).

direction than for the supported data, but more than for the normal levitation case.

2. Discussion. The boundary conditions are different without the supports connecting the separatrix and the ring: When the plasma is injected into a fully levitated Octupole, the equipotentials have a different shape than when the Octupole is supported, as is observed in the normal levitation contours, Fig. 5.11. However, when the plasma is injected and the supports are pulled out afterwards (Fig. 5.12), a cell pattern similar to that of a supported plasma is observed. This occurs because the cell structure that is set up initially takes a long time to damp for the collisionless plasma.

The levitated V_f profiles in ψ are different from the supported profiles. In the supported contours ψ_s is shorted to the hoop by the levators, and there is a negative cell between the ring and the separatrix. The levitated contours show the potential rising from the ring towards the separatrix, with a positive peak; when the levators come back in the cell that forms is positive, even though the separatrix is now shorted to the hoop.

It remains to take a full scan for the levitated data to assess the magnitude of the spectrum in θ. This should be done for all three cases under the same operating conditions. This is crucial because the longest-wavelength modes are the ones causing the most diffusion (see Chapter VII). If our interpretation of the bump on the spectrum for the supported case is correct, it should be absent for the normal levitation case but present in the late levitation spectrum.

It is not possible to estimate the azimuthal spectrum from the levitated contours because the range in θ does not cover one full period of the lowest frequency mode present, and without a spectrum it is not possible to compute D_v or T^*.

C. <u>Summary</u>. In the collisionless plasma, ion viscosity is too small to account for the damping of the electric fields. The decay of the spectrum indicates that the electric field and the electron temperature decay at roughly the same rate; physically this occurs because the plasma will tend to short out fields larger than kT_e/e. Therefore the effective temperature $T^* \propto E^2$ decays twice as fast as T_e.

Profile evolution diffusion studies for the collisionless plasma in a purely poloidal, levitated, mode[51] indicate that levitation made little change in the level of enhanced diffusion. Therefore we can assume that roughly the same amount of vortex energy is present in the plasma with the Octupole supported or levitated, and that the difference is mainly in the distribution of energy in the spectrum. This remains to be investigated.

The magnitudes of D_v and T^* calculated from the supported data agree reasonably well with the diffusion study results[25]. However, the data is somewhat limited and the question of the effect of the supports on the cell structure needs to be investigated more thoroughly. The principal experimental problem is that the collisionless plasma is not very reproducible, and operating parameters tend to drift. This problem is discussed further in Chapter VII in the recommendations for further work.

V.2   COLLISIONAL PLASMA

A.   Supported Data.   The collisional plasma in a pure-
ly poloidal field was examined in detail.   Three experi-
ments were performed with the hoops supported.   The experi-
ments paralleled the profile evolution studies[26] (the
results of these studies were summarized in Chapter I.)

a.   Contours were plotted for a quarter segment
of the private flux of the LIH, at three values of the
average magnetic field, B_{ave}.   The high-field case ($B_{ave} \sim 2kG$)
corresponds to a plasma with vortex diffusion scaling.   For
the intermediate field ($B_{ave} \sim 600G$) case, the diffusion
scales as vortex diffusion initially; then, as the vortex
spectrum is damped, the diffusion makes a transition to a
collision-dominated diffusion.   The last case ($B_{ave} \sim 360G$)
corresponds to a plasma with collisional diffusion on the
LOH.   The results of the experiment showed that the presence
of potential structure correlated roughly with vortex
diffusion, and its absence with collisional diffusion.

b.   In this experiment, a full scan was made of
a single ψ-surface in the private flux of the LOH at two
values of B_{ave}: $B_{ave} \sim 600G$ (vortex diffusion) and B_{ave}
$\sim 180G$ (collisional diffusion).

c.   A full scan ($\theta = 360^{\circ}$, six ψ-surfaces) was
taken of the private flux of the LIH, at $B_{ave} \sim 480G$. D_v was
calculated as a function of ψ, and was shown to have the
same general shape as the diffusion coefficient obtained in
the studies of the profile evolution[26], $D(\psi) \propto n(\psi)^{-1/2}$.

la. Experimental Observation. A series of
scans was made for the collisional plasma in which the
bank voltage for the poloidal field was varied by a factor
of 5.5. Data is presented in Figs. 5.14 to 5.16.

The first set of data (Fig. 5.14a-e) was taken in the
private flux of the LIH with 2.5kV on the poloidal bank.
This corresponds to an average magnetic field $B_{ave} \sim 2kG$.
The scans show a considerable amount of structure at all
times. The separatrix region is relatively flat, while
the psi-surfaces near the ring have much more azimuthal
variation in the potential. The cells move around and
change initially, establishing a recognizable shape with a
large cell located between $\psi=3$ and $\psi=4$. The large cell
does not decay in amplitude after the 17ms contour, and
retains roughly the same shape.

At 10ms after injection the gap voltage is on the
order of .1V for the crowbarred field at 2.5kV on the
bank. The question arises from examining Fig. 5.14 at 7ms
and 12ms after injection whether this is the cause of the
structure at the gap. The data was corrected by Drake's
method (see Chapter II); $.003V/^{\circ}$ was subtracted from the
data. If there is as much as a factor of 2 difference be-
tween this and the actual flux density at the gap, over
the 6° segment in which there appears to be a large field
gradient, the difference would account for $\sim.016V$. The
voltage step on the plots is on the order of .1-.2V, so
the possibly incorrect adjustment would not be responsible
for $\sim 1/6$ of the voltage step at the gap with a flux asymme-
try of a factor of 2. If this factor is larger, the
correction could account for more of the gap structure.
Detailed comparisons have not been made.
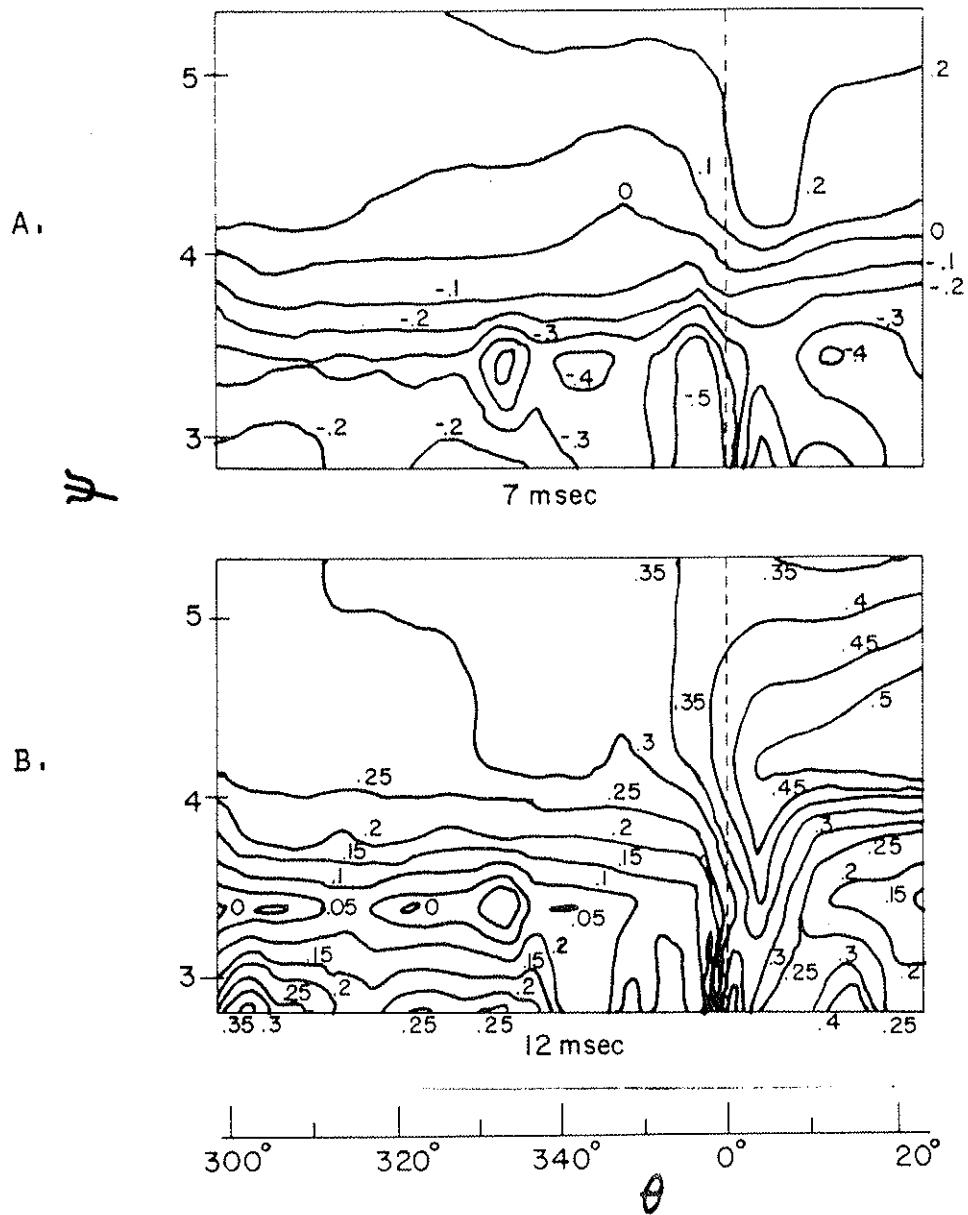
FIG. 5.14A AND B. FLOATING POTENTIAL CONTOURS; COLLISIONAL HE PLASMA; SUPPORTED; PRIVATE FLUX OF LIH; $B_{P\ AVE}$=2KG (2.5KV).

V_f

C.

17 ms

+ .8, - .1

D.

27 ms

+ .9, - .1

ψ

E.

37 ms

+ .9, - .1

300   320   340   0 θ

GAP
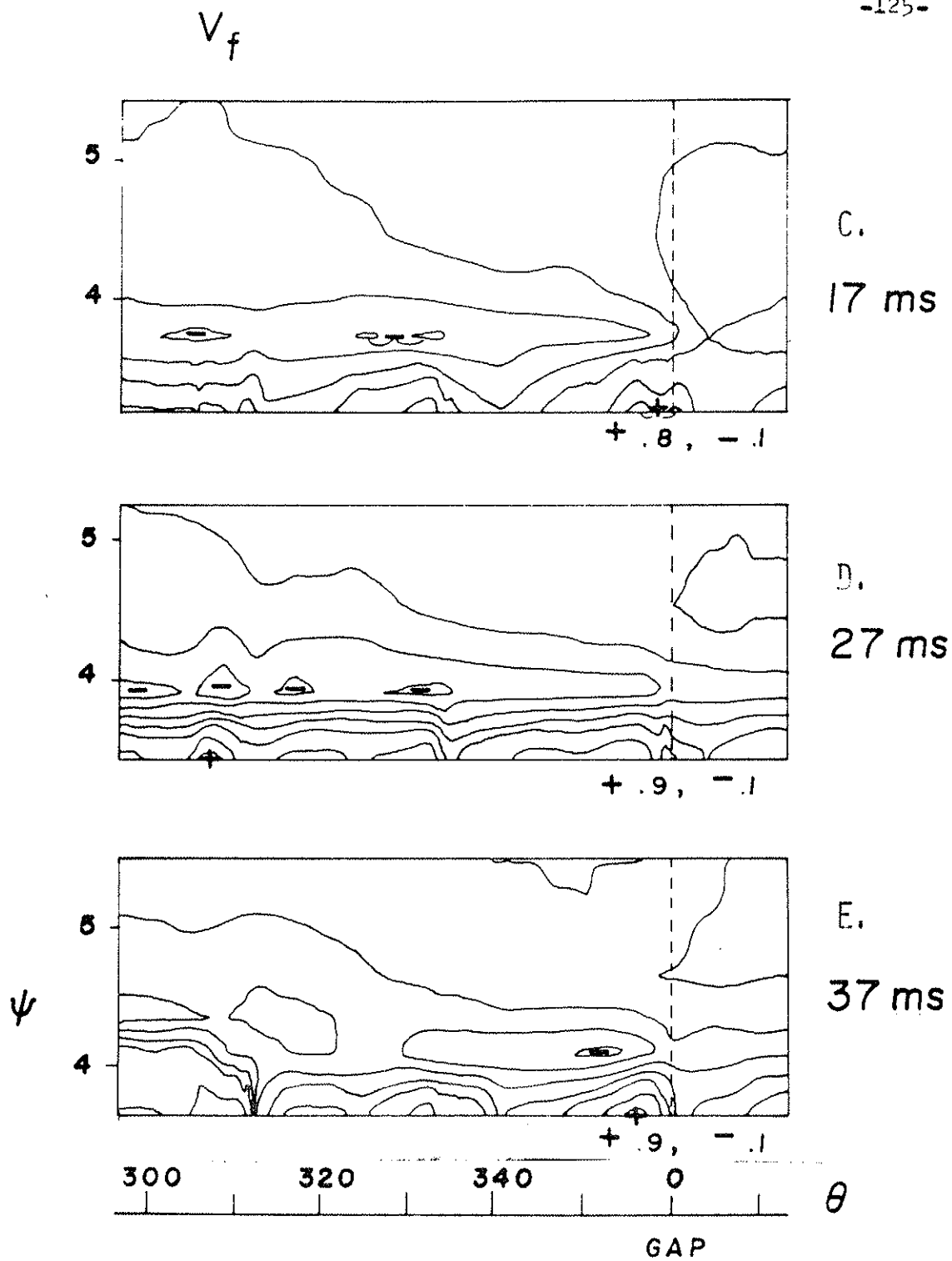
FIG. 5.14c, d, AND E. FLOATING POTENTIAL CONTOURS:
COLLISIONAL HE PLASMA; SUPPORTED; PRIVATE
FLUX OF LIH; $B_{P\ AVE}$=2KG (2.5KV).
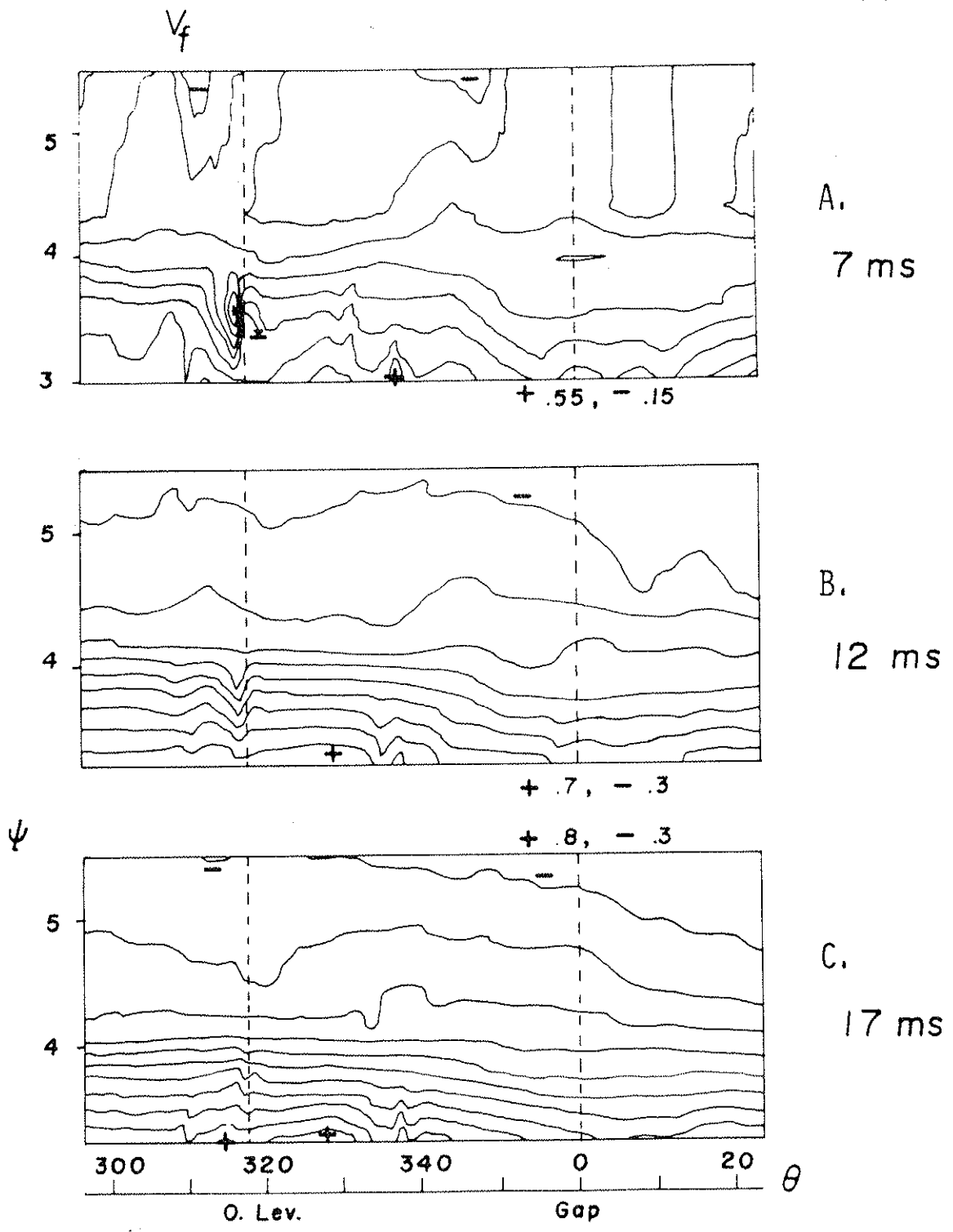
FIG. 5.15A-C. FLOATING POTENTIAL CONTOURS; COLLISIONAL
HE PLASMA; SUPPORTED; PRIVATE FLUX - LIH;
$B_{P\ AVE}$=600G (750V).
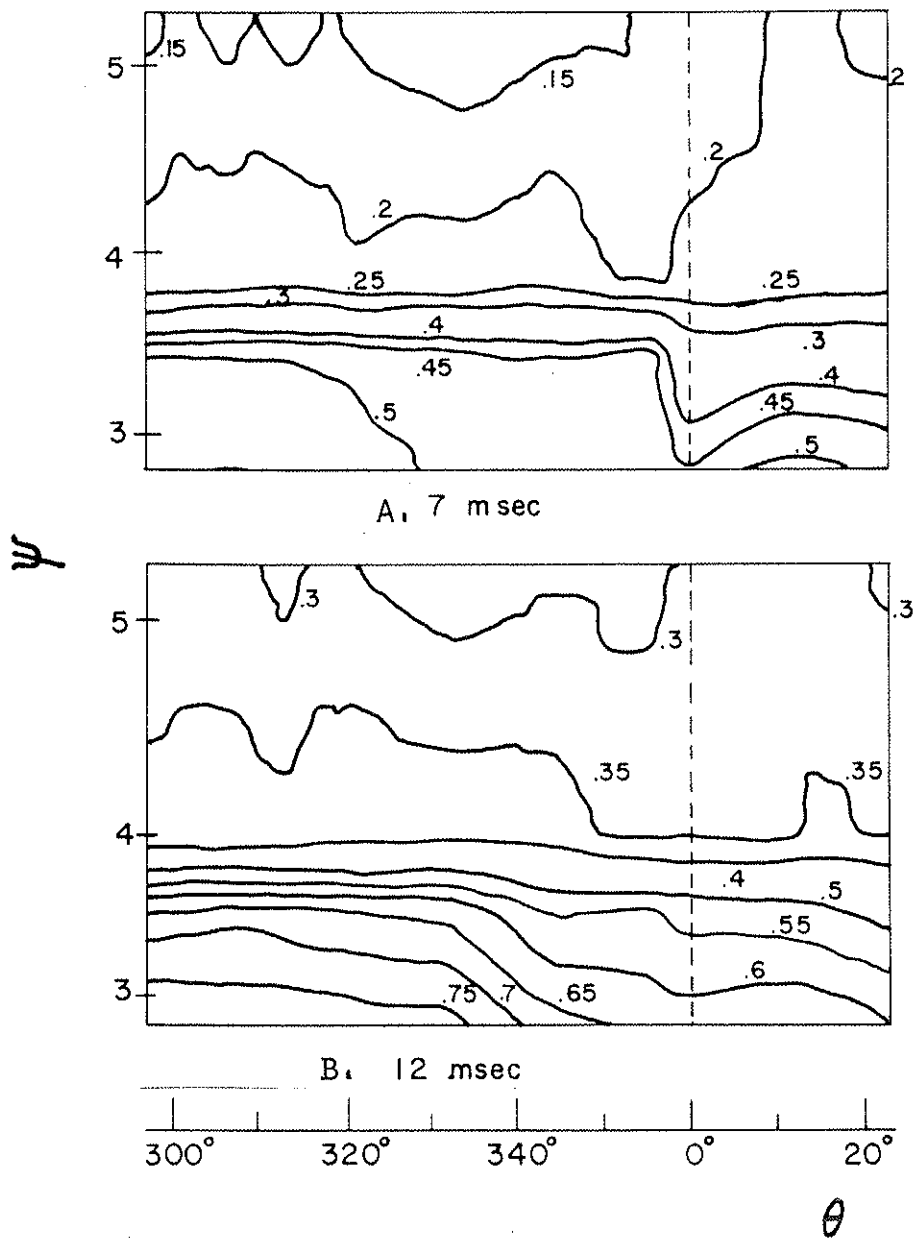
FIG. 5.16A AND B. FLOATING POTENTIAL CONTOURS; COLLISIONAL
HE PLASMA; SUPPORTED; PRIVATE FLUX - LIH;
$B_{P\ AVE}$=360G (450V).
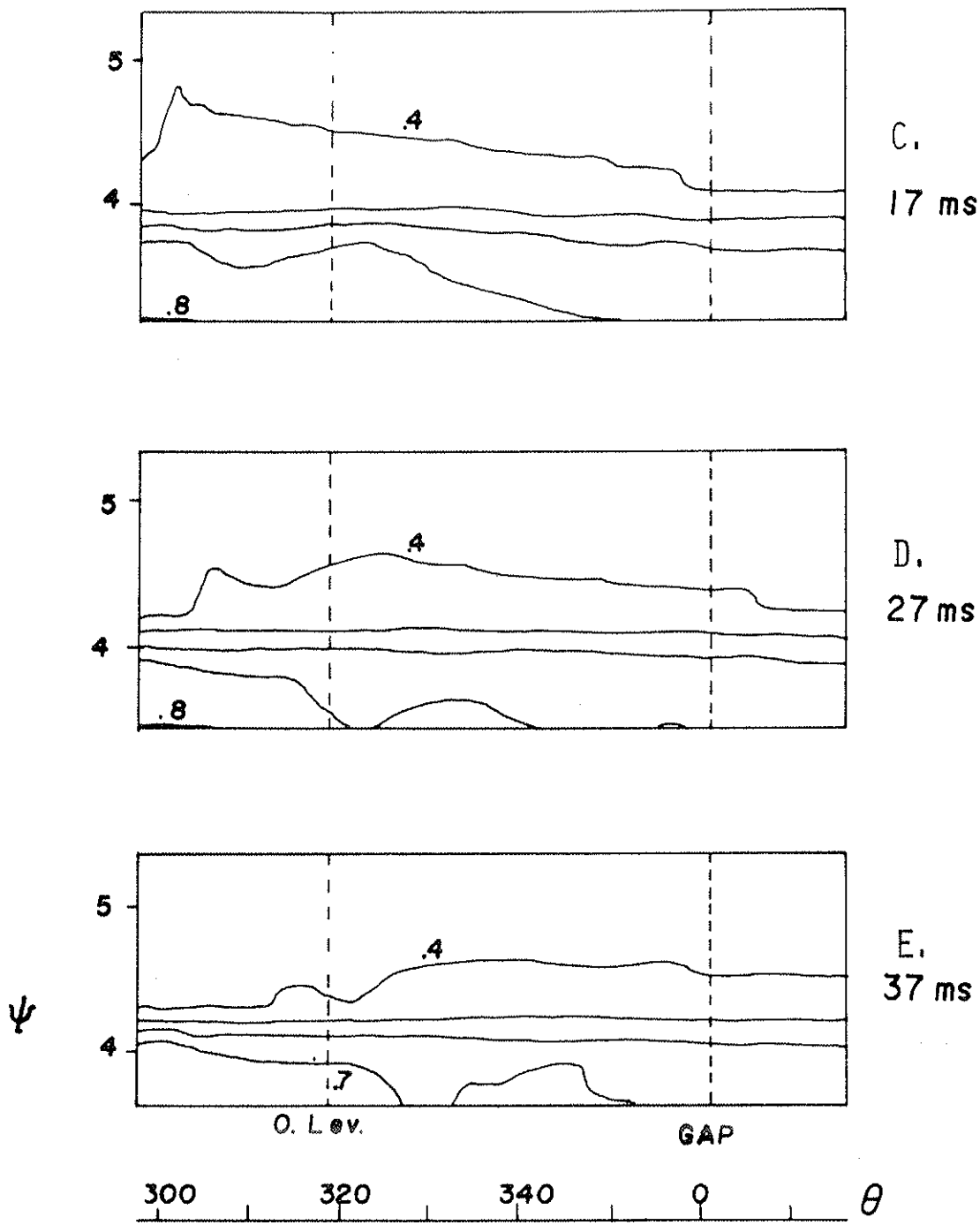
FIG. 5.16c-E. FLOATING POTENTIAL CONTOURS; COLLISIONAL HE PLASMA; SUPPORTED; PRIVATE FLUX — LIH; $B_{P\ AVE}$ = 360G (450V).

The second set of data (Fig. 5.15) was taken with 750V on the poloidal field bank. This corresponds to B_{ave} ∿300G in the private flux of the outer hoops, and ∿600G in the private flux of the LIH where the contours were measured. The first contour shown, at 7ms after injection, has a fair amount of structure, including a small cell at ∿320°. The later contours are much smoother. It is not just the disappearance of the small cell that is apparent, but the smoothing out of the potential in general. As in the previous data, the potential gradients are smaller in the separatrix volume.

The third set of contours (Fig. 5.16) is for 450V on the bank (360G B_{ave} LIH). The potential contours are very much flatter than those shown in Fig. 5.14 for the high-field case, even though the actual voltages (∿.2 to .8V) are of the same order. The potential gradients in ψ are steeper near the ring, and the separatrix volume is flat.

The three sets of contours show that as the magnetic field is decreased, the floating potential contours go from having large azimuthal variations to being azimuthally symmetric. The difference in these three sets of contours is one of shape, not magnitude, as a comparison of the data shows that the potentials in all three cases are of the same order (0-.8V). The potential gradients in ψ are also of the same order. The electric fields, though are not; E_θ is much smaller for the low-field case than for the high-field case.

2a. Discussion. As summarized in Chapter I, the diffusion studies using the density profile evolution have shown that for high magnetic fields the diffusion

coefficient scales as vortex diffusion, and at very low fields the diffusion is collisional. Fig 5.17 (taken from Ref. 26) shows the profile evolution for three cases covering about the same range of magnetic field.

If the potential structure is the source of the enhanced diffusion at higher field strengths, we would expect to see little structure at low field, where collisional diffusion dominates. Fig. 5.16 is consistent with this interpretation. The contours are relatively flat and the azimuthal electric fields are small. Asymmetries due to plasma injection, etc., are damped out in the first few milliseconds.

At the intermediate value of B the time needed to damp out the vortex structure is longer because the ion viscosity is smaller. Therefore we would expect the vortex structure (Fig. 5.15) to take longer to damp out; this is what is observed in the contours.

Finally, at high fields, where the viscous damping time is of the order of the length of the experimental pulse or longer, we would not expect the potential structure to disappear.

The sequence of the contours as the field strength is increased is consistent with the interpretation we have made that the potential structure is the source of the enhanced temperature. However, the data was taken on the inner hoop which has a higher average field strength than the outer hoop; thus the transition from vortex to classical diffusion takes longer than it would for the LOH, even if all other factors are equal.

$B_{AVERAGE}$	$\tau_\mu \sim L^2/\mu_\perp$	OBSERVED DIFFUSION	OBSERVED PROFILE AT 3 MSEC	OBSERVED PROFILE AT 13 MSEC
100 Gauss	0.3 msec	CLASSICAL DIFFUSION		
300 Gauss	2.8 msec	TRANSITION		
800 Gauss	20 msec	VORTEX DIFFUSION		
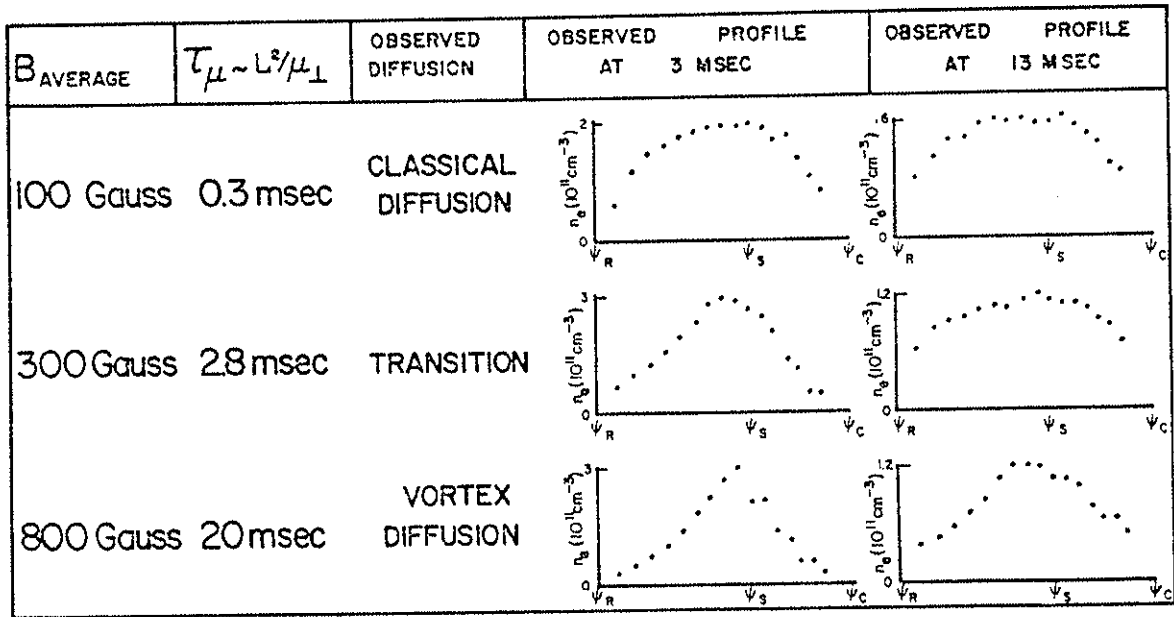
FIG. 5.17 PROFILE EVOLUTION (DENSITY) VS. TIME.
WITH CLASSICAL DIFFUSION, THE DENSITY PROFILE
IS CONVEX; WITH VORTEX DIFFUSION, THE PROFILE
IS CONCAVE TOWARDS THE RING.

(FIGURE TAKEN FROM REF. 26.)

lb. Experimental Observations . The toroidal spectrum of $\phi(k)$ was measured for a single ψ-surface ($\psi=3.4$,LOH) in the private flux. Fig. 5.18 shows $\phi(k)$ vs. k for 1.5kV on the poloidal bank ($B_{ave}\sim600G$), and Fig. 5.19 shows $\phi(k)$ for 250V on the bank ($B_{ave}\sim180G$). The spectra are plotted at 2ms, 10ms, and 20ms, after injection. Both show that $\phi(k)$ is a decreasing function of k; the electric field spectrum for the low-field case drops off faster with increasing k than the high-field case.

The time decay of the sum of all the modes is shown in Fig. 5.20. For both cases, the decay constant is $\sim$5ms. The magnitude of the high-field case is approximately three times larger than the low-field case. The time decay of several individual modes is plotted in Figs. 5.21 and 5.22 for the high- and low-field cases respectively. The individual modes also decay with a $\sim$5ms time constant.

2b. Discussion. This case is not well understood. The vortex spectrum in θ decays at about the same rate for both scans. We would expect the low-field case to damp much more rapidly than the high-field case.

D_V is plotted in Fig. 5.23 and 5.24. The electric field spectrum is smaller in magnitude at the low-field case. However, the vortex diffusion coefficient is an order of magnitude larger. We can calculate D_{cl} for both cases[15], using

$$D_{cl} = 1.65\times10^{-4} \text{ cm}^5\text{eV}^{1/2}\text{G}^2\text{sec}^{-1} \frac{n}{B^2T_e^{1/2}} \qquad (5.1)$$
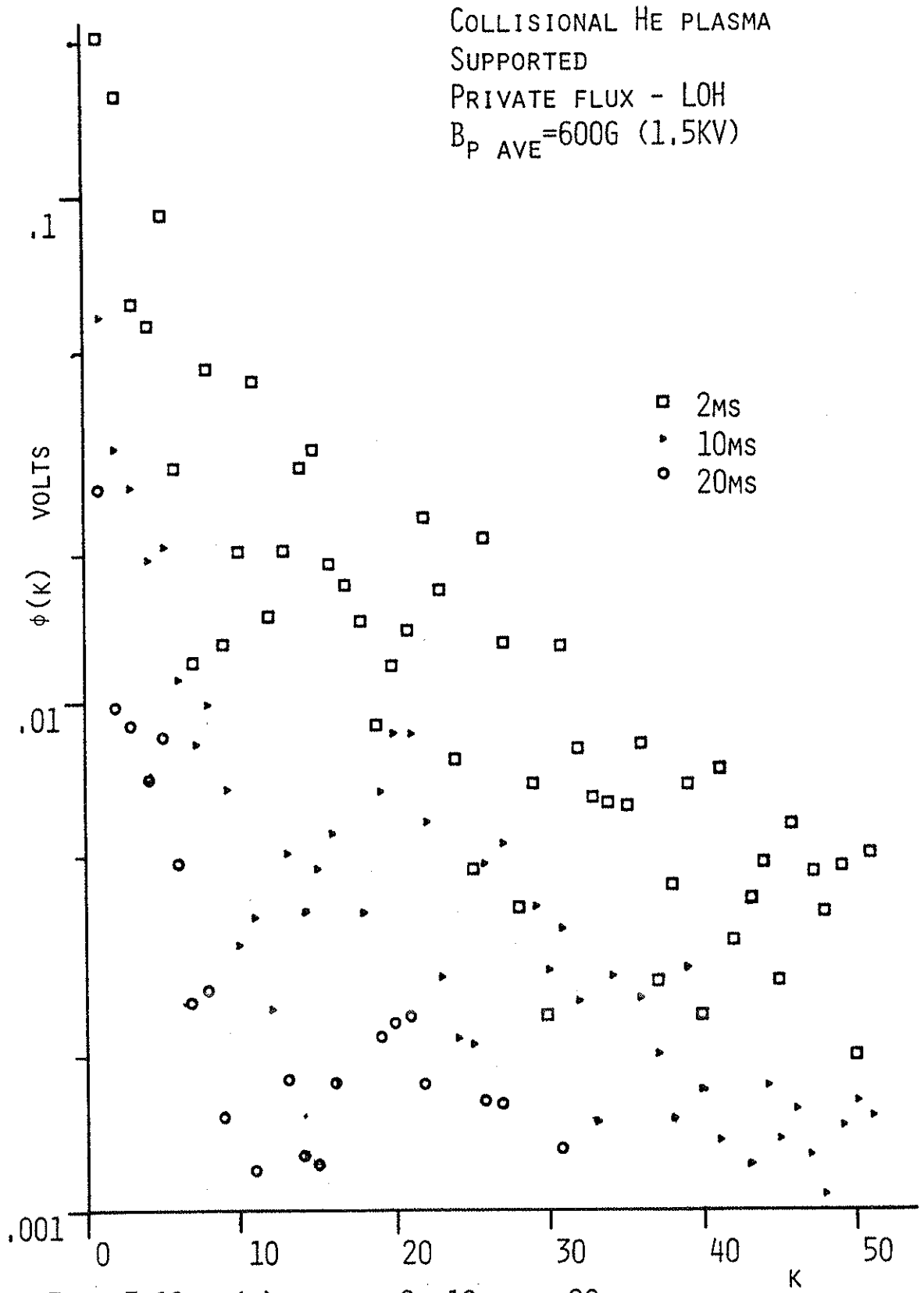
FIG. 5.18 φ(K) VS. K; 2, 10, AND 20MS.
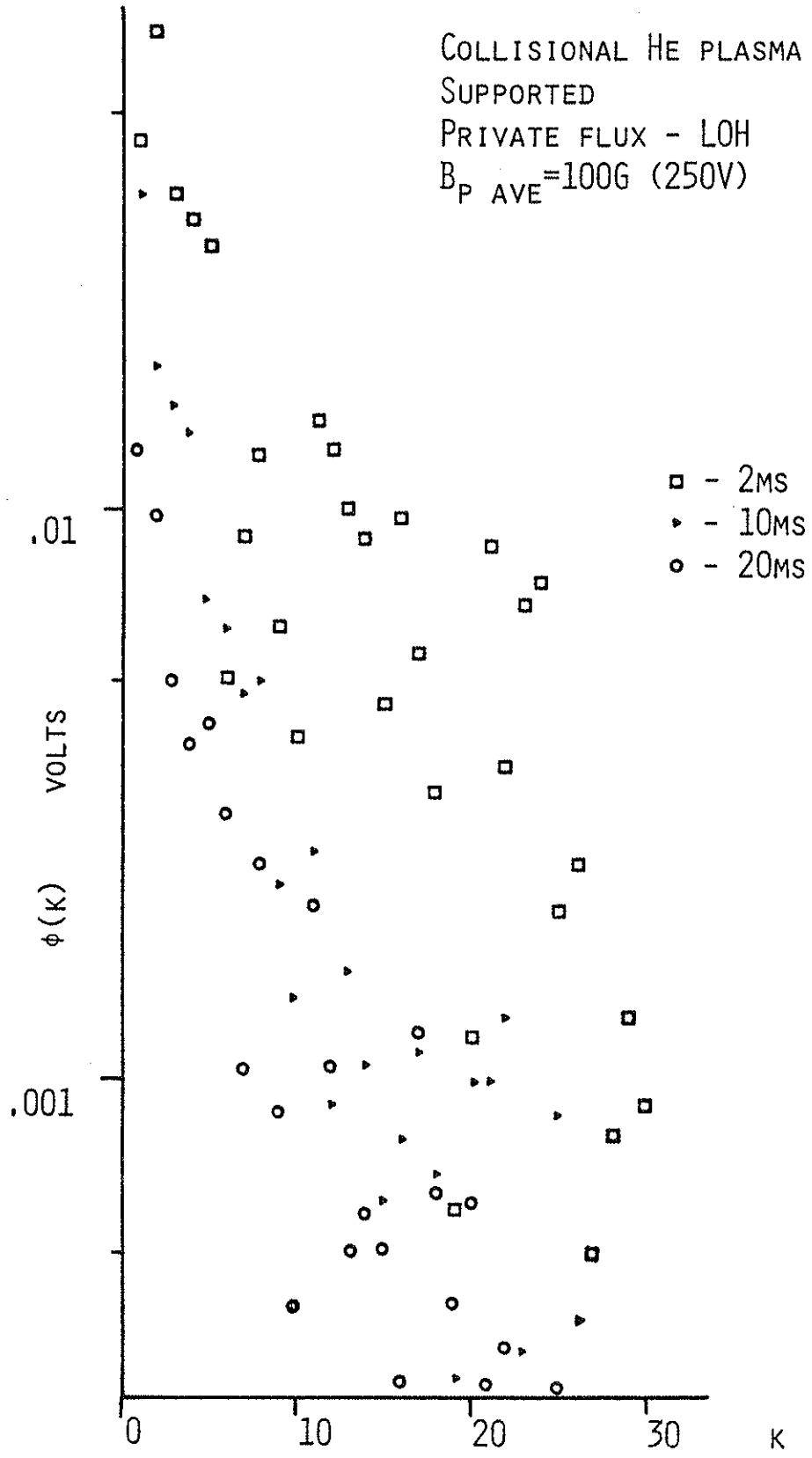
FIG. 5.19 φ(κ) vs. κ; 2, 10, AND 20ms.
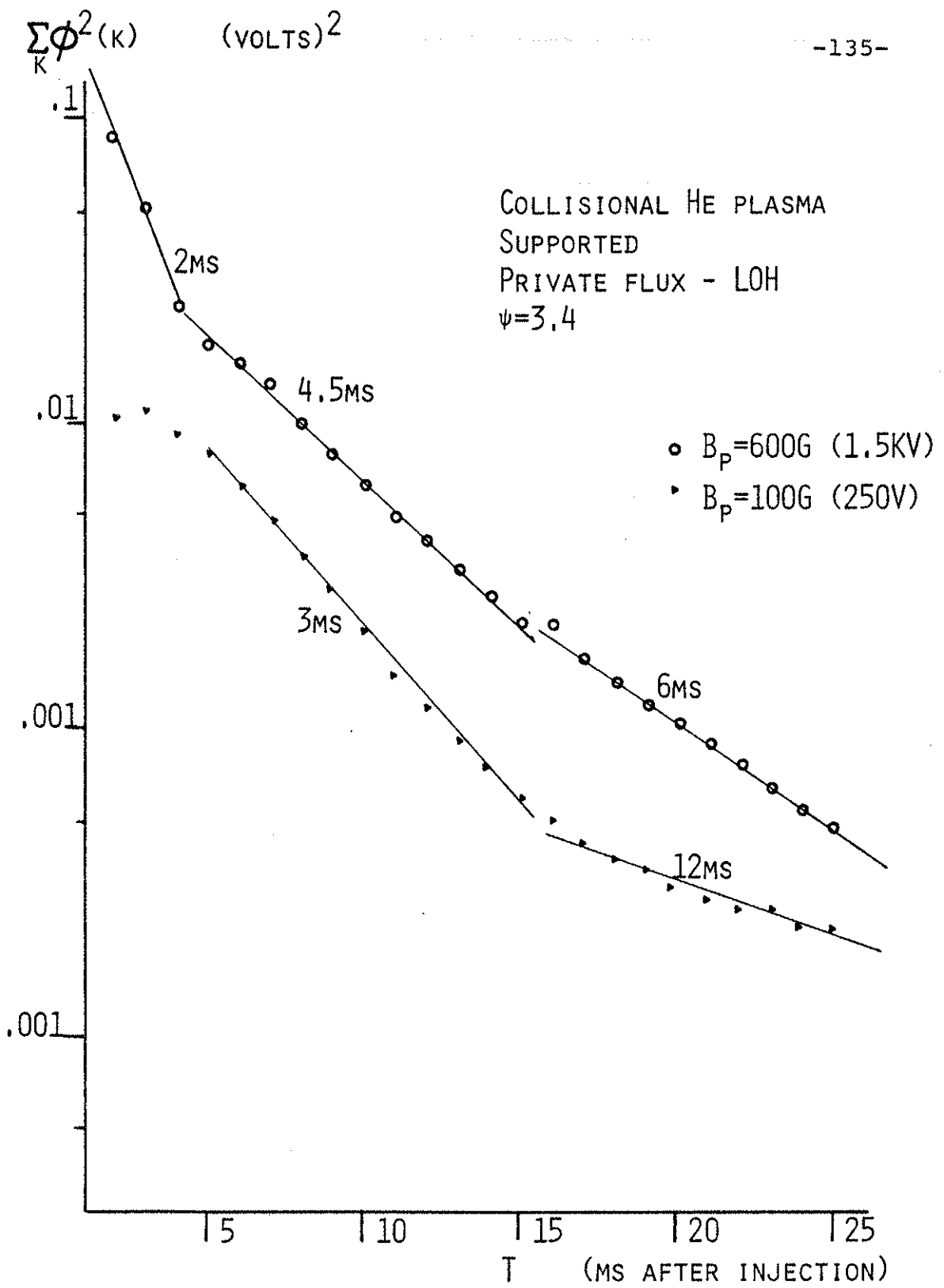
FIG. 5.20 TIME DECAY OF $^{\Sigma}\phi^2(K)$; $B_{P\ AVE}$=600G AND 100G.
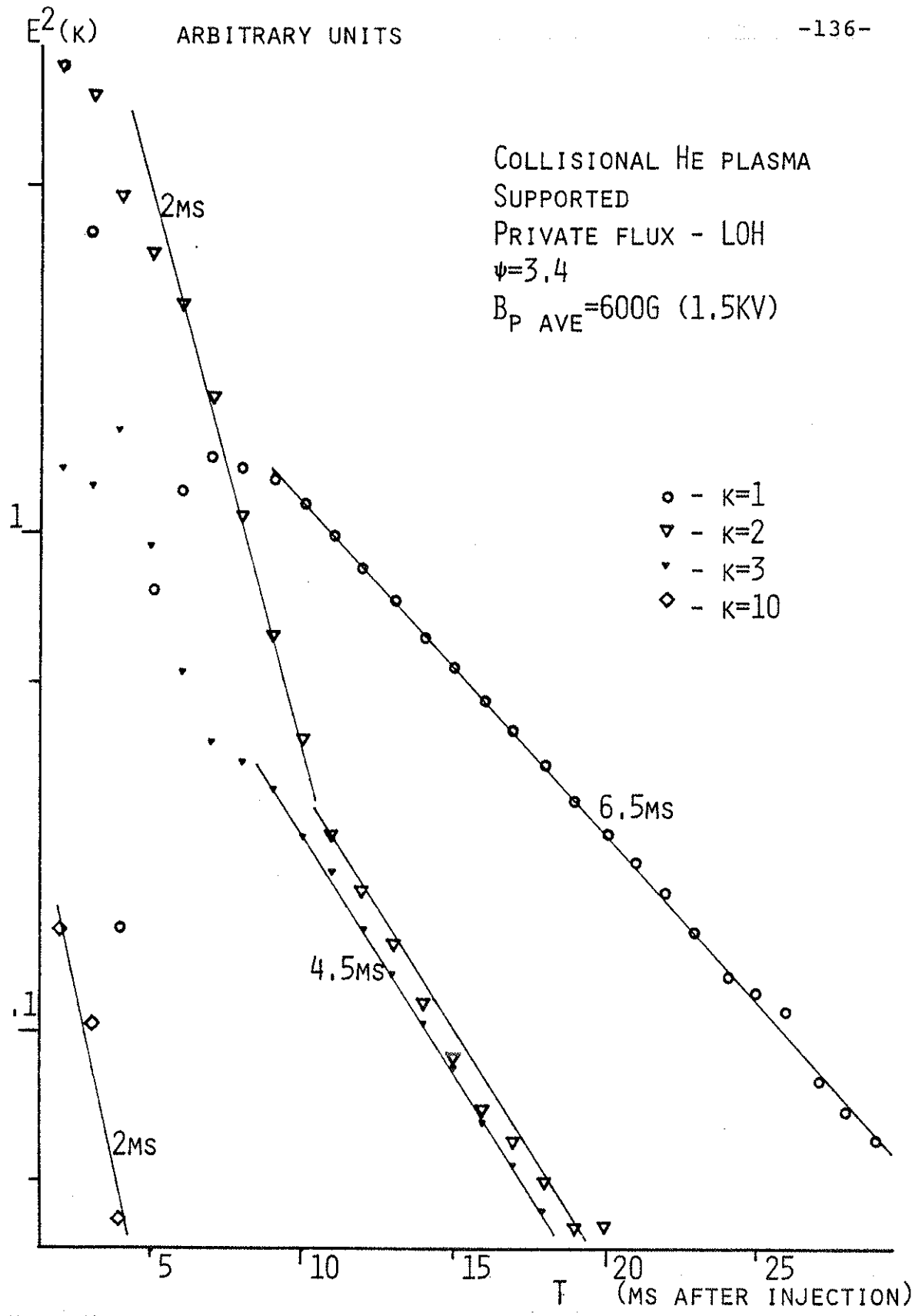
FIG. 5.21 TIME DECAY OF INDIVIDUAL ELECTRIC FIELD MODES.
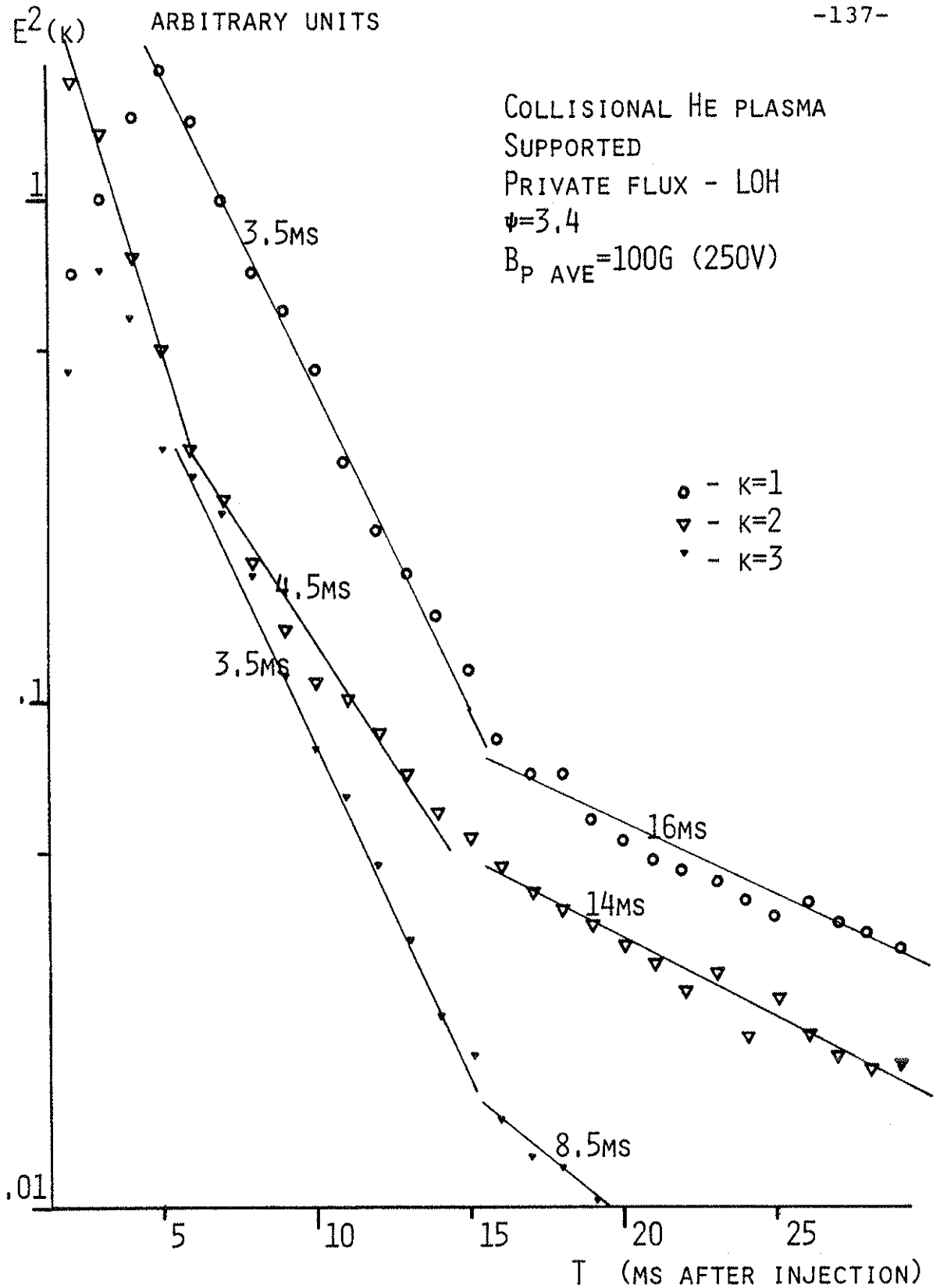
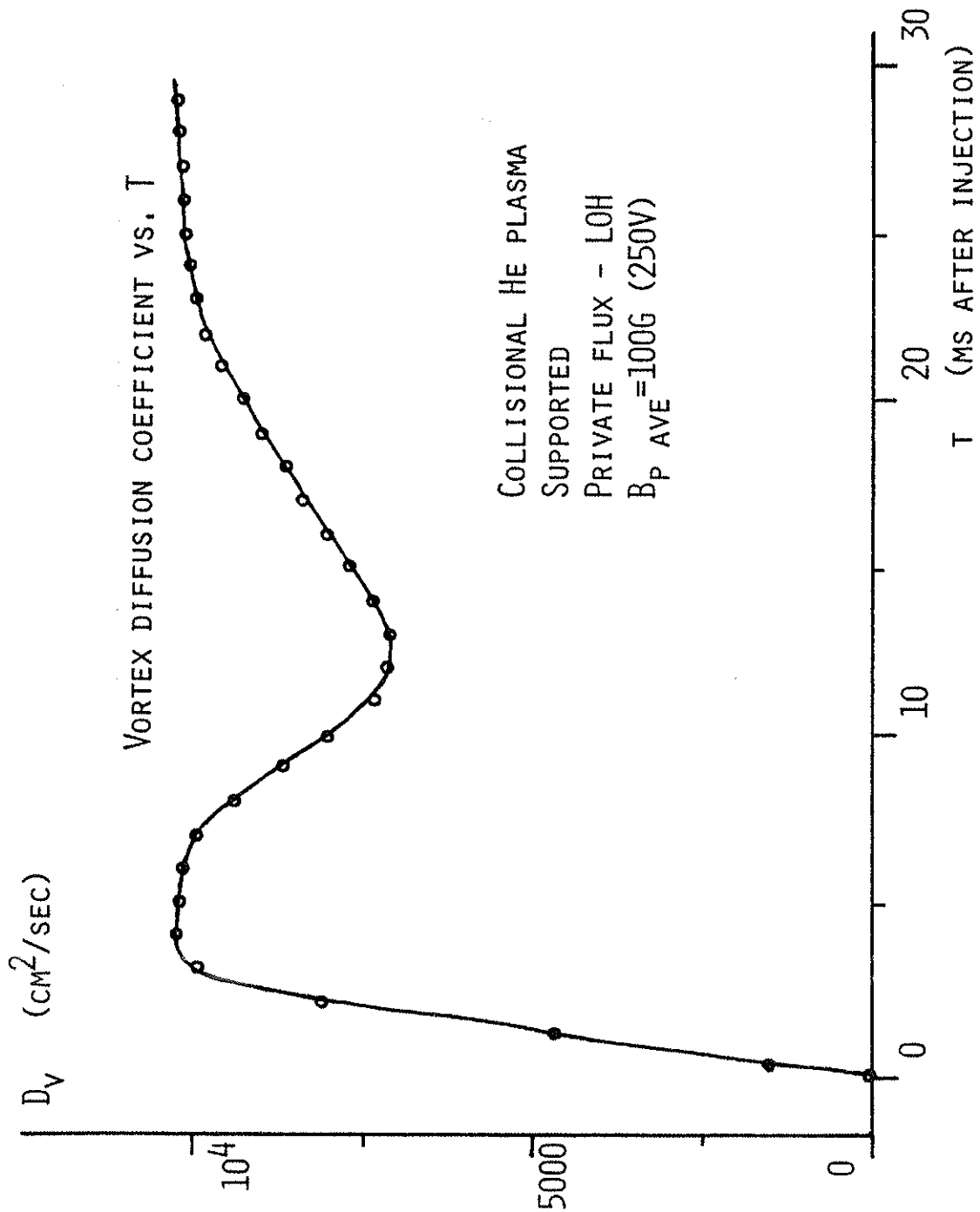FIG. 5.22 TIME DECAY OF INDIVIDUAL ELECTRIC FIELD MODES.

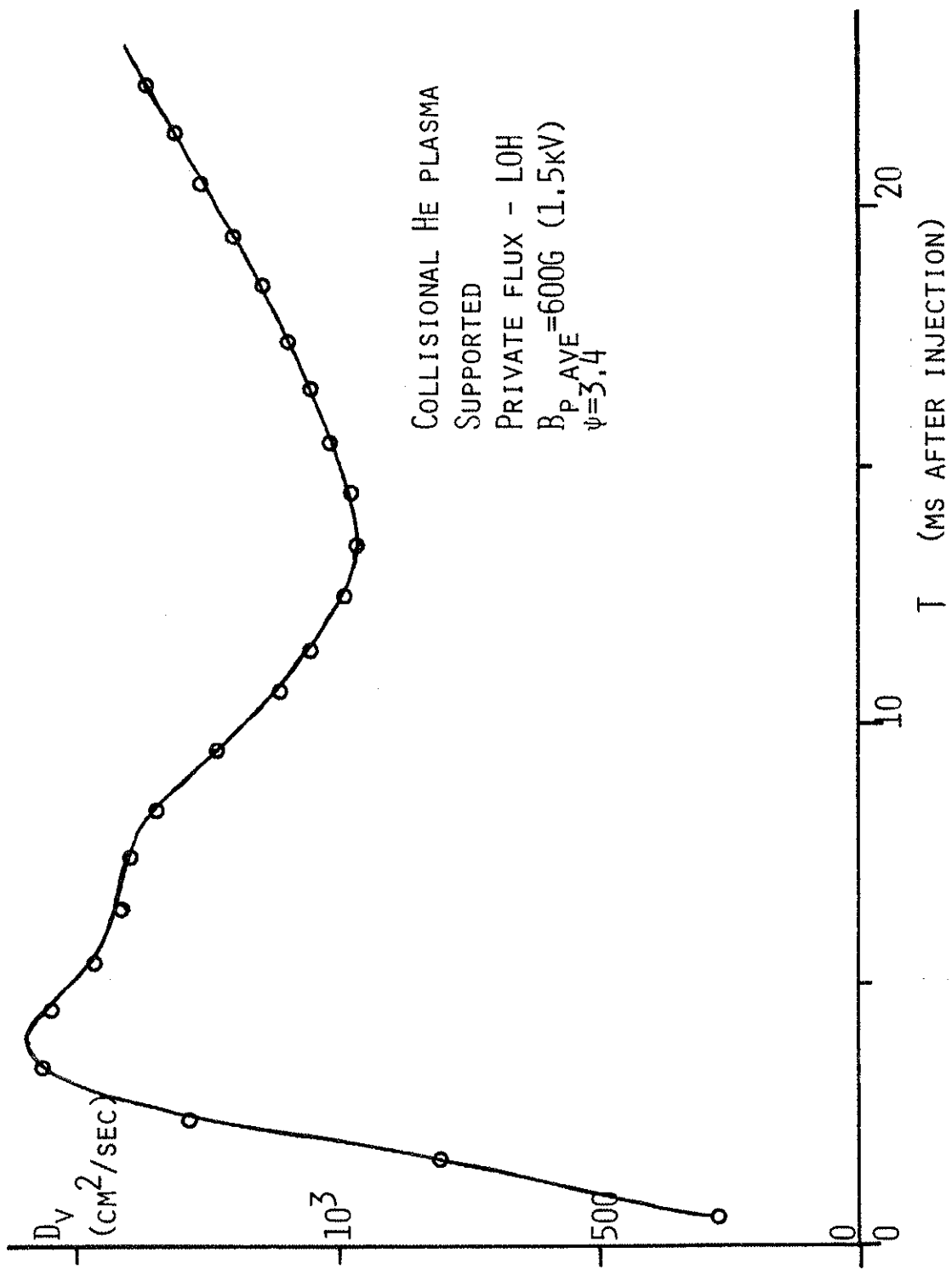FIG. 5.23 D_V VS. T; COLLISIONAL HE PLASMA; B_P=100G (250V)

FIG. 5.24 DIFFUSION COEFFICIENT VS. TIME

With $n \sim 2 \times 10^{11}$, $T_e \sim .2eV$, we find $D_{cl}(B_{ave} \sim 600G) = 200 cm^2/sec$, so that $D_v > D_{cl}$ for the high-field case. However, for the low-field case, $D_{cl} = 1200 cm^2/sec$, and $D_v \sim 10^4 cm^2/sec$.

Part of the discrepancy may lie in the different shape of $D(\psi)$. The shapes for the classical diffusion coefficient ($D \propto n$) and the vortex diffusion coefficient ($D \propto n^{-1/2}$) are sketched in Fig. 5.25. From this figure we note that it might be possible for D_v to be larger than D_{cl} at the position where the scan was made ($\psi \sim 3.4$, with $\psi_s \sim 5.7$ and $\psi_r \sim 2.4$), while $D_{cl} > D_v$ in the bulk of the private flux volume. However, this may not account for the factor of 10 difference in the numerical values obtained. It will be necessary to examine more ψ-surfaces to account for this discrepancy, and a larger range of magnetic fields. This is discussed in the recommendations for further work in Chapter VII.

The viscous damping time of a cell with wavenumber k is $\tau_\mu \propto 1/\mu k^2$. As discussed previously, the largest 20-30 toroidal modes which fit into the Octupole share the same $k_{\psi 1}$, with $\lambda \sim 5cm$. Therefore, the longest cells have the same damping times, and $\tau_\mu \propto 1/\mu k^2 \sim 25 cm^2/\mu$. For a .1eV collisional He plasma with $n \sim 10^{11}$ we can estimate the damping times using LIH average values. These are shown in Table V.1. The damping times in the table are consistent with what is observed in the time decay of the contour plots, but full scans are needed in addition to more information about E_ψ, to see if the long modes actually damp in unison.
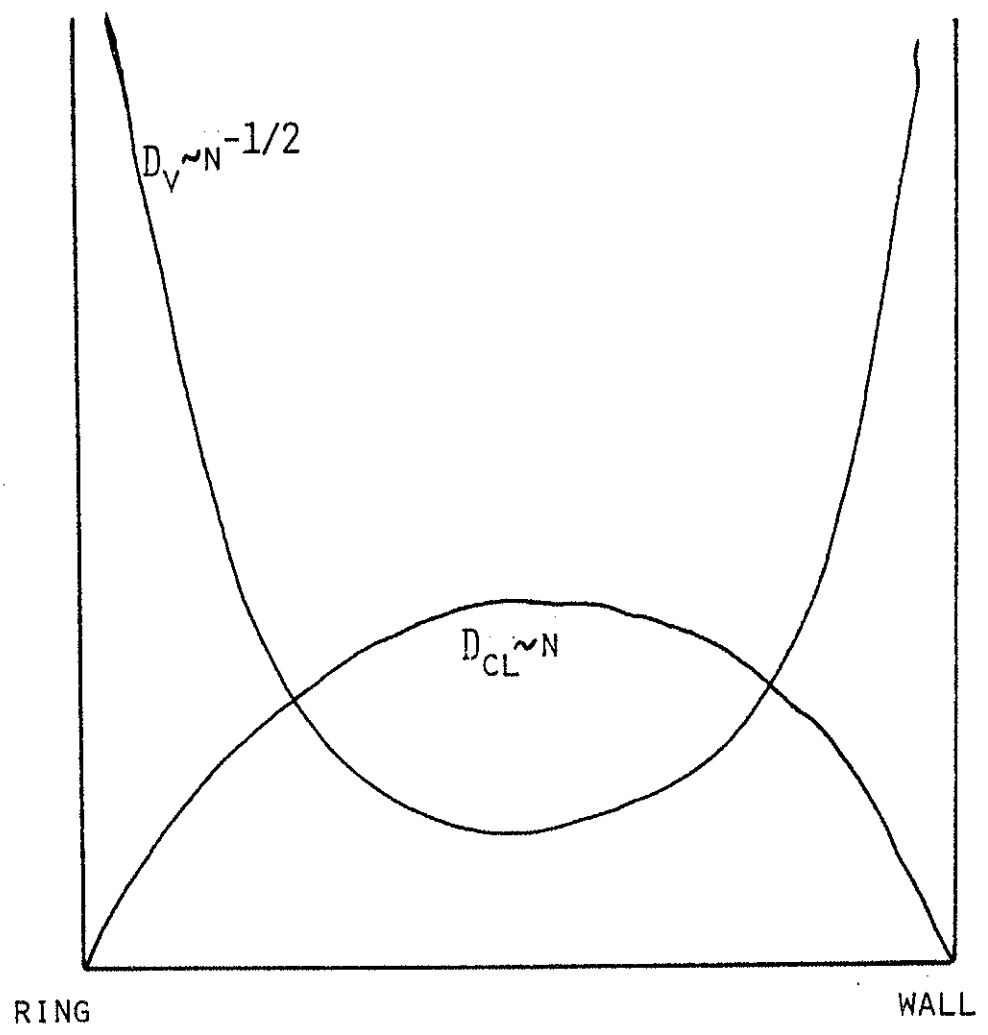
FIG. 5.25 SKETCH OF THE SPATIAL DEPENDENCE
OF THE DIFFUSION COEFFICIENT

Table V.1 *

B_{ave} (G)	τ_μ (ms)	Bank Voltage (kV)	Hoop
100	.3	.250	O
200	1.2	.250	I
240	1.7	.600	O
300	2.8	.750	O
480	6.9	.600	I
600	11	.750	I
		1.5	O
800	20	2	O
1000	30	2.5	O
1200	43	1.5	I
1600	77	2	I
2000	120	2.5	I

* $\tau_\mu \propto 1/k^2 \mu$
$\mu \propto n/B^2$, k^2 and n assumed constant.

Table V.1 $B_{p\ ave}$ as a function of poloidal bank voltage and hoop; viscous damping times for a 5cm vortex.

1c. Experimental Observations. A 360° scan of six ψ-surfaces in the private flux of the LIH was made at 600V on the poloidal bank ($B_{ave} \sim 480G$ LIH). The contour plots are shown in Fig. 5.26. The cell pattern is very clear. There are two large cells: a positive cell centered roughly at $\psi=2.75$, $\theta=250^O$, and a negative cell centered at $\psi=4.5$, $\theta=70^O$, halfway around the machine in θ from the positive cell. The cell structure does not lose its identity in the 70ms observation period, although it decays in amplitude by about a factor of 2 over the same period.

The power spectrum for the six ψ-surfaces, $E^2_\theta(m)$, is shown in Fig. 5.27a-f (3ms after injection) and Fig. 5.28a-f (7ms). The plots show that E^2 is a decreasing function of k. The plots at 3ms after injection show a small bump at $m \sim 60$; by 7ms the bump has disappeared.

The E_θ power spectrum is a strong function of position in ψ. The separatrix has little structure; the amount of structure increases towards the ring. $\Sigma E^2_\theta(k)$ is plotted in Fig. 5.29 for the six ψ-surfaces measured, at 4 times. The earliest time plotted is 10ms after injection; at earlier times the structure is not reproducible.

The decay of E^2_θ as a function of time is plotted for all six ψ-surfaces in Fig. 5.30a and b. The plots show that after an initial decay ($t \sim 10ms$), the electric fields on the ψ-surfaces in the main body of the plasma remain constant. The spectrum at $\psi=2.77$ decays gradually with (very roughly) a 20ms time constant.
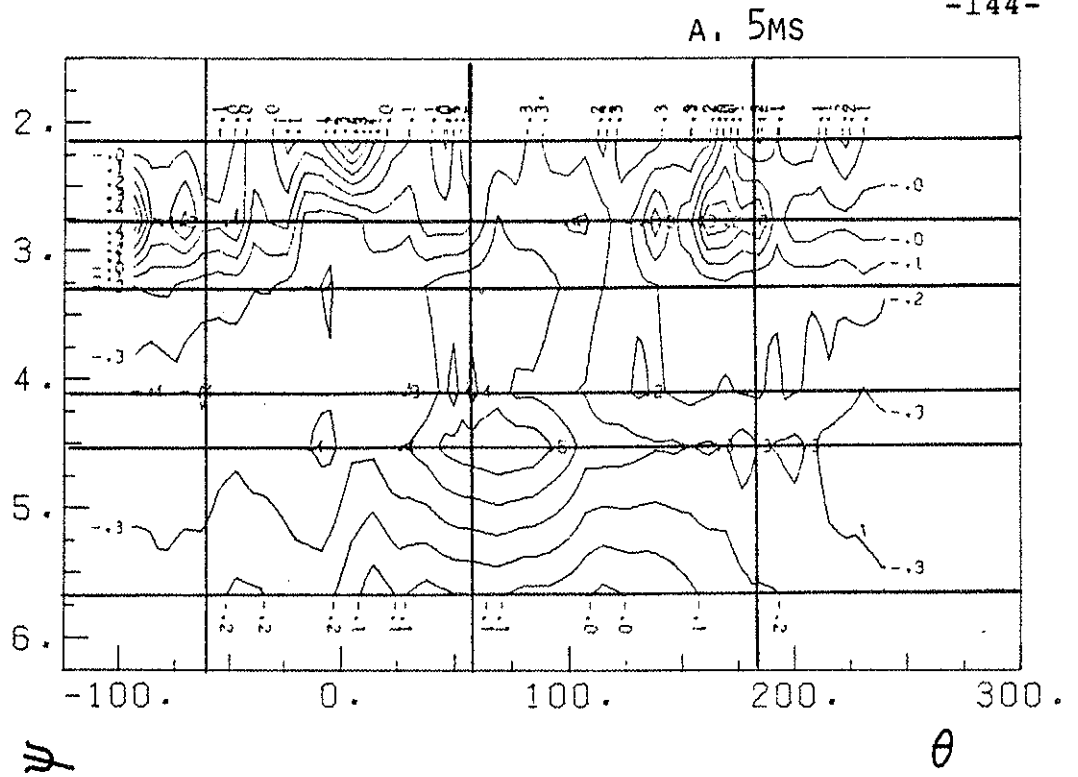
A. 5ms

B. 7ms
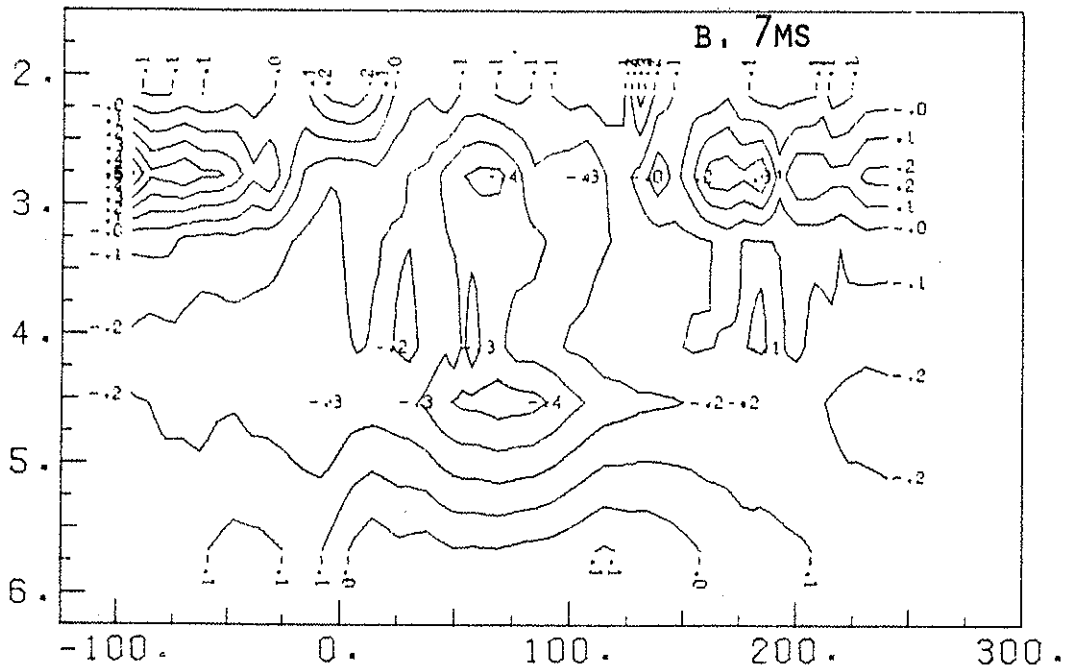
FIG. 5.26A AND B. FLOATING POTENTIAL CONTOURS; SUPPORTED;
COLLISIONAL HE PLASMA; PRIVATE FLUX OF THE LIH;
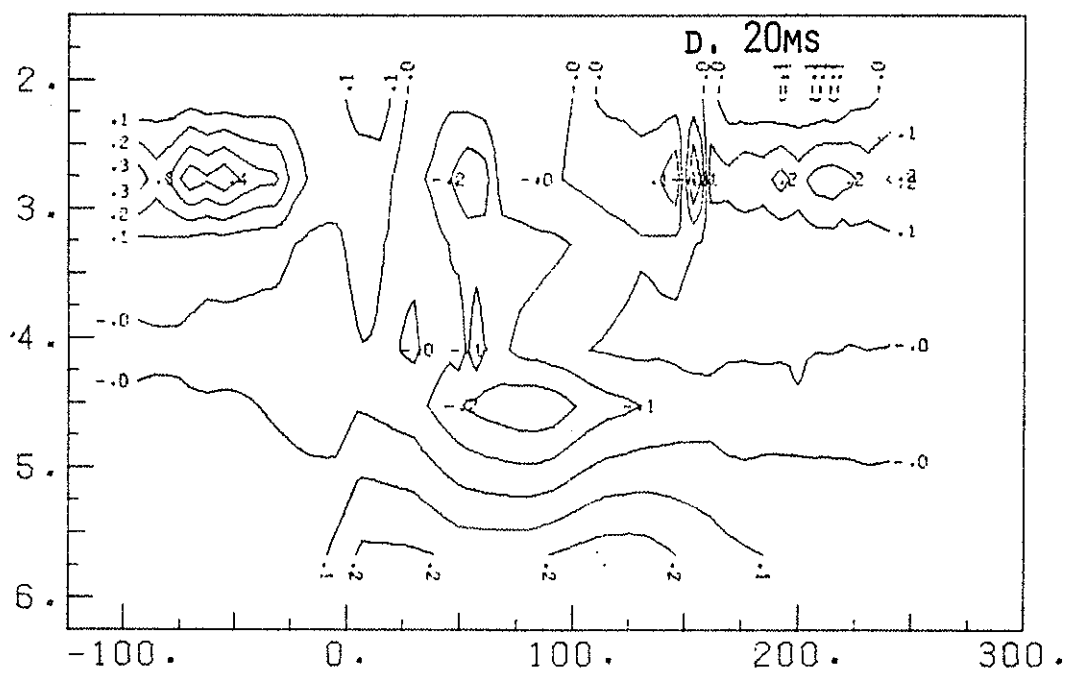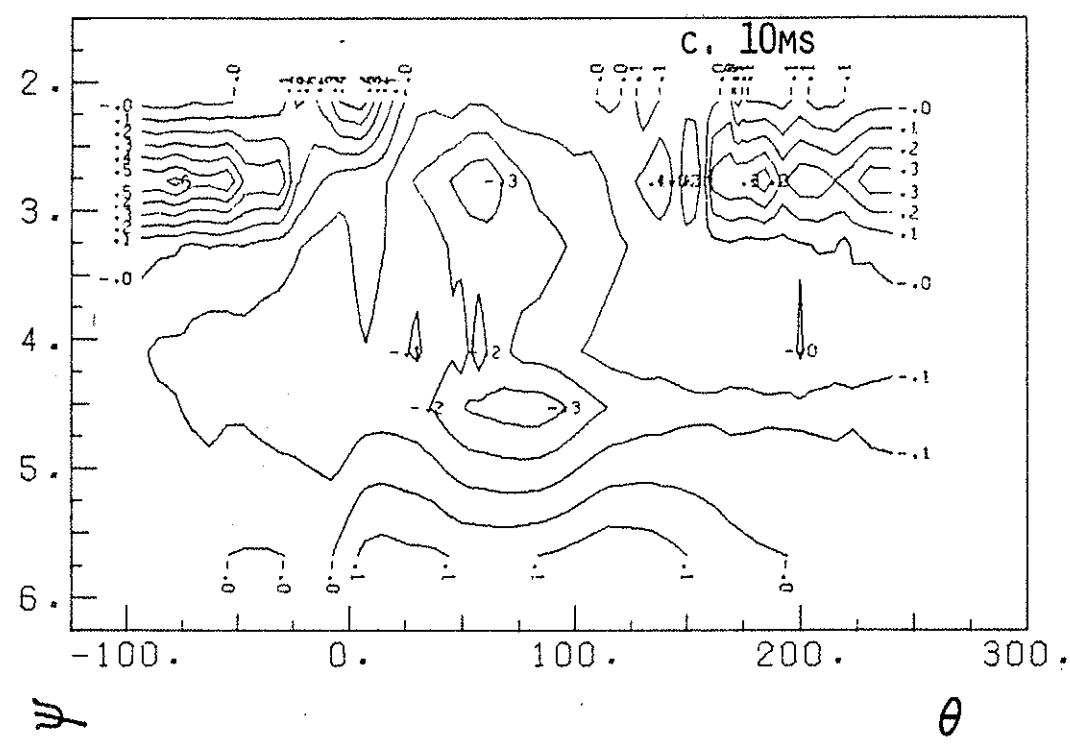$B_{P\ AVE}$=480G (600V).

FIG. 5.26C AND D. FLOATING POTENTIAL CONTOURS; SUPPORTED;
COLLISIONAL HE PLASMA; PRIVATE FLUX OF THE LIH;
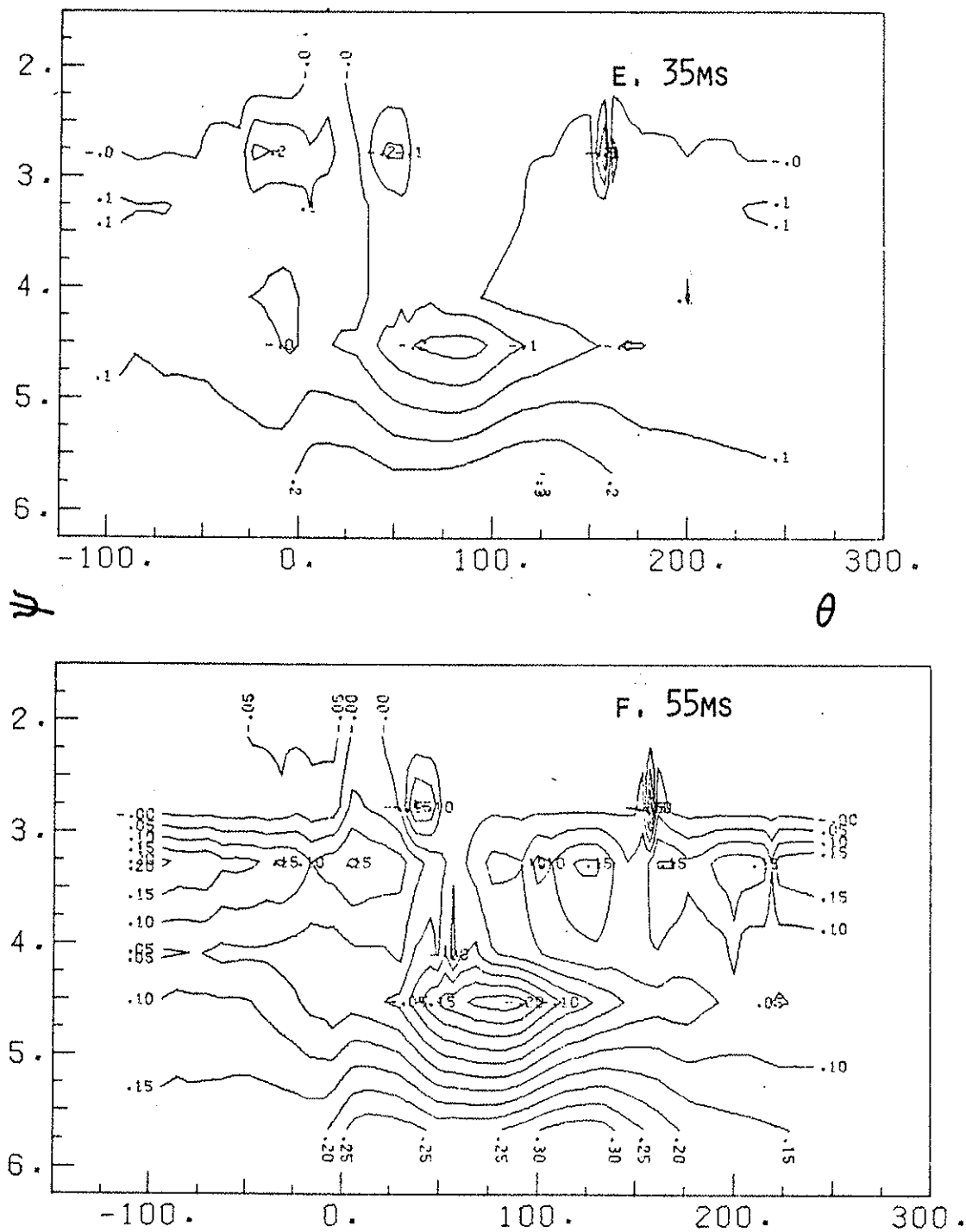$B_{P\ AVE}$=480G (600V).

FIG. 5.26E AND F. FLOATING POTENTIAL CONTOURS; SUPPORTED;
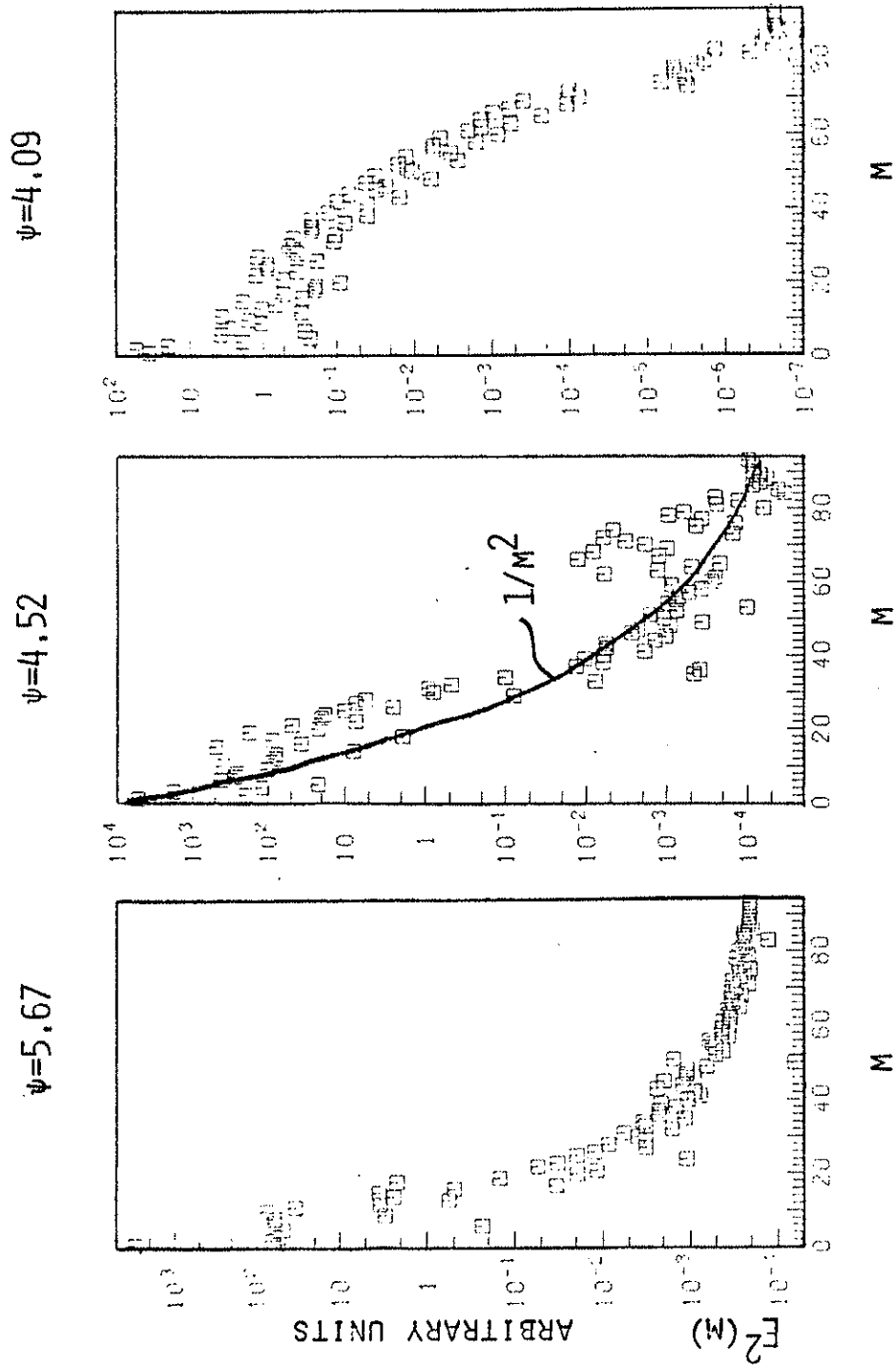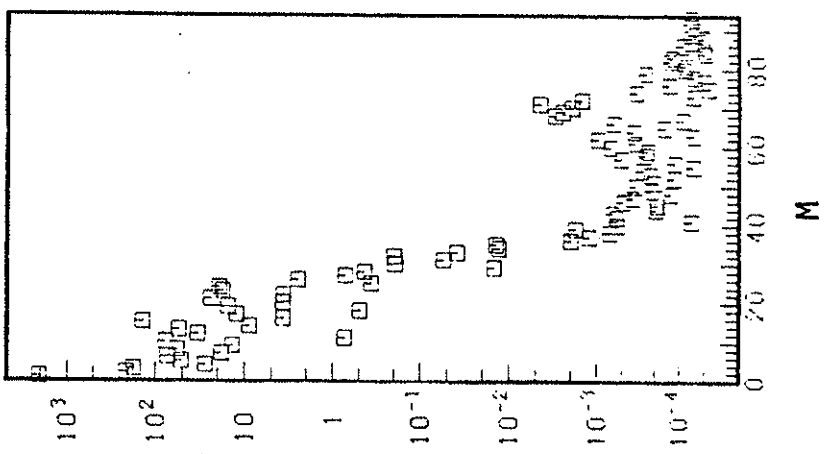COLLISIONAL HE PLASMA; PRIVATE FLUX OF THE LIH;
$B_{P\ AVE}$=480G (600V).

FIG. 5.27 $E^2(M)$ VS. M; 3MS AFTER INJECTION; COLLISIONAL
HE PLASMA; SUPPORTED; PRIVATE FLUX OF THE LIH;
$B_{P\ AVE}$=480G (600V).
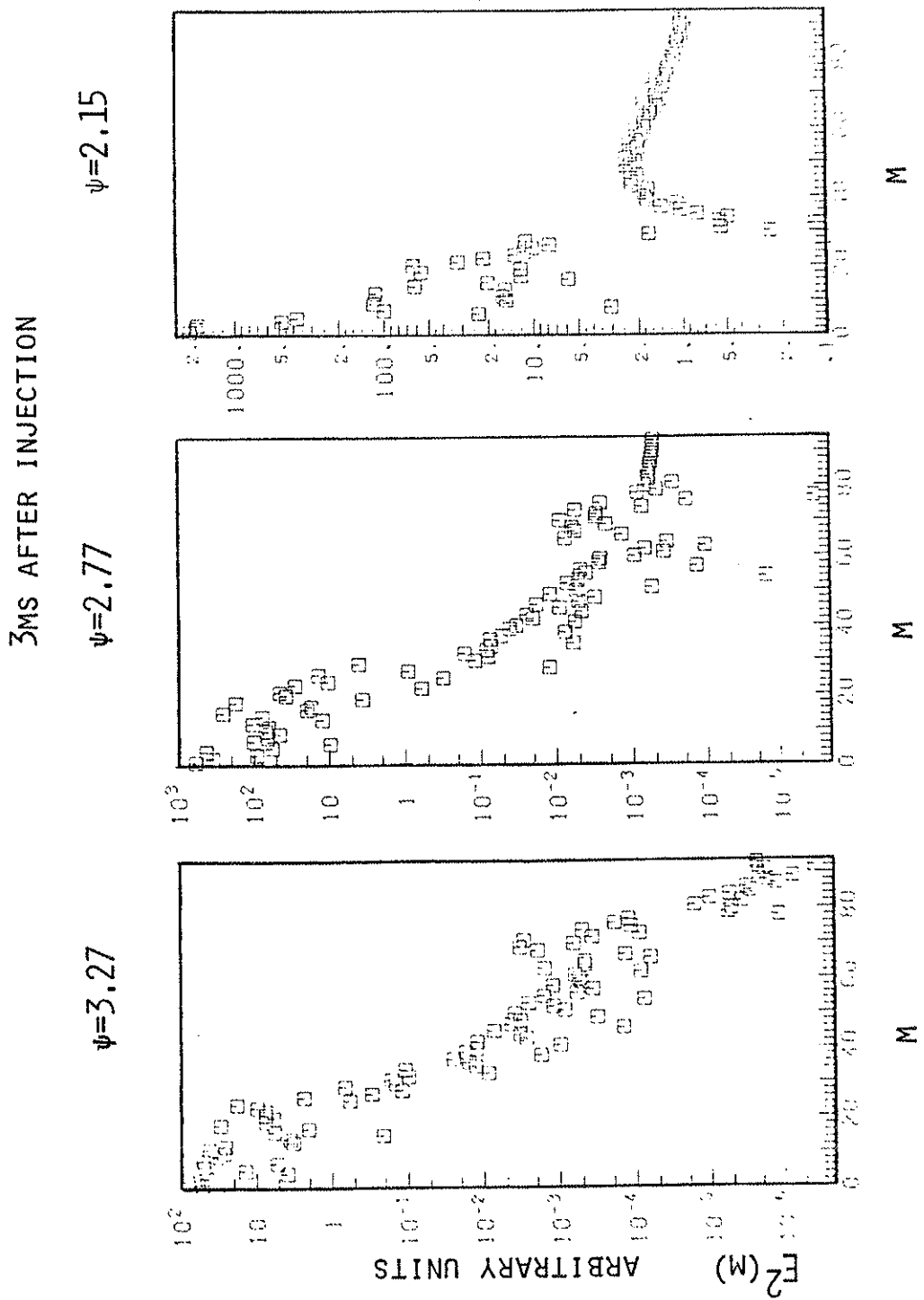
FIG. 5.27 $E^2(M)$ VS. M; 3MS AFTER INJECTION; COLLISIONAL HE PLASMA; SUPPORTED; PRIVATE FLUX OF THE LIH; $B_{P\ AVE}$=480G (600V).
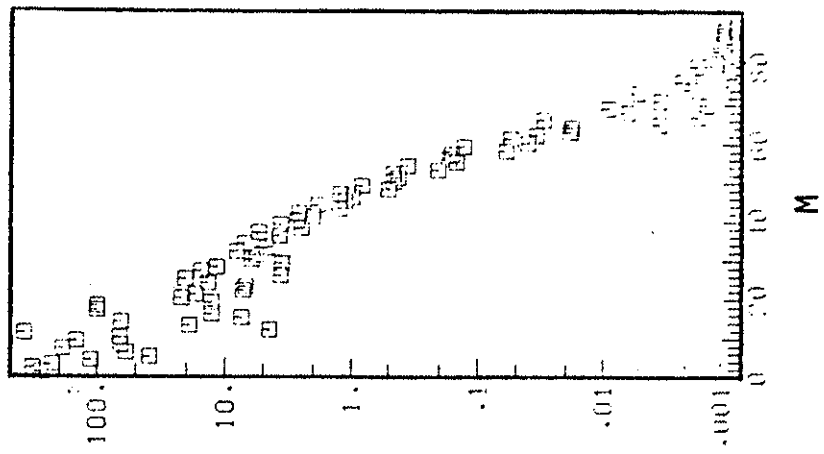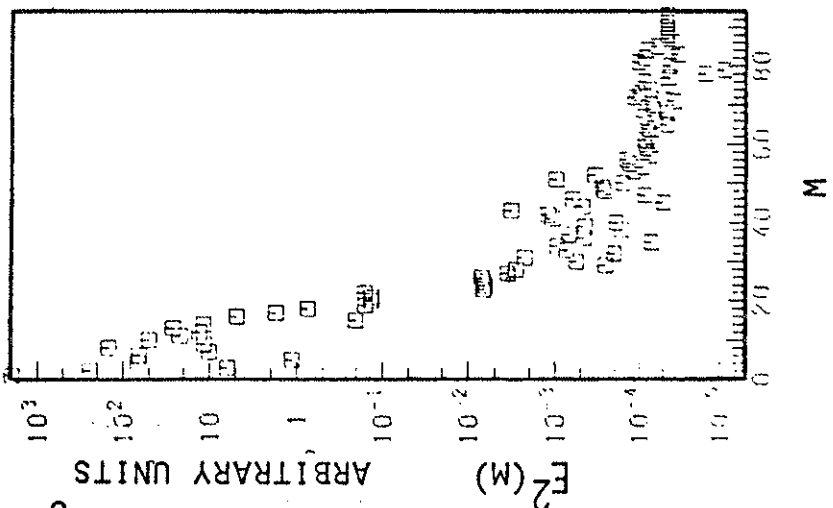
FIG. 5.28 E^2(M) VS. M; 7MS AFTER INJECTION; COLLISIONAL HE PLASMA; SUPPORTED; PRIVATE FLUX OF THE LIH; B_pAVE=480G (600V).

$$\sum_K E^2(K) \qquad (V/M)^2$$

FIG. 5.30A TIME DECAY OF TOROIDAL ELECTRIC FIELD POWER
SPECTRUM; COLLISIONAL HE PLASMA; SUPPORTED;
PRIVATE FLUX OF THE LIH; $B_{P \ AVE}$=480G (600V).
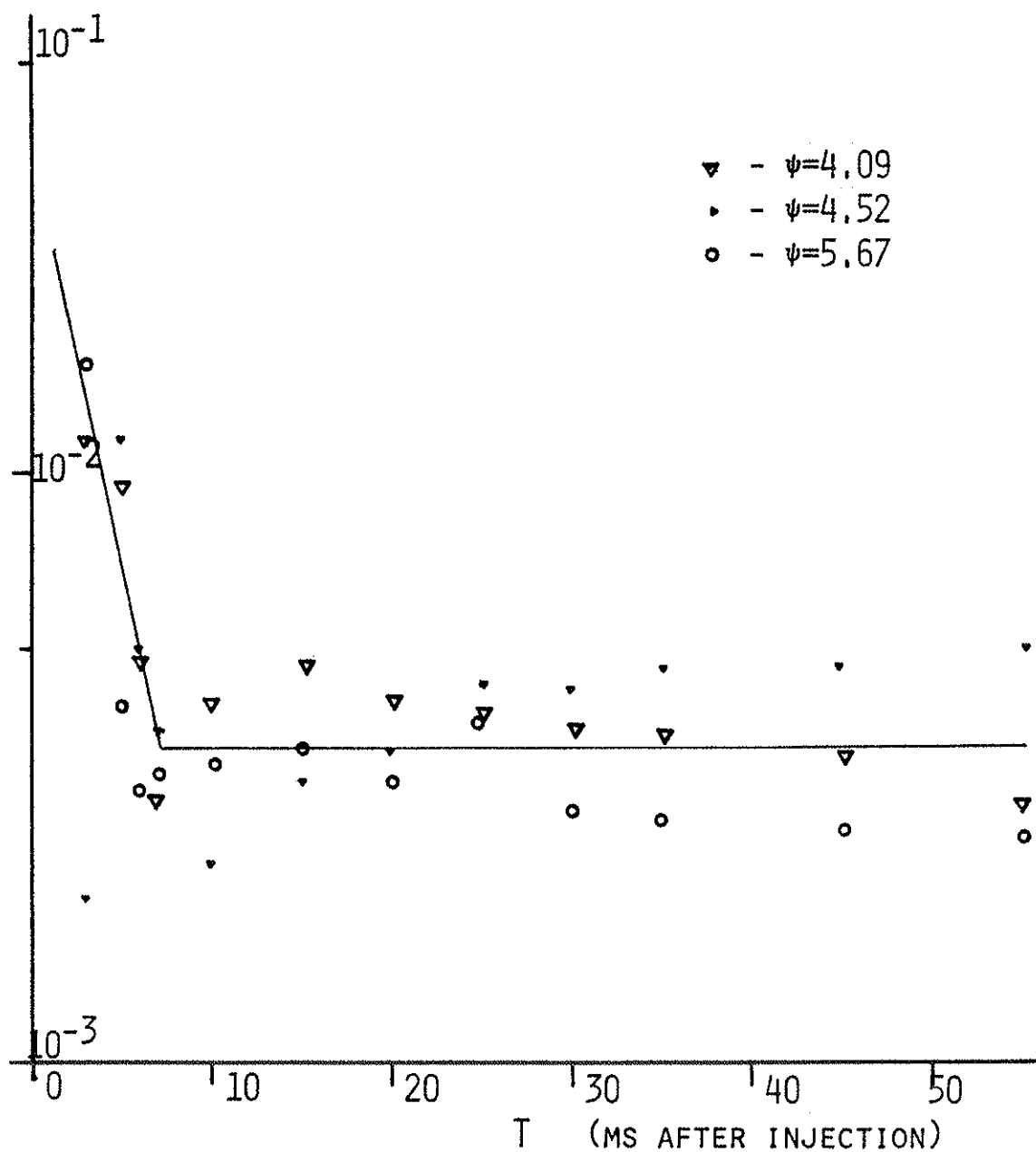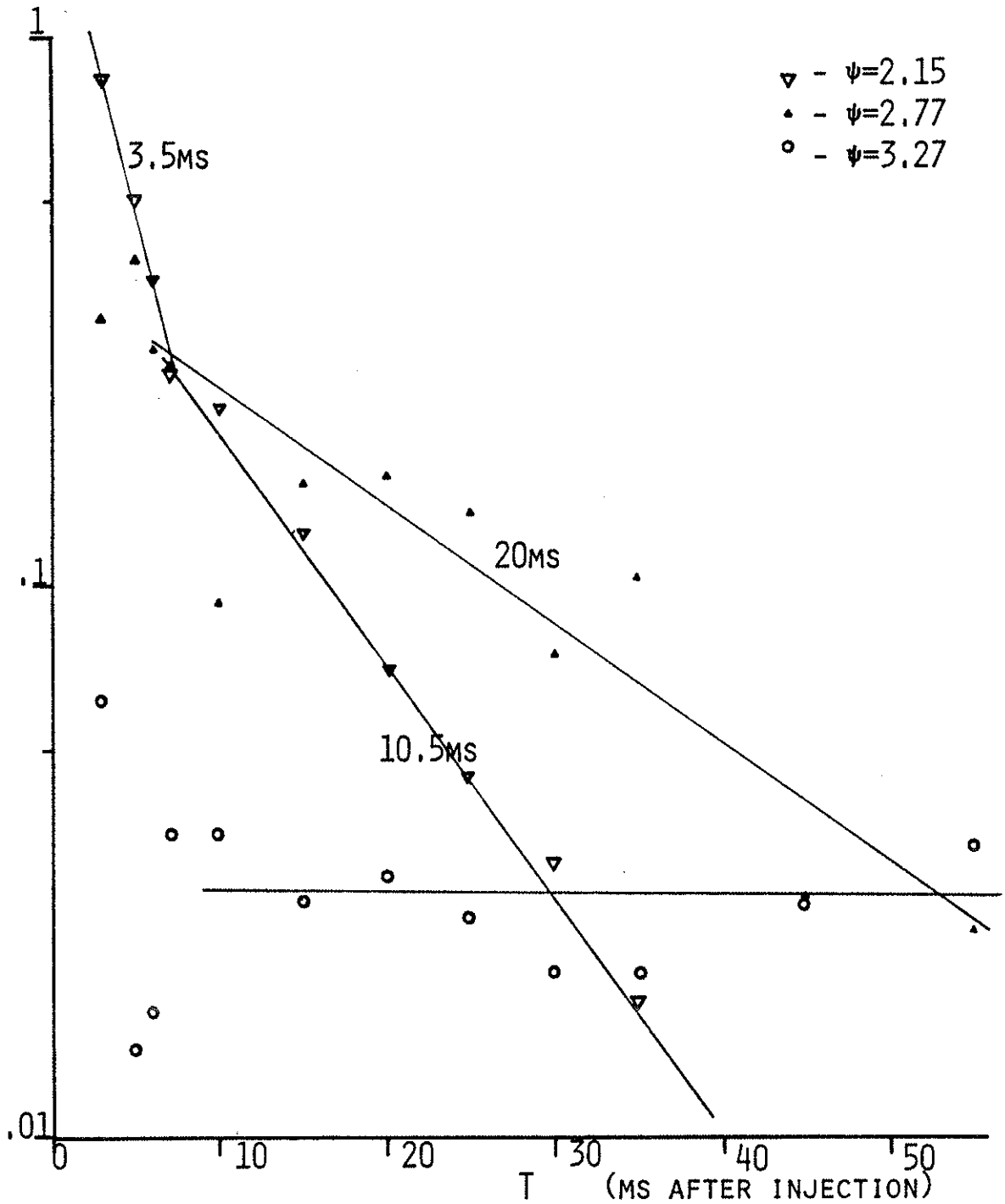
FIG. 5.30B TIME DECAY OF TOROIDAL ELECTRIC FIELD POWER
SPECTRUM; COLLISIONAL HE PLASMA; SUPPORTED;
PRIVATE FLUX OF THE LIH; $B_{P\ AVE}$=480G (600V).

The last ψ-surface measured is at $\psi=2.15$. This field line intersects the hoop; however, on the low-field side of the hoop this field line is still accessible (see Fig. 2.6). This is probably the reason that the electric fields on this ψ-surface decrease in time.

2c. Discussion. Because the plasma is very collisional, $\lambda_{mfp}<\lambda_f$, and the support does not connect all of the field lines at its azimuth together. The bump on the 3ms spectra is much smaller than the one on the colli- sionless spectra, and at a higher mode number. If the bump is due to the supports in both cases, then the support is not an additional boundary condition for the collisional plasma, as expected.

We have used the E^2 data to estimate the diffusion coefficient for this plasma as a function of ψ-surface and time, as discussed in Chapter IV. The results are presented in Fig. 5.31. Because of the ψ-dependence of E_θ^2, the diffusion coefficient is also ψ-dependent, with the separa- trix region having the smallest values of D_v. The diffusion increases during the first 5-10ms and then becomes constant, except for the two ψ-surfaces closest to the ring. D_v is smallest lowest near the separatrix, where it has a value $\sim 500 cm^2/sec$.

We can estimate $T^*(k)$ as for the collisionless plasma, using $n \sim 10^{11}/cm^3$, B=480G, E(m=1)=.02V/m, which leads to $T^*(m=1)=5.6\times 10^7 eV$.

The magnitude of D_v and T^* for this plasma are in reasonable agreement with the results shown in Ref. 26, and the shape of $D_v(\psi)$ is roughly what would be expected for $D_v \propto n^{-1/2}$ (see, for example, Ref. 13, Fig. 3.21).
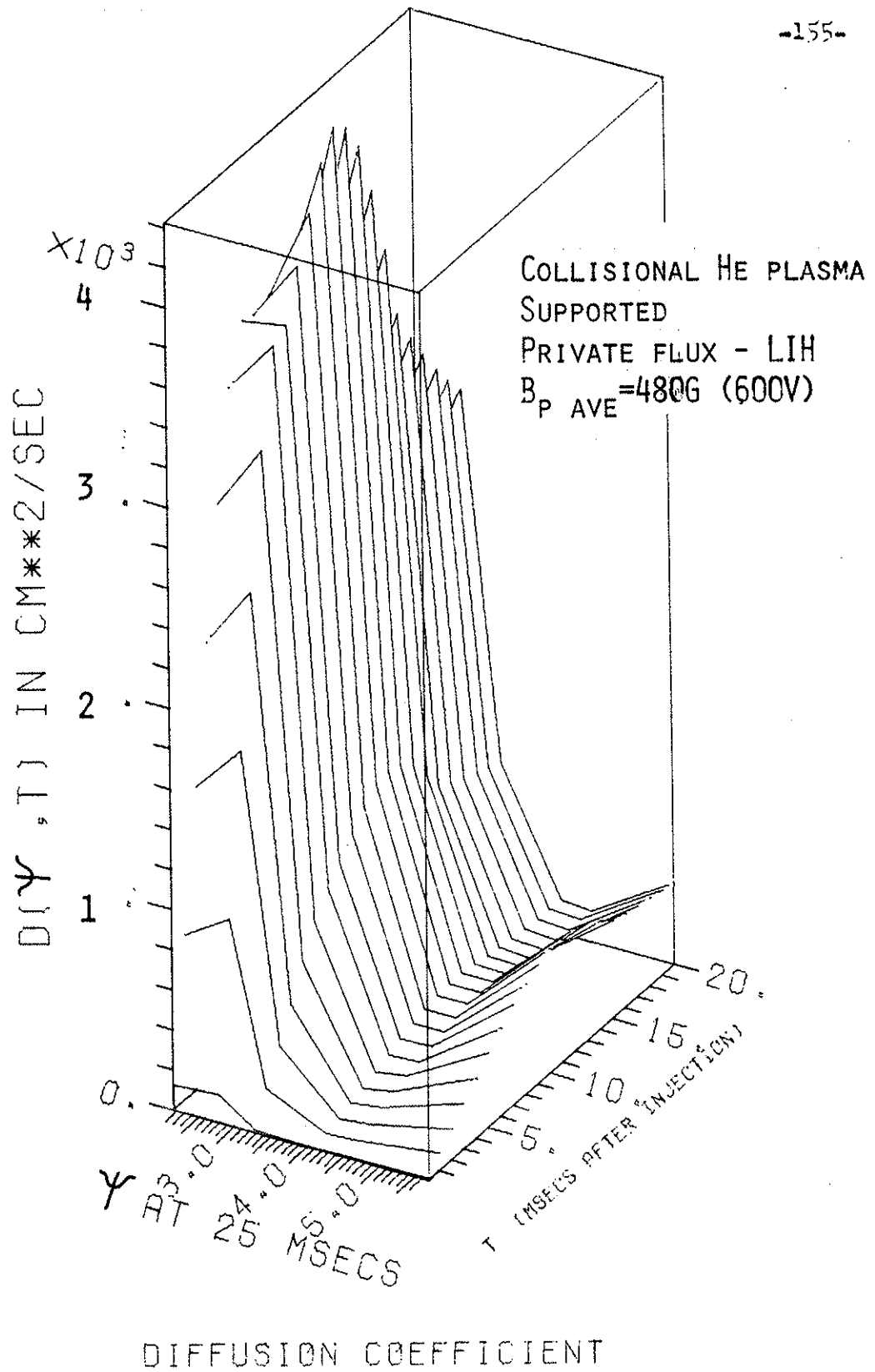
COLLISIONAL HE PLASMA
SUPPORTED
PRIVATE FLUX - LIH
$B_{P\ AVE}$=480G (600V)

DIFFUSION COEFFICIENT

FIG. 5.31 SPATIAL AND TEMPORAL DEPENDENCE OF D_V

It is interesting to see that the time decay of the spectrum is different on different ψ-surfaces. The theory is not sophisticated enough to predict details such as time decays except in a general way, and more study is necessary to understand the spatial dependence on ψ. However, even with a simple model it has been possible to estimate a diffusion coefficient from the electric field spectrum, and show that the vortices can be responsible for diffusion in the Octupole.

B. Levitated Data. V_f contours from a partial scan of the Octupole for the collisional plasma are shown in Fig. 5.32. The machine was fully levitated when the plasma was injected and during the next 20ms; after this the supports started to come back in. The data was taken in the private flux of the LIH, with 2.5kV on the poloidal bank (corresponding to $B_{ave} \sim 2kG$). The plot covers an 80° segment from -20°, through the gap at 0°, to $+60^O$ in θ.

1. Experimental Observations. The data shows the development of the vortices. There is cell structure present from the earliest time plotted (4ms after injection), throughout the levitated period (to ~ 45ms after injection), and after the supports come back in. The structure is not stationary, but evolves slowly in time over the experimental pulse. There is little structure at the separatrix by 5ms after injection; during the levitated portion the steepest potential gradients in ψ occur near the ring. The contours show cell development in the region between $\psi \sim 4$ and $\psi \sim 5$, and between the ring and $\psi \sim 4$.
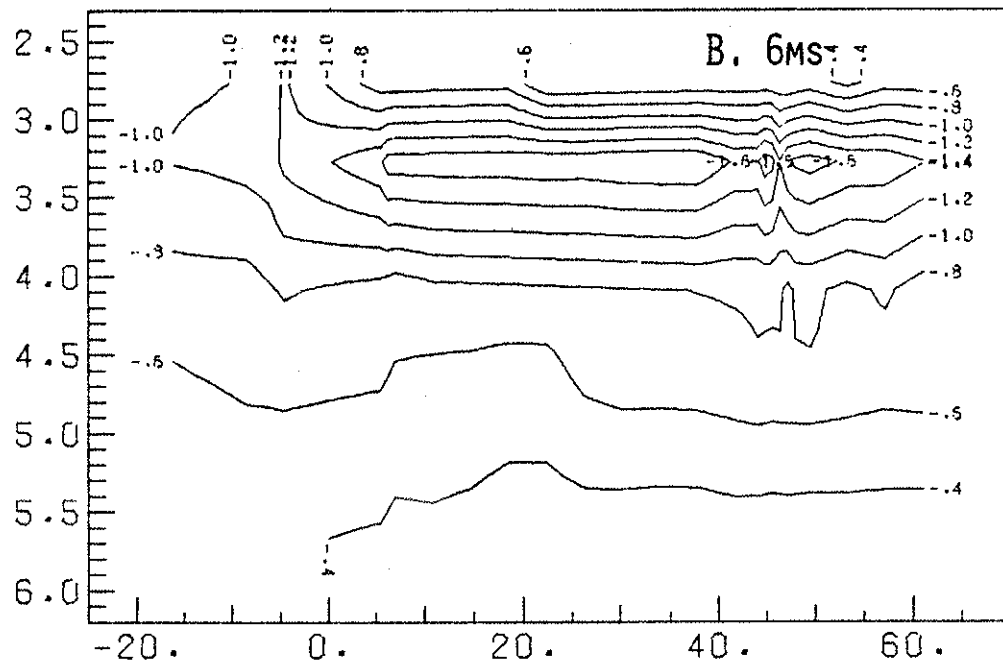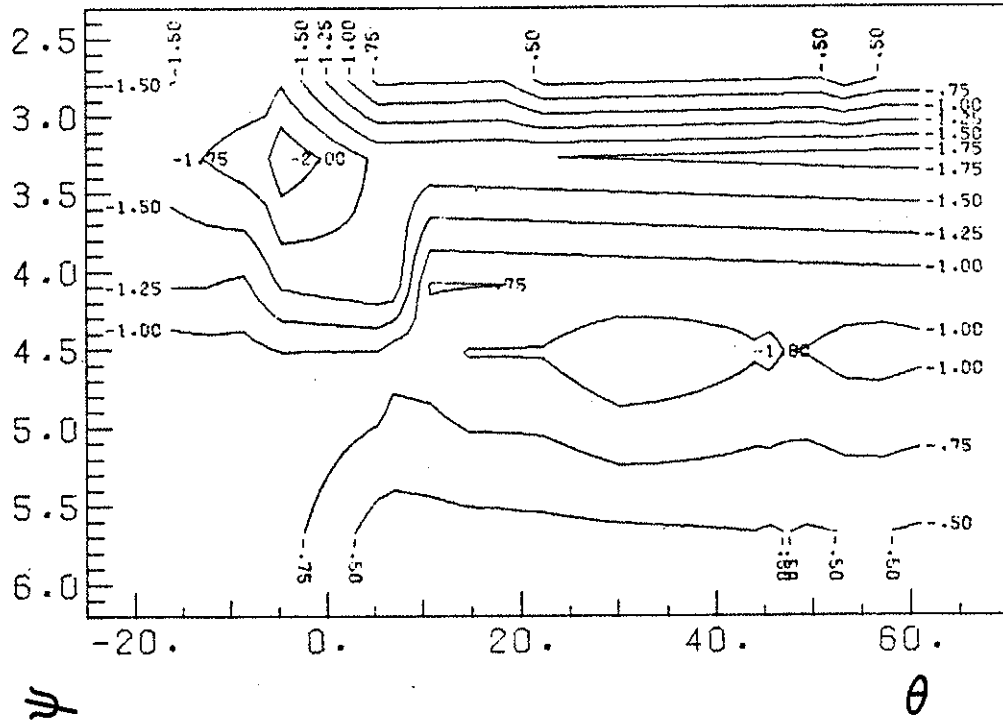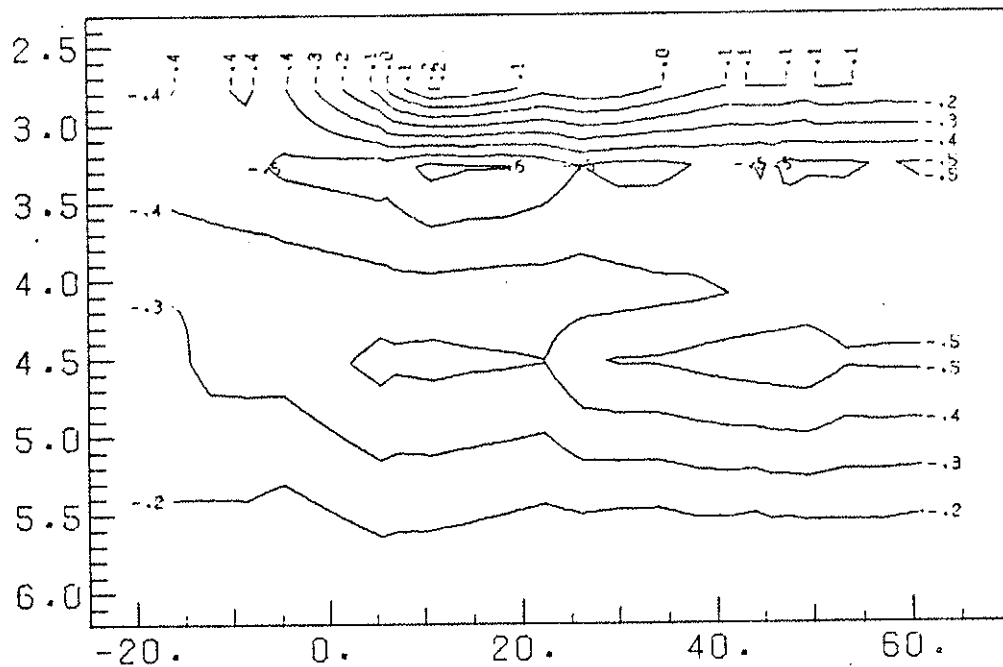
A. 4MS

ψ θ

B. 6MS

FIG. 5.32A AND B. FLOATING POTENTIAL CONTOURS; LEVITATED;
COLLISIONAL HE PLASMA; PRIVATE FLUX OF THE LIH;
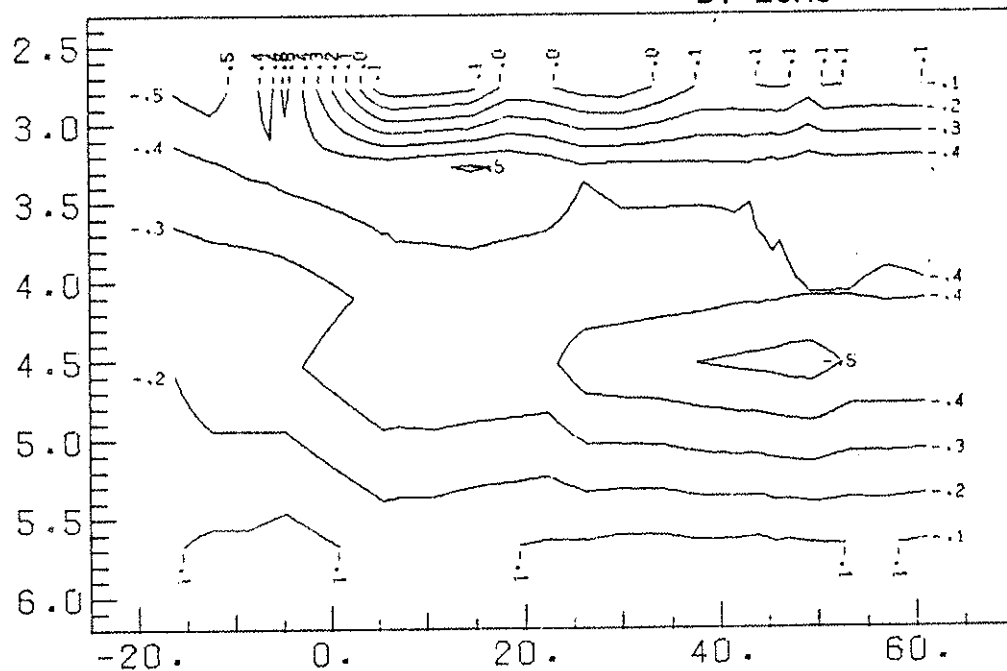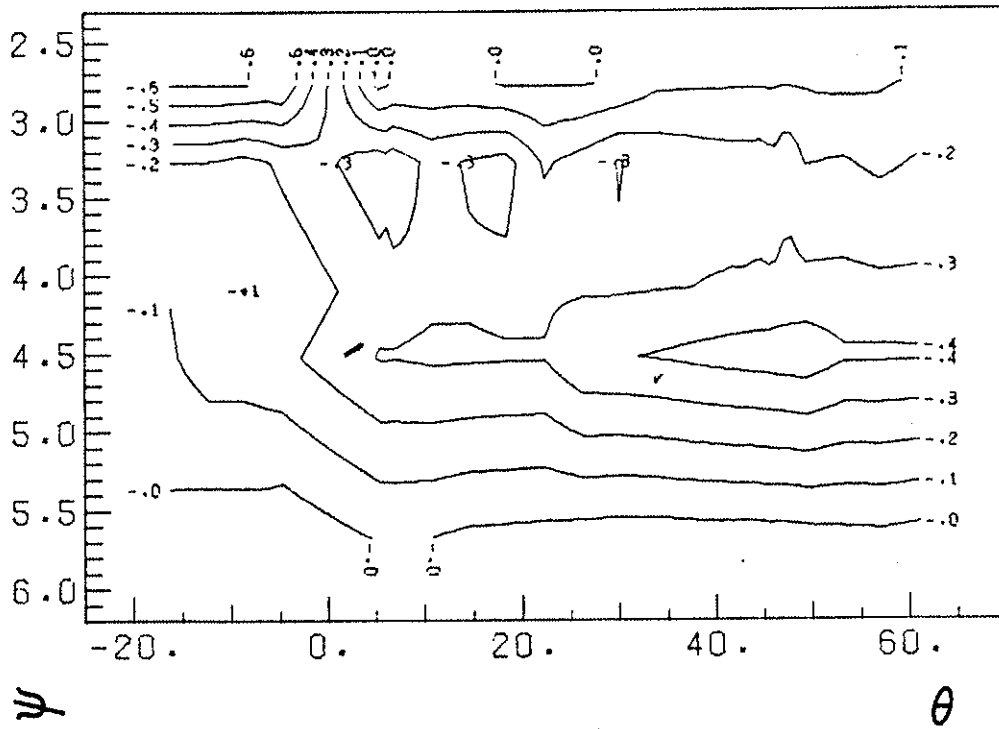$B_{P\ AVE}$=2KG (2.5KV).

c. 15ms

d. 20ms

FIG. 5.32c AND D. FLOATING POTENTIAL CONTOURS; LEVITATED;
COLLISIONAL HE PLASMA; PRIVATE FLUX OF THE LIH;
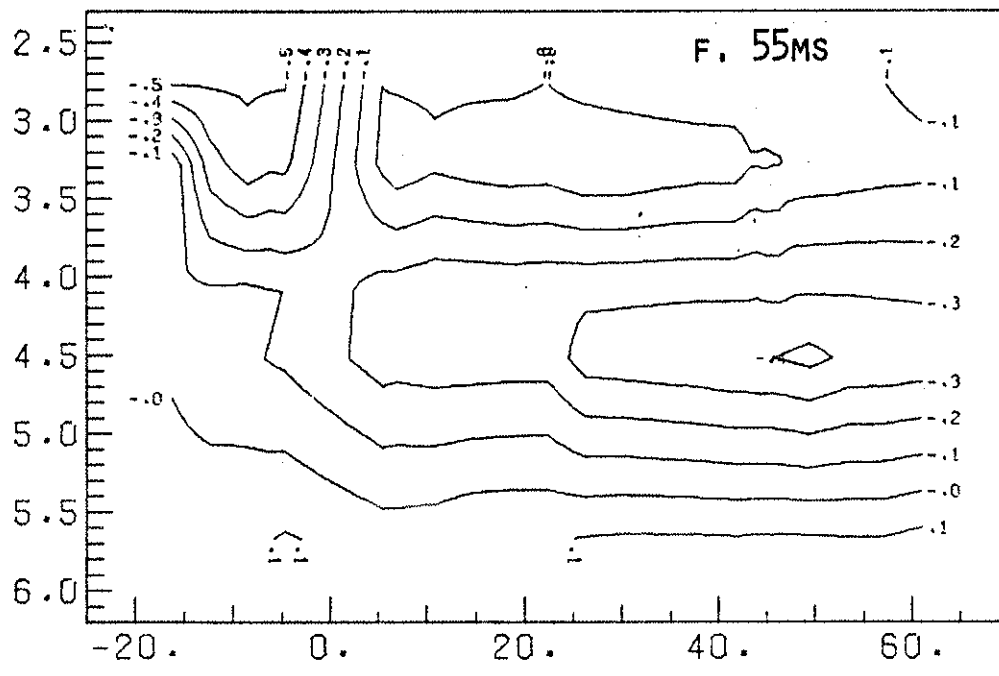$B_{P\ AVE}$=2KG (2.5KV).

E. 35MS

F. 55MS

FIG. 5.32E AND F. FLOATING POTENTIAL CONTOURS; LEVITATED;
COLLISIONAL HE PLASMA; PRIVATE FLUX OF THE LIH;
$B_{P\ AVE}$=2KG (2.5KV).

2. Discussion. The levitated contours are similar in shape to the supported contours for this plasma, but the potential gradients in ψ are a factor of 4 or so larger. The difference between the levitated and supported contours is smaller for the azimuthal electric fields; however, without a full scan in θ it is not possible to make detailed comparisons. Because the plasma is collisional, the supports are a very localized perturbation in the plasma, and there is little disturbance a few mean-free-paths away. The supports do, however, connect the high-dielectric-constant separatrix to the rings, serving as a path to short out some of the electric fields at ψ_s. Because of this the levitated contours (Fig. 5.32) have a higher energy density than the supported contours (Fig. 5.14), and should have a higher T^*.

This agrees with diffusion data taken by Navratil[15], who noted that for the collisional plasma in a levitated Octupole the transition from vortex diffusion to classical diffusion occurs at a lower value of the poloidal field, which indicates a higher initial T^*; also, the profile did not take on the classical shape by the initial observation (3ms after injection) even for the lowest poloidal field available $(B_{ave} \sim 40G, LOH)$[54]. Thus the interpretation of having the cells be the source of the vortex diffusion is consistent with the profile evolution data for the collisional plasma with the Octupole levitated, but more information about the spectrum is necessary before an estimate of the magnitude of D_v or T^* can be made.

C. Summary. The data shown for the collisional plasma supports the theory that the macroscopic vortices in

the plasma are the observable part of a non-thermal spectrum with an enhanced temperature $\sim 10^7$ eV. Many details remain to be worked out in the 2-D fluid theory for the Octupole. However, we see that the trends in the data are generally in the correct direction: When the field is reduced, the spectrum damps. The diffusion coefficient calculated from the supported data is of the right order of magnitude and shape. The levitated contours appear to have a higher energy density than the supported contours. And the shape of the contours is similar to the fluid solutions proposed in Fig. 4.2, as expected, since for the collisional plasma the levators do not form additional boundary conditions as in the case of the collisionless plasma.

CHAPTER VI - EFFECT OF B_T ON COLLISIONLESS
AND COLLISIONAL PLASMAS

With a purely poloidal field, Octupole magnetic field lines close upon themselves after one revolution in χ in a constant-azimuth plane. When a toroidal field is added, the field lines advance $\Delta\theta$ in the azimuthal direction for each revolution about the minor axis ($\Delta\chi=2\pi$). The transform angle, $\Delta\theta$, is given by

$$\Delta\theta = \oint \frac{B_t}{RB_p}\, d\ell_{B_p} = \alpha \oint \frac{1}{R^2 B_p}\, d\ell_{B_p} \tag{6.1}$$

where $B_t = \alpha/R$. $\Delta\theta$ approaches infinity at the field null, and is different for each Octupole ψ-surface, leading to a sheared magnetic field. If the ratio $\iota = \Delta\theta/\Delta\chi$ is a rational number, the field line will close upon itself after an integral number of revolutions in the azimuthal direction; otherwise the field line will generate a flux surface. In either case, the length of the field line will increase.

Potential structure has been observed in the Octupole for plasmas with a poloidal and toroidal field, but it is no longer necessarily true that the potential is constant along a field line, and in general, $\phi=\phi(\chi,\theta,\psi)$.

Vortex diffusion theory is applicable to 3-D plasmas[18,21]; the vortex contribution to D comes from modes with $k_z=0$. The cart probe has access to a limited portion of the Octupole, and it is not possible to measure the electric field spectrum as was done in Chapter V: rotating the contours around the ring will not produce the 3-D

potential structure. For this reason the discussion will be more qualitative than in the previous chapter, but it is still possible to investigate many of the features of 3-D convective cells.

VI.1 COLLISIONLESS PLASMA

The ion mean-free-path for the collisionless plasma can be estimated from

$$\lambda_{mfp} = v_{th\ i} \cdot \tau_i = \frac{2.1 \times 10^{12}}{(\lambda/10)} \frac{T_i^2}{n} \text{ cm} \qquad (6.2)$$

where

$$v_{th\ i} = (T_i/m_i)^{1/2} \qquad (6.3)$$

$$\tau_i = \frac{3}{4} \frac{\sqrt{m_i}}{\sqrt{\pi}} \frac{T_i^{3/2}}{\lambda e^4 z^4 n_i} \qquad \text{(Ref. 52)} \qquad (6.4)$$

$$\lambda = \ln\Lambda = 23.4 - 1.15 \log n + 3.45 \log T_e \qquad (6.5)$$

Using parameters from Table I.1, $\lambda_{mfp\ i} \sim 2000$m initially, and decreases to ~ 40m at 30ms after injection (when n $\sim 8 \times 10^8$ cm^{-3}, Ref. 25).

With a purely poloidal field, excess charge on a magnetic field line cannot dissipate because the field line is closed. When a toroidal field is added the field lines become very long. The minimum field line length (λ_f) is the length of the line through the poloidal field null, $\lambda_f \sim 2\pi (R=1.4m) \sim 8.8$m. For field lines that form flux surfaces, $\lambda_{mfp} << (\lambda_f \to \infty)$. This means that unless there are other mechanisms which inhibit free flow of charge, we would expect to see any excess charge dissipate quickly by parallel flow along the field line.

Magnetic mirror trapping. If electrons are trapped in a magnetic mirror, the excess charge can only be dissipated if the electrons are scattered out of the mirror by collisions, or more ions are collisionally trapped. Kamimura and Dawson[27] investigated the effect of mirror trapping in a thermal plasma by means of computer simulations, and showed that convective diffusion is enhanced. The appropriate damping mechanism is collisional detrapping, with a time constant proportional to the collisional lifetime and the mirror ratio, $\tau \propto \tau_c \ln(B_{max}/B_{min})$; the diffusion coefficient is

$$D_{KD} \propto \frac{T^{3/2}}{n} , \quad \text{independent of B} \qquad (6.6)$$

Diffusion studies have observed this scaling for the collisionless plasma with a poloidal and toroidal field (in the private flux of the LOH). The magnitude of $D_\perp$ indicated an effective temperature T^* of 500eV. An additional experiment performed with collisionless electrons and collisional ions indicated that the trapped particles were electrons; the scaling remained the same, but the effective temperature was lower, $\sim$150eV. [Note: fluctuations measured in this region could account for only a small percentage ($\simeq$2%) of the diffusion[56].]

In the common flux trapped ion modes were observed[56]: a dissipative mode in the region $5.7 \lesssim \psi \lesssim 6.1$, and a collisionless mode (in the ion diamagnetic drift direction) outside ψ=6.1. It was noted, however, that the fluctuations could account for all the diffusion in this region.

A. Experimental Observations. Cell structure was measured for the low density plasma ($n \sim 10^9 cm^3$, $T_i \sim 20$-2eV in

20ms). The magnitude of the toroidal field (in series with
the poloidal field) was 380G on axis. The poloidal field
bank voltage was 2.5kV, corresponding to $B_{ave} \sim 2kG$ (LIH).

Because λ_{mfp} for this plasma is long, thermal flow
along the field lines intersected by the supports accounts
for a significant loss of plasma. For this reason the data
was taken with all four hoops levitated (as were the diffu-
sion studies[56,57]).

Data for the private flux of the LIH is presented in
Fig. 6.1a-f. The private flux exhibits a good deal of
potential structure for the duration of the levitated
period ($\sim$20ms.), Fig. 6.1a-e. The structure damps signifi-
cantly between 15 and 25ms (Fig. 6.1e and f) during the
time the supports come back in, and remains at approximately
the same amplitude for the remainder of the experiment.

The contours are similar to the supported data with a
purely poloidal field (Figs. 5.1 and 5.3), with closed
cells in the region $3.5 \lesssim \psi \lesssim 4.5$. However, we note that there
is relatively little structure near the ring ($2.5 \lesssim \psi \lesssim 3.5$).
The separatrix is also flatter than the bulk of the plasma,
as was the case for the B_p-only data.

Common flux data is shown in Figs. 6.2a-d. There is
cell structure for the levitated portion of the experiment.
The cell structure (private and common flux combined) is
similar to the solutions proposed in Chapter IV, Fig. 4.1b,
col. 3. The observed cells are positive in the common flux
and negative in the private flux.
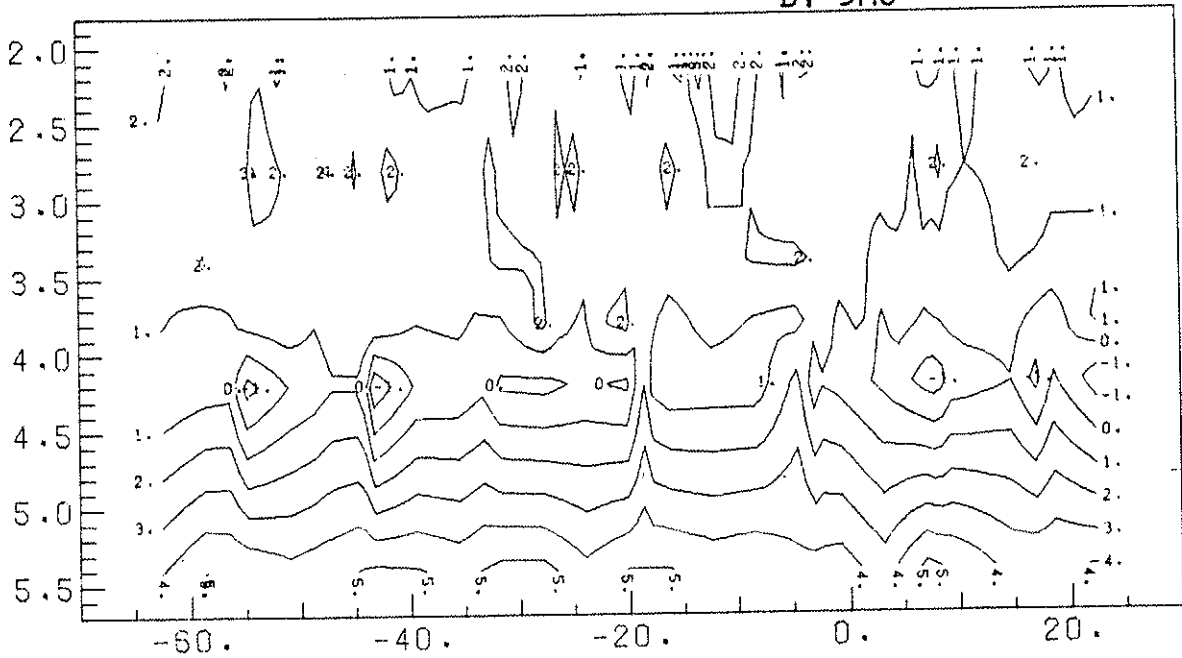
A. 3ms
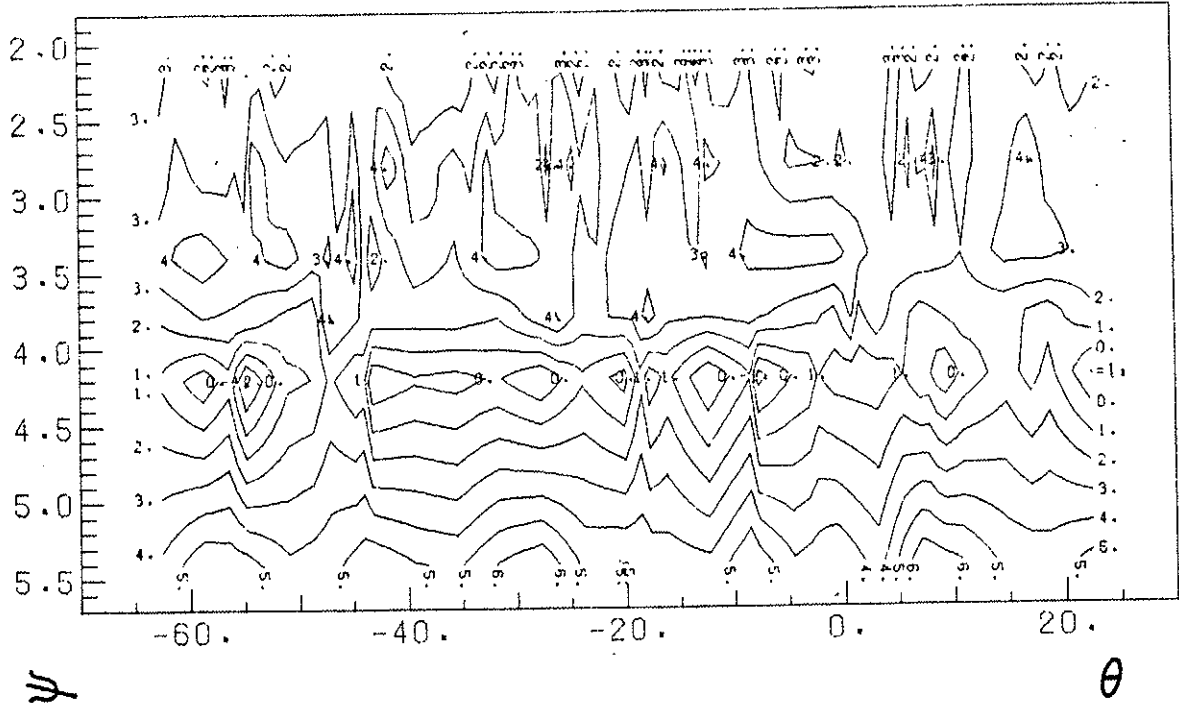
B. 5ms

Fig. 6.1a and b. Floating potential contours; levitated; collisionless H plasma; private flux of the LIH; $B_{P \ AVE}$=2KG (2.5KV); B_T=380G on axis.

c. 7MS

D. 10MS
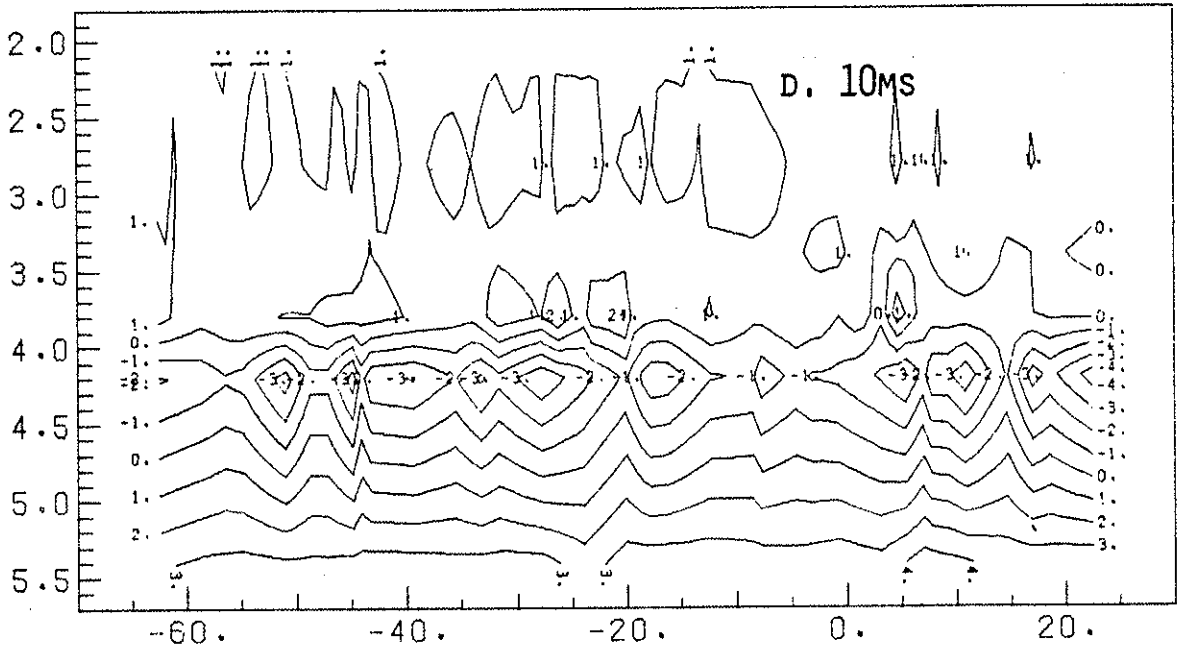
FIG. 6.1c AND D. FLOATING POTENTIAL CONTOURS; LEVITATED;
COLLISIONLESS H PLASMA; PRIVATE FLUX OF THE LIH;
$B_{P\ AVE}$=2KG (2.5KV); B_T=380G ON AXIS.
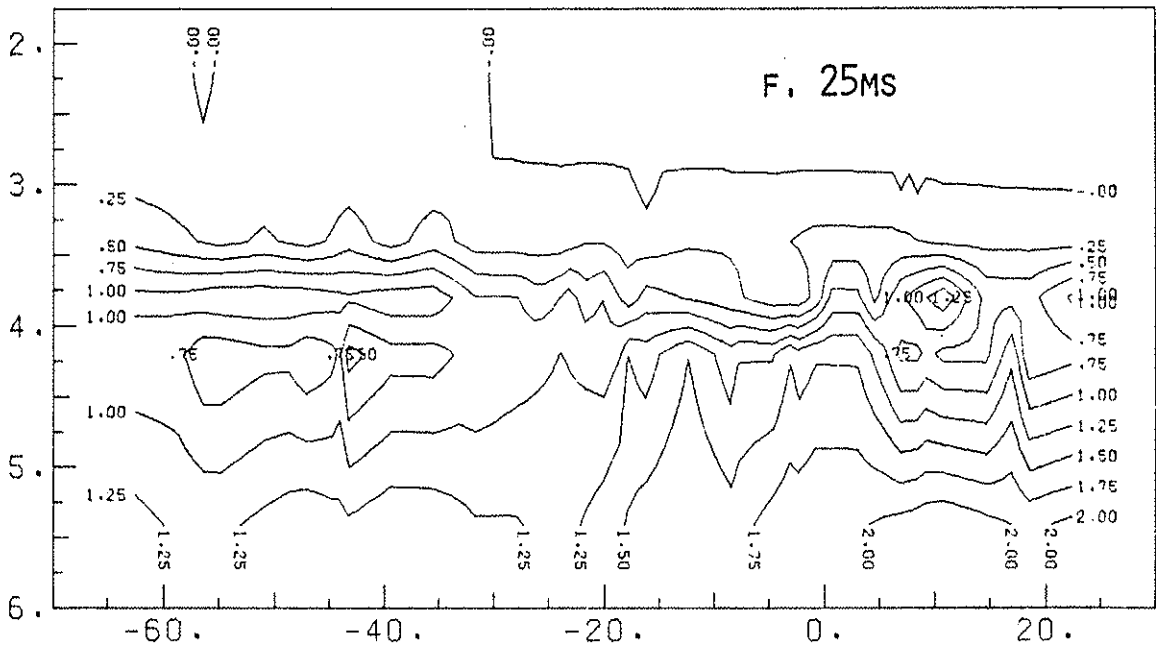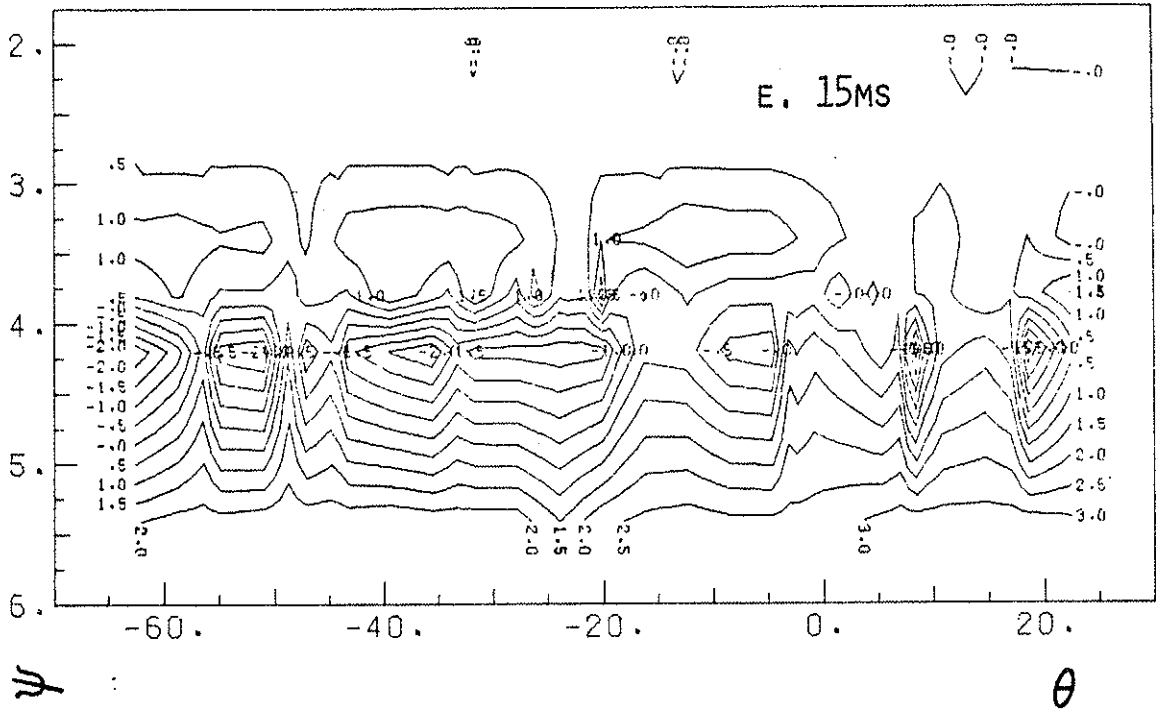
FIG. 6.1E AND F. FLOATING POTENTIAL CONTOURS; LEVITATED; COLLISIONLESS H PLASMA; PRIVATE FLUX OF THE LIH; $B_{P\ AVE}$=2KG (2.5KV); B_T=380G ON AXIS.
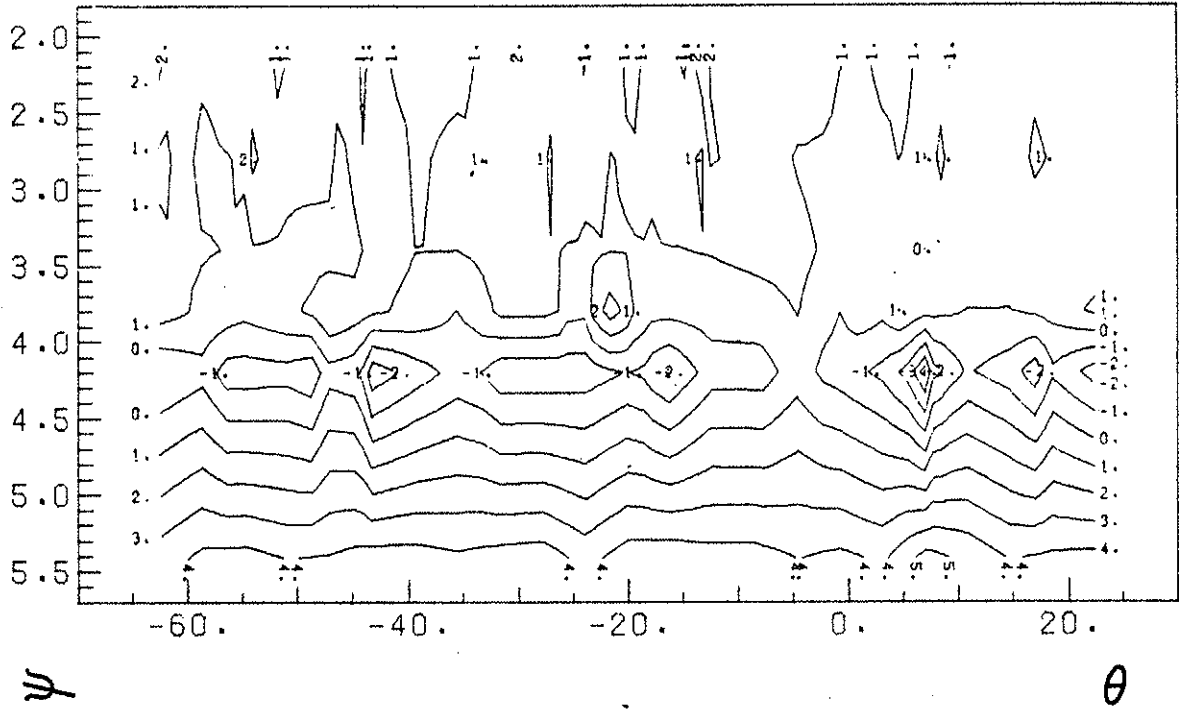
A. 3MS
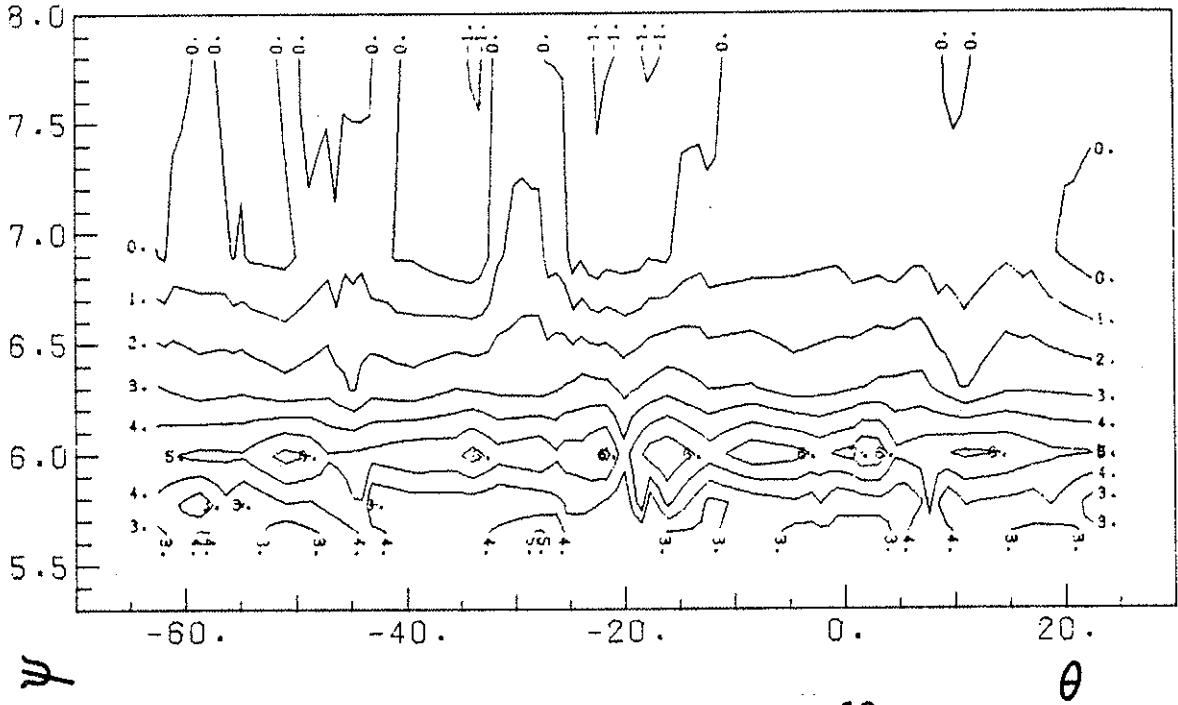
B. 10MS

FIG. 6.2A AND B. FLOATING POTENTIAL CONTOURS; LEVITATED;
COLLISIONLESS H PLASMA; COMMON FLUX - INNER NOSE;
$B_{P \; AVE}$=2KG (2.5KV); B_T=380G ON AXIS.

c. 15ms

d. 30ms
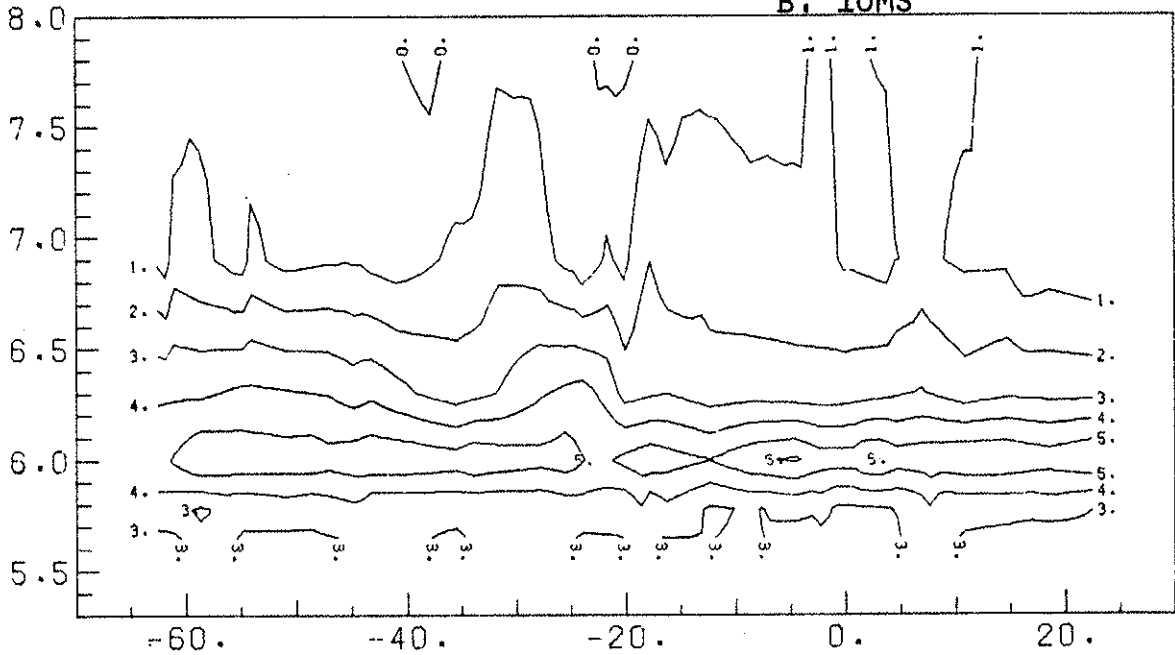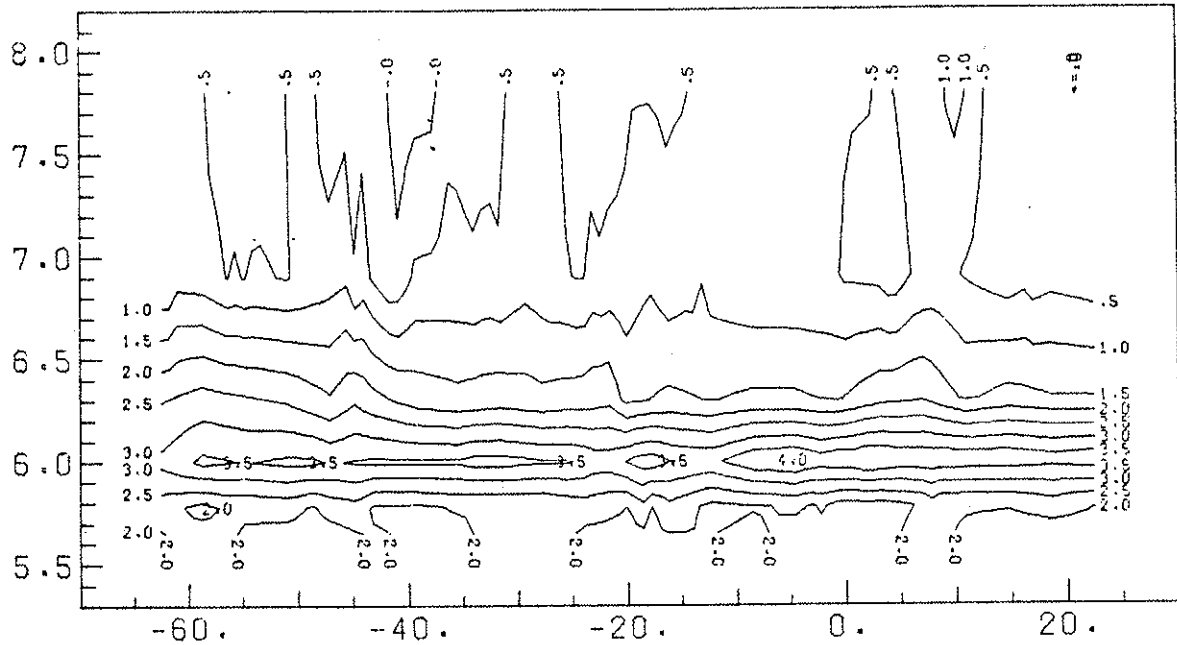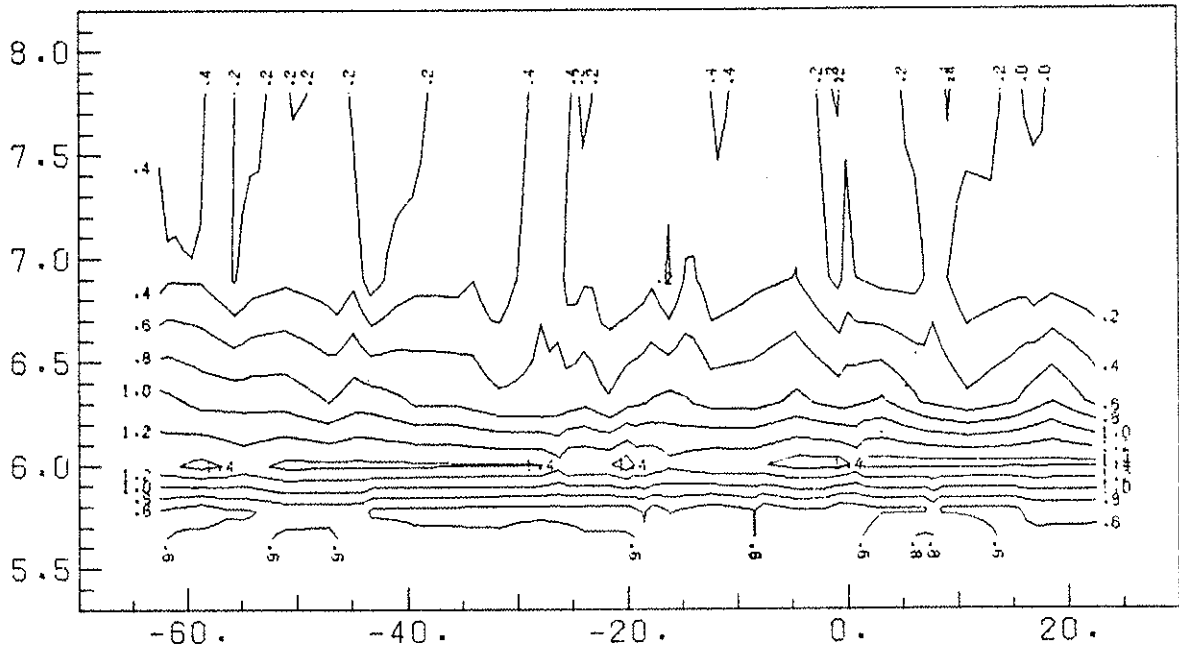
FIG. 6.2c AND D. FLOATING POTENTIAL CONTOURS; LEVITATED;
COLLISIONLESS H PLASMA; COMMON FLUX - INNER NOSE;
$B_{P\ AVE}$=2KG (2.5KV); B_T=380G ON AXIS.

B. Discussion. The data presented is consistent with what is expected if the potential structure is the source of D_v. Since the cart probe passes approximately through the trough of the lower inner hoop mirrors in both the private and common flux regions, we observe cells. We would expect the observed cell structure to be close to the maximum value for the ψ-surface, because it is measured at the bottom of the mirrors. Measurements[58] of the potential fluctuations on the LOH indicate a factor of two to five difference in the potential between the low- and high-field sides of the hoop, and we assume that the inner hoop is similar.

To calculate the power spectrum (and thus estimate T^*) we need to measure $\phi(\chi,\theta,\psi)$. We can't get this information from the contour plots, but we can show by a very rough estimate that the magnitude of T^* is much smaller than the value for this same plasma without a toroidal field.

From Fig. 6.1 the magnitude of $E(k,t)$ on the low-field side of the hoop is .5-1.0V/m, which is of the order of the potential structure for the case with no toroidal field. If E on the high-field side is a factor of 5 smaller than the low-field side, then E^2 will be smaller by a factor of 25 on the high-field side of the ring. Then T^*, which is the integral of E^2 over the volume of the plasma, would be between

$$400 = \frac{10^4 \text{eV}}{25} < T^* < 10^4 \text{eV}$$

where 10^4eV is the value for the same plasma without a toroidal field. Since part of the energy would be in modes with a $k_{//}$ (which do not contribute to $D_\perp$), we would expect

an even smaller T^* value as the enhanced temperature for the vortex modes with $k = 0$.

It is not possible to obtain the shape of the spectrum in θ from a partial scan, but it sould also be expected that the longest wavelength modes would be damped and that the cells would be smaller due to localized trapping. Since the long-wavelength modes contribute the most to D_v, this would also reduce the effective T^*.

We note that the contours show more structure towards the separatrix. This is consistent with what one would expect from a physical picture, since there is more trapping (and hence more structure) on the field line with the largest mirror ratio.

It is not possible to state, given this data, what the scaling of D is for this plasma; however, the information available from the contours is not inconsistent with a Kamimura-Dawson diffusion coefficient, and the rough estimate of T^* given indicates that the power spectrum has more energy than a thermal spectrum.

VI.2 COLLISIONAL PLASMA

With a toroidal field added to the poloidal field, the length of a field line increases, and excess charge can be shorted out as the field line connects regions of positive and negative charge. The collisional mean-free-path (for both species) is smaller than the length of the poloidal field mirrors; therefore we do not expect trapped particle effects[27] like those in the case of the collisionless

plasma. After the vortex spectrum is damped, we expect to see classical diffusion in this plasma; we would also expect to see very little potential structure in the contour plots.

The results of the diffision studies on the collisional plasma in a sheared magnetic field are reported in Ref. 59. The experiments were done for $B_{p \ ave}$=600G (poloidal bank voltage=1.5kV), and the results can be summarized as follows:

1) with a very small toroidal field (20G on axis), D scaled as the vortex diffusion coefficient.

2) with weak shear (75-100G) the diffusion in the plasma became classical even in the presence of large density fluctuations ($\delta n/n \sim 20\%$).

A. <u>Experimental Observations</u>. For this plasma it has been shown[51] that plasma losses and diffusion are not changed by the presence or absence of supports. Therefore, the two experiments to be discussed were made with the hoops supported to minimize wear on the levators.

1. <u>Inner hoop</u>. The first set of data consisted of floating potential scans of 5 psi-surfaces, taken in the private flux of the lower inner ring. The scans covered about a quarter of the machine, including the poloidal field gap. The poloidal field bank voltage was 1.5kV ($B_{p \ ave} \sim 1.2kG$). Scans were made for B_t=20G and 100G (on axis).

For the first case, B_t=20G on axis and cells are present for all times. The potential structure has its

steepest gradients in the region closest to the ring
(Fig. 6.3a-d); the separatrix region has less structure.

With B_t=100G on axis, Fig. 6.4a-d, the structure
becomes much flatter; the steepest gradients in the poten-
tial are still located nearest the rings, but the variations
in the azimuthal direction, which give rise to the cross-
field diffusion, are very much smaller than with B_t=20G.

2. <u>Outer hoop</u>. The data consists of a full scan
(360°) of a single psi-surface ($\psi \sim 3.4$) on the lower outer
hoop for $B_{p\ ave}$=600G (1.5kV on the poloidal bank), with and
without B_t=100G. This psi-surface is in the private flux
between the ring ($\psi \sim 2.4$) and the separatrix ($\psi \sim 5.6$).

Fig. 6.5 and Fig. 5.5 show the electric field power
spectrum obtained from the azimuthal gradient of the
floating potential, with $B_{p\ ave}$=600G, with and without
B_t=100G, respectively. The power spectrum vs. toroidal
mode number is shown at 5ms, 10ms, and 15ms, after injection.
(The B_p-only data is discussed in Chapter V.) The spectra
are quite noisy, but we can make a few qualitative state-
ments about them. A comparison of the spectra shows that
both decrease in time. At any given time, E^2(k) is a
decreasing function of k, and E(t) for a given mode k is
smaller with a toroidal field than without one. The B_p+B_t
data lacks the "bump" on the spectrum (at $k \sim 20$-30) present
in the B_p data, and decreases more rapidly as a function of
k. Overall, the shapes of the spectra are somewhat diffe-
rent, with the B_p data proportional to $1/k^2$, and the B_p+B_t
spectrum more closely proportional to $1/k$. (These estimates
are by eye only, not by curve-fitting techniques.)

FIG. 6.3A AND B. FLOATING POTENTIAL CONTOURS; SUPPORTED;
COLLISIONAL HE PLASMA; PRIVATE FLUX OF THE LIH;
$B_{P AVE}$=1.2KG (1.5KV); B_T=20G ON AXIS (20V).

c. 10ms

d. 15ms

Fig. 6.3c and d. Floating potential contours; supported;
collisional He plasma; private flux of the LIH;
$B_{P \text{ AVE}}$=1.2KG (1.5KV); B_T=20G on axis (20V).
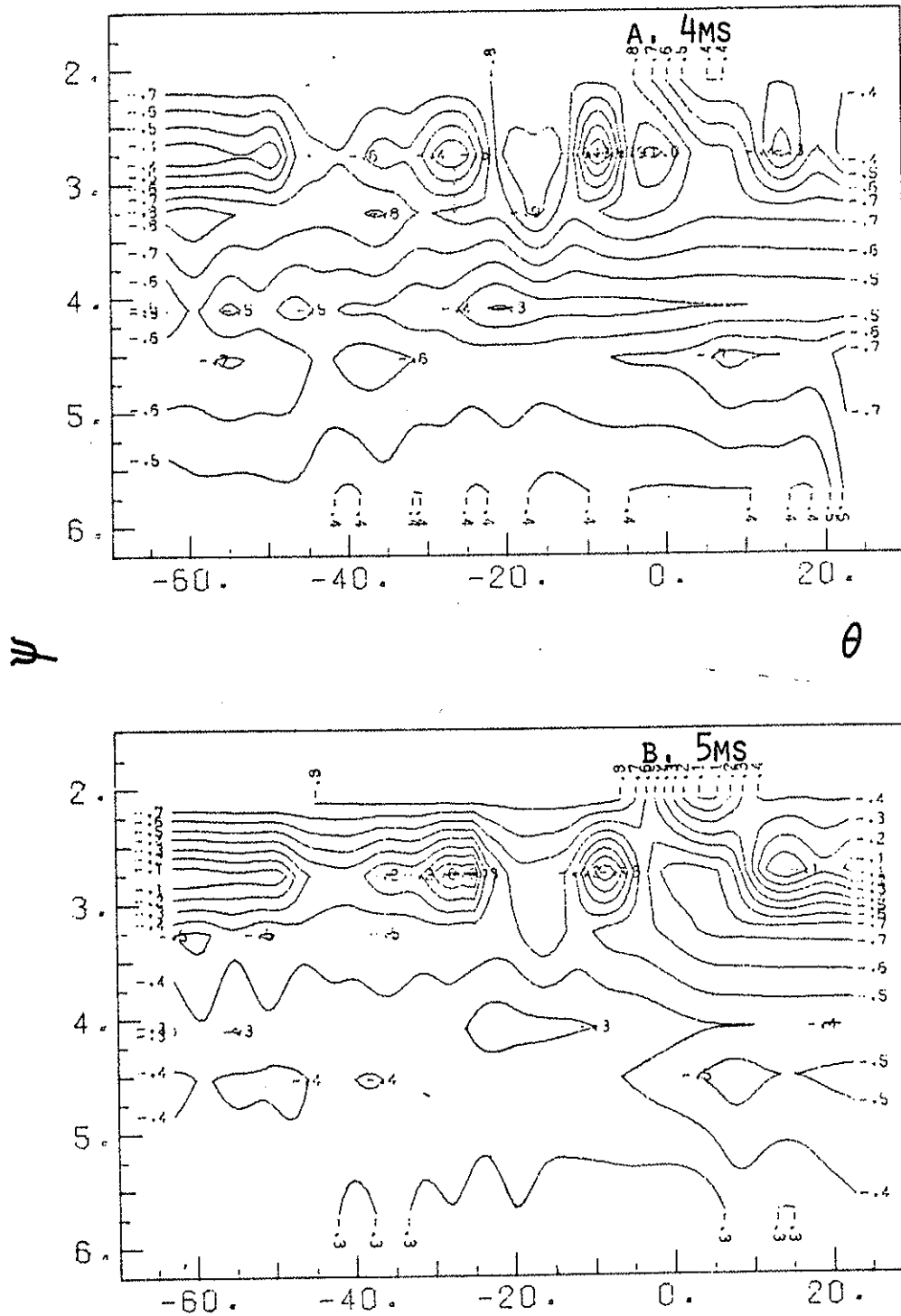
A. 4MS

θ

B. 5MS

FIG. 6.4A AND B. FLOATING POTENTIAL CONTOURS; SUPPORTED;
COLLISIONAL HE PLASMA; PRIVATE FLUX OF THE LIH;
$B_{P\ AVE}$=1.2KG (1.5KV); B_T=100G ON AXIS (100V).
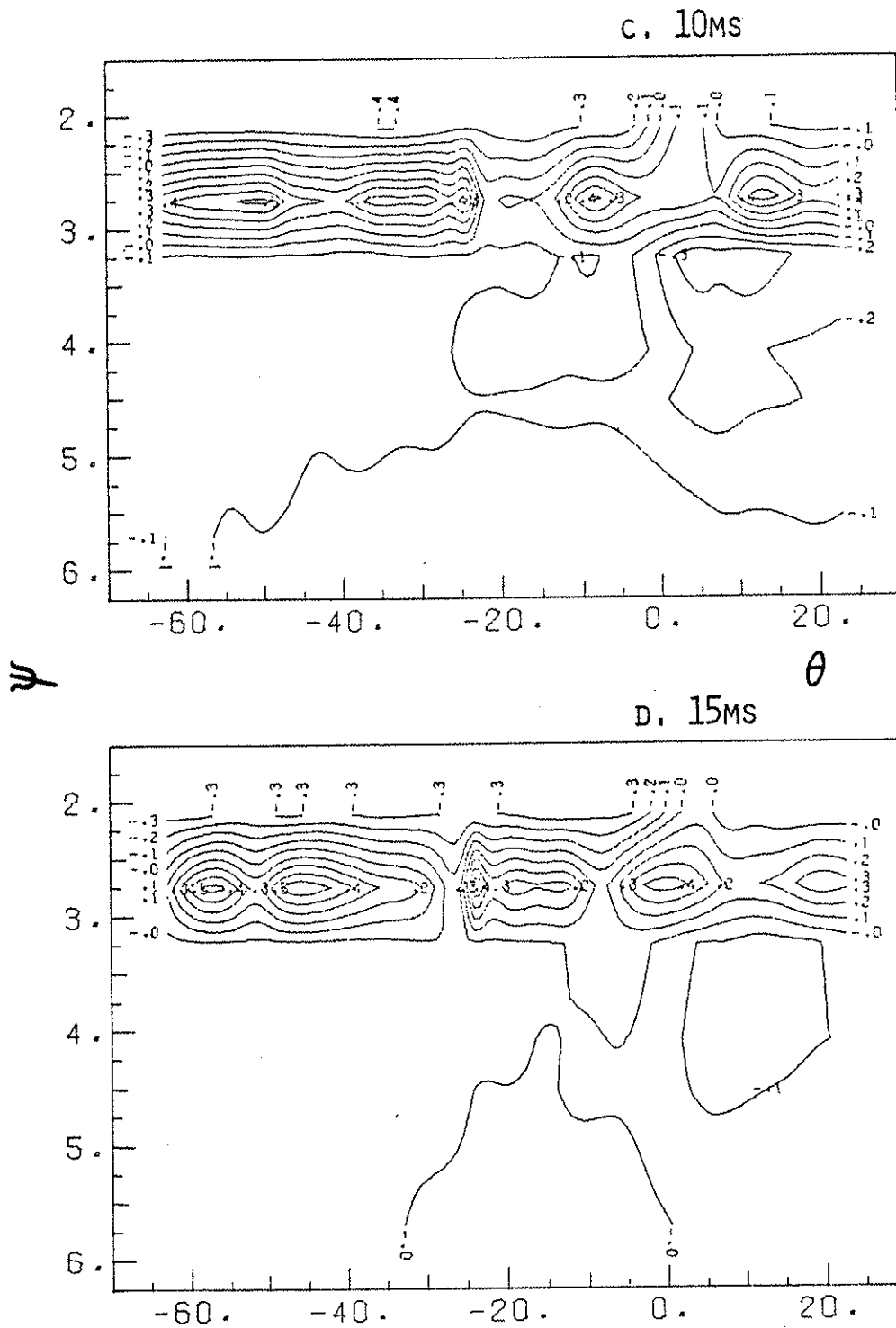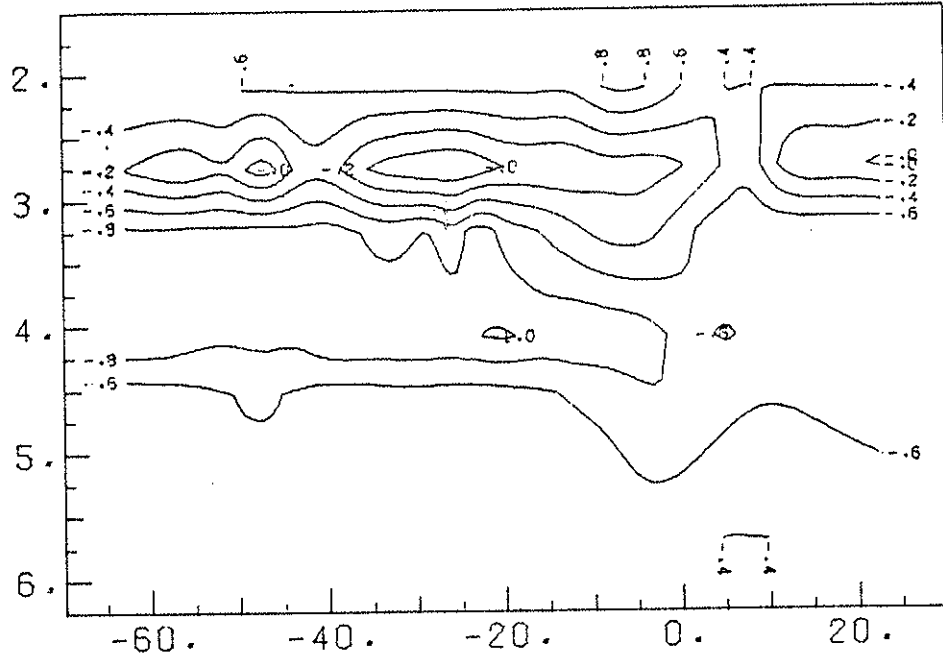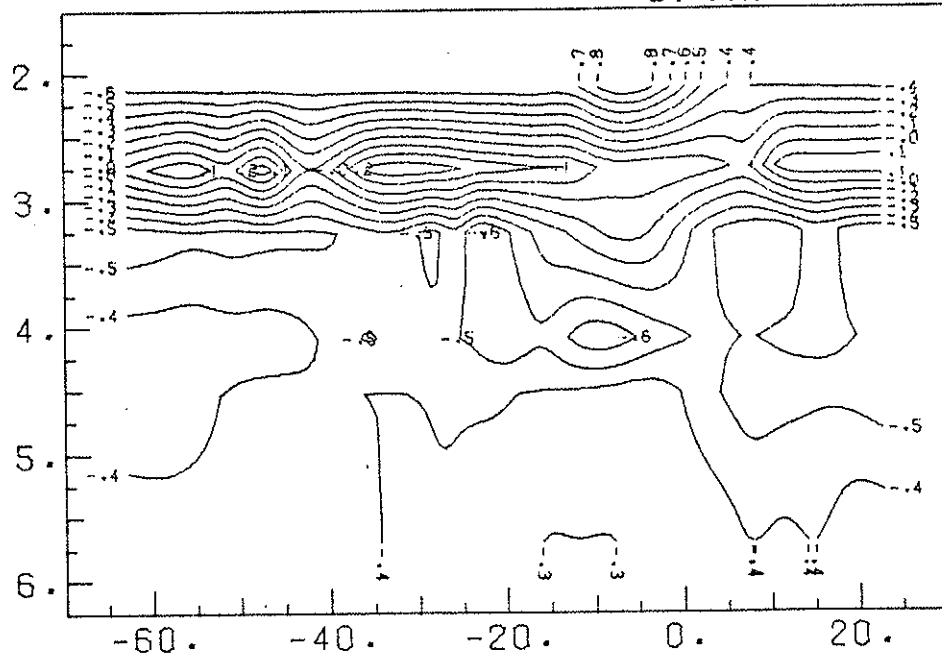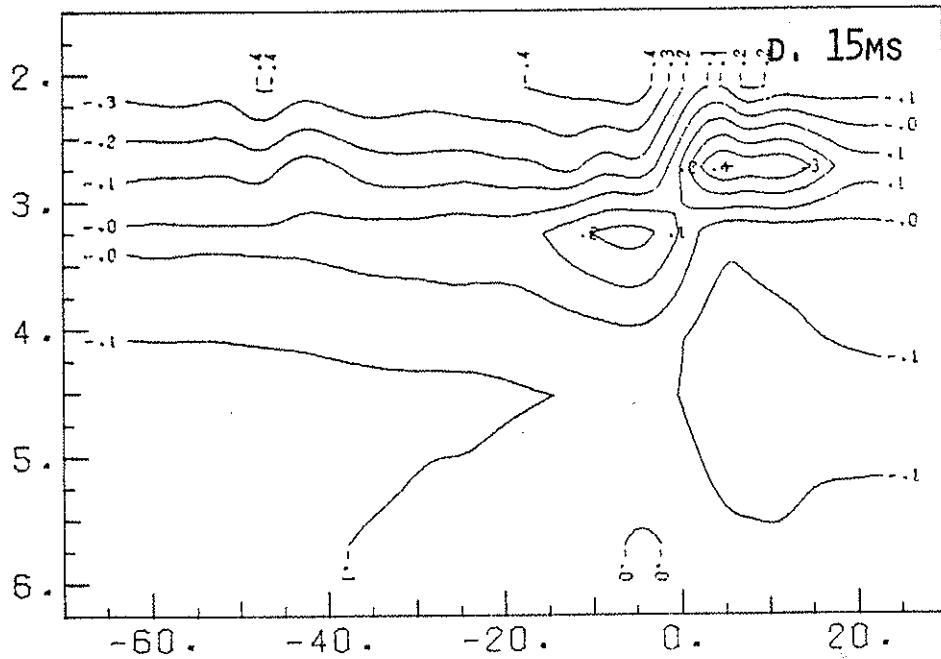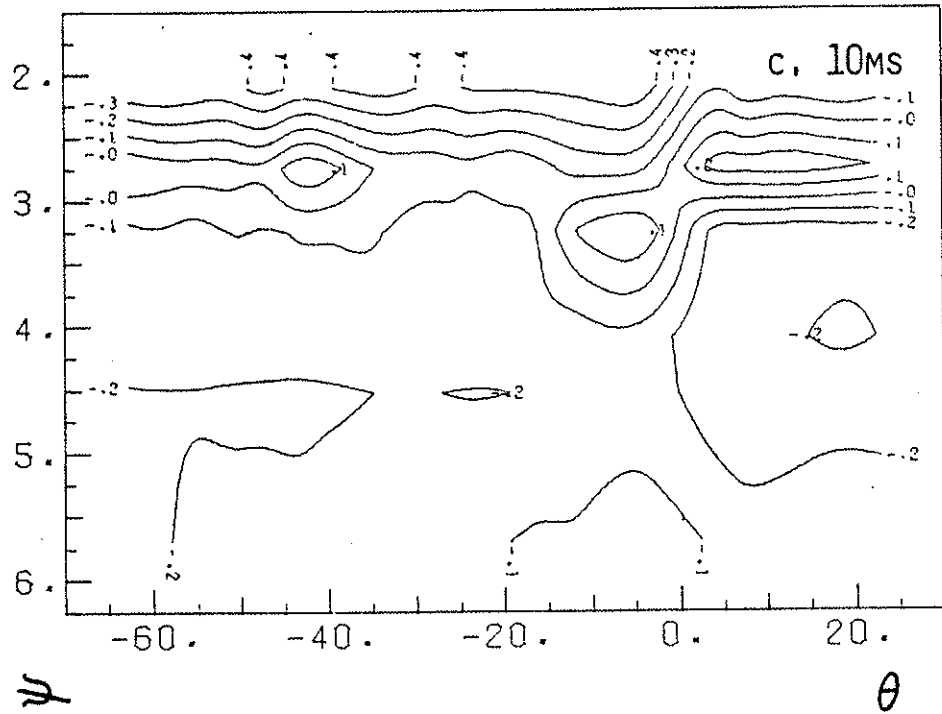
FIG. 6.4c AND D. FLOATING POTENTIAL CONTOURS; SUPPORTED;
COLLISIONAL HE PLASMA; PRIVATE FLUX OF THE LIH;
B_P AVE=1.2KG (1.5KV); B_T=100G ON AXIS (100V).
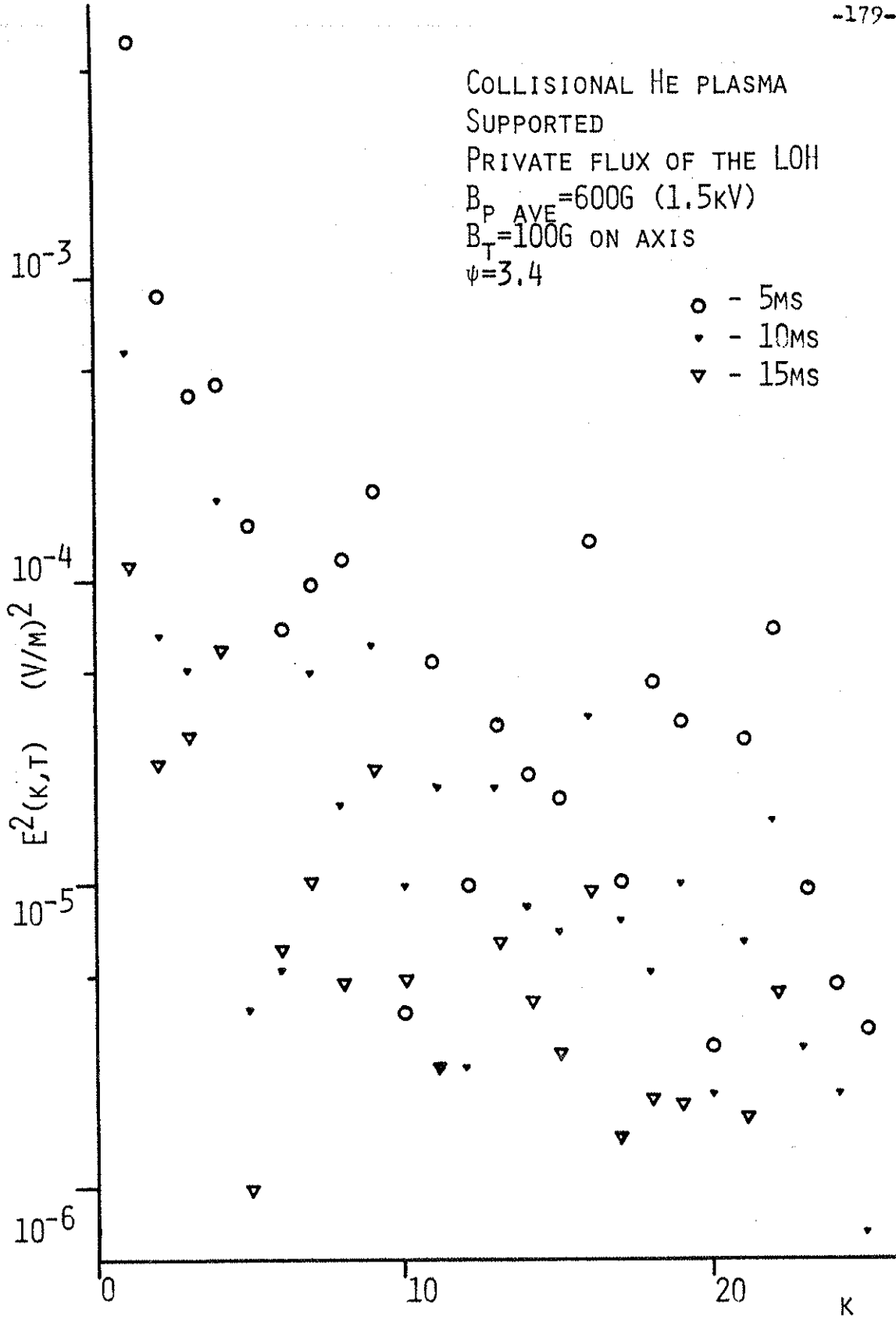
FIG. 6.5 TOROIDAL ELECTRIC FIELD SPECTRUM

Fig. 6.6 shows the time decay of the power spectra summed over all the modes. This figure compares the data with and without a toroidal field on the same scale. We note two things in particular. During the early times, the total energy is smaller with an added toroidal field by an order of magnitude. It is also decaying faster: at 10 ms after injection, $\tau \sim 2$ms with a toroidal field, and 4.5ms without one. At later times, however, the toroidal field data decreases more slowly than the poloidal field data, although the total energy in the poloidal field spectrum still remains larger by an order of magnitude at 50ms after injection.

Data for individual modes is plotted in Figs. 6.7 and 5.21, which show the time decay with and without B_t, for m=1, 2, 3, and 10. Time decays at 10ms after injection (τ_E and $\tau_E 2$) are summarized in Table VI.I for several toroidal mode numbers, and τ_E is plotted as a function of k in Fig. 6.8. With the toroidal field the longest-wavelength modes damp very quickly ($\tau_E \sim 1$–2ms) for about the first 10-15ms of the experiment.

B. Discussion

    1. Inner hoop contours. The diffusion measurements[59] on this plasma indicate that with very weak shear (B_t=20G) the diffusion is essentially the same as without a toroidal field; with a larger amount of shear the diffusion becomes classical. Thus we would expect to observe cell structure for the first case, and to see either flat contours, or damping cells, for the second. The cell plots with B_t=20G on axis agree with this expectation: a large
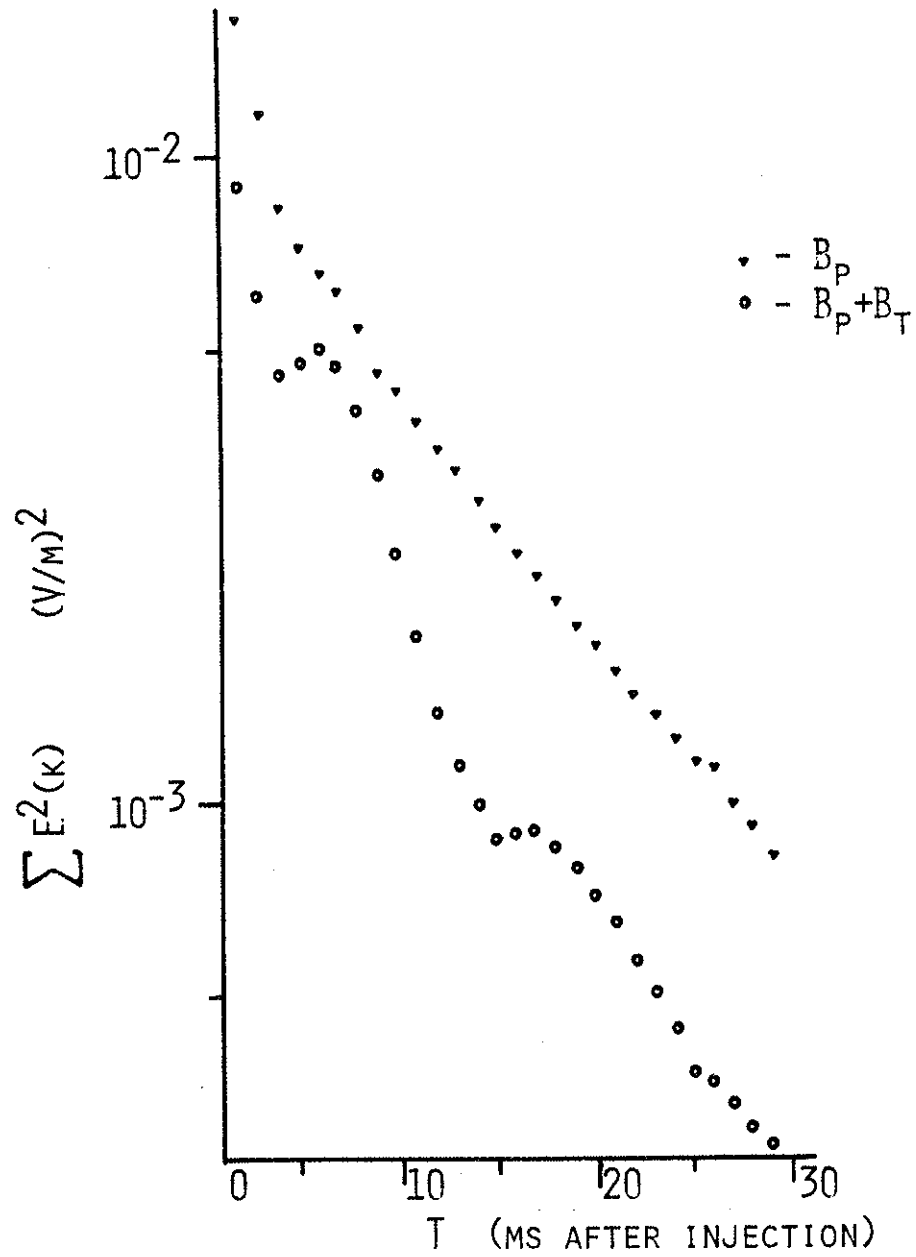
FIG. 6.6 DECAY OF ENERGY IN TOROIDAL ELECTRIC FIELD;
COLLISIONAL HE PLASMA; SUPPORTED; PRIVATE FLUX
OF THE LOH; $B_{P \; AVE}$=600G (1.5KV); B_T=100G ON AXIS;
ψ=3.4.

COLLISIONAL HE PLASMA
SUPPORTED
PRIVATE FLUX - LOH
$\psi=3.4$
$B_{P\ AVE}=600G$ (1.5KV)
$B_{T}=100G$ ON AXIS (100V)

○ – $\kappa=1$
△ – $\kappa=2$
▸ – $\kappa=3$
◇ – $\kappa=10$
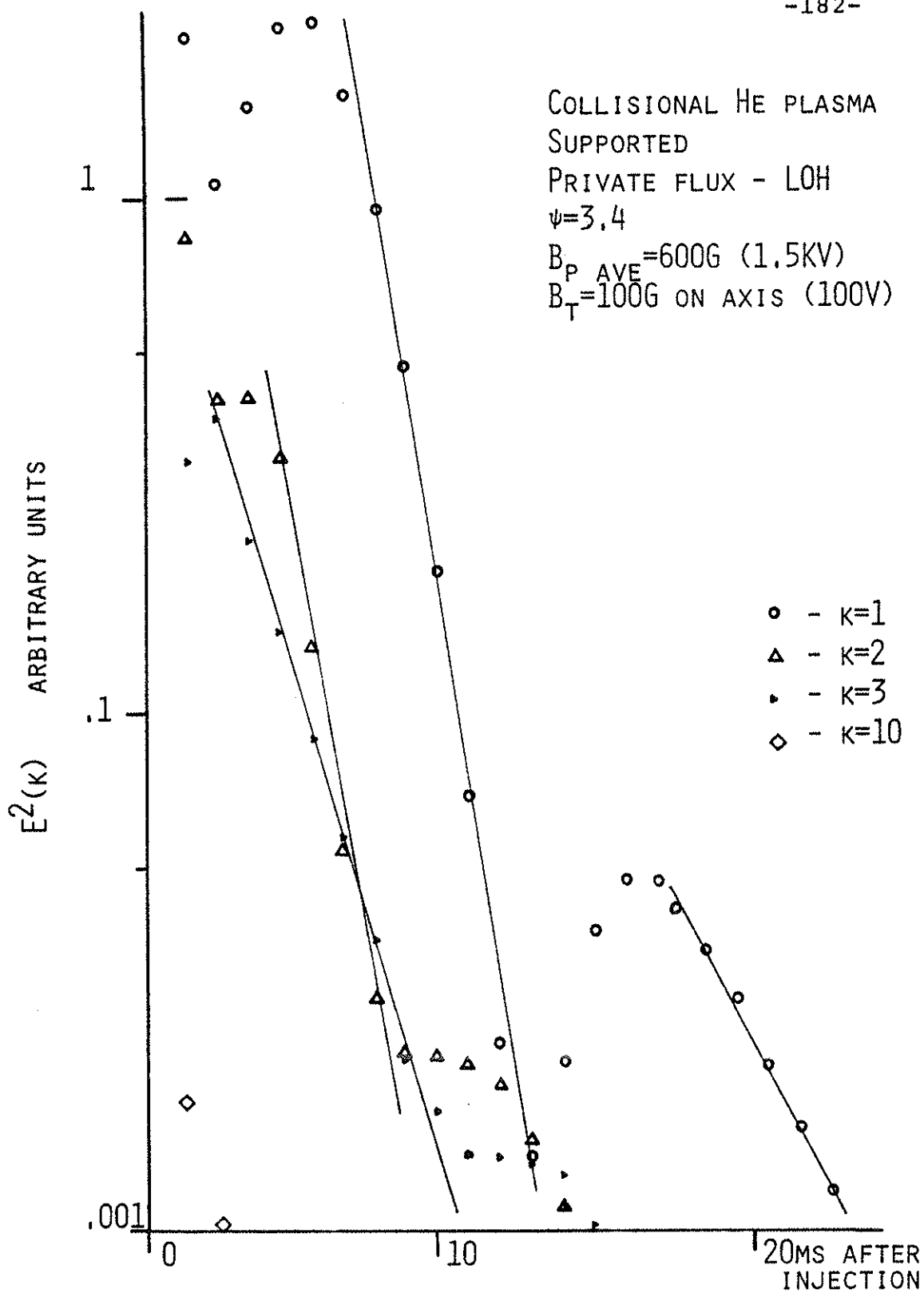
FIG. 6.7 TIME DECAY OF INDIVIDUAL MODES, $B_P + B_T$.

Table VI.1

k	B_p		$B_p + B_t$	
	τ_E^2	τ_E	τ_E^2	τ_E
1	6.5	13	1	2
2	4	8	1.5	3
3	4.5	9	2	4
10	3	6	5	10
15	3	6	4	8
20	4	8	3	6
$\sum_k E^2(k)$	4.5		2	

Table VI.1   Decay times (in msec) for toroidal electric
field modes; collisional He plasma; supported;
private flux of the lower outer hoop;
10msec after injection; $B_{p\ ave}$=600G (1.5kV);
B_t=100G on axis.
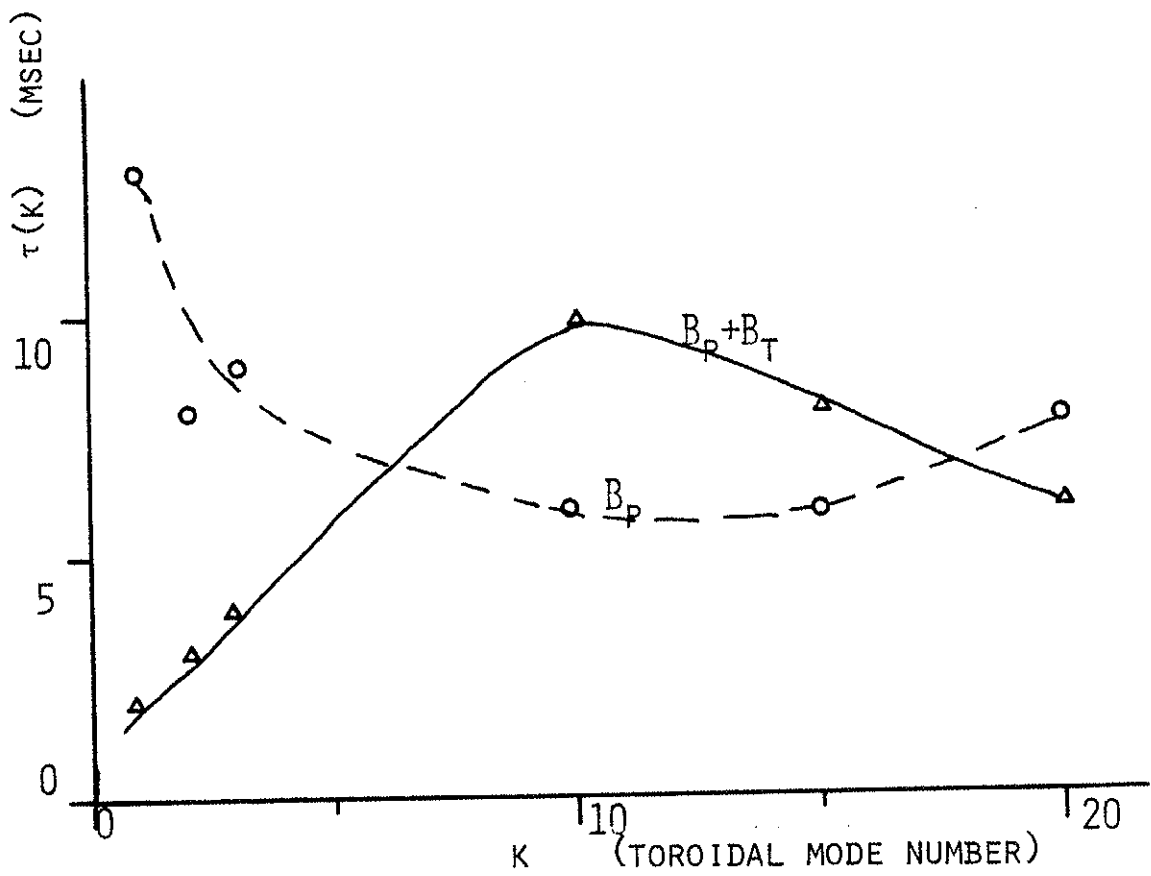
FIG. 6.8 $\tau(K)$ VS. K AT 10MS AFTER INJECTION; COLLISIONAL
HE PLASMA; SUPPORTED; PRIVATE FLUX — LOH;
$B_{P\ AVE}$=600G (1.5KV); B_T=100G ON AXIS.

amount of vortex structure is present in the inner hoop contours (Fig. 6.3a-d), and the cells persist in time.

The LIH contours taken with B_t=100G have much less structure, and the cells damp quickly. However, comparison with the classical contours in Chapter V (Fig. 5.16) shows that the latter have somewhat less structure. Although 100G was enough to damp the vortex structure on the lower outer hoop[59], it seems likely that more would be required on the inner hoop which has a higher average poloidal field ($B_{p\ ave}$∿1.2kG vs 600G). It is not known whether the relationship is linear (so that it would require the same ratio B_t/B_p to damp the vortex structure).

We have discussed two ways of obtaining a plasma where classical diffusion is the dominant diffusion mechanism. With a purely poloidal field, the vortex spectrum is damped by collisional ion viscosity if the field is small enough ($\mu\propto1/B^2$); lowering B_p increases μ most near the rings. When a toroidal field is added, however, shear is strongest near ψ_s, and we would expect to see the vortex spectrum damp first in the separatrix volume.

We have noted that for both B_p and B_p+B_t, the cell structure is flattest near ψ_s. Part of this effect is the dielectric screening of the electric fields which is strongest in the separatrix region, but it seems to be more pronounced an effect with a toroidal field. This may be due to the different ψ-dependence of the two damping mechanisms.

2. Outer hoop; single ψ-surface. The effect of the toroidal field (B_t=100G on axis) is very clear:

first, the long wavelength modes are damped very quickly.
We would expect this from a physical point of view, since
a long-range order is required to maintain the largest
cells. And since it has been shown that the longest
wavelengths cause the most damage to containment, this
preferential damping is the reason why a small amount of
shear makes a large change in the diffusion, even if the
vortex spectrum is not completely damped out. Second, the
total energy in the spectrum, $\Sigma E^2(k,t)$, also decreases by
the addition of a toroidal field, as shown in Fig. 6.6.
Both these effects will reduce the vortex diffusion coeffi-
cient calculated from the spectrum.

D_V was calculated from this data for a purely poloidal
field in Chapter V. With an added toroidal field, we can
estimate D_V is we assume that the spectrum measured at one
value of χ (with $\Delta\theta=2\pi$) is an approximation to the spectrum
on the whole ψ-surface. To justify this approximation, the
spectrum would have to be measured at several values of χ;
this cannot be done with the cart.

The diffusion coefficient obtained using this assump-
tion has been plotted in Fig. 6.9 along with D_V calculated
for the same plasma without a toroidal field. The magnitude
of D_V is observed to decrease by a factor of 3-4 when B_t is
added, to $\sim 500 cm^2/sec$.

The diffusion study results showed that, for this
plasma, the diffusion becomes classical when a toroidal
field of 100G is added to the 600G average poloidal field.
The classical diffusion coefficient is $\sim 500 cm^2/sec$ (using
$n=5\times 10^{11} cm^{-3}$), which is of the same order as D_V estimated
from the $B_p + B_t$ data. It can't be stated conclusively from
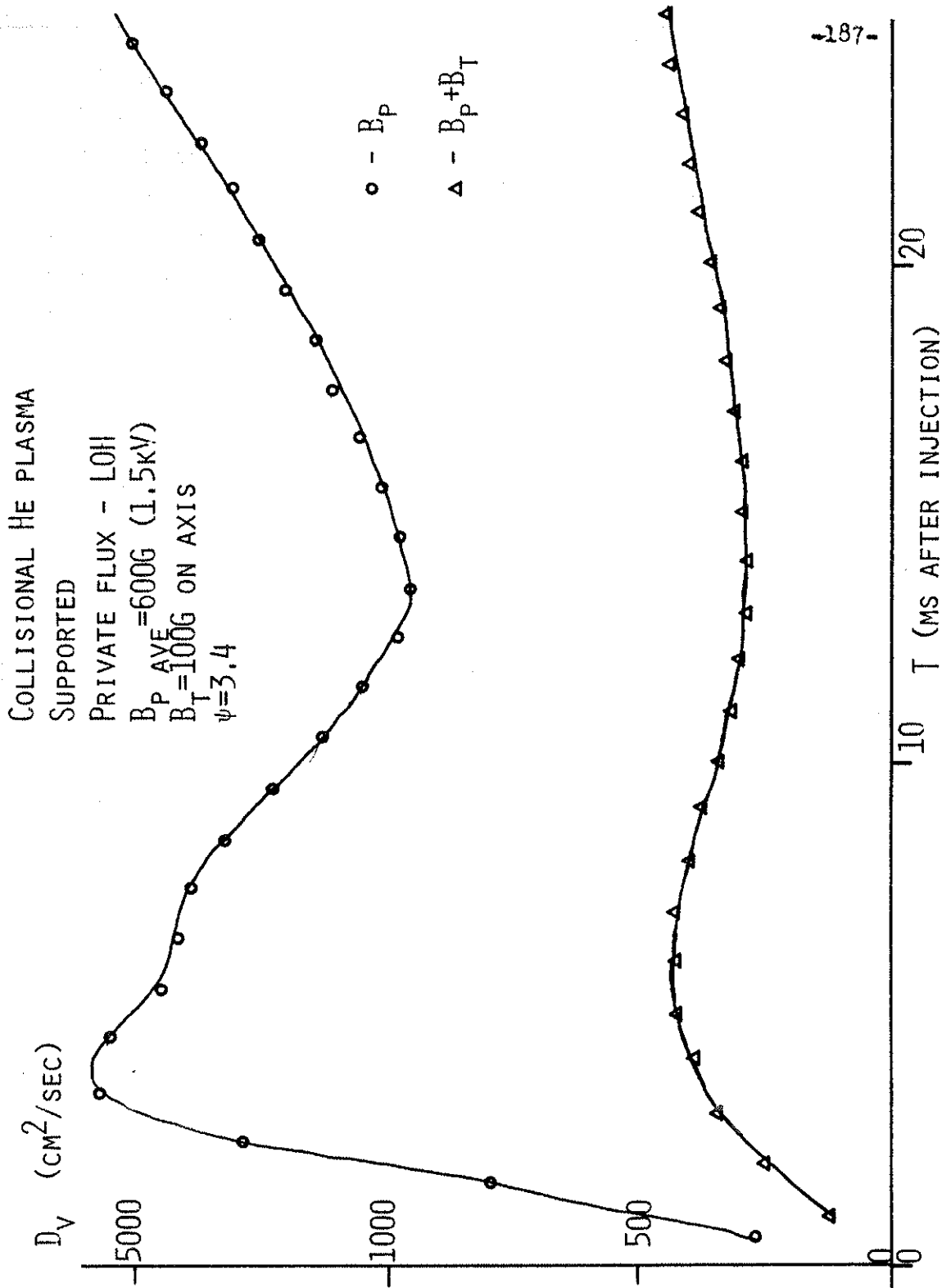
FIG. 6.9 VORTEX DIFFUSION COEFFICIENT VS. TIME;
POLOIDAL FIELD WITH AND WITHOUT ADDED TOROIDAL
FIELD; COLLISIONAL HE PLASMA; SUPPORTED; LOH.

this scan that the magnitude of D_v is reduced to less than
the magnitude of D_{cl} when a toroidal field is added; how-
ever, the trend is definitely in the expected direction: B_t
reduces the vortex spectrum, and long-wavelength modes are
preferentially damped. In addition it is known[62] that with
an added toroidal field, collisional diffusion in this
plasma at early times includes higher-order modes (the nor-
mal mode[25,26] is reached in 9ms vs. <3ms for a purely
poloidal field). These modes have higher fluxes than the
normal mode, so that it is possible that the flux from the
collisional modes is larger than that from the vortex
modes.

We conclude that this data is consistent with the
interpretation that the potential structure is the source
of vortex diffusion in the Octupole. It must be clearly
understood that this is an order-of-magnitude calculation
and it depends on using a method developed for two dimen-
sions in a three-dimensional situation.

CHAPTER VII - CONCLUSION

VII.1   EXPERIMENTAL RESULTS

The first objective of this thesis has been accomplished: Potential contours have been plotted for a wide range of Octupole parameters using two different plasmas. In addition, toroidal spectra have been presented (for 360^0 scans), as a function of time and toroidal mode number.

The second objective was to investigate the relationship between the cells and vortex diffusion in the Octupole. There is a strong correlation: Cells are present when the diffusion (calculated from the profile evolution and collector measurements) scales as D_v, and much reduced in amplitude when $D_v < D_{cl}$. The toroidal spectra have been used to estimate D_v and T^* from the potential structure, and the results agree reasonably well with the results of the diffusion studies[25,26]. Discrepancies will be discussed later.

The physical model that emerges from the theory and the data is as follows. The initial injection process creates a plasma with a large amount of energy (from charge separation) in turbulent vortex modes. During the first few milliseconds, this initial, non-reproducible distribution evolves into a reproducible structure with the energy concentrated at the longest wavelengths. The spectrum then retains this shape, and decays on a much longer time scale than the one required to produce the long-wavelength distribution. Diffusion is caused by the vortex modes when the electric fields become uncorrelated. The magnitude of

D_v depends on both the magnitude of the electric fields, and the correlation times.

This interpretation also accounts for the enhanced magnitude of D_v obtained in the diffusion studies over the Okuda-Dawson diffusion coefficient, while preserving the scaling. There is then no need to postulate complicated local models to show how convective cells may account for plasma losses. However, there are several discrepancies which must be taken care of before we can state unequivocally that the electric field vortex structure is the sole source of the diffusion. The remainder of this section is dedicated to examining these discrepancies.

A possible discrepancy was noted for the collisionless plasma injected into a fully levitated Octupole. The potential contours were much flatter for the levitated case than for the supported case. However, without a full scan it is impossible to determine whether the longest-wavelength modes are similar in both cases. This would be expected, as T^* is the same for both[25,15]. This case should be examined in more detail, and a full scan taken as discussed in the next section, with the Octupole levitated and supported. If the vortex interpretation is correct, both cases will have similar spectra, except that the spectrum for the levitated case will lack the bump at $m \sim 30$.

A more important discrepancy arose in connection with the collisional plasma in a supported Octupole. The vortex diffusion coefficient is independent of B over the range in which $\epsilon \gg 1$. This scaling was confirmed experimentally for the profile evolution in the Octupole[26]. The initial particle density in the machine varies by only

a factor ~ 2 in the magnetic field ranges studied. There-
fore, if

$$D_v \propto \sqrt{\sum \frac{E^2}{k^2 B^2}} = \sqrt{\sum \frac{\phi^2}{B^2}}$$

then for different values of B (but constant $D=D_v$) the re-
lationship

$$\frac{\phi^2}{B^2} \sim \text{constant}$$

should be maintained. That is, on the average, if B de-
creases by a factor of 4 we would expect $\sqrt{\Sigma \phi(k)^2}$ to de-
crease by the same factor.

In the experiment referred to in Section V.2A, a scan
was taken of a single ψ-surface in the LOH private flux for
the collisional plasma, at 1.5kV on the poloidal bank ($D=D_v$
from the diffusion studies; $B_{ave}=600G$), and 250V ($D=D_{cl}$,
$B_{ave}=100G$). Although the magnitude of the electric field
spectrum decreased when the magnetic field was reduced, the
ratio of E/B increased, and D_v calculated from the spectrum
increased. $D_{cl}(\propto 1/B^2)$ also increased, but it was still
smaller than D_v. This case should also be examined experi-
mentally in more detail, as the observation that D_v in-
creases is based on a scan of a single ψ-surface.

VII.2   RECOMMENDATIONS FOR FURTHER WORK

The general correlation of vortices with vortex diffu-
sion is strong. However, although the potential structure
has been mapped for many different cases, the information
about some of these cases is incomplete. We will discuss
here some improvements to the method used to take data,

and recommend a series of experiments which should shed more
light on the questions which arose during the writing of
this thesis.

A.   Method improvements.   The preferred data set for a
given case would include a 360° scan of several ψ-surfaces.
Since it has been shown that the toroidal electric field
spectrum is a decreasing function of the toroidal mode num-
ber, and that the first 10-20 modes are the most important,
it is suggested that scans cover the 360° in θ by taking
data at 40 equispaced azimuthal points.   The cart is limi-
ted to carrying four signal cables by its construction.
Without major changes to the cart, a large improvement
would be accomplished by using the four probe tips to mea-
sure the potential on four ψ-surfaces in the private flux
simultaneously.   This requires construction of a probe such
as the one illustrated in Fig. 7.1.

This type of specialized probe would be useful only in
a limited region (note that at position B the probe tips are
practically all on the same ψ-surface).   However, it may be
possible, by careful placement of the four tips, to find
another position α', such that two scans in θ would produce
eight ψ-surfaces reasonably well spaced, and provide more
information about the potential as a function of ψ.   A probe
like this would have to be carefully constructed and cali-
brated, but would quadruple the data-taking rate for the
LOH private flux, allowing experiments to be accomplished
before operating parameters drift, or making it possible
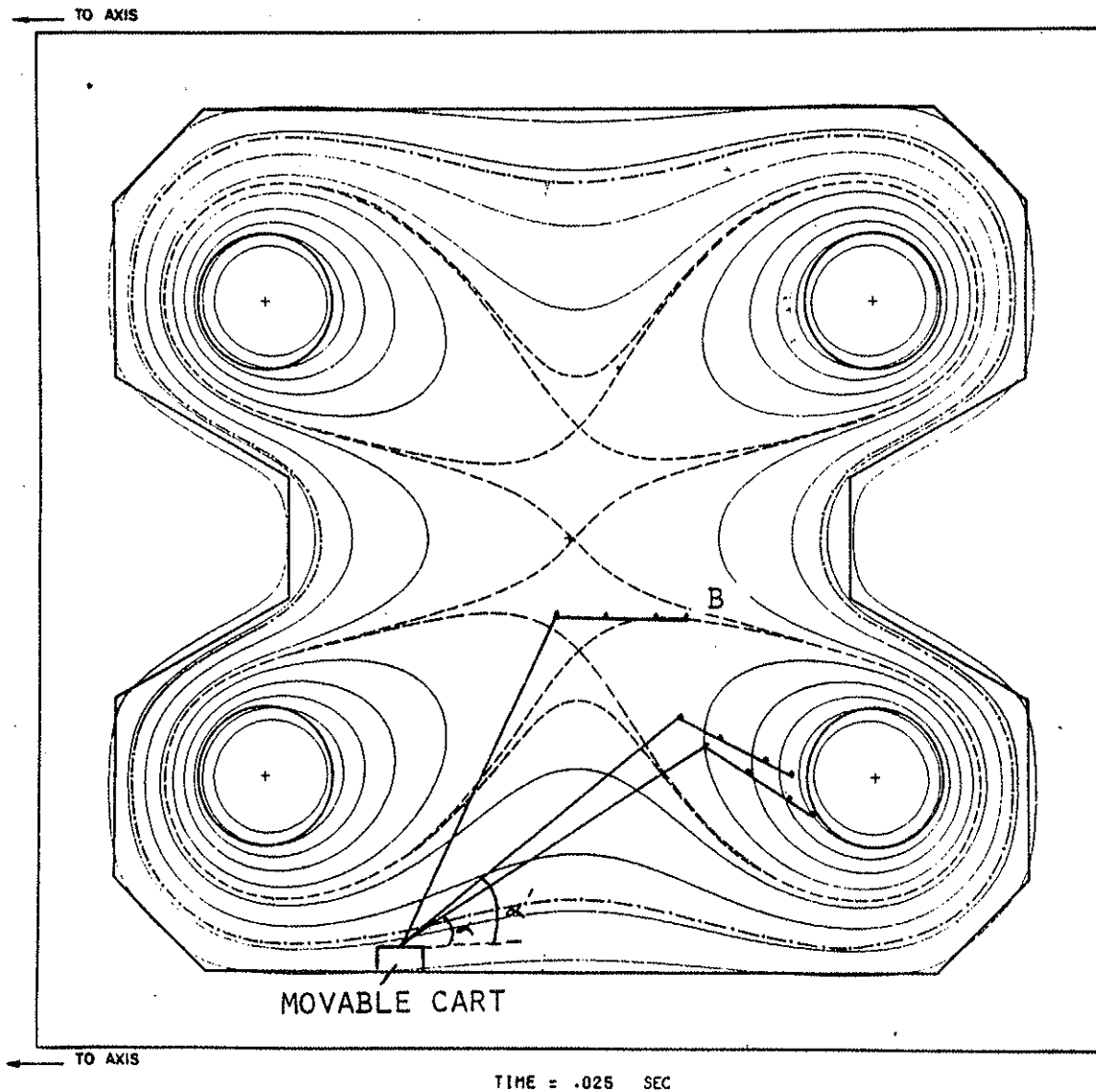to examine full scans for cases with different parameters
on the same day.

FIG. 7.1 PROPOSED CART PROBE, WITH TIPS PLACED SO AS TO
MEASURE V_F ON FOUR ψ-SURFACES IN THE PRIVATE
FLUX OF THE LOH SIMULTANEOUSLY.
AT B, ALL FOUR TIPS ARE APPROXIMATELY AT THE
SAME VALUE OF ψ.
WITH THE PROBE AT THE ANGLE α, THE TIPS ARE ON
$\psi \cong$ 2, 3, 4.3, AND 5.
AT α', $\psi \cong$ 2.5, 3.7, 4.8, AND 5.3.

For direct comparison with profile evolution results,
it is also recommended that density profile scans be taken
simultaneously. Any efforts that result in more reprodu-
cible plasmas will also increase the number of cases that
can be examined, by decreasing the number of rejected shots.

The model developed in Chapters III and IV is a very
simple one. Extensions to the theory are necessary to in-
clude factors such as density gradients, curved field lines,
and non-rectangular geometries. It is also necessary to
produce a set of fully two-dimensional equations, and exa-
mine the terms which were neglected in Section IV.6. Much
work remains to be done on the subject of electric field
correlations in the Octupole, and a comparison with Taylor
and McNamara's assumption of a jointly-normal distribution.

Solution of the $\sinh\Psi$ equation on an annulus, rather
than a rectangular box, would be relatively simple, and
could lend weight to the Octupole fluid solutions proposed
in Chapter IV.

B. _Further experiments_. More detailed scaling infor-
mation could be obtained by examining potential contours
(full scans) in the LOH private flux for the collisional
plasma in a purely poloidal field. A set of values of B_{ave}
should cover the low-field case (where $D_{cl}>D_v$), the transi-
tion case, and several values of B_{ave} in the region where
$D_v>D_{cl}$. In the latter region, as B is changed, the ratio
E/B should be constant.

The collisionless plasma could be examined in the
same way, over a range of fields with $D=D_v$. In addition,
it is necessary to compare the toroidal spectra of the

electric field for the levitated and supported cases; this would determine whether the 'bump' on the supported spectrum at m~30 is in fact one of the effects of the supports. Since the diffusion studies imply that T^* is the same for the two cases, we would also expect the spectra to have the same magnitude.

APPENDIX A

DIFFERENTIAL OPERATORS IN OCTUPOLE COORDINATES

$$\vec{B}_p = \vec{\nabla}\chi = \vec{\nabla}\psi \times \vec{\nabla}\theta \tag{A.1}$$

$$ds_\psi = \frac{d\psi}{2\pi RB} \qquad e_1 = \frac{1}{2\pi RB} \tag{A.2}$$

$$ds_\theta = Rd\theta \qquad e_2 = R \tag{A.3}$$

$$ds_\chi = \frac{d\chi}{B} \qquad e_3 = \frac{1}{B} \tag{A.4}$$

$$\vec{\nabla}n = \hat{\psi}2\pi RB\frac{\partial n}{\partial\psi} + \frac{\hat{\theta}}{R}\frac{\partial n}{\partial\theta} + \hat{\chi}B\frac{\partial n}{\partial\chi} \tag{A.5}$$

$$\vec{\nabla}\cdot\vec{v} = 2\pi B^2 \frac{\partial}{\partial\psi}\left(\frac{Rv_\psi}{B}\right) + \frac{1}{R}\frac{\partial}{\partial\theta}(v_\theta) + B^2\frac{\partial}{\partial\chi}\left(\frac{v_\chi}{B}\right) \tag{A.6}$$

$$\vec{\nabla}\times\vec{v} = 2\pi B^2 \left[\frac{\hat{\psi}}{2\pi RB}\left(\frac{1}{B}\frac{\partial v_\chi}{\partial\theta} - \frac{\partial}{\partial\chi}(Rv_\theta)\right) \right.$$
$$+ \hat{\theta}R\left(\frac{1}{2\pi}\frac{\partial}{\partial\chi}\left(\frac{v_\psi}{RB}\right) - \frac{\partial}{\partial\psi}\left(\frac{v_\chi}{B}\right)\right)$$
$$\left. + \frac{\hat{\chi}}{B}\left(\frac{\partial}{\partial\psi}\left(Rv_\theta\right) - \frac{1}{2\pi RB}\frac{\partial}{\partial\theta}\left(v_\psi\right)\right) \right] \tag{A.7}$$

$$\nabla^2\phi = \nabla\cdot\nabla\phi = (2\pi B)^2\frac{\partial}{\partial\psi}\left(R^2\frac{\partial\phi}{\partial\psi}\right) + \frac{1}{R^2}\frac{\partial^2\phi}{\partial\theta^2} + B^2\frac{\partial^2\phi}{\partial\chi^2} \tag{A.8}$$

$$dV = \int_0^{2\pi}\int_0^{2\pi}\int \frac{1}{2\pi B^2}\,d\chi\,d\theta\,d\psi \tag{A.9}$$

REFERENCES

1. J. R. Drake, U. Wisconsin Ph. D. Thesis, PLP 549, (1974)

2. R. A. Dory, D. W. Kerst, D. M. Meade, W. E. Wilson, and C. W. Erickson, Phys. Fl. $\underline{9}$ (5), 997 (May 1966)

3. Gerald O. Barney and J. C. Sprott, Phys. Fl. $\underline{12}$ (3), 707 (1969)

4. J. A. Schmidt, U. Wisconsin Ph. D. Thesis (1969)

5. A. W. Molvik, U. Wisconsin Ph. D. Thesis (1971)

6. H. Forsen, D. Kerst, F. Mills, A. Molvik, J. Scmidt, J. Sprott, and K. Symon, in Third Conference on Plasma Physics and Controlled Nuclear Fusion Research, Novosibirsk, USSR (1968), paper CN-24/c-1

7. D. E. Lencioni, J. W. Poukey, J. A. Schmidt, J. C. Sprott, and C. W. Erickson, Phys. Fl. $\underline{11}$, 1115 (1968)

8. E. Mosburg, J. Appl. Phys. $\underline{40}$, 5290 (1969)

9. D. E. Lencioni and D. W. Kerst, Bull. Am. Phys. Soc. $\underline{15}$, 1466 (1970)

10. A. J. Cavallo, U. Wisconsin Ph. D. Thesis, PLP 628 (1975)

11. Alfred J. Cavallo, Phys. Fl. $\underline{19}$ (3), 394 (March 1976)

12. J. R. Drake, Phys. Fl. $\underline{16}$ (9), 1554 (Sept. 1973)

13. J. R. Greenwood, U. Wisconsin Ph. D. Thesis, PLP 658 (1975)

14. A. G. Butcher (A. Butcher Ehrhardt), Research Proposal, U. Wisconsin PLP 673 (April 1975)

15. G. A. Navratil, U. Wisconsin Ph. D. Thesis (1976)

16. J. R. Drake, James G. Berryman, Phys. Fl. $\underline{20}$ (5), 851 (May 1977)

17. J. B. Taylor and B. McNamara, Phys. Fl. $\underline{14}$ (7), 1492 (1971)

18. Hideo Okuda and John M. Dawson, Phys. Fl. <u>16</u> (3), 408 (March 1973)

19. G. Joyce and D. Montgomery, J. Plasma Physics <u>10</u> (1), 107 (1973)

20. D. Montgomery and G. Joyce, Phys. Fl. <u>17</u> (6), 1139 (1974)

21. J. B. Taylor, Phys. Lett. <u>40A</u> (1), 1 (1972)

22. D. Montgomery, Phys. Lett. <u>39A</u> (1), 7 (1972)

23. D. Montgomery, Physica <u>82C</u>, 111-124 (1976)

24. C. E. Seyler, Jr., Yehuda Salu, David Montgomery, and Georg Knorr, Phys. Fl. <u>18</u> (7), 803 (July 1975)

25. J. R. Drake, J. R. Greenwood, G. A. Navratil, R. S. Post, Phys. Fl. <u>20</u> (1), 148 (Jan. 1977)

26. G. A. Navratil, R. S. Post, A. Butcher Ehrhardt, Phys. Fl. <u>20</u> (1), 156 (Jan. 1977)

27. T. Kamimura and J. M. Dawson, Phys. Rev. Lett. <u>36</u> (6), 313 (Feb. 1976)

28. G. A. Navratil, private communication (to be published)

29. J. Rudmin, U. Wisconsin Ph. D. Thesis, (1974), PLP 587

30. G. A. Navratil, U. Wisconsin PLP 629

31. J. A. Schmidt and G. L. Schmidt, Phys. Fl. <u>13</u>, 1351 (1970)

32. M. Zarnstorff, U. Wisconsin PLP

33. Kenneth Evans, Jr., Phys. Fl. <u>16</u> (12), 2330 (1973)

34. K. Evans, U. Wisconsin PLP 458

35. K. Evans, U. Wisconsin PLP 491

36. D. Montgomery, presented at the India-USA Workshop on Plasma Physics, Ahmedabad, India (1976)

37. T. D. Lee, J. Appl. Math. <u>10</u>, 69 (1952)

38. S. Corrsin, *Advances in Geophysics*, No. 6, Atmospheric Diffusion and Air Pollution (Academic Press, New York, 1959)

39. Glenn Joyce, David Montgomery, and Mark Emery, Phys. Fl. <u>17</u> (1), 110 (Jan. 1974)

40. M. True and H. Okuda, Bull. Am. Phys. Soc. <u>19</u>, 879 (1974)

41. T. Ohkawa and D. W. Kerst, Il Nuovo Cimento <u>4</u>, 784 (1961)

42. C. Z. Cheng and H. Okuda, Princeton Plasma Physics Lab Report PPPL-1316 (Jan. 1977)

43. C. Z. Cheng and H. Okuda, Princeton Plasma Physics Lab Report PPPL-1204 (1976)

44. James W. Poukey, Phys. Fl. <u>10</u> (10), 2253 (Oct. 1967)

45. Gerald O. Barney, U. Wisconsin PLP 118 (April 1967)

46. Francis F. Chen, *Introduction to Plasma Physics*, Plenum Press, New York (1974)

47. D. L. Book, Shalom Fisher, and B. E. McDonald, Phys. Rev. Letts. <u>34</u> (1), 4 (6 Jan. 1975)

48. B. E. McDonald, J. of Comp. Phys. <u>16</u>, 360-370 (1974)

49. R. Saison, H. K. Wimmel and F. Sardei, Plasma Physics <u>20</u>, 1-20 (1978)

50. personal communication by S. Fisher to B. E. McDonald, quoted in ref. 48

51. G. A. Navratil and R. S. Post, Effect of Unguarded Internal Ring Supports in the Wisconsin Levitated Octupole, to be published.

52. S. I. Braginskii, in *Reviews of Plasma Physics*, ed. M. A. Leontovich (Consultants Bureau, N. Y., 1965), Vol. I, P. 214.

53. A. B. Ehrhardt, U. Wisconsin PLP 703 (Nov. 1976)

54. G. A. Navratil, private communication

55. David Montgomery and Glenn Joyce, Phys. Fl. $\underline{17}$ (6) 1139 (June 1974).

56. J. R. Drake, D. W. Kerst, G. A. Navratil, R. S. Post, University of Wisconsin, Madison, and S. Ejima, et al., General Atomic Co., IAEA-CN-35/D11, paper COO-2387-76.

57. J. R. Drake, D. W. Kerst, G. A. Navratil, R. S. Post, University of Wisconsin PLP 688.

58. R. S. Post, private communication

59. G. A. Navratil, R. S. Post, and A. Butcher Ehrhardt, Observation of the Effect of Shear on Vortex Diffusion in a Collisional Plasma, to be published.

60. R. H. Kraichnan, Phys. Rev. $\underline{113}$ (1959) 1181; J. Fluid Mech. $\underline{5}$ (1959) 497; Phys. Fl. $\underline{7}$ (1964) 1030.

61. J. R. Herring, S. A. Orszag, R. H. Kraichnan, and D. G. Fox, J. Fluid Mech. $\underline{66}$ (1974) 417.

62. G. A. Navratil and R. S. Post, Observation of Classical Diffusion in the Presence of Large Amplitude Fluctuations, to be published